SYNTHESIS AND CHARACTERIZATION OF CUCURBITURIL BASED PHOTOACTIVE MULTIFUNCTIONAL ASSEMBLIES

A DISSERTATION SUBMITTED TO
THE GRADUATE SCHOOL OF ENGINEERING AND SCIENCE
OF BILKENT UNIVERSITY
IN PARTIAL FULFILLMENT OF THE REQUIREMENTS FOR
THE DEGREE OF
DOCTOR OF PHILOSOPHY
IN
CHEMISTRY

By
Ahmet KOÇ
January 2019

SYNTHESIS AND CHARACTERIZATION OF CUCURBITURIL BASED PHOTOACTIVE MULTIFUNCTIONAL ASSEMBLIES

By Ahmet KOÇ
January 2019

We certify that we have read this dissertation and that in our opinion it is fully adequate, in scope and in quality, as a thesis for the degree of Doctor of Philosophy.

Dönüş TUNCEL (Advisor)

Hilmi Volkan DEMİR

Engin Umut AKKAYA

Canan ÜNALEROĞLU

Özdemir DOĞAN

Approved for the Graduate School of Engineering and Science:

Ezhan KARAŞAN
Director of the Graduate School

ABSTRACT

SYNTHESIS AND CHARACTERIZATION OF CUCURBITURIL BASED PHOTOACTIVE MULTIFUNCTIONAL ASSEMBLIES

Ahmet KOÇ
Ph.D. in Chemistry
Advisor: Dönüş TUNCEL
January 2019

Preparation of cucurbituril based functional materials and their use in various applications ranging from biomedicine to optoelectronics have been studied intensely over the last decade. Supramolecular assemblies, networks and nanostructures constructed through noncovalent interactions of cucurbiturils with π-conjugated, photoactive compounds have also been investigated and potential applications in the areas of theranostics, imaging, sensing and catalysis have been shown. In these cucurbituril based architectures, however, cucurbituril is disabled to act as a molecular receptor since they do not involve the covalent conjugation of cucurbituril directly to chromophore. The main motivation of this study is to synthesize multifunctional assemblies and nanostructures in which cucurbituril is covalently attached to various conjugated compounds including porphyrin, conjugated oligomers and polymers.

A new multifunctional porphyrin-cucurbituril conjugate based on a photoactive mannosylated porphyrin and monoporpargyloxycucurbit[7]uril was synthesized. Azido-functionalized tetraphenylporphyrin (TPP) was used as a building block. TPP was first mannosylated by copper-catalyzed azide-alkyne cycloaddition (CuAAC), then a monoporpargyloxycucurbit[7]uril was covalently attached to the mannosylated TPP with a second CuAAC reaction. Singlet oxygen generation efficiency of the supramolecular assembly was measured and found to be significantly higher than that of unfunctionalized TPP. ^{1}H NMR experiments were performed using a suitable guest,

bisimidazolium, to prove the availability of CB7 in the assembly as a host. Bisimidazolium guest was observed to form inclusion complex with CB7, which is a promising result for the potential use of this supramolecular assembly as a drug carrier in conjunction with photodynamic therapy.

Conjugated oligomers and polymers were synthesized from suitably-functionalized monomers via Pd-catalyzed cross-coupling reactions and their characterizations were performed. Their assemblies and nanostructures with covalently attached functionalized cucurbiturils were investigated. Redox sensitive crosslinked conjugated oligomer nanoparticles (CONs) were synthesized from a conjugated oligomer, OFVBt-N_3 and a disulfide bond-containing crosslinker via ultrasound-assisted copper-free click reaction in THF. These spherical and approximately 50 nm-sized CONs preserved their stability and size (≈60 nm) after dispersing them in water. The behavior of the CONs in the presence of glutathione (GSH) was studied in aqueous medium. It was observed that the CONs are rapidly disrupted by GSH, which is an effective S-S bond cleaving biomolecule that is overexpressed in cancer cells. These results imply that when nanoparticles are loaded with an anticancer drug, targeted delivery of the drug to cancer cells can be achieved by cooperative action of enhanced permeability and retention (EPR) effect and S-S bond cleavage by GSH.

Keywords: cucurbituril, porphyrin, click reaction, cross-coupling, photodynamic therapy, singlet oxygen, conjugated oligomer, nanoparticle, crosslinker.

ÖZET

KÜKÜRBİTÜRİL TABANLI ÇOK İŞLEVLİ FOTOAKTİF YAPILARIN SENTEZİ VE KARAKTERİZASYONU

Ahmet KOÇ
Kimya, Doktora
Tez Danışmanı: Dönüş TUNCEL
Ocak 2019

Kükürbitüril tabanlı işlevsel malzemelerin hazırlanması ve biyomedikalden optoelektroniğe uzanan farklı uygulamalarda kullanımı son yıllarda yoğun şekilde çalışılmaktadır. Kükürbitürillerin konjuge π-bağı içeren fotoaktif maddelerle kovalent olmayan etkileşimler aracılığıyla oluşturdukları supramoleküler yapılar, ağlar ve nanomalzemeler de araştırılmakta ve teranostik, görüntüleme, moleküler algılama ve kataliz alanlarındaki olası uygulamaları gösterilmektedir. Fakat, kükürbitüril tabanlı bu mimarilerde, kükürbitüril doğrudan kovalent bağlarla kromofora bağlanmadığından, bir moleküler reseptör olarak işlev gösterememektedir. Bu çalışmanın temel motivasyonu ise kükürbitürilin kovalent bağlarla porfirine, konjuge oligomere ve polimere bağlandığı çok işlevli platformların ve nanoyapıların sentezidir.

Fotoaktif mannozlanmış porfirin ve monoproparjiloksikükürbit[7]üril tabanlı yeni bir çok işlevli porfirin-kükürbitüril konjugesi sentezlendi. Azido-fonksiyonlu tetrafenilporfirin (TPP) yapı taşı olarak kullanıldı. Öncelikle, TPP, bakır katalizörlü azit-alkin siklokatılma (CuAAC) tepkimesi ile mannozlandı. Sonrasında, monoproparjiloksikükürbit[7]üril, ikinci bir CuAAC tepkimesi ile mannozlu TPP'ye kovalent bağla bağlandı. Elde edilen supramoleküler platformun singlet oksijen üretme verimliliği ölçüldü ve işlevselleştirilmemiş TPP'ninkinden önemli derecede yüksek olduğu kanıtlandı. Supramoleküler platformun yapısında bulunan kükürbit[7]ürilin konak molekül olarak elverişliliğinin kanıtlanması amacıyla uygun bir konuk molekül,

bisimidazolyum, kullanarak ^{1}H NMR deneyleri yapıldı. Bisimidazolyumun kükürbit[7]üril ile kuşatan kompleks oluşturduğu gözlemlendi ki bu sentezlenen supramoleküler platformun, fotodinamik tedavinin yanında ilaç taşıyıcı olarak da kullanılma potansiyelini gösteren umut verici bir sonuçtur.

Uygun şekilde fonksiyonel gruplarla donatılmış monomerler arasında Pd katalizli çapraz eşleşme reaksiyonları ile farklı yapıdaki konjuge oligomer ve polimerler sentezlendi ve karakterize edildi. Bu konjuge malzemelerin kovalent bağlanmış kükürbitüril ile oluşturdukları platformlar ve nanoyapılar çalışıldı. Bir konjuge oligomer, OFVBt-N_3, ve bir disülfit bağı içeren çapraz bağlayıcı kullanarak THF içinde ultrason yardımlı bakırsız çıt-çıt tepkimesi ile redoks duyarlı konjuge oligomer nanoparçacıkları (CONs) sentezlendi. Ortalama 50 nm boyutlu ve küresel yapıdaki bu nanoparçacıklar suda dağıldıktan sonra da boyut (≈60 nm) ve kararlılıklarını korudular. Nanoparçacıkların sulu ortamda, glutatiyon (GSH) varlığındaki davranışları çalışıldı ve kanser hücrelerinde aşırı üretilen bir biyomolekül ve etkili bir S-S bağı kırıcısı olan GSH tarafından nanoparçacıkların bozulduğu görüldü. Dolayısıyla, bu nanoparçacıklar bir kanser ilacıyla yüklendiğinde, ilacın kanser hücrelerine hedeflenmiş iletimi, artmış geçirgenlik ve alıkonma (EPR) etkisi ve S-S bağının GSH tarafından kırılmasının işbirliği ile başarılabilir.

Anahtar sözcükler: kükürbitüril, porfirin, çıt-çıt tepkimesi, çapraz eşleşme, fotodinamik terapi, singlet oksijen, konjuge oligomer, nanoparçacık, çapraz bağlayıcı.

Acknowledgement

First off, I must express my debt of gratitude to my advisor Assoc. Prof. Dönüş Tuncel, who has taught me a lot, given me the chance to conduct my Ph.D. studies in a warm and fruitful laboratory environment and guided me in the best way during hard times.

I would like to thank all other examining committee members, Prof. Dr. Hilmi Volkan Demir, Prof. Dr. Engin Umut Akkaya, Prof. Dr. Canan Ünaleroğlu and Prof. Dr. Özdemir Doğan for their time to review and evaluate my thesis.

I would like to extend my deepest thanks to all esteemed faculty members of the Chemistry Department of Bilkent University who has contributed to my scientific knowledge. I also thank Chemistry Department of Bilkent University and TUBİTAK for the financial support throughout my Ph.D. studies.

I need to express my deepest gratitudes to Dr. Rehan Khan for his guidance, expertise and help thanks to which I have been able to get through the toughest situations in the work. I would like to thank to my other current labmates, Dr. Yogesh Kumar, Dr. Aysan Khaligh Vazirabadi, Seyed Ehsan Hadi and Melis Özkan for their support and fruitful discusssions on my way to graduation. And of course, to the old members of the lab that I have met so far, Dr. Timuçin Balkan, Dr. Masoomeh Bazzar, Emre Köken, Obadah Albahra, Sinem Gürbüz, Esra Soner, Muazzam Idris, Hamidou Keita, Dr. Jousheed Pennakalathil and Alp Özgün, I extend my thanks for their support and help.

I would like to express my sincere thanks to Zeynep Erdoğan for her fruitful discussions on mass spectrometry.

I am glad that I met with Polatlı Cycling Club members who have been eternal friends to me and gave me the chance to release some stress during my Ph.D. works by joining their awesome activities and trainings.

Finally, I have to offer my most special thanks to my parents İbrahim Koç and Gülfer Koç and my siblings Gülşah and İlay, who have been the biggest energy sources for me to make it till now.

Dedication

To Fazlı Gür, who desired deeply to hear my graduation, yet passed away...

Contents

CHAPTER 1 Introduction.....1

1.1. Supramolecular Chemistry.....1

1.1.1. Host-Guest Chemistry.....5

1.1.1.1. Common Host Molecules in Host-Guest Chemistry.....7

1.1.1.1.1. Crown Ethers.....9

1.1.1.1.2. Cyclodextrins.....10

1.1.1.1.3. Cucurbiturils.....11

1.1.1.1.3.1. Synthesis of Cucurbituril Homologues and Their Derivatives.....11

1.1.1.1.3.2. Structural, Physical and Recognitive Properties of Cucurbit[n]urils.....14

1.2. Conjugated Compounds.....17

1.2.1. Conjugated Polymers and Oligomers.....17

1.2.1.1. Synthesis with Cross-Coupling Reactions.....18

1.2.1.2. Properties and Applications.....19

1.2.1.3. Conjugated Polymer and Oligomer Nanoparticles.....21

1.2.2. Porphyrins.....22

1.2.2.1. Synthesis of Porphyrins.....23

1.2.2.2. Photodynamic Therapy with Porphyrins.....24

1.3. Supramolecular Frameworks Constructed with Cucurbiturils and Conjugated Compounds.....26

1.3.1. Frameworks of CB[n]s with Conjugated Polymers and Oligomers.....26

1.3.2. Frameworks of CB[n]s and Porphyrins.....29

CHAPTER 2 Experimental.....32

2.1. Materials.....32

2.2. Characterization Techniques.....32

2.2.1. ^{1}H and ^{13}C NMR Spectroscopy.....32

2.2.2. Electrospray Ionization-Mass Spectrometry.....33

2.2.3. FT-IR Spectroscopy.....33

2.2.4. UV-Vis Absorbance Spectroscopy.....33

2.2.5. Fluorescence Spectroscopy....33
2.2.6. Dynamic Light Scattering and Zeta Potential....33
2.2.7. Thermal Gravimetric Analysis....34
2.2.8. Scanning Electron Microscopy....34
2.2.9. Transmission Electron Microscopy....34
2.2.10. Time-Resolved Fluorescence Spectroscopy....34
2.3. Syntheses....35
2.3.1. Clicked Porphyrin-Cucurbit[7]uril Conjugate....35
2.3.1.1. Synthesis of Cucurbit[n]urils....35
2.3.1.2. Synthesis of MonohydroxyCB7 (2)....36
2.3.1.3. Synthesis of MonopropargyloxyCB7 (3)....38
2.3.1.4. Synthesis of 1,4-Bis(imidazole-1-ylmethyl)benzene (4)....39
2.3.1.5. Synthesis of 1,1'-(1,4-phenylenebis(methylene)bis(3-methyl-1H-imidazol-3-ium) (5)....39
2.3.1.6. Synthesis of 5,10,15,20-tetrakis(α-bromo-p-tolyl)porphyrin (6)....40
2.3.1.7. Synthesis of 5,10,15,20-tetrakis(α-azido-p-tolyl)porphyrin (7)....41
2.3.1.8. Synthesis of Zinc 5,10,15,20-tetrakis(α-azido-p-tolyl)porphyrin (8)....42
2.3.1.9. Synthesis of Acetylated Mannose-attached Zn-TPP-N_3 (9)....43
2.3.1.10. Synthesis of Hydrolyzed Mannose-attached Zn-TPP-N_3 (10)....44
2.3.1.11. Synthesis of CB7-conjugated Mannose-attached TPP (11)....45
2.3.1.12. $^1O_2$ quantum yield measurement....46
2.3.2. Synthesis of Red-emitting Conjugated Polymer....47
2.3.2.1 Synthesis of 2-(2,5-dibromothiophen-3-yl)ethan-1-ol (M1)....47
2.3.2.2. Synthesis of 2,5-dibromo-3-(2-bromoethyl)thiophene (M2)....48
2.3.2.3. Synthesis of 3-(2-azidoethyl)-2,5-dibromothiophene (M3)....49
2.3.2.4. Synthesis of Azide-functionalized Thiophene Based Red-emitting Polymer (P1)....50
2.3.2.5. Procedure for Quantum Yield Measurement of P1....51
2.3.3. Synthesis of Tetrathiophene Oligomer....51
2.3.3.1. Synthesis of 2-(5-Bromo-2-thienyl)ethanol (M4)....51
2.3.3.2. Synthesis of 2,2'-([2,2':5',2'':5'',2'''-quaterthiophene]-5,5'''-diyl)diethanol (O1)....52

2.3.3.3. Synthesis of 5,5'''-bis(2-(prop-2-yn-1-yloxy)ethyl)-2,2':5',2'':5'',2'''-quaterthiophene (O2) 54
2.3.4. Crosslinked Conjugated Oligomer Nanoparticles 55
2.3.4.1. Synthesis of Crosslinked OFVBt-N_3 Nanoparticles in THF 55
2.3.4.2. Dispersion of Oligomer Nanoparticles in Water (NP3) 56
2.3.4.3. Disulfide Bond Cleavage by Glutathione (GSH) 57
CHAPTER 3 Results and Discussions 58
3.1. Introduction 58
3.2. "Clicked" Porphyrin-Cucurbit[7]uril Conjugate 58
3.2.1. Aim of the Study 58
3.2.2. Synthesis of Cucurbit[n]urils 61
3.2.3. Synthesis of MonohydroxyCB7 (2) 64
3.2.4. Synthesis of MonopropargyloxyCB7 (3) 67
3.2.5. Synthesis of 5,10,15,20-tetrakis(α-bromo-*p*-tolyl)porphyrin (6) 69
3.2.6. Synthesis of TPP-N_3 (7) 72
3.2.7. Synthesis of Zn-TPP-N_3 (8) 73
3.2.8. Glycosylation of Zn-TPP-N_3 75
3.2.9. Synthesis of TPP-2Man-2CB7 (14) 76
3.2.10. Characterization of TPP-Az-3AcMan (9) 83
3.2.11. Synthesis of TPP-Az-3Man (10) 85
3.2.12. Synthesis of TPP-3Man-CB7 (11) 87
3.2.13. Comparison of ^{1}H NMR and FT-IR spectra of TPP-Az-3AcMan, TPP-Az-3Man and TPP-3Man-CB7 90
3.2.14. Investigation of CB7's Behaviour as a Host in the Assembly 91
3.2.15. Photophysical Properties of TPP-Az-3AzMan, TPP-Az-3Man and TPP-3Man-CB7 92
3.2.16. Singlet Oxygen ($^1O_2$) Generation Capacities of TPP-Az-3AcMan, TPP-Az-3Man and TPP-3Man-CB7 93
3.3. Synthesis of Supramolecular Nanomaterials through Covalent Attachment of Cucurbiturils to Conjugated Polymers 96
3.3.1. Aim of the Study 96
3.3.2. Synthesis of Azide-functionalized Conjugated Polymer 99
3.3.2.1. Synthesis of 2-(2,5-dibromothiophen-3-yl)ethan-1-ol (M1) 99

3.3.2.2. Synthesis of 2,5-dibromo-3-(2-bromoethyl)thiophene (M2) 100
3.3.2.3. Synthesis of 3-(2-azidoethyl)-2,5-dibromothiophene (M3) 102
3.3.2.4. Synthesis of Red-emitting Azide-functionalized Thiophene-Benzothiadiazole Copolymer (P1) 103
3.3.2.5. Photophysical Properties of P1 105
3.3.3. Synthesis of Tetrathiophene Oligomer 106
3.3.3.1. Synthesis of 2-(5-Bromo-2-thienyl)ethanol (M4) 106
3.3.3.2. Synthesis of 2,2'-([2,2':5',2'':5'',2'''-quaterthiophene]-5,5'''-diyl)diethanol (O1) 107
3.3.3.3. Synthesis of 5,5'''-bis(2-(prop-2-yn-1-yloxy)ethyl)-2,2':5',2'':5'',2'''-quaterthiophene (O2) 109
3.3.3.4. Synthesis and Characterization of Crosslinked Polymer Nanoparticles (NP1) 110
3.4. Crosslinked Conjugated Oligomer Nanoparticles 114
3.4.1. Aim of the Study 114
3.4.2. Characterization of OFVBt-N_3 (16) and Disulfide Crosslinker (M8) 116
3.4.3. Synthesis of Crosslinked OFVBt-N_3 Nanoparticles in THF (NP2) 119
3.4.4. Dispersion of Crosslinked OFVBt-N_3 Nanoparticles in Water (NP3) 121
3.4.5. Disulfide Bond Cleavage by Glutathione (GSH) 123
CHAPTER 4 Conclusions and Future Works 125
References 127
Appendix 138

List of Figures

Figure 1.1 Relationships and differences between the scope of molecular and supramolecular chemistry....2

Figure 1.2 Illustration for how molecular building blocks come together to constitute various supramolecular systems: (a) host-guest complexation, (b) lattice inclusion, (c) self-assembly of complementary molecules....4

Figure 1.3 Enzyme-substrate complexation via induced-fit model. The binding site of the enzyme undergoes conformational change to attain a better steric match to the binding site of the substrate....6

Figure 1.4 Cation-binding hosts: **(a)** a crown ether, **(b)** a lariat ether, **(c)** a cryptand, **(d)** a calixarene. 8

Figure 1.5 Neutral guest-binding hosts: **(a)** a cyclophane, **(b)** a cyclodextrin, **(c)** a carcerand, **(d)** a resorcarene, **(e)** a cucurbituril....8

Figure 1.6 Chemical structure and anatomies of α-, β-, and γ-cyclodextrin....10

Figure 1.7 X-ray crystal structures of main CB[n] homologues 15

Figure 1.8 Structures of some common conjugated polymers....17

Figure 1.9 Catalytic cycles for **(a)** Suzuki and **(b)** Stille coupling reactions. 19

Figure 1.10 Band gap comparison of metals (conductors), semiconductors and insulators....20

Figure 1.11 Jablonski energy diagram showing radiative and nonradiative relaxation pathways. 21

Figure 1.12 (a) Structure of the parent porphyrin and **(b)** characteristic UV-Vis absorbance spectrum of porphyrins....23

Figure 1.13 Jablonski energy diagram for the generation of $^1O_2$. 25

Figure 1.14 Chemical structure and AFM images of PF-BT.CB7....27

Figure 1.15 Structure of the polyrotaxane and organic matrix elements (sucrose and trehalose) used in the construction of highly luminescent solid-state materials. 28

Figure 1.16 Synthesis of CB7-capped red-emitting oligomer NPs loaded with CPT and pH-triggered release of CPT from the NPs. 29

Figure 1.17 Preparation of AgNPs **(a)** pre- and **(b)** post-functionalized with CB7 and binding and release mechanism for TMPyP. 30

Figure 3.1 ^{1}H NMR spectrum of CB7 in D_2O. 62

Figure 3.2 ^{13}C NMR spectrum of CB7 in D_2O. 63

Figure 3.3 +ESI-MS spectrum of CB7. 63

Figure 3.4 FT-IR absorption spectrum of CB7. 64

Figure 3.5 ^{1}H NMR spectrum of CB7-$(OH)_1$ in D_2O. 65

Figure 3.6 ^{13}C NMR spectrum of CB7-$(OH)_1$ in D_2O. 65

Figure 3.7 +ESI-MS spectrum of CB7-$(OH)_1$. 66

Figure 3.8 FT-IR absorption spectrum of CB7-$(OH)_1$. 66

Figure 3.9 ^{1}H NMR spectrum of CB7-(O-propargyl)$_1$ in D_2O+NaCl. 67

Figure 3.10 ^{13}C NMR spectrum of CB7-(O-propargyl)$_1$ in D_2O+NaCl. 68

Figure 3.11 +ESI-MS spectra of CB7-(O-propargyl)$_1$. 68

Figure 3.12 FT-IR absorption spectrum of CB7-(O-propargyl)$_1$. 69

Figure 3.13 TGA graph of CB7-(O-propargyl)$_1$. 69

Figure 3.14 ^{1}H NMR spectrum of TPP-Br in $CDCl_3$. 71

Figure 3.15 +ESI-MS spectra of TPP-Br. 71

Figure 3.16 UV-Vis absorbance and fluorescence spectra of TPP-Br in DMSO. 72

Figure 3.17 ^{1}H NMR spectrum of TPP-N_3 in $CDCl_3$. 72

Figure 3.18 +ESI-MS spectrum of TPP-N_3. 73

Figure 3.19 ^{1}H NMR spectrum of Zn-TPP-N_3 in $CDCl_3$. 73

Figure 3.20 +ESI-MS spectrum of Zn-TPP-N_3. 74

Figure 3.21 FT-IR spectrum of Zn-TPP-N_3. 74

Figure 3.22 UV-Vis absorbance and fluorescence spectra of Zn-TPP-N_3 in chloroform. 75

Figure 3.23 TGA graph of Zn-TPP-N_3. 75

Figure 3.24 ^{1}H NMR spectrum of TPP-2Az-2AcMan in DMSO-d_6 77

Figure 3.25 ^{13}C NMR spectrum of TPP-2Az-2AcMan in DMSO-d_6 77

Figure 3.26 +ESI-MS spectrum of TPP-2Az-2AcMan 78

Figure 3.27 FT-IR spectrum of TPP-2Az-2AcMan. 78

Figure 3.28 ^{1}H NMR spectrum of TPP-2Az-2Man in DMSO-d_6. 79

Figure 3.29 ^{13}C NMR spectrum of TPP-2Az-2Man in DMSO-d_6. 80

Figure 3.30 -ESI-MS spectrum of TPP-2Az-2Man. 80

Figure 3.31 FT-IR spectrum of TPP-2Az-2Man 81

Figure 3.32 ^{1}H NMR spectrum of TPP-2Man-2CB7 in DMSO-d_6. 82

Figure 3.33 FT-IR spectrum of TPP-2Man-2CB7. 82

Figure 3.34 ^{1}H NMR spectrum of TPP-Az-3AcMan in DMSO-d_6. 83

Figure 3.35 ^{13}C NMR spectrum of TPP-Az-3AcMan in $CDCl_3$. 84

Figure 3.36 +ESI-MS spectrum of TPP-Az-3AcMan. 84

Figure 3.37 FT-IR spectrum of TPP-Az-3AcMan. 85

Figure 3.38 ^{1}H NMR spectrum of TPP-Az-3Man in DMSO-d_6 86

Figure 3.39 ^{13}C NMR spectrum of TPP-Az-3Man in DMSO-d_6 86

Figure 3.40 -ESI-MS spectrum of TPP-Az-3Man. 87

Figure 3.41 FT-IR spectrum of TPP-Az-3Man 87

Figure 3.42 ^{1}H NMR spectrum of TPP-3Man-CB7 in DMSO-d_6. 88

Figure 3.43 ^{13}C NMR spectrum of TPP-3Man-CB7 in DMSO-d_6. 89

Figure 3.44 +ESI-MS spectrum of TPP-3Man-CB7. 89

Figure 3.45 FT-IR spectrum of TPP-3Man-CB7. 90

Figure 3.46 Overlay of ^{1}H NMR spectra of **(A)** TPP-3Man-CB7, **(B)** TPP-Az-3Man and **(C)** TPP-Az-3AcMan (Spectra were recorded in DMSO-d_6). 90

Figure 3.47 Overlay of FT-IR spectra of **(A)** TPP-Az-3AcMan, **(B)** TPP-Az-3Man and **(C)** TPP-3Man-CB7. 91

Figure 3.48 ^{1}H NMR spectra of **(A)** 1,1'-(1,4-phenylenebis(methylene))bis(3-methyl-1H-imidazol-3-ium) iodide, (bisimidazolium) (in D_2O); **(B)** CB7-$(OH)_1$+1 equiv. bisimidazolium, (in DMSO-d_6:D_2O mixture, 1:2, v/v); **(C)** TPP-3Man-CB7+1 equiv. bisimidazolium (1.2 mM, in DMSO-d_6:D_2O mixture, 2:1, v/v); **(D)** TPP-3Man-CB7 (1.2 mM, DMSO-d_6). 92

Figure 3.49 Normalized UV-Vis absorbance and fluorescence spectra of TPP-Az-3AcMan (green), TPP-Az-3Man (blue),and TPP-3Man-CB7 (red) in DMSO. 93

Figure 3.50 Time-resolved fluorescence spectra of **(A)** TPP-Az-3Man and **(B)** TPP-3Man-CB7 in DMSO. 93

Figure 3.51 Decrease in the absorbance intensity of DPBF with 10 sec irradiation intervals in the presence of **(A)** methylene blue, **(B)** TPP-Az-3AcMan, **(C)** TPP-Az-3Man and **(D)** TPP-3Man-CB7. 94

Figure 3.52 Linearized plots based on the decrease in the absorbance intensity of DPBF in the presence of methylene blue, TPP-Az-3AcMan, TPP-Az-3Man and TPP-3Man-CB7 irradiated at 460 nm with 10 sec intervals. 95

Figure 3.53 ^{1}H NMR spectrum **M1** in $CDCl_3$. 99

Figure 3.54 ^{13}C NMR spectrum of **M1** in DMSO-d_6. 100

Figure 3.55 ^{1}H NMR spectrum of **M2** in $CDCl_3$. 101

Figure 3.56 ^{13}C NMR spectrum of **M2** in $CDCl_3$. 101

Figure 3.57 ^{1}H NMR spectrum of **M3** in $CDCl_3$. 102

Figure 3.58 ^{13}C NMR spectrum of **M3** in $CDCl_3$. 102

Figure 3.59 FT-IR spectrum of **M3**. 103

Figure 3.60 ^{1}H NMR spectrum of **P1** in $CDCl_3$. 104

Figure 3.61 ^{13}C NMR spectrum of **P1** in $CDCl_3$. 104

Figure 3.62 FT-IR spectrum of **P1**. 105

Figure 3.63 UV-Vis absorbance and fluorescence spectra of **P1** in THF..... 105

Figure 3.64 ^{1}H NMR spectrum of **M4** in $CDCl_3$..... 106

Figure 3.65 ^{13}C NMR spectrum of **M4** in $CDCl_3$..... 107

Figure 3.66 ^{1}H NMR spectrum **O1** in DMSO-d_6..... 108

Figure 3.67 ^{13}C NMR spectrum **O1** in $CDCl_3$..... 108

Figure 3.68 +ESI-MS spectrum **O1**..... 109

Figure 3.69 ^{1}H NMR spectrum of **O2** in $CDCl_3$..... 110

Figure 3.70 ^{13}C NMR spectrum of **O2** in $CDCl_3$..... 110

Figure 3.71 TEM, DLS and UV-vis absorbance and fluorescence graphs of **(a) P1:15** (4:1), **(b) P1:15** (8:1) and **(c) P1:15** (16:1)..... 112

Figure 3.72 FT-IR spectra of **P1:15** (1:8) before (red) and after (black) NP formation..... 113

Figure 3.73 ^{1}H NMR spectrum of OFVBt-N_3 in $CDCl_3$..... 116

Figure 3.74 FT-IR spectrum of OFVBt-N_3..... 117

Figure 3.75 UV-Vis absorbance and fluorescence spectra of OFVBt-N_3 in THF..... 117

Figure 3.76 ^{1}H NMR spectrum of **M8**..... 118

Figure 3.77 FT-IR spectrum of **M8**..... 118

Figure 3.78 Time-dependent FT-IR spectra of **16:M8** (1:2) NPs..... 119

Figure 3.79 **(a)** DLS and **(b)** zeta potential results of **16:M8** (1:2) NPs in THF..... 120

Figure 3.80 **(a)** SEM and **(b)** TEM image of **16:M8** (1:2) NPs in THF..... 120

Figure 3.81 UV-Vis absorbance and fluorescence spectra of **16:M8** (1:2) NPs in THF..... 121

Figure 3.82 **(a)** DLS and **(b)** zeta potential results of **NP3** at 0.5 mg/mL, and **(c)** DLS and **(d)** zeta potential results of **NP3** at 1.0 mg/mL..... 122

Figure 3.83 **(a)** SEM and **(b)** TEM images of **NP3** at 0.5 mg/mL..... 122

Figure 3.84 UV-Vis absorbance and fluorescence spectra of **16:M8** (1:2) NPs in THF (red) and **NP3** at 0.5 mg/mL (blue). 123

Figure 3.85 DLS results of **NP3** upon addition of GSH after **(a)** 1 hour and **(b)** 1 day. 124

Figure A1 ^{1}H NMR spectrum of compound **4** in D_2O. 138

Figure A2 ^{1}H NMR spectrum of compound **5** in DMSO-d_6. 138

Figure A3 ^{13}C NMR spectrum of Zn-TPP-N_3 in DMSO-d_6. 139

Figure A4 ^{1}H NMR spectrum of acetylated propargylated mannose in $CDCl_3$. 139

Figure A5 FT-IR spectrum of acetylated propargylated mannose. 140

Figure A6 ESI-MS spectra of TPP-Az-3AcMan. 140

Figure A7 Photos of the TLC plate of crude mixture after mannosylation of TPP and TLC monitoring of the silica gel column for the separation of products: TPP-3Az-AcMan, TPP-2Az-2AcMan, TPP-Az-3AcMan, TPP-4AcMan. 141

Figure A8 A sample of TPP-3Man-CB7 (**11**) in water/DMSO (4/1, v/v) mixture. Solution is clear over several days. 141

Figure A9 Monitoring the change in absorbance intensity of DPBF saturated with O_2 with 10 sec irradiation intervals in the absence of any photosensitizers. Its seen that absorbance intensity of DPBF does not decrease when there is no photosensitizer in the solution that can generate $^{1}O_2$. 142

Figure A10 UV-Vis absorbance spectra of **P1** at different concentrations and absorbance vs. concentration plot for the calculation of molar extinction coefficient. 143

Figure A11 UV-Vis absorbance and fluorescence spectra of **P1** (A, B), Fluorescein (C, D) and Rhodamine 6G (E, F) at various concentrations for fluorescence quantum yield calculations. 144

Figure A12 Linearized integrated PL intensity vs. absorbance graphs of **P1** (A, B), Fluorescein (C, D) and Rhodamine 6G (E, F) at various concentrations for fluorescence quantum yield calculations. 145

List of Schemes

Scheme 1.1 Accidental synthesis of dibenzo[18]crown-16, the first crown-ether. 9

Scheme 1.2 Synthesis of CB[n] homologues. 12

Scheme 1.3 Synthesis of (a) perhydroxylated and peralkylated and (b) monohydroxylated and monoalkylated CB[n]s. 13

Scheme 3.1 (a) Synthesis of monofunctionalized CB7: (i) $K_2S_2O_8$, K_2SO_4, H_2O, 85 °C; (ii) NaH, propargyl bromide, DMSO, 0°C-25 °C, N_2(g), 48 h. **(b)** (iii) Synthesis of the assembly: $CuSO_4.5H_2O$/Na-L-Ascorbate, THF/H_2O, 60 °C; 14 h (iv) $NaOCH_3$, MeOH, 25 °C, 14 h; (v) $CuSO_4.5H_2O$/Na-L-Ascorbate, DMSO/H_2O, 48 h. 60

Scheme 3.2 (a) Depolymerization of paraformaldehyde. **(b)** Formation mechanism of CB[n]. 61

Scheme 3.3 One-pot synthesis of TPP-Br. Condensation of the aldehyde with pyrrole yields porphyrinogen, which is then oxidized to TPP-Br. 70

Scheme 3.4 Reaction between $^1O_2$ and DPBF and subsequent formation of colorless 1,2-dibenzoylbenzene. 94

Scheme 3.5 Synthetic pathway for azide-functionalized conjugated polymer (**P1**).97

Scheme 3.6 Preparation of Red-emitting crosslinked polymer nanoparticles (**NP1**). 97

Scheme 3.7 Synthesis of propargylated tetrathiophene. 98

Scheme 3.8 Preparation of **O2-CB7** conjugate through CuAAC. 98

Scheme 3.9 Formation mechamism of **M1**. 99

Scheme 3.10 Formation mechanism of **M2** through Appel reaction. 100

Scheme 3.11 Formation mechanism of **M4** through Appel reaction. 106

Scheme 3.12 Synthetic routes for **(a)** OFVBt-N_3 oligomer **(b)** disulfide bond-containing crosslinker (**M8**). 115

Scheme 3.13 Preparation of crosslinked OFVBt-N_3 NPs (**NP2**) in THF. (Note the given crosslinking pattern within the NPs is just a probable pattern out of many possibilities)..... 115

List of Tables

Table 1.1 Summary of covalent and noncovalent interactions..... 3

Table 1.2 Binding constants of some crown ethers towards given cations in methanol at 20 °C (log K)..... 9

Table 1.3 Structural parameters of uncomplexed CB[n], iCB[n] and CD homologues 15

Table 1.4 Some examples of suitably-sized guests for CB[n] homologues (n = 5-8) 16

List of Abbreviations

CB	Cucurbituril
CD	Cyclodextrin
CONs	Conjugated Oligomer Nanoparticles
CPNs	Conjugated Polymer Nanoparticles
DCM	Dichloromethane
DLS	Dynamic Light Scattering
DMF	Dimethylformamide
DMSO	Dimethylsulfoxide
DPBF	1,3-diphenylisobenzofuran
ESI-MS	Electrospray Ionization Mass Spectrometry
EtOAc	Ethyl acetate
FRET	Förster Resonance Energy Transfer
FT-IR	Fourier Transfer Infrared Spectroscopy
Man	Mannose
MeOH	Methanol
NMR	Nuclear Magnetic Resonance
NPs	Nanoparticles
PDT	Photodynamic Therapy
PL	Photoluminescance
PS	Photosensitizer
SEM	Scanning Electron Microscopy
TBAB	Tetra-n-butylammonium bromide
TCBQ	Tetrachloro-*p*-benzoquinone
TEM	Transmission Electron Microscopy
TGA	Thermogravimetric Analysis
THF	Tetrahydrofuran
TLC	Thin Layer Chromatography
TPP	Tetraphenylporphyrin
$^1O_2$	Singlet oxygen
λ	Wavelength
Φ_f	Fluorescence quantum yield
Φ_Δ	Singlet oxygen quantum yield

List of Compound Names and Codes

1	Cucurbit[7]uril (CB7)
2	MonohydroxyCB7 (CB7-$(OH)_1$)
3	MonopropargyloxyCB7 (CB7-(O-propargyl)$_1$)
4	1,4-Bis(imidazole-1-ylmethyl)benzene
5	1,1'-(1,4-phenylenebis(methylene)bis(3-methyl-1H-imidazol-3-ium)
6	5,10,15,20-tetrakis(α-bromo-*p*-tolyl)porphyrin (TPP-Br)
7	5,10,15,20-tetrakis(α-azido-*p*-tolyl)porphyrin (TPP-N_3)
8	Zinc 5,10,15,20-tetrakis(α-azido-*p*-tolyl)porphyrin (Zn-TPP-N_3)
9	Acetylated mannose-attached TPP (TPP-Az-3AcMan)
10	Hydrolyzed mannose-attached TPP (TPP-Az-3Man)
11	CB7-conjugated mannose-attached TPP (TPP-3Man-CB7)
12	Acetylated mannose-attached TPP (TPP-2Az-2AcMan)
13	Hydrolyzed mannose-attached TPP (TPP-2Az-2Man)
14	CB7-conjugated mannose-attached TPP (TPP-2Man-2CB7)
15	Multipropargylated CB8
16	Azide-functionalized fluorene-benzothiadiazole oligomer (OFVBt-N_3)
M1	2-(2,5-dibromothiophen-3-yl)ethan-1-ol
M2	2,5-dibromo-3-(2-bromoethyl)thiophene
M3	3-(2-azidoethyl)-2,5-dibromothiophene
M4	2-(5-Bromo-2-thienyl)ethanol
M8	Disulfide crosslinker
NP1	Crosslinked P1 nanoparticles in water
NP2	Crosslinked OFVBt-N_3 NPs in THF
NP3	Dispersion of NP2 in water
O1	2,2'-([2,2':5',2'':5'',2'''-quaterthiophene]-5,5'''-diyl)diethanol
O2	5,5'''-bis(2-(prop-2-yn-1-yloxy)ethyl)-2,2':5',2'':5'',2'''-quaterthiophene
P1	Azide-functionalized thiophene based red-emitting polymer

CHAPTER 1

Introduction

1.1. Supramolecular Chemistry

Supramolecular chemistry is a field of chemistry that encompasses the formation of new chemical entities by noncovalent interactions between molecules and investigates molecular recognition properties. Because it deals with high-order frameworks, it is also described as "chemistry beyond the molecule". The emergence of supramolecular chemistry as a well-established field of chemistry dates back to 1987 when the Nobel Prize in Chemistry was awarded to Donald James Cram, Jean-Marie Lehn and Charles John Pedersen *"for their development and use of molecules with structure-specific interactions of high selectivity".*[1]

Molecular chemistry and supramolecular chemistry cannot be thought as independent from each other. The building blocks of a *supramolecule,* conventionally named as 'host' and 'guest', are individually *molecules* and their structural, chemical and physical properties are within the scope of molecular chemistry. *Supramolecule* acquires specific characteristics, functions and properties once the host and the guest come together via noncovalent interactions as illustrated in Figure 1.1.

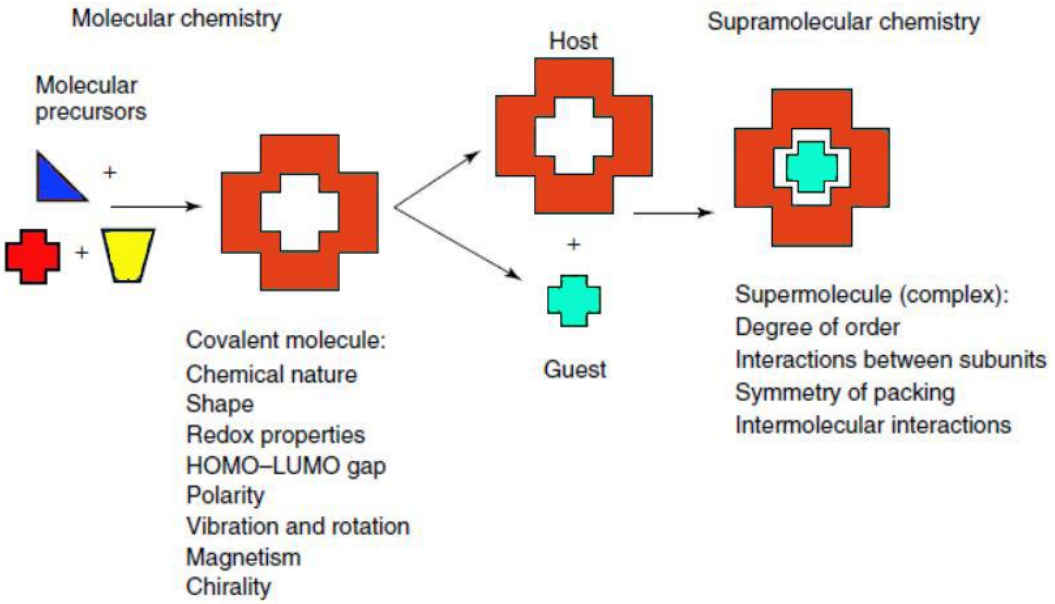


Figure 1.1 Relationships and differences between the scope of molecular and supramolecular chemistry.

The noncovalent interactions leading up to the development of supramolecular assemblies span a wide range of forces: ion-ion, ion-dipole, dipole-dipole, H-bonding, anion-π, cation-π, π-π, van der Waals and hydrophobic interactions. As summarized in Table 1.1, the strength of covalent bonds vary between 150-1075 kJ mol^{-1} while that of noncovalent interactions range from 1 to 350 kJ mol^{-1}. Although noncovalent interactions are significantly weaker than covalent interactions, the joint action of multiple of these noncovalent interactions can create a stable supramolecular complex.[2]

The scope of supramolecular chemistry is not only restricted to *host-guest* type of complexes. It also spans a broad area of *self-assembly* processes which include molecular machines, devices, logic gates and molecular recognition. What distinguishes these two branches of supramolecular chemistry is the differences in size and structure of building blocks. Donald J. Cram defines the host as *"an organic molecule or ion whose binding sites converge in the complex"* and the guest as *"any molecule or ion whose binding sites diverge in the complex"*.[4] As implied in Cram's definition, the 'host' must

Interaction	Type	Strength (kJ mol^{-1})	Example
Covalent			
	Single bond	150-450	C-C
	Double bond	420-750	C=C
	Triple bond	835-1075	C≡N
Noncovalent			
	Ion-ion	100-350	Tetrabutylammonium chloride
	Ion-dipole	50-200	Sodium [15]crown-5
	Dipole-dipole	5-50	Acetone
	Hydrogen bond	4-120	Double helix of DNA
	Cation-π	5-80	K^+ in benzene
	π-π	0-50	Benzene and graphite
	van der Waals	<5 but variable depending on surface area	Argon; packing in molecular crystals
	Hydrophobic	Related to solvent-solvent interaction energy	Cyclodextrin inclusion compounds

Table 1.1 Summary of covalent and noncovalent interactions.[2]

be big enough to accomodate the 'guest' by wrapping around it or, in other words, the 'guest' must be small enough to be encircled by the 'host' (Figure 1.2a). Enzyme-substrate complexation in biological systems is one of the widely known example for the host-guest systems, namely *inclusion compounds*. *Clathrates*, the solid state inclusion compounds, can only be synthesized in crystalline form because the guest is accomodated inside a hole formed in consequence of the packing of the host crystal lattice (Figure 1.2b).[2] On the contrary, the sizes of the building blocks are more or less the same in the case of self-assembly as illustrated in Figure 1.2c. The double helix structure of DNA, for instance, is a result of self-assembly between two strands of nucleotides through hydrogen bonding and π-π stacking interactions.

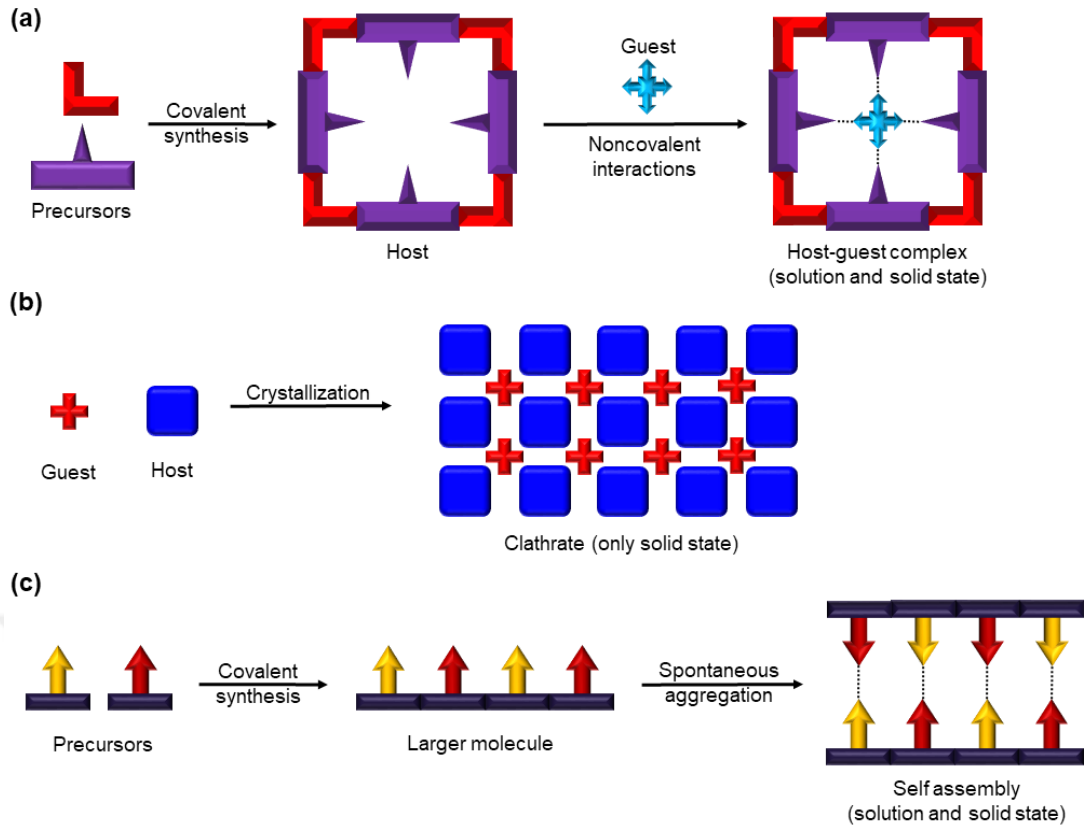


Figure 1.2 Illustration for how molecular building blocks come together to constitute various supramolecular systems: (a) host-guest complexation, (b) lattice inclusion, (c) self-assembly of complementary molecules.

The supramolecular constructions has been extensively studied in a number of fields such as molecular machines and logic gates, molecular recognition, molecular sensors, chemical catalysis, drug delivery, gas capture, and nanoreactors.[5] Meanwhile, supramolecular chemistry has also provided a powerful manner for the understanding of the concept of chemical information that is being stored at the molecular level and applied in the supramolecular level in the construction of small or large scale assemblies. Therefore, the universal notion of self organization that is responsible from the development of complex matter in the universe can now be based on much stronger evidences thanks to supramolecular chemistry.[6]

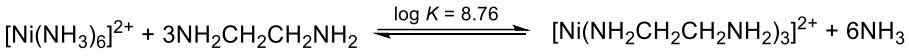
1.1.1. Host-Guest Chemistry

As mentioned in the previous section, host-guest chemistry is a branch of supramolecular chemistry which studies inclusion complexes constituted by large 'host' molecules and small 'guest' molecules via noncovalent interactions summarized in Table 1.1. Host molecules possess converging binding sites while guest molecules have diverging binding sites. Host-guest complexes are typically divided into two based on their stabilities in solution: cavitates and clathrates. A cavitate is a host-guest aggregate formed by a host (cavitand) that has an intrinsic molecular cavity with particular guest binding sites. Cavitates are most likely to preserve their complex structures in solution and solid states since cavitands act as a host in both solution and solid phases.[2] Clathrates are comprised of a host (clathrand) that is stable only in the solid form due to the formation of extended crystal lattice. The empty sites in the crystal lattice can accomodate suitably-sized guest molecules. However, the whole lattice structure of a clathrate disrupts in the solution phase, extramolecular cavities vanish and no host-guest complexation could be possible between the clathrate and the guest.[3] The term 'clathrate' was introduced in 1948 by H. M. Powell, suggesting that there are such compounds where one molecule is firmly enclosed by the other without any strong attractive forces, i.e., covalent bonds.[7]

Host-guest systems are also classified based on which type of attractive forces acting between host and guest. If the major forces that keep host and guest together are electrostatic interactions like ion-dipole, dipole-dipole or H-bonding, the host-guest aggregate is called *complex*. In the case of weaker and non-directional interactions (including van der Waals, hydrophobic or crystal close-packing forces), the aggregates are named *clathrates* or *cavitates*. However, these subclasses are not sharply separated and most frequently the term 'complex' is preferred for all of them.

The discussion of interaction between host and guest can now be moved to a different ground: 'selectivity' of the host. The concept of selectivity can be discussed with three important subconcepts: cooperativity, complementarity and preorganization.

- *Cooperativity:* In supramolecular chemistry, cooperativity means that a host molecule with two or more binding sites form a more stable complex than a host molecule with only one binding site. This is an extended version of *chelate effect* in coordination chemistry. Consider the example below:



As logarithm of the binding constant (log K) indicates, nickel complex with bidentate ethylenediamine ligand is 10^8 times more stable than that with unidentate ammonia ligand. The greater stability of chelate arises from a decrease in enthalpy (ΔH°) and increase in entropy (ΔS°) during the above reaction, which finally gives a lower total free energy of complexation (ΔG°) according to following equation: $\Delta G^\circ = \Delta H^\circ - T\Delta S^\circ$.[8]

- *Complementarity:* Structural and chemical complementarity between the binding sites of host and guest is needed to achieve a stable supramolecular complex. The host must possess binding sites that are of the correct size and shape to have sterical fit with the binding sites of the guest. In addition to steric fit, the binding sites of the host must also be of the proper electronic (chemical) character to complement those of the guest. The host molecule can undergo conformational changes to achieve the best complementary state towards the guest as in the case of enzyme-substrate complexation via induced-fit model (Figure 1.3).

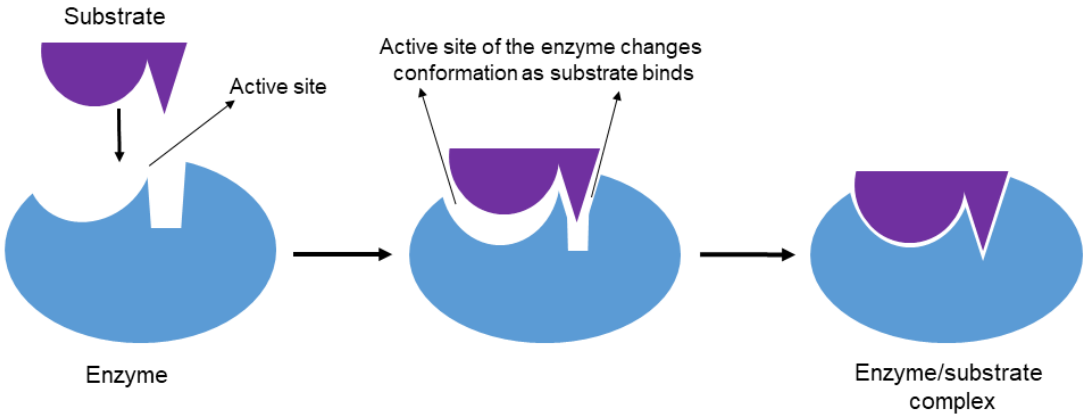


Figure 1.3 Enzyme-substrate complexation via induced-fit model. The binding site of the enzyme undergoes conformational change to attain a better steric match to the binding site of the substrate.

- *Preorganization:* Exceptional stability of most of the supramolecular host-guest complexes stems from the presence of preorganized hosts. In such hosts, the binding sites are organized in such a way that no significant conformational change is required to bind to a guest in the most stable

manner.[9] The hosts are generally in macrocyclic form and have well-defined binding sites. Overall, the preorganization of the host in macrocylic structure results in an enhanced guest binding due to both enthalpic and entropic effects.[2] This discussion is limited here, but further discussions are presented in ref. 2.

The degree of selectivity of a host towards a guest is described by to what extent the host is able to recognize the target guest from a pool of various guests. Two sorts of selectivity are taken into account when evaluating the overall selectivity of a host: (1) *Thermodynamic selectivity* is given by the ratio: Selectivity = K_{Guest1} / K_{Guest2} and it can be related to the total Gibbs free energy change of the system by $\Delta G = -RT \ln K$. Hosts can be rationally designed as thermodynamically selective for certain guests.[2] (2) *Kinetic selectivity* is defined by the transformation rate of competing guests (substrates) through a reaction path. To make it clear, a host (enzyme) would be selective for a substrate with higher transformation rate rather than a substrate with stronger binding constant.[3]

1.1.1.1. Common Host Molecules in Host-Guest Chemistry

In solution host-guest chemistry, the nature of a guest molecule is an important factor in determining what kind of host molecule should be designed in order to form a stable host-guest complex. As it is discussed in Section 1.1.1, chemical (electronic) complementarity between host and guest is one of the key elements for good selectivity. The electronic nature of the guests can be defined as cationic, anionic or neutral and therefore the hosts can be evaluated in three different groups: cation-binding, anion-binding and neutral guest-binding.

Plenty of cation binding hosts have been designed including crown ethers, cryptands, lariat ethers and podands, spherends, hemispherends, cryptaspherends, heterocrowns, heterocryptands, calixarenes and cucurbiturils. Structures of some of them are given in Figure 1.4. The complexation of these hosts with cationic guests occurs generally via hydrogen bonding, ion-dipole, cation-π or π-π interactions.[2]

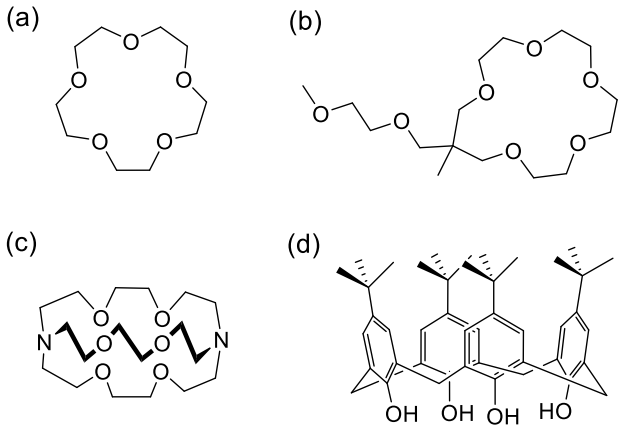


Figure 1.4 Cation-binding hosts: **(a)** a crown ether, **(b)** a lariat ether, **(c)** a cryptand, **(d)** a calixarene.

Anion-binding hosts can be neutral (e.g. zwitterions, amide-based receptors, urea and thiourea derivatives, peptide-based receptors) or positively-charged (e.g. katapinands, azacorands, cyclophanes, guanidium-based receptors).[10,11] Positively-charged hosts are usually obtained by changing the pH of the solution of a cation-binding host. Electrostatic interactions and H-bonding play role in anion binding.

A neutral guest-binding host has a highly-preorganized structure with an intrinsic curvature. Cyclophanes, calixarenes, resorcarenes, carcarands, hemicarcarands, cyclodextrins and cucurbiturils are well-known neutral guest-binding receptors (Figure 1.5). Ion-dipole, dipole-dipole, cation-π, π-π and hydrophobic interactions play role in host-neutral guest complexations.

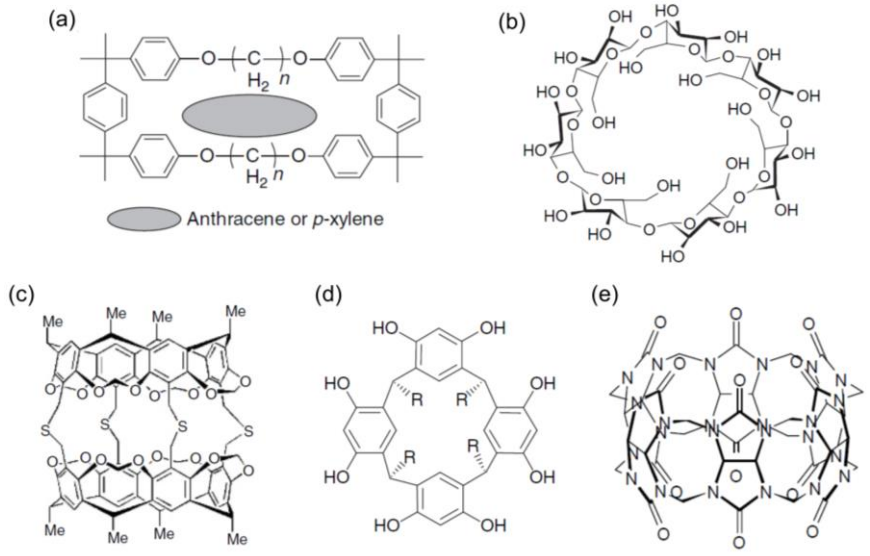
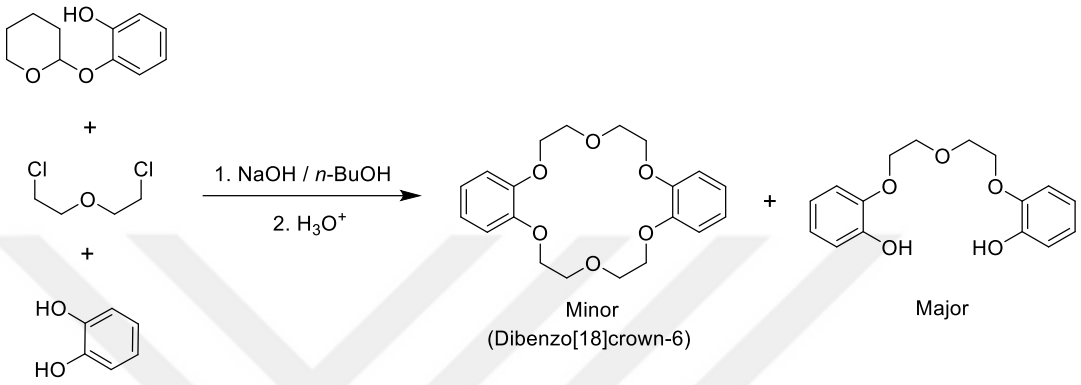


Figure 1.5 Neutral guest-binding hosts: **(a)** a cyclophane, **(b)** a cyclodextrin, **(c)** a carcerand, **(d)** a resorcarene, **(e)** a cucurbituril.

1.1.1.1.1. Crown Ethers

Crown ethers are one of the macrocyclic host molecules with high binding affinities for metallic and organic cations. The first example of crown ethers (dibenzo[18]crown-6) was incidentally synthesized as a result of the reaction given in Scheme 1.1 by Charles J. Pedersen in 1967, which later on brought him a Nobel Prize in 1987.[3,12]



Scheme 1.1 Accidental synthesis of dibenzo[18]crown-16, the first crown-ether.

Pedersen's further studies revealed important information on cation binding affinities of crown ethers and the synthesis of crown ether derivatives (azacrowns and thiacrowns). Crown ethers simply wrap around the cationic guest by changing their conformations in a way that maximizes M^+····O electrostatic interactions. Binding constants of various crown ethers are given in Table 1.2. The size and charge of the metal cation, and the size of the crown ether are significant factors for the value of log K.[2]

Crown ether	Na^+	K^+	Rb^+	Cs^+	Ca^{2+}	NH_4^+
[12]crown-4	1.70	1.30	-	-	-	-
[15]cronw-5	3.24	3.43	-	2.18	2.36	3.03
[18]crown-6	4.35	6.08	5.32	4.70	3.90	4.14
[21]crown-7	2.52	2.35	-	5.02	2.80	3.27
Benzo[18]crown-6	4.30	5.30	4.62	3.66	3.50	-

Table 1.2 Binding constants of some crown ethers towards given cations in methanol at 20 °C (log K).[2]

1.1.1.1.2. Cyclodextrins

A rigid macrocyclic structure with an intrinsic cavity is a requirement for complexation with organic guests.[3] Cyclodextrins, which were discovered by A. Villier in 1891 while he was working on the enzymatic degradation and reduction of cellulose, are among such structures having an intrinsically rigid and deep cavity.[13] They are usually composed of six to eight D-glucopyranoside units connected through a 1,4-glycosidic bond and their frameworks are bowl-shaped which is fixed by intramolecular H-bonding. The most common cyclodextrin homologues are called α-, β-, and γ-cyclodextrin that contain six, seven and eight glucopyranoside units, respectively (Figure 1.6).[3] Water soluble 1:1 or 1:2 inclusion complexes can be obtained in the presence of hydrophobic guests. The hydrophobic cavity easens the encapsulation of suitably-sized hydrophobic molecules and hydroxyl groups in the upper and lower rims helps to solubilize the complex in water. Due to their high water solubility (especially α- and β-cyclodextrins), good complexation and decomplexation properties and ease of functionalization to adjust solubility and affinity properties for a specific guest, cyclodextrins are today extremely important agents in industries such as pharmaceuticals, food and cosmetics. They are most generally used as compound-delivery, slow release or enzyme-mimetic agents.[3]

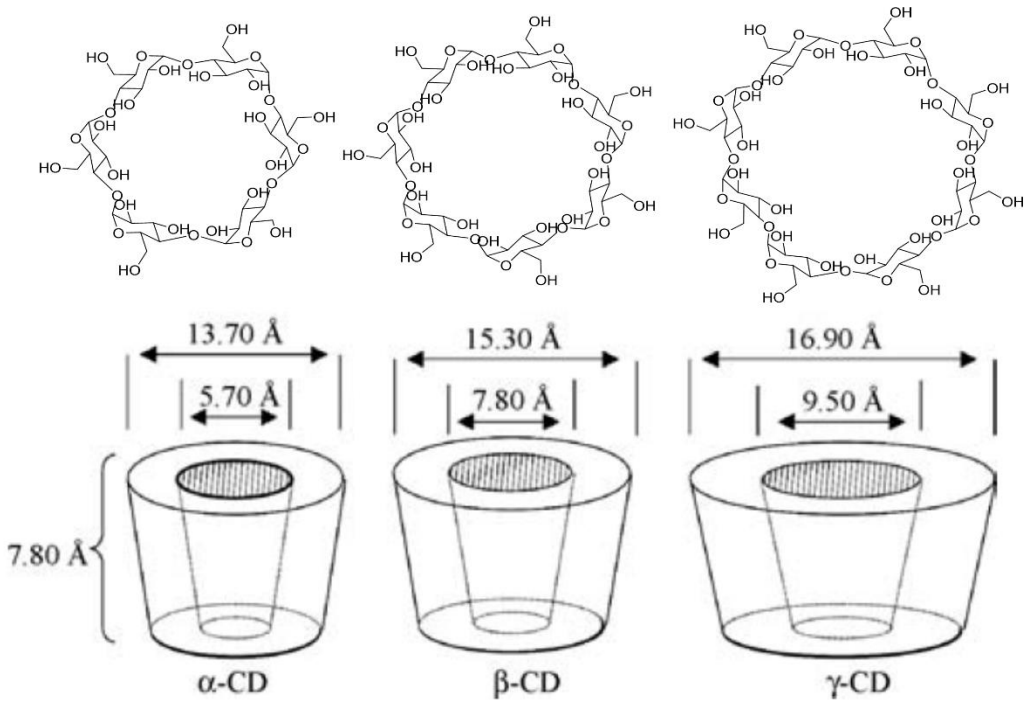


Figure 1.6 Chemical structure and anatomies of α-, β-, and γ-cyclodextrin.[3]

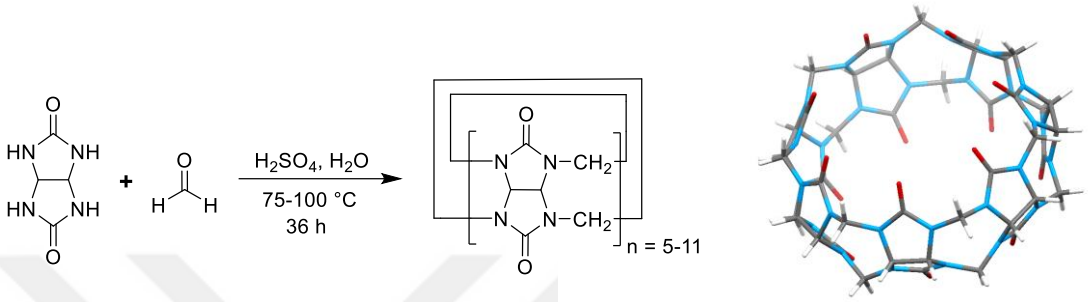
1.1.1.1.3. Cucurbiturils

The robust macrocyclic structures that are synthesized from the condensation reaction of glycoluril with formaldehyde in the presence of an acid catalyst are called 'cucurbiturils', abbreviated as 'CB'. This interesting name is given since the shape of this particular macrocycle resembles to a pumpkin, which is under *cucurbitaceae* botanic family. In 1905, a German chemist named Robert Behrend and his coworkers were for the first time able to synthesize the molecule, investigate its complexation properties with various metal salts and organic molecules, and identify its water solubility in the presence of cationic species.[14] Despite these initial findings, no further development has been made in CB chemistry until 1980s because its molecular structure was an unknown for scientists through many decades. In 1981, Mock and his coworkers finally came up with the unique pumpkin-shaped macrocyclic hexameric structure of cucurbit[6]uril (CB6), that is composed of two hydrophilic portals decorated with carbonyls and a hydrophobic cavity.[15] In the beginning of 2000s, independent studies of Kimoon Kim and Anthony Day resulted in the discovery of new CB[n] homologues, that are CB5, CB7, CB8, and CB10, comtaining 5, 7, 8 and 10 glycoluril units, respectively.[16,17] All these CB homologues having differences in their cavity size, guest binding affinity, size selectivity and water solubility have drawn interest by chemists in recent years.[18-22] Scientists are now trying to employ CBs in various applications such as drug delivery[23-27], catalysis[28-30], molecular switches[31-33], rotaxanes and polyrotaxanes[34,35] and molecular sensing[36,37].

1.1.1.1.3.1. Synthesis of Cucurbituril Homologues and Their Derivatives

Procedures used today for the synthesis of CB homologues have been developed in previous decade by Kimoon Kim[16], Anthony Day[17] and Lyle Isaacs[38]. The general procedure involves heating a mixture of glycoluril and formaldehyde (or paraformaldehyde) in the presence of HCl or H_2SO_4 to 80-100 °C for 10-100 hours (Scheme 1.2).[18] The reaction yields a mixture of CB[n]s (n = 5-8 and 10, CB6 with the highest amount) and other noncyclic oligomers. The protocols for the isolation and purification of different homologues are designed based on

their differential solubility in water, methanol and HCl. CB7, the most water soluble CB[n] homologue, is simply separated from a mixture of CB[n]s by solubilizing it in a hot 20% aqueous glycerol solution.[17,39] Scherman *et al.* proposed an alternative approach for the isolation of CB5 and CB7, which involves complexation of CB7 with a suitably sized guest (1-ethyl-3-methylimidazolium bromide) followed by anion exchange.[40]

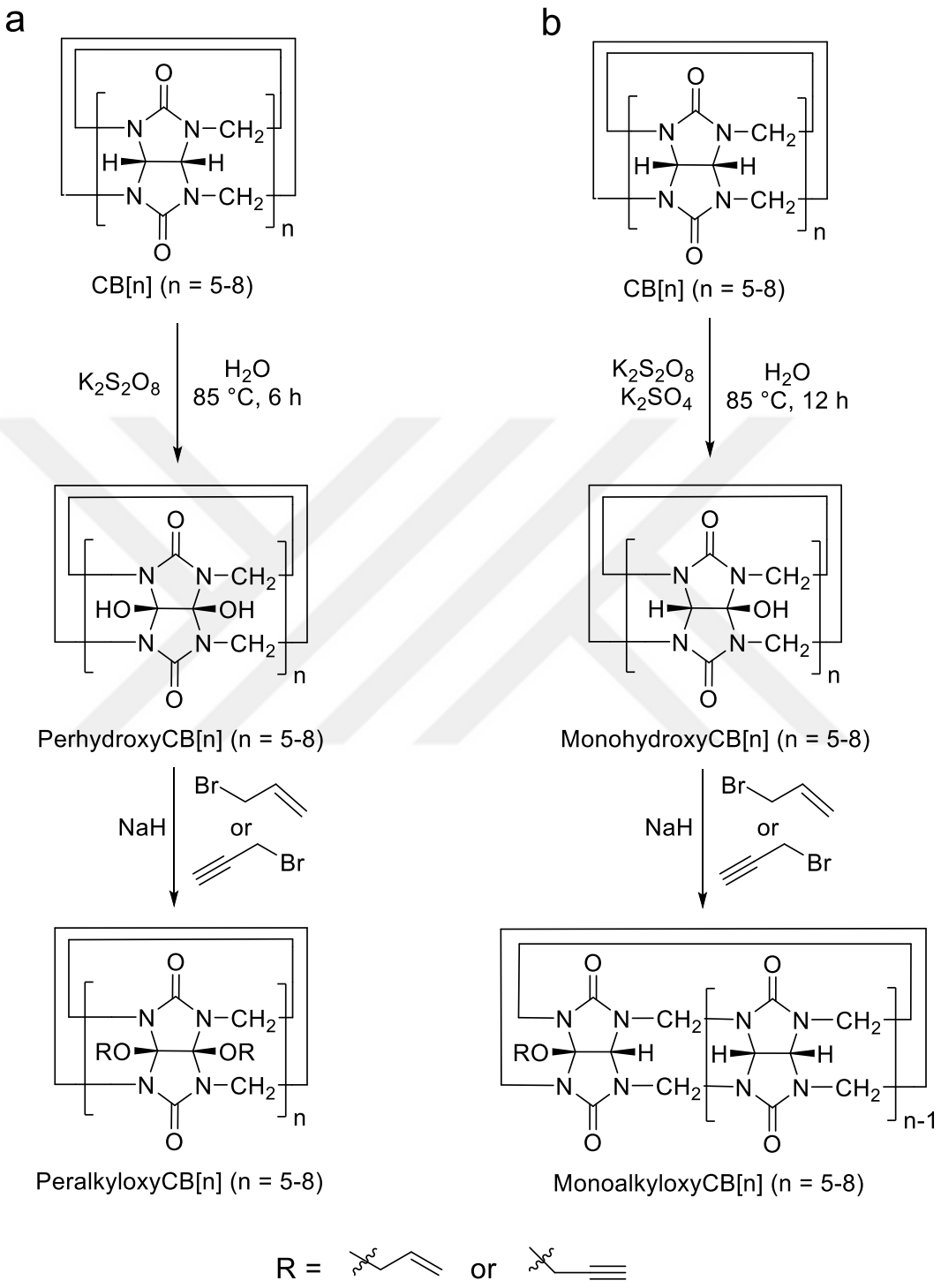


Scheme 1.2 Synthesis of CB[n] homologues.

Chemists have studied a lot on the synthesis of new CB[n] derivatives to increase their solubility or to render them more versatile in various applications. The first example dates back to a study by Fraser Stoddart *et al.* in 1992, in which they prepared equatorially permethylated CB5 (Me_{10}CB5).[41] Then, in 2001, Kim *et al.* successfully synthesized cyclohexaneCB5 and –CB6 through the reaction of cyclohexaneglycoluril with formaldehyde using HCl as catalyst. Parent CB[n]s are insoluble in all organic solvents, but these derivatives decorated with cyclohexane have high solubility in organic solvents such as DMSO and methanol, as well as their water solubility is 170 times increased.[42] These sort of alkylations on CB[n]s have been useful to obtain more soluble compounds and to achieve better host-guest complexations. In 2003, Kim *et al.* were first to achive the facile synthesis of functionalized CB[n]s. They succeeded in replacing the equatorial protons with hydroxyl groups using $K_2S_2O_8$ as an oxidizing agent at elevated temperature. Afterwards, they easily converted the hydroxyl groups into desired functional groups, generally resulting in an increased organic solvent solubility.[43]

Monofunctionalized CB[n] derivatives have also been synthesized in order to have well-defined and controlled structures on nanoscale. In 2012, Oren Scherman *et al.* came up with monohydroxyCB6 synthesis via controlled oxidation of CB6 in the presence of a suitably-sized bisimidazolium guest and it was further functionalized with propargyl group.[44] One year later, Kim *et al.*

showed the direct synthesis of monohydroxy- and monoallyloxyCB7 that is used in a supramolecular velcro application.[45]



Scheme 1.3 Synthesis of (a) perhydroxylated and peralkylated and (b) monohydroxylated and monoalkylated CB[n]s.

Another method for monofunctionalizing the equatorial position on CB7 has been proposed by Isaacs *et al.* in which they react a six-membered glycoluril

oligomer with a glycoluril bis(cyclic ether) with one chloropropyl group attached on the equatorial position. The resulting chloropropyl-attached monofunctionalized CB7 was converted to azide functionalized one, which enables conjugation with other molecules through azide-alkyne click reaction.[46]

The third way of synthesizing functionalized CB[n]s is to react a prefunctionalized aldehyde with glycoluril, yielding a monofunctionalized CB[n] on the methylene bridge. In 2014, Sindelar *et al.* reported the synthesis of CB6 that is substituted with phenyl on the methylene brigde. [47]

There have been various other derivatives of CB[n]s including inverted CB6 and CB7[48], hemiCB6[49], bis-nor-*sec*-CB10[50], the chiral (±)-bis-nor-*sec*-CB6[51] and bambus[6]uril[52], but they are not within the scope of this thesis.

1.1.1.1.3.2. Structural, Physical and Recognitive Properties of Cucurbit[n]urils

As previously mentioned, the structural information on CB6 was first revealed by the study of Mock *et al.* in 1981. They first noticed the presence of intense carbonyl absorption at 1720 cm^{-1} in the infrared spectrum of the product, suggesting glycoluril nucleus is retained. ^{1}H NMR spectrum showed 3 sets of equally intense signals: a singlet at 5.75 ppm was assigned to glycoluril methines and two doublets at 4.43 and 5.97 were assigned to methylene hydrogens that are magnetically nonequivalent due to endo- and exocyclic orientations.[15] Thus, they concluded the unique pumpkin-shaped rigid macrocyclic structure of CB6 with two upper and lower negatively-charged carbonyl portals and a hydrophobic inner cavity.

CB[n] molecules have quite rigid skeletons unlike other macrocycles as confirmed by crystallographic studies. X-Ray crystal structures of the most common CB[n] homologues are illustrated in Figure 1.7. As summarized in Table 1.3, all CB[n] homologues have the same height (9.1 Å), but their outer diameters, inner cavity sizes and volumes vary with different number of glycolurils in the structure.[20,53]

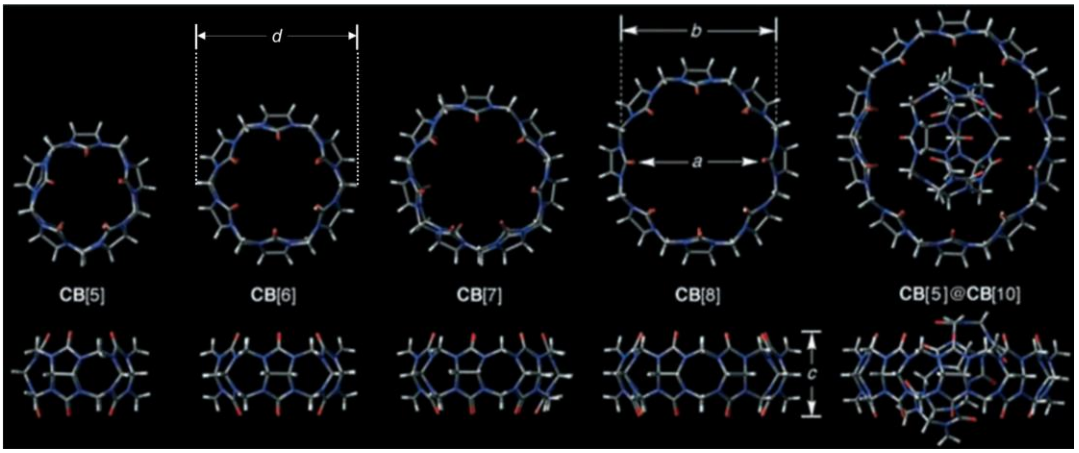


Figure 1.7 X-ray crystal structures of main CB[n] homologues. (Reprinted with permission from ref. 53. Copyright, 2005 John Wiley & Sons, Ltd.)

	M_r	a[Å]	b[Å]	c[Å]	d[Å]	V[Å^3]
CB5	830	2.4	4.4	9.1	13.1	82
CB6	996	3.9	5.8	9.1	14.4	164
CB7	1163	5.4	7.3	9.1	16.0	279
CB8	1329	6.9	8.8	9.1	17.5	479
CB10	1661	10	11.7	9.1	20.0	870
iCB6	996	4.3-3.9	3.8-5.8	9.1	10.7-14.4	-
iCB7	1163	6.7-5.4	5.4-7.3	9.1	11.2-16.0	-
α-CD	972	4.7	5.3	7.9	15.2	174
β-CD	1135	6.0	6.5	7.9	16.6	262
γ-CD	1297	7.5	8.3	7.9	17.7	427

Table 1.3 Structural parameters of uncomplexed CB[n], iCB[n] and CD homologues.[16]

Vast majority of CB[n] homologues and derivatives discovered so far have much less water solubility than other macrocyclic hosts such as cyclodextrins. Water solubility of odd numbered CB[n] homologues, CB5 and CB7, are higher (20-30 mM)[54] compared to even numbered ones, CB6 (0.018 mM)[55] and CB8 (<0.01 mM)[54] because of the intrinsic dipole moments they have. However, their solubility increases strikingly in concentrated aqueous acid. For example, CB6 has 61 mM solubility in formic acid/water (1:1) and CB7 has 700 mM solubility in 3 M HCl.[53,56] CB[n] homologues have high thermal stability such that TGA results showed no decomposition until 420 °C for CB5, CB6 and CB8, while decomposition of CB7 starts at a relatively lower temperature at 370 °C.[54]

One of the most pronounced properties of CB[n]s is that they show extremely high binding affinity towards suitably-sized and –shaped molecules. For instance, 1:1 inclusion complexes of CB7 with adamantanes[57], ferrocenes[58], cobaltocenes[59] and diamantanes[60,61] have binding constants, K, in between 10^9-10^{17} M^{-1} (K for biotin-avidin pair, the strongest noncovalent interaction in nature, is 10^{15} M^{-1}).[20]

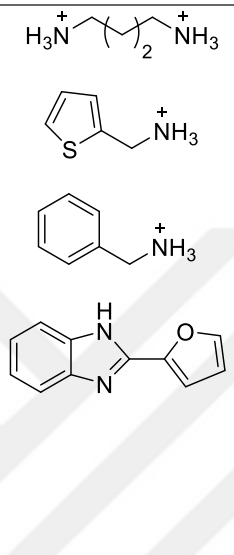
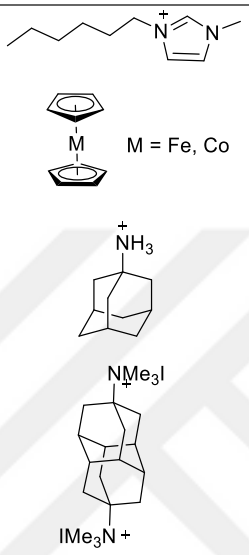
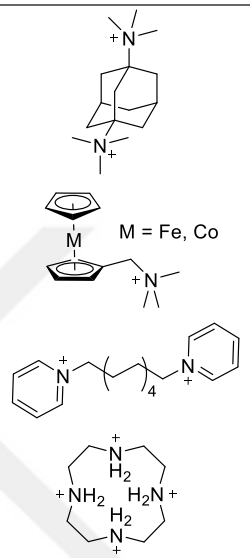
CB5	CB6	CB7	CB8
Alkali and alkaline earth cations: Na^+, K^+, Ca^{2+}, etc. NH^{4+} Multicharged cations: Co^{2+}, Ni^{2+},Cr^{2+}, Fe^{2+}			

Table 1.4 Some examples of suitably-sized guests for CB[n] homologues (n = 5-8).[22,152]

Molecular recognition properties of CB[n] homologues are hugely affected by the negative electrostatic potential they cary on their carbonyl portals and in their cavities. Thus, their binding affinity towards cationic guests is in general larger than that of neutral or anionic guests. Host-guest chemistry of CB[n] family largely driven by three main interactions: ion-dipole, dipole-dipole and hydrophobic effect. Mock and coworkers made extensive host-guest complexation studies with CB6 and alkylammonium ions and concluded that the binding affinity of CB6 depends on the chain length of the guest.[62,63] Later on, this phenomenon was confirmed also for the other CB[n] homologues (Table 1.4). Besides the charge and length of the guest, its hydrophobicity also affects the binding affinity and complex stability. Mock *et al.* investigated this effect by studying the binding affinities toward heteroatom-containing guests and obtained the following order of binding strengths: $H_2N(CH_2)_5NH_2$ > $H_2N(CH_2)_2S(CH_2)_2NH_2$ > $H_2N(CH_2)_2O(CH_2)_2NH_2$, which is in accordance with relative hydrophobicity of alkyl, thioether and alkoxy groups, respectively.[62]

1.2. Conjugated Compounds

German chemist Johannes Thiele was the first who described the term 'conjugated' for the molecules that have alternating single and double bond system in which π-electrons in overlapping p-orbitals delocalize over the whole conjugation. Conjugation generally stabilizes the molecule by lowering the overall energy. Graphite, graphene, carbon nanotubes, conductive or fluorescent polymers and oligomers, porphyrins are well-known examples for conjugated materials.

1.2.1. Conjugated Polymers and Oligomers

Conjugated polymers are semiductive materials due to the presence π-electrons delocalized along the polymer backbone. Polyaniline (PAN) was the first conjugated polymer synthesized by Runge in 1834.[64] Henry Letheby, in 1862, studied on the electrochemical behavior of PAN.[64] However, it was after 1950s that scientists started to discover other conjugated polymers like polyacetylene (PA), polythiophenes, polypyrroles, and so on (Figure 1.8).[65-66] Shirakawa *et al.* published their results regarding a remarkable enhancement in electrical conductivity of PA upon iodine doping.[67] Later, in 2000, A. Heeger, A. MacDiarmid and H. Shirakawa were awarded with Nobel Prize in Chemistry *"for the discovery and development of conductive polymers"*.[68]

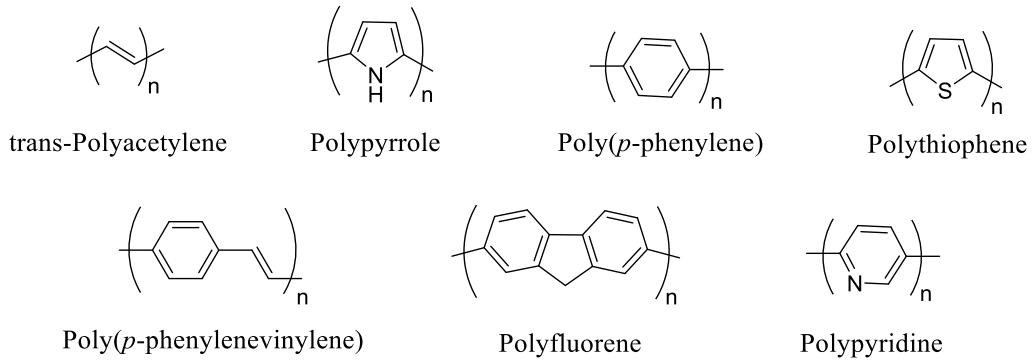


Figure 1.8 Structures of some common conjugated polymers.

1.2.1.1. Synthesis with Cross-Coupling Reactions

Polymerization of conjugated compounds requires a C-C bond formation between two sp^2 hybridized C atoms in the conjugated units. Scientists established chemical[69] and electrochemical[70,71] oxidative polymerization techniques long before. Another facile manner of synthesizing conjugated polymers was introduced during 1970s by R. Heck, E-I. Negishi and A. Suzuki, who were then awarded Nobel Prize in Chemistry in 2010 *"for palladium-catalyzed cross couplings in organic synthesis"*.[72] Today, there are many variations of cross-coupling reactions, some of which are Suzuki, Negishi, Stille, Heck and Sonogashira reactions. The palladium-catalyzed cross couplings occur in three steps: (1) oxidative addition through C-X bond of an electrophile is catalyzed by Pd catalyst, (2) Transmetallation with an organometallic or organoboronic nucleophile takes place and, (3) C-C bond is formed after reductive elimination.

Heck *et al.* in 1972 reported the first Pd-catalyzed cross-coupling reaction that is forming C-C bond between an aryl halide and alkene and yielding the product selectively in trans form.[73]

In 1978, Stille *et. al.* successfully carried out the Pd-catalyzed coupling reaction between organohalide and organotin compounds. It is a versatile reaction tolerating various electrophiles and functional groups (Figure 1.9b).[74,75]

Suzuki *et al.* discovered in 1979 the cross-coupling reactions between organoboronic esters or acids and organohalide in the presence of a Pd(0) catalyst and a base (Figure 1.9a).[76,77] Suzuki coupling is preferred in most cases over the other cross-coupling reactions due to being more environmentally-friendly compared to Stille or Negishi couplings (organoboranes are used instead of organostannane or organozinc nucleophiles) and being able to use water as a solvent. In addition, the organoborane reagents are easy to prepare and are cheaper, as well as the side products can be easily get rid of after the reaction. Stille and Suzuki couplings that incorporate two different conjugated monomers are widely used in the synthesis of alternating conjugated copolymers.[78]

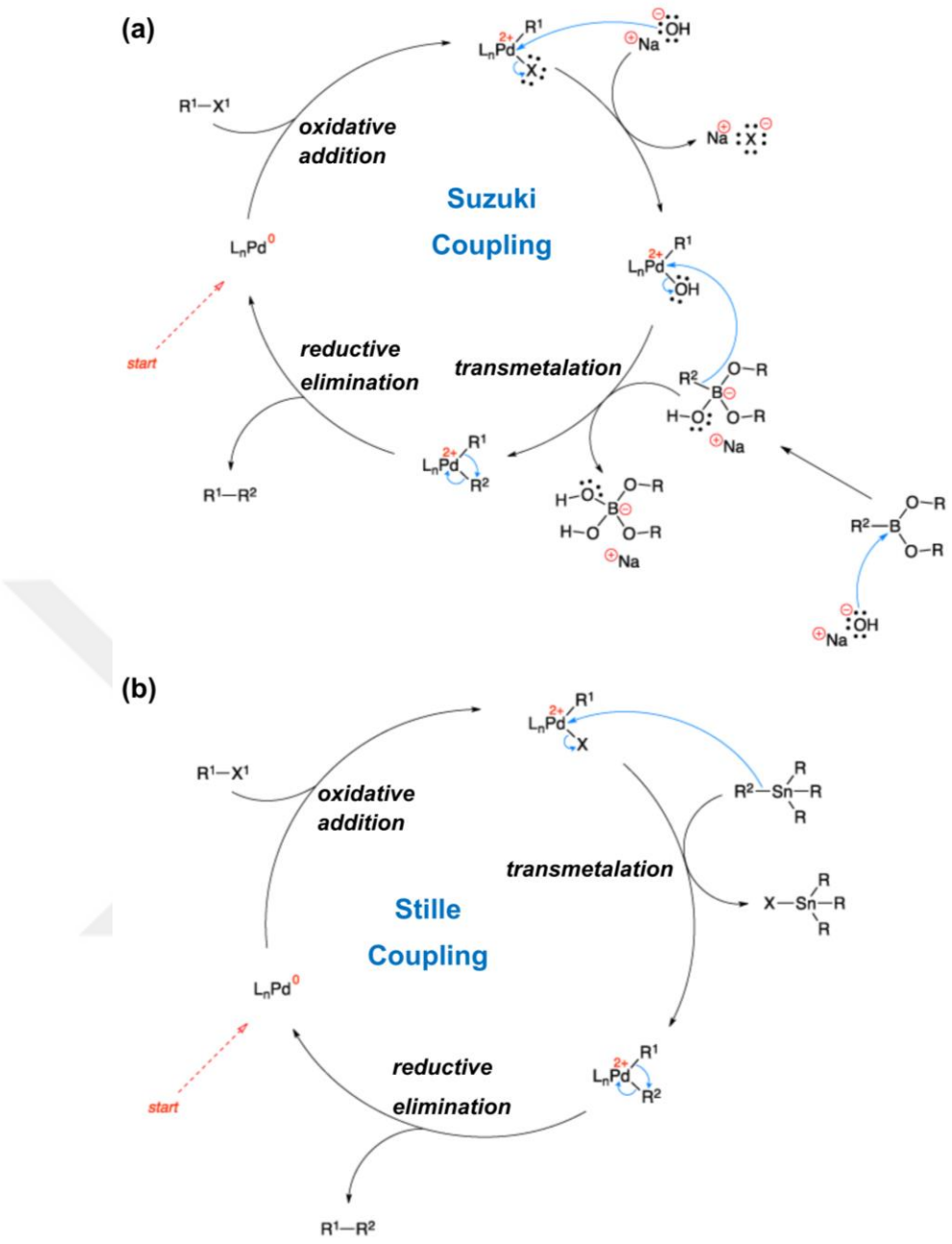


Figure 1.9 Catalytic cycles for **(a)** Suzuki and **(b)** Stille coupling reactions.

1.2.1.2. Properties and Applications

Unlike the commonly used insulating polymers such as polystyrene, polyethylene, polypropylene, poly(ethylene terephthalate), conjugated polymers have metal-like properties, that is, they are electrically conductive or semiconductive thanks to their -electrons delocalized throughout the whole conjugated system. π-electrons of a conjugated polymer in the ground state form the highest occupied molecular orbital (HOMO). The next available

energy state is called the lowest unoccupied molecular orbital (LUMO) and π-electrons can jump to this orbitals when they are excited (ππ*-electrons). The energy difference between HOMO and LUMO is called the band gap and its magnitude is the key factor for the electrical and optical features of the conjugated polymer. Usual band gap values for semiconducting polymers lie in the range of 0.5-3.5 eV and there is an inverse proportion between the magnitude of the band gap and electrical conductivity of the material.[79] In metals, for example, there is no energy gap between HOMO (valence band) and LUMO (conduction band) so they are very good electrical conductors (Figure 1.10).

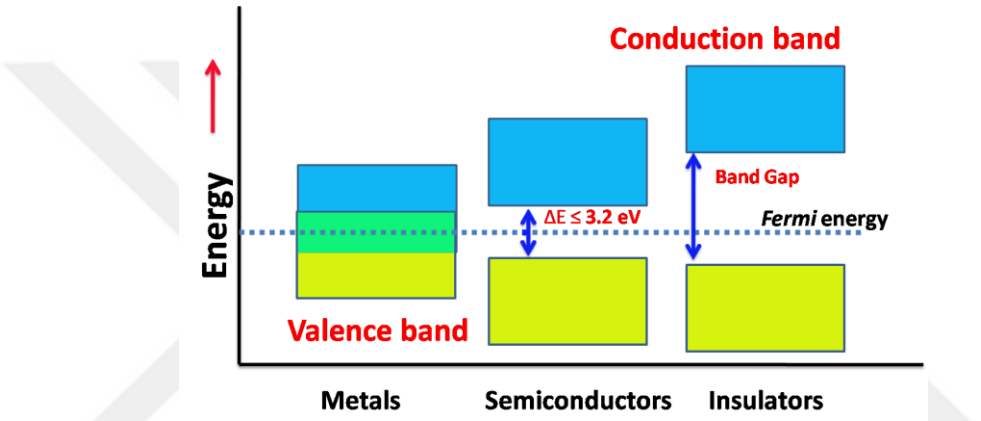


Figure 1.10 Band gap comparison of metals (conductors), semiconductors and insulators.[79]

A conjugated polymer goes to the excited state upon absorbing light with enough energy. However, the electrons that are excited to the LUMO cannot stay there forever because it is an extremely unstable state. Unstable electrons can go back to the stable ground state HOMO in two possible ways: fluorescence or phosphorescence. *Fluorescence* occurs when the electrons in singlet excited state directly relax back to singlet ground state. This results in the emission of photons that has less energy than the absorbed photons because some energy was dissipated via vibrational relaxations in the excited state known as 'internal conversion'. Sometimes the excited state electrons follow a nonradiative relaxation pathway from singlet excited state to triplet excited state, which is known as 'intersystem crossing'. Radiative relaxation from triplet excited state to singlet ground state is called *phosphorescence*. All these phenomena are illustrated as Jablonski energy diagram in Figure 1.11. In the case of conjugated polymers, fluorescence is the major emission pathway unless

some heavy atoms such as bromine and iodine are incorporated into polymer structure for better spin-orbit coupling.[80]

Band gap of conjugated polymers can be tuned by careful selection of the monomer(s) and adjusting the extent of conjugation. They can have very high fluorescence quantum yield and photostability. They do not contain toxic heavy metals and their structures can be modified to increase water solubility and biocompatibility. They already possess the major advantages of common polymers such as robustness, processability and flexibility. All these properties make conjugated polymers excellent materials for various applications ranging from optoelectronic devices such as solar cells[81-84], light-emitting diodes (LEDs)[85-87] and laser diodes[88] to sensors such as chemosensors[89] and biosensors[90], as well as biomedical applications such as drug delivery and cell imaging[91-94].

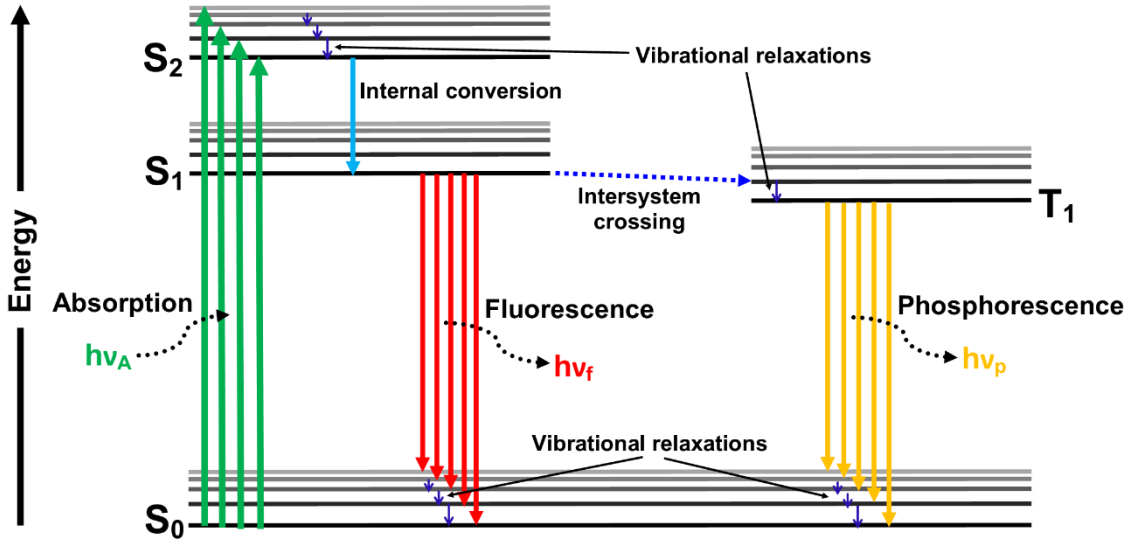


Figure 1.11 Jablonski energy diagram showing radiative and nonradiative relaxation pathways.

1.2.1.3. Conjugated Polymer and Oligomer Nanoparticles

The use of conjugated polymers and oligomers in biomedical applications such as targeted delivery, drug release and cellular imaging can only be possible if they are water soluble. The most widely used way of rendering conjugated polymers water soluble (water dispersible, more precisely) is to fabricate their nanoparticles. Either miniemulsion or nanoprecipitation techniques can be used

to produce water-dispersed conjugated polymer nanoparticles (CPNs). In miniemulsion technique, conjugated polymer dissolved in a good organic solvent is injected into an aqueous surfactant solution under ultrasonication. As the organic solvent evaporates, nanoparticles form with sizes in the range of 30-500 nm.[95] In nanoprecipitation method, the hydrophobic polymer is dissolved in a good organic solvent (THF, acetone, DMSO, etc.) and then dropped onto a bad solvent (water) while stirring or ultrasonicating. As soon as the hydrophobic polymer encounters water, it starts to shrink and acquire a spherical structure so as to minimize the interaction with water. The organic solvent must be evaporated at the end to stabilize the nanoparticles. The sizes of nanoparticles depend on several parameters such as the concentration of polymer in organic solvent, molecular weight of the polymer, the amount of water and rate of stirring or ultrasonication. Under 100 nm CPNs can easily be prepared with nanoprecipitation method without any need for surfactants.[96]

Applications of CPNs in electronic devices such as LEDs[97-98] and solar cells[99-100] have been investigated intensely in the last decades. There are also many examples of CPNs used in biological applications such as cellular imaging[101-103], drug or gene delivery[93,104,105] or antibacterials studies[106-107]. CPNs can be designed in such a way that they can possess multifunctional properties for diagnosis and therapy of diseases. To illustrate, the major disadvantage of conventional drug-based chemotherapy is that most of the anticancer drug is being eliminated from the body before it reaches to the cancerous tissue. For this reason, traditional chemotherapy requires the administration of high doses of drug, which results in many undesired side effects including nausea, fever, fatigue and alopecia. However, with multifunctional CPNs, it would be possible to diagnose a disease by cellular imaging and deliver active molecules to the related parts of the body for the treatment of that disease. Therapeutic agents that are able to bind to the targets in the cancerous tissues can also be incorporated in the CPN structure to increase target specificity.

1.2.2. Porphyrins

Porphyrins are a group of macrocyclic organic compounds, made up of four modified pyrrole subunits interconnected through methine bridges at their α

carbon atoms. Porphyrin has a planar structure and a conjugated system that is composed of 26 π-electrons (18 of them are contributing to electron delocalization pathway at a time), making them aromatic (Figure 1.12a). As a result of the large conjugated system, porphyrins have very intense absorption bands in the visible region. It has a very strong absorption band around 405 nm (Soret band) and four relatively weak absorption bands (Q bands) between 500-630 nm (Figure 1.12b). Porphyrins naturally occur in several forms. The heme group in hemoglobin protein of red blood cells is a derivative of porphyrin that has iron atom in its core and is an oxygen carrier. Another example is chlorophyll, which plays a key role in photosynthesis by absorbing energy of light and is responsible for green color of plants. Its structure is also based on a porphyrin derivative with magnesium bound to its core.

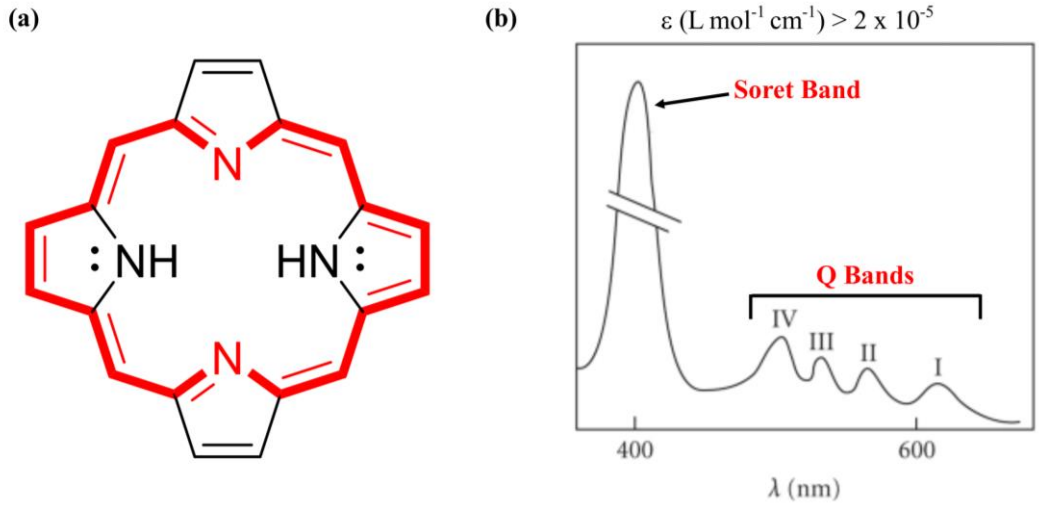


Figure 1.12 (a) Structure of the parent porphyrin and **(b)** characteristic UV-Vis absorbance spectrum of porphyrins.

1.2.2.1. Synthesis of Porphyrins

There are various methods for synthesis of porphyrin derivatives, but the procedure introduced by Paul Rothemund in 1935 still underlies the most widely used procedures. This procedure is based on the high temperature condensation of pyrrole and an aldehyde and subsequent oxidation with air, resulting in tetramerized pyrrole and aldehyde units in a cyclic fashion.[108-110] Later on, in 1966, an advanced version of porphyrin synthesis was reported by Adler and Longo, which suggests refluxing benzaldehyde and pyrrole in the presence of carboxylic acids such as acetic acid and propionic acid as solvent

and following air oxidation.[111] This method brought about facile isolation of the products but very low yields as well as the problems associated with the use of acid sensitive aldehyde derivatives.[112,113] In 1987, Lindsey *et al.* came up with an updated procedure which gives higher yields and eliminates the problem that may occur when acid sensitive aldehydes are employed. They reacted benzaldehyde and pyrrole at room temperature using trace amount of acid catalyst, boron trifluoride diethyl ethereate ($BF_3.Et_2O$) or trifluoroaacetic acid (TFA), which yields porphyrinogen. The porphyrinogen was then irreversibly converted to tetraphenylporphyrin (TPP) by oxidizing with 2,3-dicholoro-5,6-dicyano-1,4-benzoquinone (DDQ) or *p*-chloranil. They examined various reaction conditions by changing the oxidant, acid catalyst, concentration of the reaction mixture, duration of the condensation and water amount in the solvent. They concluded that the best yield occurs when pyrrole and benzaldehyde reacts in dried dicholoromethane (DCM) with 10^{-2} M concentration in the presence of $BF_3.Et_2O$ for 1 hour at room temperature, using *p*-chloranil as oxidant and then refluxing for 1 hour. They purified the product with flash chromatography, yielding around 50% TPP.[114] However, all these methods become extremely impractical when it comes to synthesize porphyrins containing more than one kind of aldehyde in their structure. In this case, another synthetic approach that is based on self-condensation of dipyrromethanes with another aldehyde is employed.[115-116] This method also requires elaborate purification steps with column chromatography, but it ends up with considerable yields.

1.2.2.2. Photodynamic Therapy with Porphyrins

Photodynamic therapy (PDT) is a therapeutic method for the treatment of cancer that is based on the use of a photoactive drug in the presence of light and oxygen.[117] The drug used in PDT is a photosensitizer (PS) that has good light absorption at near infrared region (NIR). After the delivery of PS to malignant cells, it is excited by irradiating with a light that has emission corresponding to the absorbance band of the PS. Excited PS relaxes back to its ground state by transferring its energy to triplet oxygen ($^3O_2$). Then, $^3O_2$ is converted to highly reactive oxygen species (ROS), mainly singlet oxygen ($^1O_2$), that locally kills the cancerous cells and tissues (Figure 1.13).[118,121] It is more

effective for the treatment of cancer at early phases. PDT is especially a valuable alternative for conventional chemotherapy because of its negligible healthy tissue damage and no resistance toward the active agents.[122]

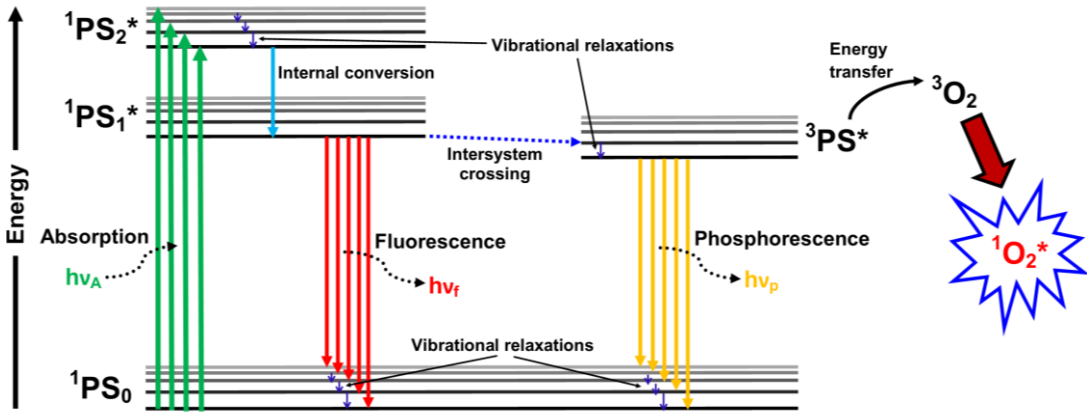


Figure 1.13 Jablonski energy diagram for the generation of $^1O_2$.

An ideal PS should have the following properties: it should be a single pure compound with known chemical structure, it should have good absorbance around red and far red region of the visible spectrum (600-800 nm) so that the light can have good tissue penetration while the light absorption can provide enough energy for the excitation of $^3O_2$ to $^1O_2$, its $^1O_2$ quantum yield should be as high as possible to provide efficient therapeutic effect, it should not be cytotoxic in dark and it should be cleared out of the body as fast as possible to reduce phototoxic adverse effects. The PSs that meet with these conditions to a large extent have been porphyrin and phthalocyanine derivatives up to now. Modern PDT studies began with a PS called hematoporphyrin derivative (HPD), a complex mixture of porphyrins selectively accumulating in malignant cells.[123] *Photofrin (porfimer sodium)*, which is made up of a mixture of porphyrin oligomers linked via ether or ester bonds, was generated by purifying the HPD and it became the first approved PS in 1993 in Canada for protecting people from bladder cancer.[118] It is still widely used as PS, but has many weaknessness that should be addressed, some of which are low absorbance at the irradiation wavelength of 630 nm, skin photosensitivity and complex chemical composition.[122] Therefore, in recent years, scientists have put enormous efforts to come up with a PS having better properties than *Photofrin*, such as a known chemical composition, longer irradiation wavelength and better tumor selectivity. To this end, some other PS have been discovered and

clinically applied for various cancer types such as Temoporfin (652 nm), Verteporfin (690 nm) and Motexafin lutetium (732 nm).[122]

Additionally, the chemical structure of porphyrin allows us to incorporate various kinds of molecules into porphyrin core, which results in the formation of multifunctional frameworks. For instance, monosaccharides are conjugated to porphyrin core in order to increase water solubility as well as cellular adhesion properties.[124] On the other hand, other macrocyclic molecules such as cyclodextrins have been attached to porphyrin core so as to construct multi-receptor containing platforms. Attaching cyclodextrin to porphyrin provides good water solubility and significantly prevents aggregation as well as cyclodextrin acts as a host moiety that can carry drugs and biolomolecules.[125] Because of these reasons, porphyrins still have great potential especially in photodynamic and medicinal applications.

1.3. Supramolecular Frameworks Constructed with Cucurbiturils and Conjugated Compounds

Conjugated, photoactive compounds have been used in many important applications in the fields of optoelectronics, theranostics, catalysis, sensing and imaging.[126-129] However, in most cases, conjugated materials are not free of problem such as low fluorescence quantum yield, poor solubility and low chemical, thermal and photostability. In the last decade, CB[n]s have started to be used for overcoming these disadvantages of conjugated compounds but there are not too many examples. We have recently published a review paper on the supramolecular assemblies of CB[n]s with photoactive, π-conjugated chromophores such as conjugated polymers/oligomers and porphyrins.[130] Following sections will include highlights from this paper.

1.3.1. Frameworks of CB[n]s with Conjugated Polymers and Oligomers

In 2007, Anderson *et al.* prepared a rotaxane by threading oligoaniline through CB7 with reductive amination.[131] Strong affinity of CB7 to radical cation

oligoaniline intermediates enhances their thermal and kinetic stability. The first oxidation potential of the conjugated polymer was decreased by 570 mV and compropartionation constant increased 10^9 times, which will result in dramatic changes in the electronic properties of oligoaniline.[131]

A CB7-threaded conjugated polyrotaxane was prepared by Farcas *et al.* via Suzuki reaction between 9,9-dioctylfluorene-2,7-diboronic acid bis(1,3-propanediol) ester and 5,5'-dibromo-2,2'-bithiophene encapsulated by CB7.[132] They reported that the conjugated polymer was threaded by CB7 with 33% efficiency. The resulting polyrotaxane, **PF-BT.CB7,** was soluble in DMSO but insoluble in water due to polymer's hydrophobic skeleton. They noted an increase in the fluorescence lifetime, but decrease in the fluorescence quantum yield of **PF-BT.CB7** compared to that of its conjugated polymer counterpart, **PF-BT**. Morphological studies with atomic force microscopy (AFM) revealed that self-assembled **PF-BT.CB7** forms extended ribbons while **PF-BT** exists as C-shaped assemblies (Figure 1.14).[132]

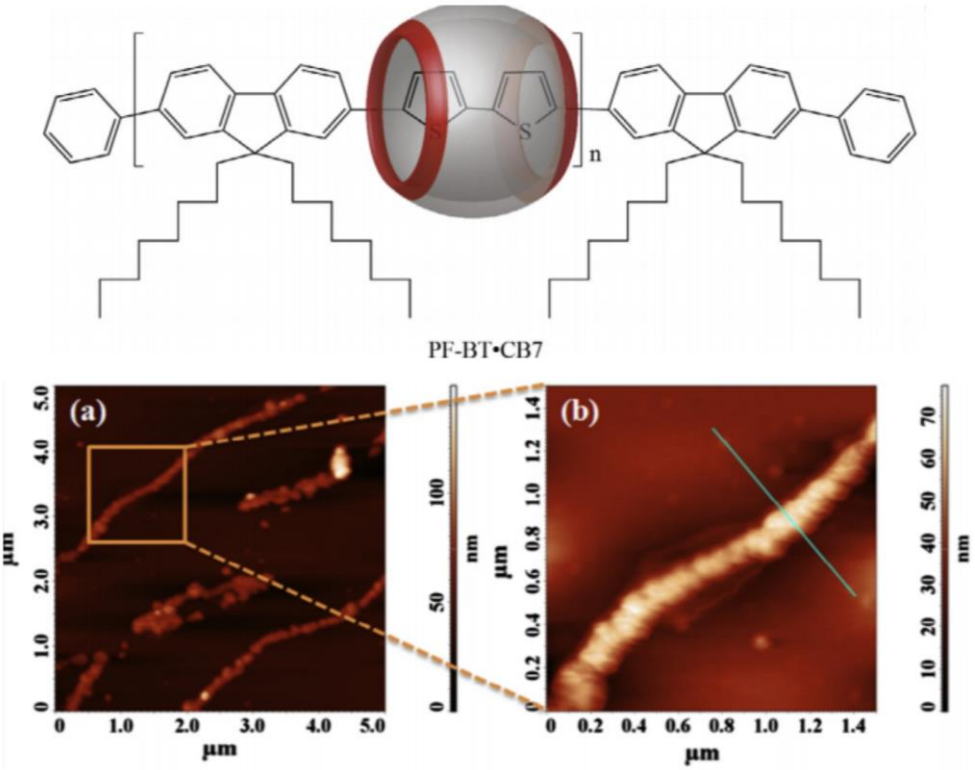


Figure 1.14 Chemical structure and AFM images of PF-BT.CB7. (Reproduced with permission from ref. 132. Copyright 2015, Elsevier)

Tuncel *et al.* have investigated the optical and thermal properties of CB7-threaded fluorene-thiophene-based conjugated polyrotaxanes.[133] The

polyrotaxanes with trimethylammoniumhexyl, **P1CB7**, and trimethylammoniumpropyl, **P2CB7**, pendant groups were synthesized with 50% and 15% threading efficiencies, respectively. Fluorescence quantum yields (Φ_f) and lifetimes of polyrotaxanes were significantly higher than their polymer counterparts, **P1** and **P2**. **P1CB7** and **P2CB7** had 0.46 and 0.55 Φ_f values, whereas that of **P1** and **P2** were 0.11 and 0.35, respectively. LEDs were fabricated using **P1CB7** and **P1.** LED made of **P1CB7** exhibited higher electroluminescence color quality with lower turn-on voltages due to steady charge injection in **P1CB7**.[133] The same group has recently reported that quenching in solid state Φ_f of these rotaxanes can be overcome by embedding them in sucrose or trehalose crystalline matrices (Figure 1.15). By this way, they achieved to maintain the solution phase $\Phi_f > 0.50$ in solid state as well. They also showed the potential of this polyrotaxane as an efficient solid state lighting material by fabricating its LED.[134]

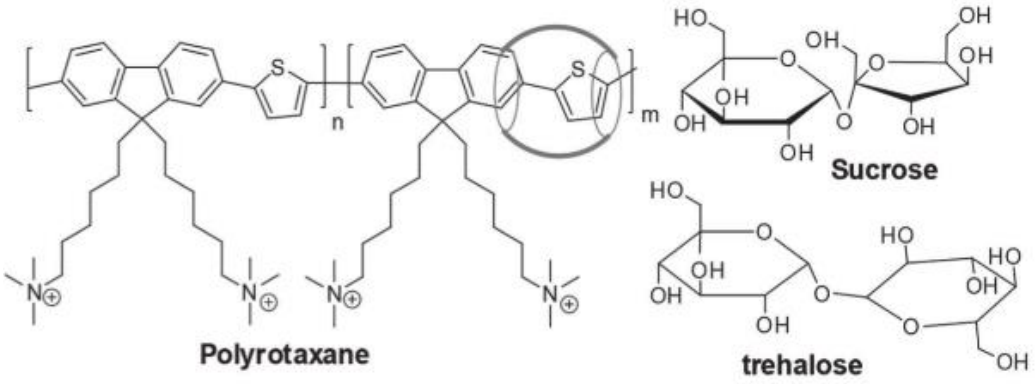


Figure 1.15 Structure of the polyrotaxane and organic matrix elements (sucrose and trehalose) used in the construction of highly luminescent solid-state materials. (Reprinted with permission from ref. 134. Copyright 2017, John Wiley & Sons, Ltd.)

Tuncel *et al.* reported the fabrication of conjugated oligomer-based nanoparticles (CONs) noncovalently decorated with CB7 for targeted drug delivery and bioimaging applications (Figure 1.16).[135] The red-emitting conjugated oligomer was synthesized via Heck coupling of propylamine-linked divinylfluorene and dibromobenzothiadiazole. First, water-dispersed CONs were prepared by nanoprecipitation method, which were found to have red fluorescence emission with high Φ_f and have high loading efficiency for anticancer drug camptothecin (CPT). IC_{50} values of CONs were found to be high against MCF7 and MDA-MB-231 breast cancer cell lines. Amine terminals were capped with CB7 in order to increase the stability of CONs in biological

enviroment because amine groups can randomly interact with proteins and destabilize the CONs. This also helped to reduce the IC_{50} values. In addition to these, drug release rate at pH=5.0 was higher than at pH=7.4, which is especially useful for the targeted drug delivery of anticancer drugs. CB7-capped CONs had even slower drug release at pH=7.4.[135]

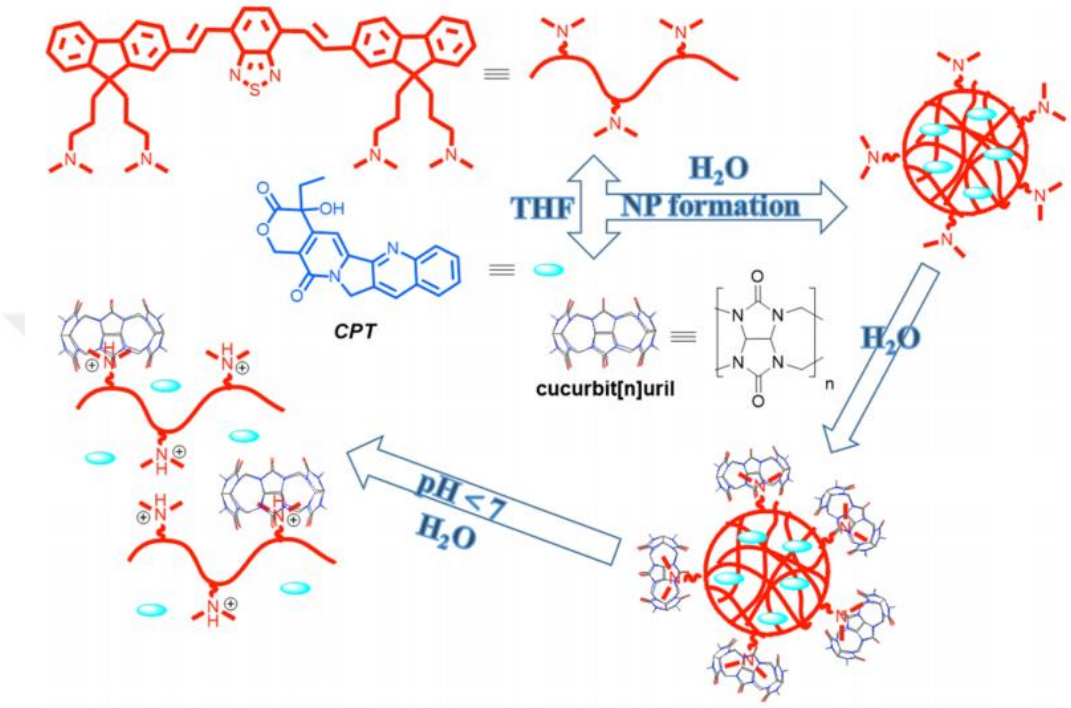


Figure 1.16 Synthesis of CB7-capped red-emitting oligomer NPs loaded with CPT and pH-triggered release of CPT from the NPs. (Reprinted with permission from ref. 135. Copyright 2017, American Chemical Society)

Apart from these examples, other biological studies related to pathogen sensing[136] and controlled antibacterial activity[137,138] have also been published.

1.3.2. Frameworks of CB[n]s and Porphyrins

In 2006, Tuncel *et al.* published the synthesis of [5]pseudorotaxane and [5] rotaxane based on CB6 anchored to a meso-TPP. They showed the pH-responsive threading and dethreading of CB6.[139]

Pal *et al.* demonstrated the water-soluble supramolecular assembly of 5,10,15,20-Tetrakis(4-*N*-methylpyridyl)porphyrin (TMPyP) with CB7.[140] They observed that CB7 strongly crowns around *N*-methylpyridyl units in 1:4 stoichiometry. Noncovalently bound CB7 altered the fluorescence emission

spectrum of TMPyP such that its usual broad emission band split into two narrow bands centered at 655 and 717 nm. They also noted an increase in its fluorescence quantum yield from 0.047 to 0.078. Mohanty *et al.* reported the synthesis of silver nanoparticles (AgNPs) surface-functionalized with CB7, which is able to complex with TMPyP (Figure 1.17).[141] They studied the binding and triggered release of TMPyP from AgNP-CB7 conjugate, which has potential to be employed in PDT.

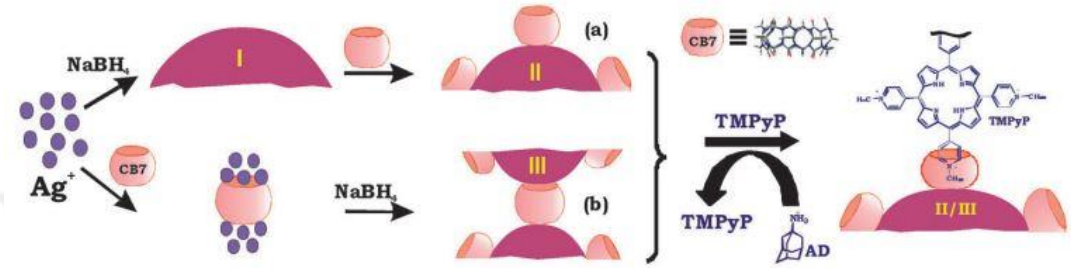


Figure 1.17 Preparation of AgNPs **(a)** pre- and **(b)** post-functionalized with CB7 and binding and release mechanism for TMPyP. (Reprinted with permission from ref. 141. Copyright 2011, Royal Society of Chemistry)

The electron transfer in a dyad consisting of porphyrin as a donor and viologen as an acceptor was modulated by exploiting the strong complex forming interactions between CB7 and dicationic viologen by Stoddart *et al.*[142] The dyad was synthesized via the click reaction of alkyne-functionalized porphyrin and azide-functionalized viologen. When this dyad is treated with CB7, a pseudorotaxane formed in which the porphyrin unit has enhanced fluorescence emission and viologen unit has a significantly shifted reduction potential.

Zhang *et al.* came up with a photosensitizer that is supramolecularly assembled from CB7 and methylpyridinium-attached porphyrin (TPOR).[143] Strong host-guest complexation between CB7 and methylpyridinium moiety in water resulted in an increased $^1O_2$ quantum yield which significantly enhances antibacterial efficiency of TPOR-CB7 assembly.[144] Its Φ_f is also higher than that of TPOR because aggregation of porphyrin is greatly inhibited in the presence of CB7.

Wang *et al.* formed a complex of TMPyP, which has good $^1O_2$ quantum yield as a potential photosensitizer in PDT, with CB8 to selectively bind to serum albumin.[145] Their results indicated that CB8-complexed TMPyP binds

more strongly to serum albumin, which stems from the formation of CB8.TMPyP.tryptophan ternary complexes. Since the lifetime of $^1O_2$ is very short, its range of diffusion in malignant tissues is rather limited. Therefore, selective binding of CB8.TMPyP complex to serum albumin that accumulate in tumor cells is very important for more efficient PDT.

Fuentealba *et al.* made an extensive research on ternary complexes of CB[n], photosensitizer and serum albumin and investigated the effect of CB[n] and photosensitizer types to the resulting photoactivity of the complexes.[146] They used acridine orange (AO^+), methylene blue (MB) and TMPyP as photosensitizers and CB7 and CB8 as supramolecular hosts. For example, AO^+ photooxidizes serum albumin better in the presence of CB7 compared to CB8. Although complexation with CB[n]s extends the triplet excited state lifetimes of all the photosensitizers, only the $^1O_2$ quantum yield of AO^+ and TMPyP increases while that of MB decreases. They attributed this diffenrence to the size of photosensitizers, reasoning that if the photosensitizer is too much buried in the cavity of CB[n]s, generated $^1O_2$ are quenched in the media.[146]

CHAPTER 2

Experimental

Some parts of this work have been reported in the following publication[155]:

A. Koc, R. Khan, D. Tuncel, "Clicked" Porphyrin-Cucurbituril Conjugate: A New Multifunctional Supramolecular Assembly Based on Triglycosylated Porphyrin and Monopropargyloxycucurbit[7]uril. *Chemistry: A European Journal*, **2018**, *24*, 15550-15555.

2.1. Materials

All reagents and solvents used in the syntheses were of analytical grade and used as received unless otherwise stated. Milli-Q water (18.2 MΩ · cm at 25 °C) was used when needed. Column chromatography was performed using silica gel (Sigma-Aldrich high-purity grade, pore size 60 Å, 70-230 mesh, 63-200 µm) or Sephadex G-15 medium. Reactions were monitored by thin layer chromatography (TLC) using silica-coated (Merck TLC Silica Gel F254) or cellulose-coated (Sigma Aldrich TLC plates, cellulose matrix) TLC plates, visualized by shortwave (254 nm) or longwave (365 nm) UV light. All deuterated solvents ($CDCl_3$, DMSO-d_6 and D_2O) used in NMR measurements were purchased from Merck. All spectroscopic measurements were performed using spectrophotometric grade solvents.

2.2. Characterization Techniques

2.2.1. ^{1}H and ^{13}C NMR Spectroscopy

Bruker Avance DPX-400 NMR spectrometer was used for structural characterization of the products by ^{1}H and ^{13}C NMR spectroscopy. The instrument operates at 400 MHz for ^{1}H NMR and at 100 MHz for ^{13}C NMR

measurements. All the spectra were recorded at room temperature in solution phase using deuterated solvents. Chemical shifts are expressed in ppm relative to the internal standard tetramethylsilane. Following notations are used for spin multiplicities: s (singlet), d (doublet), t (triplet), q (quartet), m (multiplet).

2.2.2. Electrospray Ionization-Mass Spectrometry

High resolution exact masses of the products were determined using Agilent 6224 Accurate-Mass Time-of-Flight (TOF) LC/MS and Agilent 6530 Accurate-Mass Q-TOF LC/MS systems.

2.2.3. FT-IR Spectroscopy

Chemical functional groups of the compounds were detected using Bruker Alpha-II Platinum ATR FT-IR spectrometer. The samples (solid or liquid) were introduced to the instrument as they are and the spectra were recorded at room temperature in the range of 400-4000 cm^{-1}.

2.2.4. UV-Vis Absorbance Spectroscopy

Electronic absorption spectra were obtained using Cary 300 UV-Vis spectrophotometer equipped with Xenon flash lamp. All spectra were recorded in solution using quartz cuvette with 10 mm path length.

2.2.5. Fluorescence Spectroscopy

Varian Cary Eclipse fluorescence spectrophotometer was used to record photoluminescence spectra of the compounds. All spectra were recorded in solution using quartz cuvette with 10 mm path length.

2.2.6. Dynamic Light Scattering and Zeta Potential

Malvern Zetasizer Nano ZS equipped with 663 nm laser was used to measure the sizes and zeta potentials of the nanoparticles in solution. Measurements were performed at room temperature. Disposable sizing cuvette was used for

aqueous samples and quartz cuvette was used for solutions with organic solvents.

2.2.7. Thermal Gravimetric Analysis

TA Instruments Q500 thermogravimetric analyzer was used to measure thermal stability of the compounds up to 900 °C.

2.2.8. Scanning Electron Microscopy

Morphological characterization of the assemblies and nanoparticles were done using Quanta 200 FEG instrument operated at enviromental scanning electron microscopy mode.

2.2.9. Transmission Electron Microscopy

Morphological characterization of nanoparticles were performed using FEI Tecnai G2 F30 transmission electron microscope.

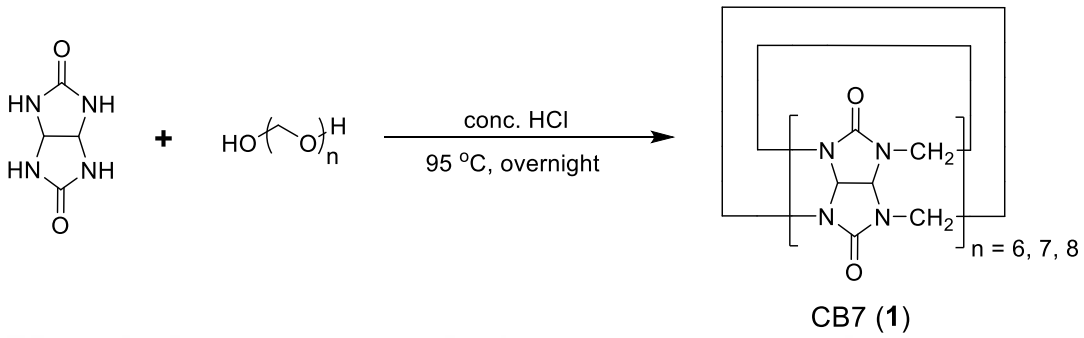
2.2.10. Time-Resolved Fluorescence Spectroscopy

Fluorescence lifetime measurements were conducted with Picoquant FluoTime 200 modular fluorescence lifetime spectrometer. Samples were introduced in solution phase.

2.3. Syntheses

2.3.1. Clicked Porphyrin-Cucurbit[7]uril Conjugate

2.3.1.1. Synthesis of Cucurbit[n]urils



Glycoluril (12.50 g, 88 mmol) and paraformaldehyde (5.54 g, 184 mmol, 2.1 eq.) were mixed homogenously in a 250-mL one-necked round-bottomed flask. The mixture was stirred while adding 22.5 mL of conc. HCl at room temperature (Addition of HCl induces gelation which prevents stirring). Then, the reaction vessel was placed into an oil bath preheated to 95 °C and stirred overnight. The color of the reaction mixture turned to orange and a white precipitate formed. After the reaction, the reaction mixture was left aside for 5 days to let crystals grow (hexagonal-shaped large crystals grew). The solution phase contains mostly CB6, CB7 and oligomers. The crystalline part consists of CB6 and CB8. The purification of CB[n] homologues (n = 6, 7, 8) was done according to literature.[16, 17]

In order to isolate CB7, the crystalline part was isolated from the orange solution by filtering through sintered glass funnel. The filtrate was poured into 300 mL methanol, yielding a large amount of whitish precipitate. The precipitate was collected on a sintered glass funnel and washed with excess of methanol to remove any starting materials and oligomers. The white solid was dried in oven, collected in a 250-mL one-necked round-bottomed flask and stirred with 100 mL 20% aqueous glycerol solution for 2 hours at 90 °C to solubilize CB7. The resulting white suspension was filtered through a sintered glass funnel and the filtrate was poured into 500 mL of methanol to precipitate CB7-rich material. ^{1}H NMR spectrum of the solid showed the presence of other homologues. Therefore, the aqueous glycerol treatment was repeated and finally pure CB7 was obtained (2.32 g, 16%). After the isolation of CB7, remaining

solid materials were collected and washed with methanol, hot water and methanol, respectively and dried in oven to give 4.77 g of pure CB6 (32%).

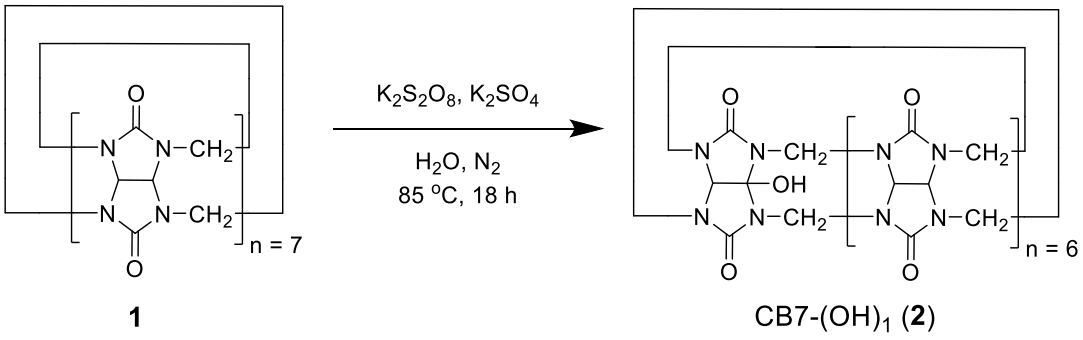
The isolated crystalline part was washed with water and methanol, respectively and dried in oven. The solid was dissolved in 120 mL HCl solution (HCl:water is 1:2 v/v) and refluxed for 1 hour. The resulting solution was hot filtered through sintered glass funnel to remove the undissolved solid. The solid was washed with aq. HCl (1:2 v/v), water, methanol and water, respectively and dried in oven to yield 740 mg of pure CB8 with 5% yield.

CB6: ^{1}H NMR (400 MHz, D_2O+Na_2SO_4, 25 °C) δ (ppm): 4.36 (d, 12 H), 5.63 (s, 12H), 5.74 (d, 12 H). ESI-MS (m/z): calcd. for $C_{36}H_{36}N_{24}O_{12}Na$ $[M+Na]^+$: 1019.2842, found: 1019.2871, $C_{36}H_{36}N_{24}O_{12}K$ $[M+K]^+$: 1035.2582, found: 1035.2524. FT-IR (v_{max}/cm^{-1}): 1724 (C=O).

CB7 (**1**): ^{1}H NMR (400 MHz, D_2O, 25 °C) δ (ppm): 4.23 (d, 14 H), 5.53 (s, 14 H), 5.80 (d, 14 H). ^{13}C NMR (100 MHz, D_2O, 25 °C) δ (ppm): 52.6, 71.3, 156.6. ESI-MS (m/z): calcd. for $C_{42}H_{42}N_{28}O_{14}Na$ $[M+Na]^+$: 1185.3333, found: 1185.3289, calcd. for $C_{42}H_{42}N_{28}O_{14}Na_2$ $[M+2Na]^{2+}$: 604.1615, found: 604.1591. FT-IR (v_{max}/cm^{-1}): 1725 (C=O).

CB8: ^{1}H NMR (400 MHz, D_2O+K_2SO_4, 25 °C) δ (ppm): 4.37 (d, 16 H), 5.65 (s, 16 H), 5.77 (d, 16 H). FT-IR (v_{max}/cm^{-1}): 1727 (C=O).

2.3.1.2. Synthesis of MonohydroxyCB7 (2)



1 CB7-(OH)$_1$ (**2**)

The reported procedure[45] for the synthesis of CB7-(OH)$_1$ was slightly modified and applied here. Compound **1** (2.0 g, 1.72 mmol), $K_2S_2O_8$ (465 mg, 1.72 mmol, 1.0 eq.) and K_2SO_4 (1.80 g, 10.3 mmol, 6 eq.) were mixed in 200 mL of degassed

water in 250-mL round-bottomed flask under N_2 atmosphere. Three times freeze-pump-thaw cycles were applied. The mixture was taken to a preheated oil bath at 85 °C and stirred under N_2 for 12 hours. The reaction flask was let to cool down to room temperature and then the precipitated material was removed by filtration. Water in the resulting filtrate was removed under reduced pressure. 45 mL of conc. HCl was added to the remaining white solid material, which produced a mixture of a yellow solution and a white precipitate. Dropwise addition of the yellow solution to the excess of methanol (400 mL) resulted in the formation of white fluffy precipitate. The precipitate was filtered by washing with plenty of methanol and the solid material was passed through sephadex G-15 column to purify the product.

Yield: 507 mg, 25%.

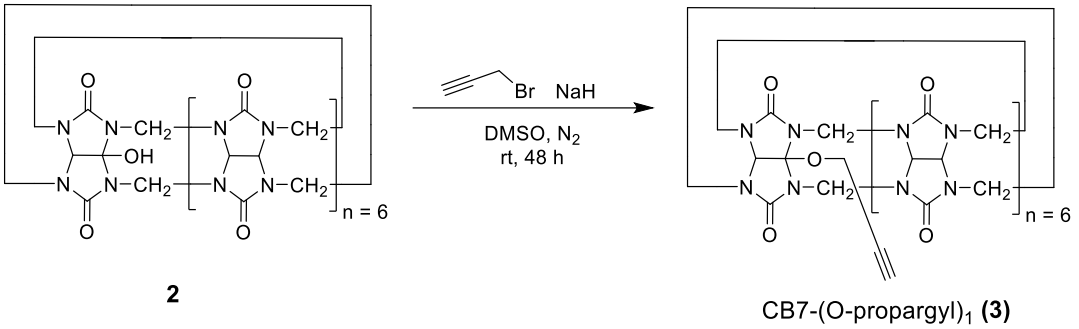
^{1}H NMR (400 MHz, D_2O, 25 °C) δ (ppm): 4.26 (d, $J = 15.4$ Hz, 10 H), 4.28 (d, 2 H), 4.55 (d, 2 H), 5.32 (s, 1 H), 5.48 (d, 2 H), 5.56 (s, 10 H), 5.60 (s, 2 H), 5.80 (d, $J = 15.6$ Hz, 10 H), 5.87 (d, 2 H). –OH proton was not observed due to fast exchange with D_2O.

^{13}C NMR (100 MHz, D_2O, 25 °C) δ (ppm): 156.7, 155.1, 93.6, 77.8, 71.3, 52.6, 46.6.

ESI-MS (m/z): calcd. for $C_{42}H_{42}N_{28}O_{15}Na$ $[M+Na]^+$: 1201.3282, found: 1201.3101, calcd. for $C_{42}H_{42}N_{28}O_{15}K$ $[M+K]^+$: 1217.3022, found: 1217.3042, calcd. for $C_{42}H_{42}N_{28}O_{15}NaK$ $[M+NaK]^{+2}$: 620.1460, found: 620.1320, calcd. for $C_{42}H_{42}N_{28}O_{15}K_2$ $[M+2K]^{+2}$: 628.1329, found: 628.1320.

FT-IR (ν_{max}/cm^{-1}): 1729 (C=O).

2.3.1.3. Synthesis of MonopropargyloxyCB7 (3)



2 CB7-(O-propargyl)$_1$ **(3)**

In a 25-mL two-necked round-bottomed flask, compound **2** (200 mg, 0.17 mmol) was dissolved in 10 mL of dried, degassed DMSO under N_2 atmosphere. NaH (20 mg, 0.85 mmol, 5 eq.) was added to this solution and the mixture was let to stir at room temperature for 1 hour. The mixture was cooled down to 0 °C and propargyl bromide (100 µL, 5 eq.) was added under N_2 flow. The reaction mixture was brought to room temperature and continued to stir under N_2 for 48 hours. The light brown reaction mixture was poured into 500 mL of diethyl ether, triturated until a solid precipitate forms. The solid was collected on a Büchner funnel and washed with plenty of diethyl ether and methanol. The resulting light brown solid product was dried in oven.

Yield: 126 mg, 61%.

^{1}H NMR (400 MHz, D_2O+NaCl, 25 °C) δ (ppm): 5.79 (d, 2 H), 5.73 (d, 12 H), 5.65 (s, 2 H), 5.55 (s, 12 H), 5.30 (s, 1 H), 4.51 (d, 2 H), 4.23 (d, 12 H), 2.52 (s, 1 H).

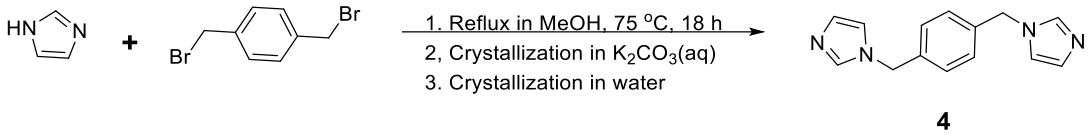
^{13}C NMR (100 MHz, D_2O+NaCl, 25 °C) δ (ppm): 156.96, 155.39, 127.21, 93.78, 77.80, 71.45, 52.86, 49.18, 46.91.

ESI-MS (m/z): calcd. for $C_{45}H_{44}N_{28}O_{15}Na$ $[M+Na]^+$: 1239.3439, found: 1239.3488, calcd. for $C_{45}H_{44}N_{28}O_{15}K$ $[M+K]^+$: 1255.3178, found: 1255.3272.

FT-IR (ν_{max}/cm^{-1}): 1723 (C=O), 2114 (-C≡C-), 3277 (C≡C-H).

TGA: starts to decompose at 376 °C and reaches maximum decomposition rate at 402 °C.

2.3.1.4. Synthesis of 1,4-Bis(imidazole-1-ylmethyl)benzene (4)



4

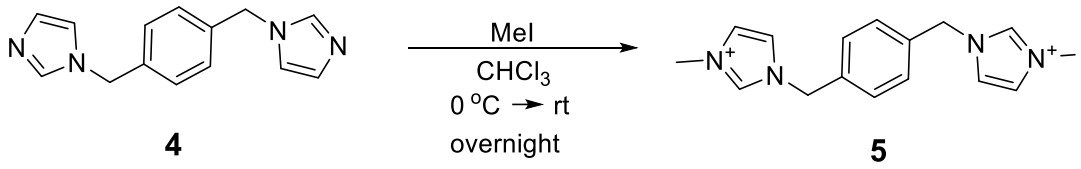
In a one-necked 250-mL round-bottomed flask, a mixture of α,α'-dibromo-*p*-xylene (1.18 g, 4.46 mmol) and imidazole (3.16 g, 46.4 mmol, 10 eq.) in 50 mL methanol was heated up to 75 °C and stirred under reflux for 18 hours. After the reaction, methanol was removed by rotavap, which resulted in a yellow syrup. Yellow material was dissolved in aqueous K_2CO_3 (6.13 g, 100 mL). This solution was kept overnight to yield crystalline bix dihydrate, which was further crystallized from water and collected by filtration.[148]

Yield: 568 mg (46%).

^{1}H NMR (400 MHz, D_2O, 25 °C) δ (ppm): 5.18 (s, 4 H), 7.01 (d, 2 H), 7.08 (d, 2 H), 7.21 (s, 4 H), 7.73 (s, 2 H).

ESI-MS (m/z): calcd. for $C_{14}H_{14}N_4$ $[M]^+$: 238.1218, found: 238.1275.

2.3.1.5. Synthesis of 1,1'-(1,4-phenylenebis(methylene)bis(3-methyl-1H-imidazol-3-ium) (5)



4 **5**

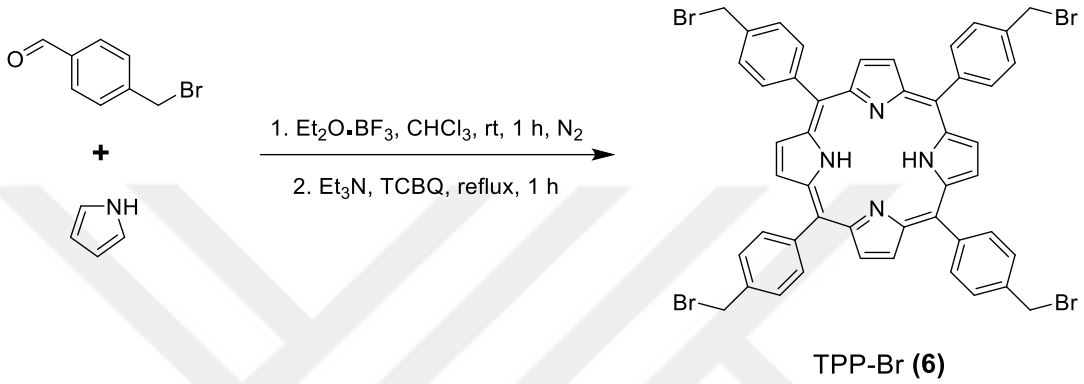
In a one-necked 100-mL round-bottomed flask, compound **4** (200 mg, 0.84 mmol) was dissolved in 40 mL chloroform. The flask was taken on an ice bath and methyl iodide (298 mg, 131 µL, 2.1 mmol, 2.5 eq.) was added dropwise while stirring. The reaction mixture was stirred on ice bath for a while and then let to stir overnight at room temperature. The product precipitates as colorless crystals (diiodide salts) and collected by filtration.

Yield: 391 mg, 89%.

^{1}H NMR (400 MHz, DMSO-d_6, 25 °C) δ (ppm): 3.85 (s, 6 H), 5.43 (s, 4 H), 7.47 (s, 4 H), 7.71 (d, 2 H), 7.76 (d, 2 H), 9.21 (s, 2 H).

ESI-MS (m/z): calcd. for $C_{16}H_{20}N_4I_2$ $[M]^+$: 521.9777, found: 521.9749.

2.3.1.6. Synthesis of 5,10,15,20-tetrakis(α-bromo-*p*-tolyl)porphyrin (6)



TPP-Br **(6)**

The procedure was adapted from the literature.[147] In a 2-L two-necked round-bottomed flask, 1.5 L of dried, distilled, degassed chloroform, *α*-bromo-*p*-tolualdehyde (1.5 g, 7.5 mmol) and pyrrole (525 mg, 7.5 mmol, 1 eq.) were added, respectively under N_2. During stirring, $Et_2O \cdot BF_3$ (350 mg, 2.5 mmol, 0.3 eq.) was added to the mixture and the mixture was let to stir for 1 hour at room temperature under N_2 (after addition of $Et_2O \cdot BF_3$, colorless solution started to turn red slowly), Then, trimethylamine (305 mg, 3.0 mmol, 0.4 eq.) and tetrachlorobenzoquinone (1.35 g, 5.6 mmol, 0.7 eq.) were added, respectively and the mixture was stirred at room temperature overnight (the system was kept open to atmosphere since this is the oxidation step). Next day, the temperature was raised to 65 °C and refluxed for 1 hour. The volume of the reaction mixture was reduced to 200 mL, the solution was passed through silica gel and the filtrate was dried using rotavap. The solid material was redissolved in toluene and passed through silica gel column using only toluene as eluent to purify the product. Collected product was dried in oven.

Yield: 794 mg, 43%.

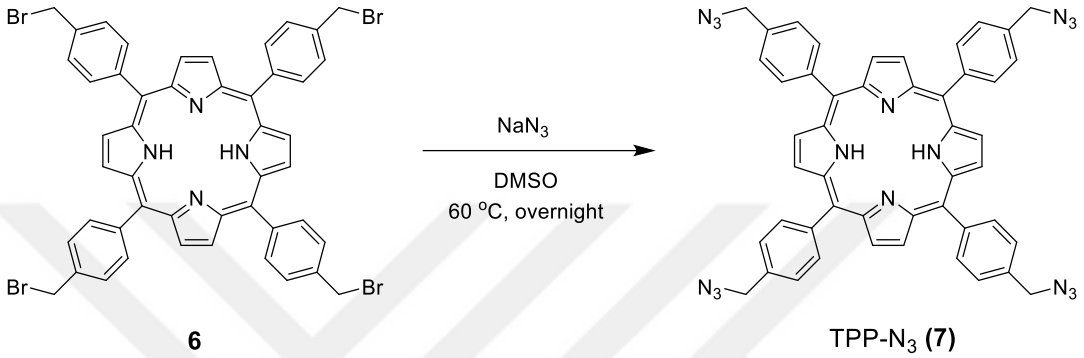
^{1}H NMR (400 MHz, $CDCl_3$, 25 °C) δ (ppm): 8.84 (s, 8 H), 8.19 (d, 8 H), 7.80 (d, 8 H), 4.86 (s, 8 H), -2.81 (s, 2 H).

ESI-MS (m/z): calcd. for $C_{48}H_{34}Br_4N_4H$ $[M+H]^+$: 982.9595, found: 982.9552.

UV-Vis (DMSO): λ_{max} (nm): 420 (Soret), 515, 551, 590, 645.

PL (DMSO): λ_{max} (nm): 652, 716.

2.3.1.7. Synthesis of 5,10,15,20-tetrakis(α-azido-p-tolyl)porphyrin (7)



6 TPP-N_3 **(7)**

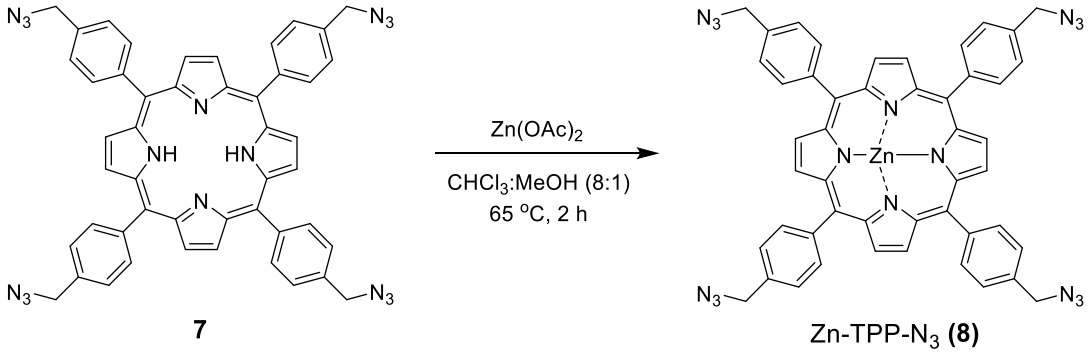
Compound **6** (602 mg, 0.61 mmol) was dissolved in 20 mL DMSO in 100-mL one-necked round-bottomed flask. NaN_3 (238 mg, 3.66 mmol, 6 eq.) was added to the reaction flask and the mixture was stirred at 60 °C overnight. Reaction mixture was transferred to a 250-mL separatory funnel and chloroform/water extraction was done for 4 times using ice-cold water. Chloroform layer was collected and trace amount of water was removed with $MgSO_4$. The product was then dried using rotavap.

Yield: 472 mg, 93%.

^{1}H NMR (400 MHz, $CDCl_3$) δ (ppm): 8.83 (s, 8 H, labelled as b), 8.24 (d, 8 H, labelled as c), 7.72 (d, 8 H, labelled as d), 4.73 (s, 8 H, labelled as e), -2.80 (s, 2 H, labelled as a).

ESI-MS (m/z): calcd. for $C_{48}H_{34}N_{16}H$ $[M+H]^+$, 835.3231, found 835.3303.

2.3.1.8. Synthesis of Zinc 5,10,15,20-tetrakis(α-azido-p-tolyl)porphyrin (8)



In a 100-mL one-necked round-bottomed flask, compound **7** (696 mg, 0.84 mmol) was dissolved in 40 mL chloroform. Zinc acetate (665 mg, 4.17 mmol, 5 eq.) was dissolved in 5 mL methanol and added to the reaction flask. The mixture was then refluxed at 65 °C for 2 hours and continued to stir at room temperature overnight. After the reaction, the solvent was removed under reduced pressure. The final product was washed with methanol and water several times, filtered and dried in oven.

Yield: 691 mg, 92%.

^{1}H NMR (400 MHz, $CDCl_3$, 25 °C) δ (ppm): 8.94 (s, 8 H, labelled as b), 8.24 (d, 8 H, labelled as c), 7.70 (d, 8 H, labelled as d), 4.71 (s, 8 H, labelled as e).

^{13}C NMR (100 MHz, DMSO-d_6, 25 °C) δ (ppm): 149.7, 142.9, 135.3-134.8, 132.0, 127.0, 120.3, 54.1.

ESI-MS (m/z): calcd. for $C_{48}H_{32}N_{16}Zn$ $[M]^+$, 896.2287, found 896.2258.

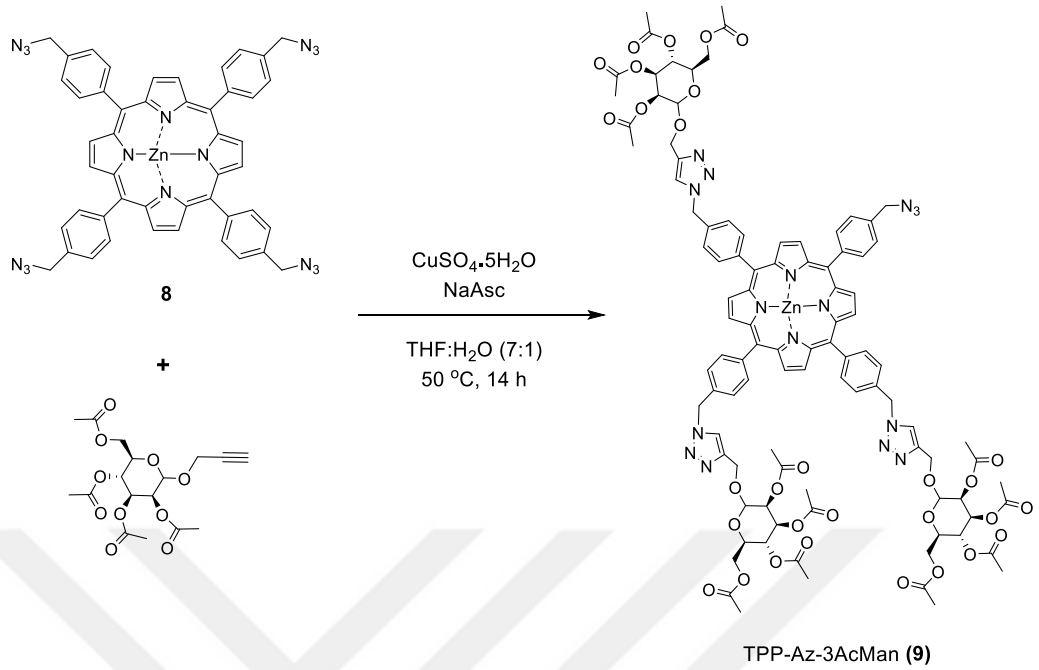
FT-IR: (ν_{max}/cm^{-1}): 2101 (-N_3).

UV-Vis ($CHCl_3$): λ_{max} (nm): 424 (Soret), 554, 595.

PL (DMSO): λ_{max} (nm): 605, 654.

TGA: Two decomposition points at 233 °C (loss of azide groups) and 517 °C (loss of benzene rings).

2.3.1.9. Synthesis of Acetylated Mannose-attached Zn-TPP-N_3 (9)



Compound **8** (691 mg, 0.77 mmol) and 1-α-propargyloxy mannose (892 mg, 2.31 mmol, 3 eq.) were dissolved in 25 mL THF in a 100-mL one-necked round-bottomed flask. $CuSO_4.5H_2O$ and sodium ascorbate were separately dissolved in 1.75 mL of water and were added to the reaction flask. The reaction mixture was stirred at 50 °C for 14 hours. The reaction was monitored by mass spectrometry and TLC (DCM:MeOH, 10:0.4). ESI-MS spectrum of the reaction mixture showed the presence of mono-, di-, tri- and tetra-clicked analogues. TLC of the crude material showed the presence of 5 components. The desired compound TPP-Az-3Man was isolated as the second last component from the silica gel-packed column with 60x4.5 cm dimensions. Separation was achieved by starting the column with 1% MeOH/DCM and slowly increasing it up to 2% MeOH/DCM.

Yield: 784 mg, 50%.

^{1}H NMR (400 MHz, DMSO-d_6, 25 °C) δ (ppm): 8.74 (s, 8 H, labelled as a), 8.55 (s, 3 H, labelled as f), 8.18 (d, 8 H, labelled as b), 7.79 (d, 2 H, labelled as c), 7.70 (d, 6 H, labelled as c_1), 6.00 (d, 6 H, labelled as e), 5.17-4.07 (m, 27 H, labelled as d, g, h, i, j, k, l, m), 2.11-1.92 (d, 36 H, labelled as n).

^{13}C NMR (100 MHz, DMSO-d_6, 25 °C) δ (ppm): 170.7, 170.0, 169.9, 150.18, 149.9, 144.0, 143.5, 143.0, 135.7, 135.4, 134.5, 133.2, 131.7, 129.7, 126.3, 125.9, 122.5, 120.4, 119.8, 96.9, 69.3, 68.9, 68.6,67.8, 66.0, 62.3, 60.2, 55.0, 54.1, 20.7.

ESI-MS (m/z): calcd. for $C_{99}H_{98}N_{16}O_{30}ZnNa$ $[M+Na]^+$: 2077.5824, found: 2077.5895.

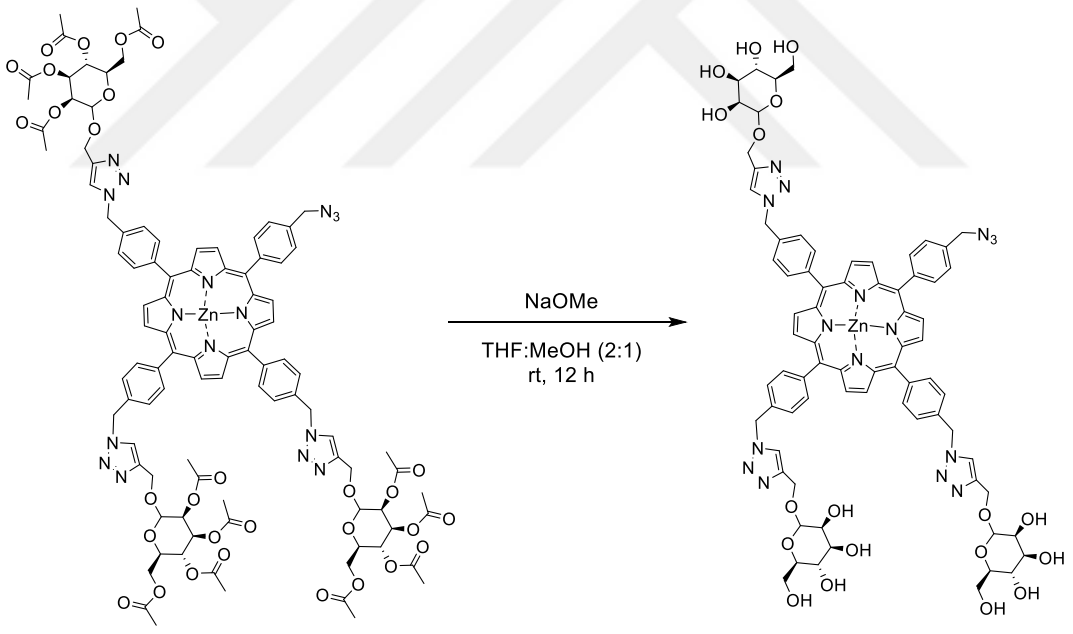
FT-IR: (v_{max}/cm^{-1}): 2099 (-N_3), 1740 (C=O).

TLC (DCM:MeOH, 10:0.4, R_f): 0.46.

UV-Vis ($CHCl_3$): λ_{max} (nm): 407, 428 (Soret), 515, 561, 601.

PL (DMSO): λ_{max} (nm): 608, 661.

2.3.1.10. Synthesis of Hydrolyzed Mannose-attached Zn-TPP-N_3 (10)



In a 25-mL one-necked round-bottomed flask, compound **9** (100 mg, 0.049 mmol) was dissolved in 6 mL of dried THF. Sodium methoxide (66 mg, 1.23 mmol, 25 eq.) dissolved in 3 mL of dried methanol was added to the reaction flask and the mixture was stirred at room temperature for 12 hours. The reaction was monitored by TLC and after 12 hours it was stopped. The solvent

was removed using rotavap and the solid was washed with excess of water to remove any by-products. The resulting purple solid product was dried in oven.

Yield: 70 mg, 90%.

^{1}H NMR (400 MHz, DMSO-d_6) δ (ppm): 8.74 (s, 8H, labelled as a), 8.49 (s, 3 H, labelled as f), 8.18 (d, 8 H, labelled as b), 7.78 (d, 2 H, labelled as c), 7.69 (d, 2 H, labelled as c_1), 5.98 (s, 6 H, labelled as e), 3.64-4.85 (m, 27 H, labelled as d, g, h, I, j, k, l, m).

ESI-MS (m/z): calcd. for $C_{75}H_{73}N_{16}O_{18}Zn$ [M-H]$^-$: 1549.4580, found: 1549.4360.

FT-IR: (v_{max}/cm^{-1}): 2099 (-N_3), 3330 (O-H).

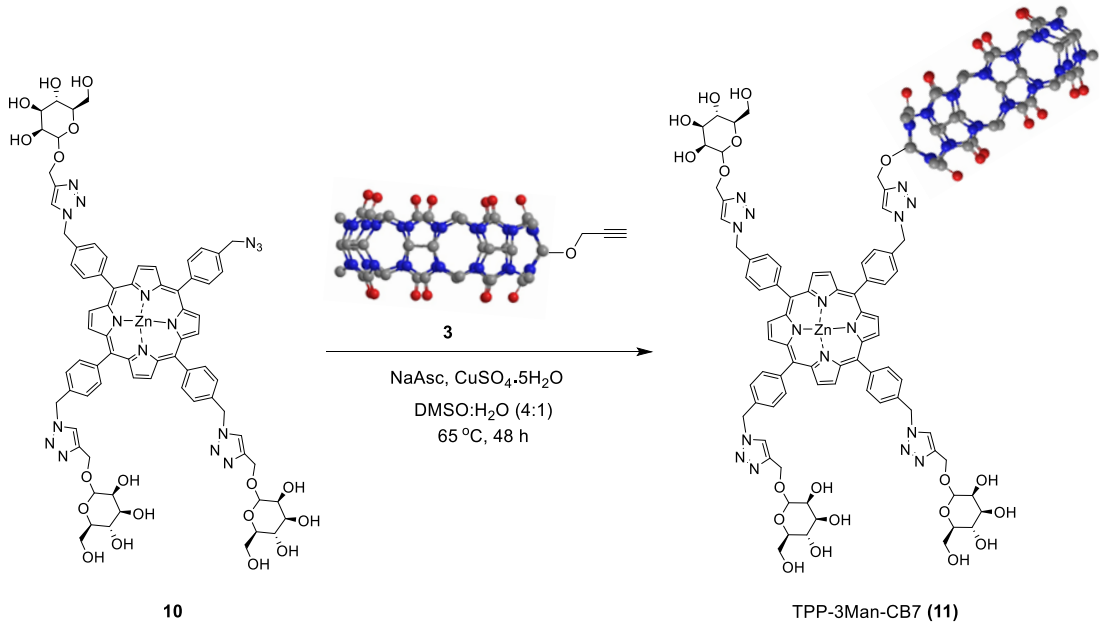
UV-Vis ($CHCl_3$): λ_{max} (nm): 407, 428 (Soret), 515, 561, 601.

PL (DMSO): λ_{max} (nm): 608, 661.

Fluorescence quantum yield: 0.041.

Fluorescence lifetime (τ/ns): 1.8.

2.3.1.11. Synthesis of CB7-conjugated Mannose-attached TPP (11)



Compound **10** (80 mg, 0.05 mmol) and compound **3** (186 mg, 0.15 mmol, 3 eq.) were dissolved in 8 mL of DMSO in a 50 mL one-necked round-bottomed flask and sonicated to obtain a homogeneous solution. Sodium ascorbate (6 mg, 0.03 mmol, 0.6 eq.) and $CuSO_4.5H_2O$ (4 mg, 0.02 mmol, 0.4 eq.) in 1 mL water each were added to the reaction flask, respectively and the mixture was stirred at 65 °C for 48 hours. DMSO was removed under reduced pressure, which resulted in a brown solid residue. The product was purified by a sephadex G-25 column (MeOH:H_2O, 1:1) and dried in oven.

Yield: 127 mg, 91%.

^{1}H NMR (400 MHz, DMSO-d_6, 25 °C) δ (ppm): 3.64-4.82 (d, g, g_1, h, i, j, k, l, m), 4.17 (br s, labelled as CB7), 5.40 (br s, labelled as CB7), 5.69, (br s, labelled as CB7), 5.98, (s, labelled as e), 7.69 (d, 8 H, labelled as c_1), 8.17 (d, 8 H, labelled as b), 8.49 (s, 4 H, labelled as f), 8.73 (s, 8 H, labelled as a).

^{13}C NMR (100 MHz, DMSO-d_6, 25 °C) δ (ppm): 31.2, 49.1, 53.3, 59.8, 61.9, 67.6, 70.8, 71.5, 74.7, 120.3, 125.4, 126.5, 132.2, 135.0, 135.8, 142.9, 149.8, 155.6.

ESI-MS (m/z): calcd. for $C_{122}H_{122}N_{44}O_{33}$ (without Zn) $[M+H]^{2+}$: 2732.2793, found: 2732.5440.

FT-IR: (ν_{max}/cm^{-1}): 1731 (C=O), 3300 (O-H).

UV-Vis (DMSO): λ_{max} (nm): 428 (ε $6.7*10^5$ $M^{-1}cm^{-1}$), 561 (ε $3.4*10^4$ $M^{-1}cm^{-1}$), 600 (ε $6*10^3$ $M^{-1}cm^{-1}$).

PL (DMSO): λ_{max} (nm): 608, 661.

Fluorescence quantum yield: 0.035.

Fluorescence lifetime (τ/ns): 1.8.

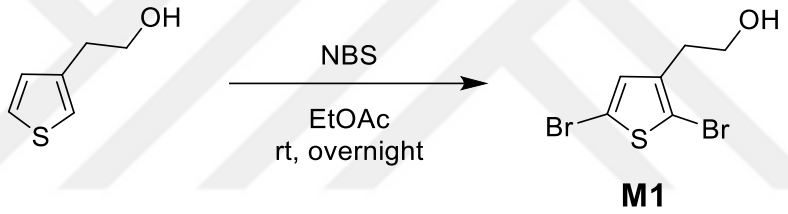
2.3.1.12. $^1O_2$ quantum yield measurement

Stock solutions were prepared as 20 µM for DPBF and 6 µM for the samples in DMSO and saturated with oxygen before measurements. First, UV-Vis absorbance spectrum of 20 µM DPBF (2 mL) was recorded. Then 100 µL from

sample stock solution was added in the dark to DPBF solution. UV-Vis absorbance graphs were recorded before and after irradiation with 460 nm LED with 10 sec intervals until seeing no more decrease in the absorbance band due to photobleaching. Since the absorbance maxima of both porphyrin-based samples and DPBF overlaps, the decrease in the absorbance shoulder of DPBF around 405 nm was taken into account for the calculations. The same procedure was applied for methylene blue which is used as standard ($^1O_2$ quantum yield = 0.52). $-\ln[DPBF]/[DPBF]_0$ vs. irradiation time was plotted for all samples and the slopes of the graphs were utilized to comparatively calculate the $^1O_2$ quantum yields of the samples with respect to methylene blue.

2.3.2. Synthesis of Red-emitting Conjugated Polymer

2.3.2.1 Synthesis of 2-(2,5-dibromothiophen-3-yl)ethan-1-ol (M1)



In a 500-mL two-necked round-bottomed flask, N-bromosuccinimide (9.92 g, 55.8 mmol, 2.5 eq.) in 200 mL of distilled, degassed ethyl acetate was sonicated for 30 minutes until complete dissolution. 3-thiopheneethanol (2.86 g, 2.5 mL, 22.3 mmol) was then added to the reaction flask and the mixture was sonicated for 90 minutes (temperature of the sonicating batch was controlled by addition of ice). The color of the mixture became yellow. The reaction flask was transferred on a magnetic stirrer, and the mixture was stirred overnight at room temperature. Next day, TLC check in cyclohexane:ethyl acetate (2:1) system showed single spot (R_f=0.3) that belongs to the product. The reaction mixture was transferred to a 500-mL separatory funnel and 5 times extraction was done with water to remove excess N-bromosuccimide. Ethyl acetate layer was collected, trace amount of water was removed by $MgSO_4$, ethyl acetate was evaporated by rotavap and the product was finally dried under vacuum.

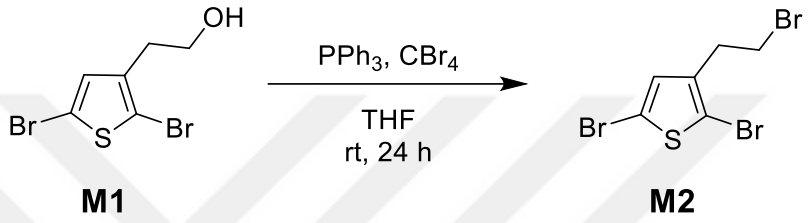
Yield: 5.87 g, 92%.

^{1}H NMR (400 MHz, $CDCl_3$, 25 °C) δ (ppm): 2.83 (t, 2 H), 3.84 (t, 2 H), 6.90 (s, 1 H).

^{13}C NMR (100 MHz, DMSO-d_6, 25 °C) δ (ppm): 33.3, 62.0, 108.7, 111.4, 132.1, 138.6.

TLC (cyclohexane:ethyl acetate = 2:1, R_f): 0.30.

2.3.2.2. Synthesis of 2,5-dibromo-3-(2-bromoethyl)thiophene (M2)



M1 **M2**

In a 250-mL two-necked round-bottomed flask, compound **M1** (5.86 g, 20.5 mmol) was dissolved in 50 mL of dried, degassed THF and the solution was shocked with vacuum several times. Triphenylphosphine (10 g, 38.1 mmol, 1.9 eq.) was added to the reaction flask while stirring under N_2 atmosphere and the mixture was cooled down by an ice bath. Carbontetrabromide (12.6 g, 38.1 mmol, 1.9 eq.) was dissolved in dried, degassed THF, transferred into an addition funnel that is connected to the reaction flask and then let to drop slowly. The mixture was stirred for 1 day at room temperature. TLC of the reaction mixture using cyclohexane as eluent showed three spots, one of which with R_f = 0.6 was expected to be due to the product. All THF was evaporated, leaving a white solid residue and yellow viscous liquid. DCM was added to the flask, the material was transferred to a 500-mL separatory funnel and extraction was done for 7 times with water. The collected DCM solution was concentrated and passed through silica-loaded sintered glass funnel (some of triphenylphosphine oxide was removed in this step). Collected material was loaded to a silica gel column and run with only cyclohexane. The desired compound M2 was the initial compound eluting from the column. The solvent from the collected fractions were removed using rotavap and the product was dried under vacuum.

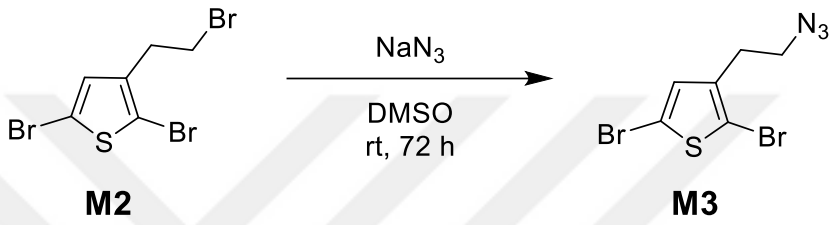
Yield: 3.57 g, 50%.

^{1}H NMR (400 MHz, $CDCl_3$, 25 °C) δ (ppm): 3.10 (t, 2 H), 3.50 (t, 2 H), 6.86 (s, 1 H).

^{13}C NMR (100 MHz, $CDCl_3$, 25 °C) δ (ppm): 31.0, 35.9, 107.7, 109.8, 131.5, 136.3.

TLC (cyclohexane, R_f): 0.60.

2.3.2.3. Synthesis of 3-(2-azidoethyl)-2,5-dibromothiophene (M3)



M2 M3

To a 100-mL one-necked round-bottomed flask, M2 (585 mg, 1.68 mmol) was transferred by washing with 7 mL of DMSO and then sodium azide (273 mg, 4.2 mmol, 2.5 eq.) was added. The reaction mixture was let to stir at room temperature for 72 hours. The TLC of the reaction mixture showed only one spot with R_f=0.2 that belongs to the azidated product M3. After the reaction, 50 mL of water was added to the reaction flask and transferred to a 250-mL separatory funnel. Extraction with chloroform was done for three times (water layer was pale yellow). Chloroform was evaporated and the product was dried under vacuum.

Yield: 480 mg, 92%.

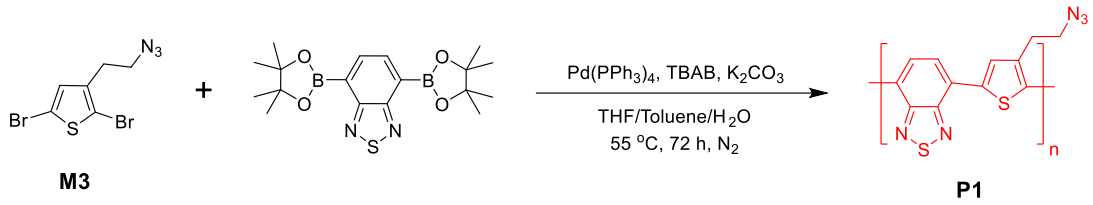
^{1}H NMR (400 MHz, $CDCl_3$, 25 °C) δ (ppm): 2.82 (t, 2 H), 3.46 (t, 2 H), 6.85 (s, 1 H).

^{13}C NMR (100 MHz, $CDCl_3$, 25 °C) δ (ppm): 29.7, 51.0, 109.1, 113.5, 132.4, 137.9.

FT-IR: (ν_{max}/cm^{-1}): 2086 (-N_3).

TLC (cyclohexane, R_f): 0.20.

2.3.2.4. Synthesis of Azide-functionalized Thiophene Based Red-emitting Polymer (P1)



In a 250-mL two-necked round bottomed flask, M3 (585 mg, 1.88 mmol) was transferred using 5 mL of degassed toluene. 2,1,3-benzothiadiazole-4,7-bis(boronic acid pinacol ester) (730 mg, 1.88 mmol, 1 eq.) was added to the reaction flask and vacuum was applied carefully for 20 minutes. Degassed THF (25 mL) and toluene (10 mL) were added and the mixture was stirred for 10 minutes. Then, aqueous K_2CO_3 solution (1.3 g, 9.4 mmol, 5 eq.) was added, followed by a catalytic amount of tetra-*n*-butylammonium bromide (0.2 mmol) and the mixture was stirred for 10 minutes (upon addition of K_2CO_3 and TBAB, color turned to green). Two freeze-pump-thaw cycles were applied and the reaction flask was filled with N_2. Catalytic amount of tetrakis(triphenylphosphine)palladium(0) (0.2 mmol) was added under N_2. The reaction mixture was heated to 55 °C and stirred for 72 hours under N_2 (In the first 1-2 hours, the solution was bright red. In time, the solution acquired a darker red color and became more viscous). After the reaction, all the solvents were evaporated under reduced pressure. Solid material was dissolved in chloroform and suction filtration was done. Chloroform was evaporated, the resulting solid was washed with methanol and the product was dried in oven.

Yield: 439 mg, 82%.

^{1}H NMR (400 MHz, $CDCl_3$, 25 °C) δ (ppm): 3.11 (m, 2 H), 3.46 (m, 2 H), 7.67-8.55 (m, 3 H).

^{13}C NMR (100 MHz, $CDCl_3$, 25 °C) δ (ppm): 29.1-30.9, 50.7-51.4, 125.3-131.7, 135.8-140.0, 152.3-154.2.

FT-IR: (ν_{max}/cm^{-1}): 2094 (-N_3).

UV-Vis (THF): λ_{max} (nm): 319, 494 (ε 1.2*10^4 M^{-1}cm^{-1}).

PL (THF): λ_{max} (nm): 620.

Fluoresence quantum yield: 0.18.

2.3.2.5. Procedure for Quantum Yield Measurement of P1

Fluorescein (in 0.1 M NaOH, $\Phi_f = 0.79$)[153] and rhodamine 6G (in ethanol, $\Phi_f = 0.94$)[154] were chosen as two standard samples and they are cross-calibrated to check whether their literature fluorescence quantum yield values can be obtained experimentally. If both standards behave as expected, they can be used in the fluorescence quantum yield calculation of the sample P1. The experimental procedure is as follows:

I. Record the UV-Vis absorbance and fluorescence graphs of fluorescein, rhodamine 6G and P1 at five different concentrations (absorbance at the excitation wavelength of 0/blank, 0.02, 0.04, 0.06, 0.08 and 0.10).

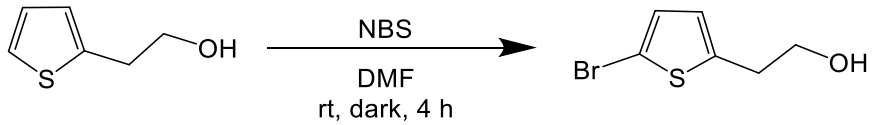
II. Integrated fluorescence intensity versus absorption maxima were plotted for each sample and fluorescence quantum yields were obtained from the following equation:

$$\Phi_A = \Phi_{ST}\left(\frac{m_A}{m_{ST}}\right)\left(\frac{\eta_A^2}{\eta_{ST}^2}\right) \qquad Eq.1$$

where A and ST stand for sample and standard, m is the slope of integrated fluorescence intensity vs. absorption maxima plot and η is the refractive index of the solvent.

2.3.3. Synthesis of Tetrathiophene Oligomer

2.3.3.1. Synthesis of 2-(5-Bromo-2-thienyl)ethanol (M4)



M4

2-thiopheneethanol (1.0 g, 7.8 mmol) was dissolved in 5 mL of dried and degassed DMF in a two-necked 50-mL round-bottomed flask. N-bromosuccinimide (1.67 g, 9.36 mmol, 1.2 eq.) was separately dissolved in 5 mL of dried and degassed DMF and added dropwise into the reaction flask while

stirring. The reaction mixture was continued to stir at room temperature under N_2 for 4 hours in dark. The reaction was followed by TLC (cyclohexane:ethyl acetate, 7:3). After the reaction, the content of reaction flask was transferred into 250-mL separatory funnel by washing with DCM and DCM/water extraction was performed for six times to get rid of excess N-bromosuccinimide. The product was further purified by passing through a silica-packed sintered glass funnel using DCM as eluent. The resulting yellow viscous product was dried under reduced pressure.

Yield: 1.404 g, 86%.

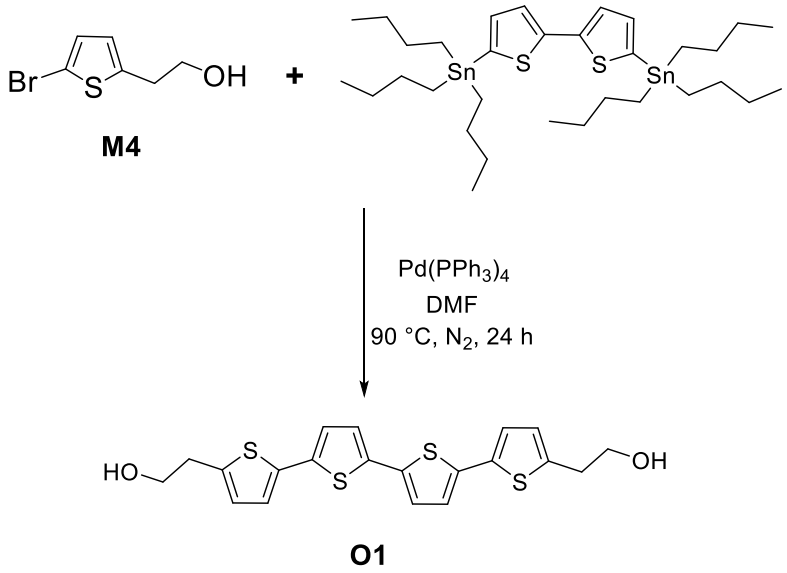
^{1}H NMR (400 MHz, $CDCl_3$, 25 °C) δ (ppm): 3.01 (t, 2 H), 3.84 (t, 2 H), 6.64 (d, 1 H), 6.90 (d, 1H).

^{13}C NMR (100 MHz, $CDCl_3$, 25 °C) δ (ppm): 33.6, 62.9, 109.9, 126.0, 129.7, 142.8.

FT-IR: (ν_{max}/cm^{-1}): 3300 (-OH).

TLC (cyclohexane:ethyl acetate, 7:3, R_f): 0.50.

2.3.3.2. Synthesis of 2,2'-([2,2':5',2'':5'',2'''-quaterthiophene]-5,5'''-diyl)diethanol (O1)



Compound **M4** (1.0 g, 4.8 mmol, 2.2 eq.) and 5,5'-bis(tributylstannyl)-2,2'-bithiophene (1.62 g, 2.18 mmol) were dissolved in 7 mL of dried and degassed

DMF in a two-necked 25-mL round-bottomed flask. Freeze-pump-thaw cycle was applied for 3 times, followed by the addition of catalytic amount of $Pd(PPh_3)_4$ (126 mg, 0.109 mmol, 0.05 eq.) (After addition of the catalyst, previously heterogenous mixture became homogenous and color of the solution first turned to bright red, then darkened over time). The reaction flask was taken to an oil bath preheated to 90 °C and the mixture was stirred for 24 hours under N_2 in dark. The progress of the reaction was followed by TLC (cyclohexane:ethyl acetate, 1:1). The reaction mixture was cooled down to room temperature and DMF was removed by rotavap. Silica filtration was done by washing with THF to remove the catalyst and then THF was removed using rotavap. Cyclohexane was added to the resulting viscous liquid and washed through a sintered glass funnel to remove stannyl by-products. The collected material was dissolved in minimum amount of THF, dropwise added into excess of cold ethanol and left overnight in fridge. The orange solid product was obtained after carefully decanting ethanol. A second precipitation in ethanol was applied to recover more product from ethanol.

Yield: 726 mg, 80%

^{1}H NMR (400 MHz, DMSO-d_6, 25 °C) δ (ppm): 2.91 (t, 4 H), 3.63 (q, 4 H), 4.86 (t, 2 H), 6.85 (d, 2 H), 7.16 (d, 2 H), 7.19 (d, 2 H), 7.26 (d, 2 H).

^{13}C NMR (100 MHz, $CDCl_3$, 25 °C) δ (ppm): 33.9, 60.8, 122.2, 123.0, 127.8, 136.3, 138.1, 143.4.

ESI-MS (m/z): calcd. for $C_{20}H_{18}S_4O_2$ $[M]^+$: 418.0190, found: 418.0205.

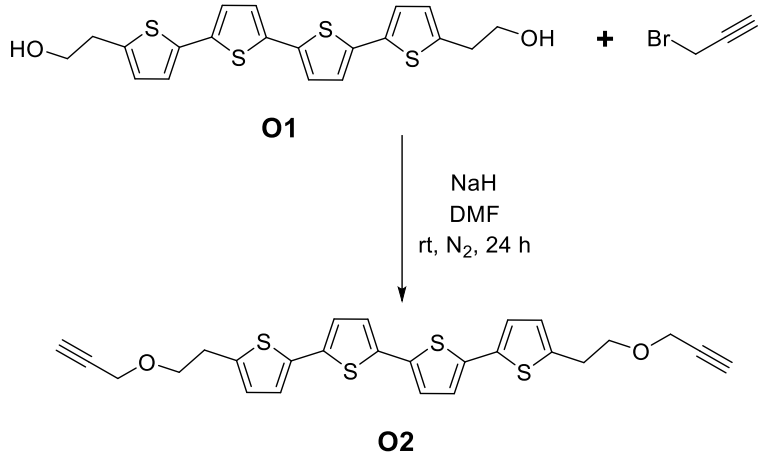
FT-IR: (ν_{max}/cm^{-1}): 3300 (O-H).

UV-Vis ($CHCl_3$): λ_{max} (nm): 368.

PL (DMSO): λ_{max} (nm): 445.

TLC (cyclohexane:ethyl acetate, 1:1, R_f): 0.36.

2.3.3.3. Synthesis of 5,5'''-bis(2-(prop-2-yn-1-yloxy)ethyl)-2,2':5',2'':5'',2'''-quaterthiophene (O2)



Compound **O1** (100 mg, 0.24 mmol) was dissolved in 5 mL of DMF and cooled down to 0 °C. NaH (50 mg, 2.17 mmol, 9 eq.) was added under N_2 atmosphere. The mixture was stirred 1 hour and propargyl bromide (1 mL from 80 wt. % in toluene, 1.33 g, 11 mmol, 46 eq.) was added. The reaction mixture was then stirred at room temperature for 24 hours under N_2. The progress of the reaction was monitored by TLC (cyclohexane:ethyl acetate, 1:1). After the reaction, solvent was removed under reduced pressure and the remaining solid was washed with water and cyclohexane, respectively. The product was isolated through a silica gel packed column using cyclohexane:DCM (95:5) as eluent.

Yield: 44 mg, 37%.

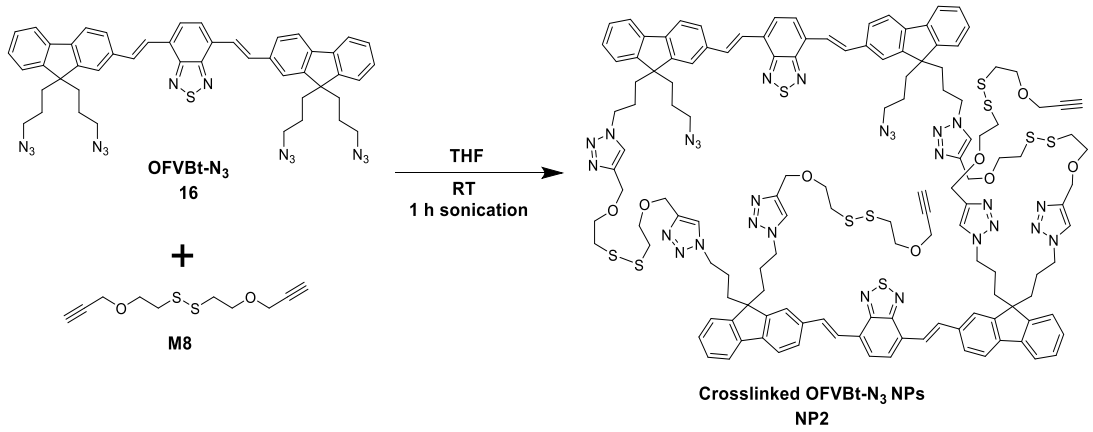
^{1}H NMR (400 MHz, $CDCl_3$, 25 °C) δ (ppm): 2.38 (t, 2 H), 3.03 (t, 4 H), 3.72 (t, 4 H), 4.14 (d, 4 H), 6.71 (d, 2 H), 6.91-6.97 (m, 6 H).

^{13}C NMR (100 MHz, $CDCl_3$, 25 °C) δ (ppm): 30.5, 61.0, 67.7, 75.4, 78.9, 121.4, 121.9, 129.3, 137.1, 137.3, 144.6.

TLC (cyclohexane:ethyl acetate, 1:1, R_f): 0.82.

2.3.4. Crosslinked Conjugated Oligomer Nanoparticles

2.3.4.1. Synthesis of Crosslinked OFVBt-N_3 Nanoparticles in THF



Crosslinked OFVBt-N_3 nanoparticles (**NP2**) were prepared by click reaction of OFVBt-N_3 (**16**) with a disulfide bridged crosslinker in the presence and absence of catalyst. First, stock solutions of **OFVBt-N_3**, **M8**, and $Cu(PPh_3)_3Br$ as catalyst were prepared as follows: 20 mg of **OFVBt-N_3** was dissolved in 8 mL of dried distilled THF (0.0029 mmol/mL). 125 mg of **M8** was dissolved in 10 mL of dried distilled THF (0.054 mmol/mL). 5.5 mg of $Cu(PPh_3)_3Br$ was dissolved in 1 mL of dried distilled THF (0.0059 mmol/mL).

In the first part, crosslinked NPs were synthesized in the presence of the catalyst as follows:

(a) 16:M8:catalyst (1:2:0.1): In a two-necked 25-mL round-bottomed flask, 4 mL of **OFVBt-N_3** (11.6 µmol) and 428 µL of **M8** (23.2 µmol) were added. 196 µL from the catalyst stock solution was also added to the mixture and total volume of the solution was brought to 5.5 mL. The mixture was ultrasonicated with probe at 70% amplitude for 1 hour.

(b) 16:M8:catalyst (1:1:0.1): In a two-necked 25-mL round-bottomed flask, 4 mL of **OFVBt-N_3** (11.6 µmol) and 214 µL of **M8** (11.6 µmol) were added. 196 µL from the catalyst stock was also added to the mixture and total volume of the solution was brought to 5.5 mL. The mixture was ultrasonicated with probe at 70% amplitude for 1 hour.

In the second part, crosslinked NPs in THFwere synthesized without catalyst as follows:

(c) 16:M8 (1:2): In a two-necked 25-mL round-bottomed flask, 4 mL of **OFVBt-N_3** (11.6 µmol) and 428 µL of **M8** (23.2 µmol) were added. Total volume of the mixture was brought to 5.5 mL. The mixture was sonicated with probe at 70% amplitude for 1 hour.

(d) 16:M8 (1:1): In a two-necked 25 mL round-bottomed flask, 4 mL of **OFVBt-N_3** (11.6 µmol) and 214 µL of **M8** (11.6 µmol) were added. Total volume of the mixture was brought to 5.5 mL. The mixture was sonicated with probe at 70% amplitude for 1 hour.

Decrease in the azide stretching peak around 2100 cm^{-1} was monitored by IR spectroscopy. The nanoparticles were characterized with UV-Vis absorbance and fluorescence spectroscopies, DLS, SEM and TEM.

2.3.4.2. Dispersion of Oligomer Nanoparticles in Water (NP3)

The crosslinked OFVBt-N_3 NPs prepared in THF (**NP2**) were dispersed in water as follows:

(a) 16:M8 (1:2) (0.5 mg/mL): The volume of **16:M8** (1:2) NPs prepared in THF was decreased to 1 mL under reduced pressure (40 °C). Then, concentrated THF solution was injected into 20 mL of Milli-Q water in a 100-mL beaker while sonicating. The mixture was sonicated for 30 minutes at room temperature. Finally, all THF was removed under reduced pressure to give water-dispersible NPs.

(b) 16:M8 (1:2) (1.0 mg/mL): NPs in THF were prepared by doubling the reagent amounts given in 2.3.4.1(c). The volume of **16:M8** (1:2) NPs prepared in THF was decreased to 1 mL under reduced pressure (40 °C). Then, concentrated THF solution was injected into 20 mL of Milli-Q water in a 100 mL beaker while sonicating. The mixture was sonicated for 30 minutes at room temperature. Finally, THF was removed under reduced pressure to yield stable water-dispersible NPs.

Water-dispersed NPs were characterized by UV-Vis absorbance and fluorescence spectroscopies, DLS, SEM and TEM.

2.3.4.3. Disulfide Bond Cleavage by Glutathione (GSH)

Cleavage of S-S bonds in **NP3** was studied using GSH as reducing agent according to below procedure:

(a) 5 mL **NP3** (5.8 µmol) was added with 2 equivalent GSH (3.6 mg, 11.6 µmol, 2.32 mM) and sonicated for 5 minutes before DLS measurement.

(b) 2.5 mL from **NP3** (2.9 µmol) was added with GSH (9 mg, 29 µmol, 10 mM) and sonicated for 5 minutes before DLS measurement.

Sizes and morphologies of **NP3** after GSH treatment were checked by DLS and SEM.

CHAPTER 3

Results and Discussions

3.1. Introduction

This chapter consists of three sections. In section 3.2, the studies on the synthesis of multifunctional covalently attached porphyrin-cucurbit[7]uril conjugate are discussed. This section also represents the studies on the singlet oxygen generation capacity of the conjugate as well as investigations for its ability to act as a molecular receptor. Section 3.3 discusses the synthesis of thiophene-based conjugated polymers and oligomers and represents the efforts to combine conjugated conpounds with functionalized cucurbiturils in the construction of multifunctional supramolecular assemblies and nanoparticles. In section 3.4, the synthesis of disulfide bond-containing crosslinked conjugated oligomer nanoparticles based on a fluorene-benzothiadiazole cooligomer is discussed. The response of these nanoparticles in reducing conditions are also investigated in this section.

3.2. "Clicked" Porphyrin-Cucurbit[7]uril Conjugate

This work has been partially reported in the following publication[155]:

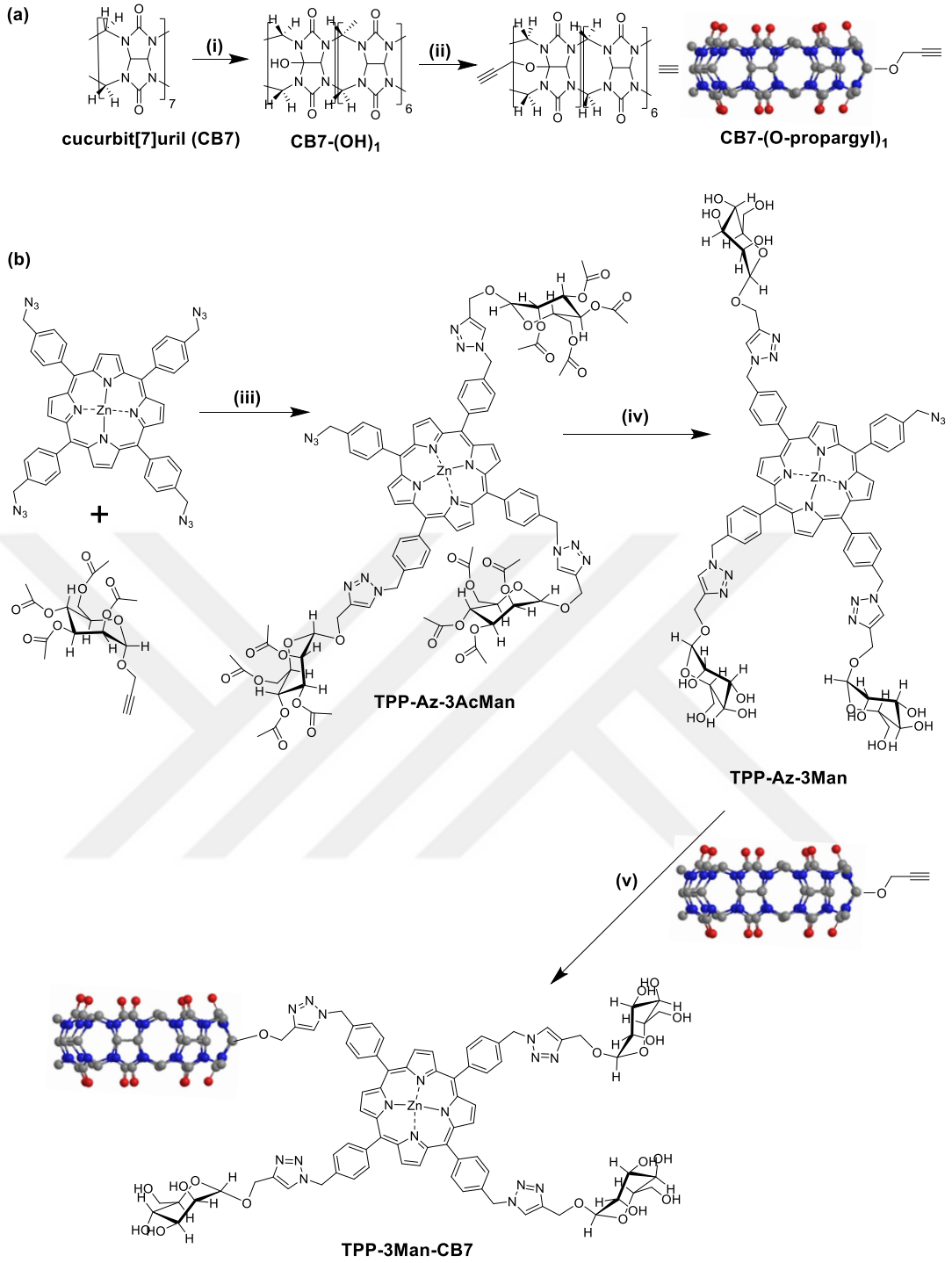
A. Koc, R. Khan, D. Tuncel, "Clicked" Porphyrin-Cucurbituril Conjugate: A New Multifunctional Supramolecular Assembly Based on Triglycosylated Porphyrin and Monopropargyloxycucurbit[7]uril. *Chemistry: A European Journal*, **2018**, *24*, 15550-15555.

3.2.1. Aim of the Study

In this study, it is aimed to fabricate a novel mulfiunctional platform that can efficienctly produce singlet oxygen, carry molecules and target cells. For this

purpose, a multifunctional supramolecular assembly based on a photoactive mannosilated porphyrin and covalently attached cucurbit[7]uril (CB7) was synthesized according to Scheme 3.1. First, azido-functionalized tetraphenylporphyrin (TPP) was synthesized and mannosilated by copper-catalyzed azide-alkyne cycloaddition (CuAAC). Monopropargyloxylated CB7 was synthesized and attached to the TPP core via a second CuAAC reaction. TPP was chosen as the core of the assembly due to its singlet oxygen ($^1O_2$) generation ability which renders it a suitable photosensitizer for anticancer and antimicrobial photodynamic therapy (PDT) applications. Mannose groups were attached to the core so that their hydrophilic nature may help to increase the water solubility of the resulting assembly as well as mannose receptors that are found in bacterial surface and overexpressed in certain tumor cells can be targeted. CB7, because of its bulkiness, can minimize the interactions between TPP units, which will enhance the $^1O_2$ quantum yield. CB7 is an excellent host, so anticancer drugs or antibiotics can be encapsulated and carried by CB7 to increase the efficacy of the therapy.

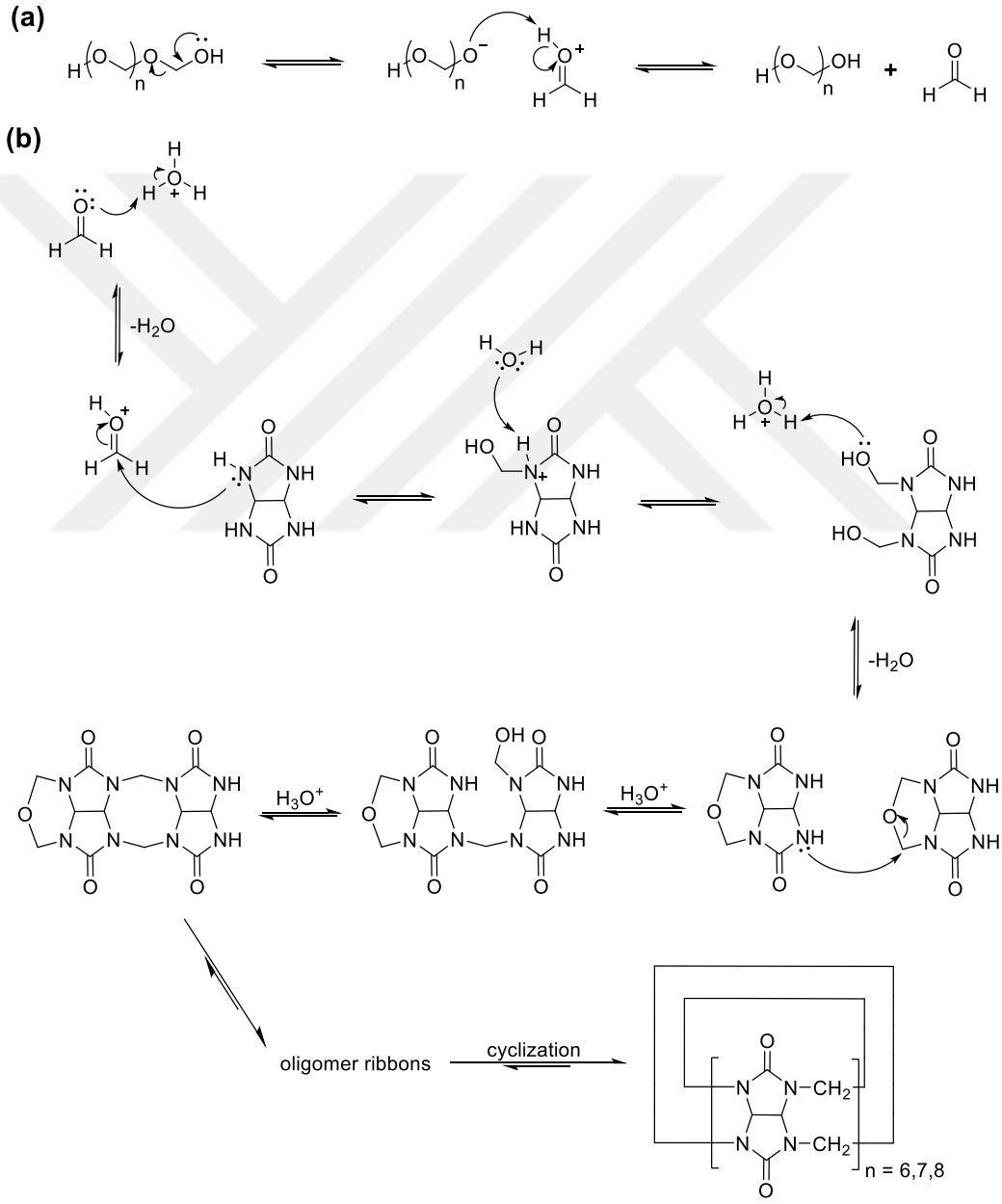
The structure of the compounds were characterized by ^1H and ^{13}C NMR, FT-IR spectroscopies and ESI-MS spectrometry. Thermal stability of certain compounds was analyzed by thermal gravimetric analysis (TGA). The photophysical properties of the TPP-based structures were investigated by UV-Vis absorbance and fluorescence and time-resolved fluorescence spectroscopies, and fluorescence quantum yield measurements. Host-guest chemistry and $^1O_2$ generation efficiency of the supramolecular assembly was studied.



Scheme 3.1 **(a)** Synthesis of monofunctionalized CB7: (i) $K_2S_2O_8$, K_2SO_4, H_2O, 85 °C; (ii) NaH, propargyl bromide, DMSO, 0°C-25 °C, N_2(g), 48 h. **(b)** (iii) Synthesis of the assembly: $CuSO_4.5H_2O$/Na-L-Ascorbate, THF/H_2O, 60 °C; 14 h (iv) $NaOCH_3$, MeOH, 25 °C, 14 h; (v) $CuSO_4.5H_2O$/Na-L-Ascorbate, DMSO/H_2O, 48 h.

3.2.2. Synthesis of Cucurbit[n]urils

CB[n]s are formed from an acid-catalyzed condensation of glycoluril with formaldehyde. However, paraformaldehyde is used in the reaction because formaldehyde itself is quite unstable and therefore it can decompose before condensing with glycoluril. Paraformaldehyde rapidly depolymerizes upon heating (Scheme 3.2a) and forms fresh formaldehyde that will rapidly react with glycoluril (Scheme 3.2b).



Scheme 3.2 **(a)** Depolymerization of paraformaldehyde. **(b)** Formation mechanism of CB[n].

The condensation reaction yields differently sized CB[n] homologues, as well as oligomers. CB6, CB7 and CB8 were successfully isolated from the mixture as explained in Section 2.3.1.1. Since we utilized only CB7 in this particular study, discussions in this section are limited to the characterization of CB7 (**1**).

Three sets of equally intense signals are seen in ^{1}H NMR spectrum of CB7 (Figure 3.1). A singlet at 5.53 ppm arises from the protons that are at the equatorial position (H_c). On the methylene bridges, the exocyclic protons (H_b) give a doublet at 4.23 ppm and the endocyclic protons (H_a) give another doublet at 5.80 ppm.

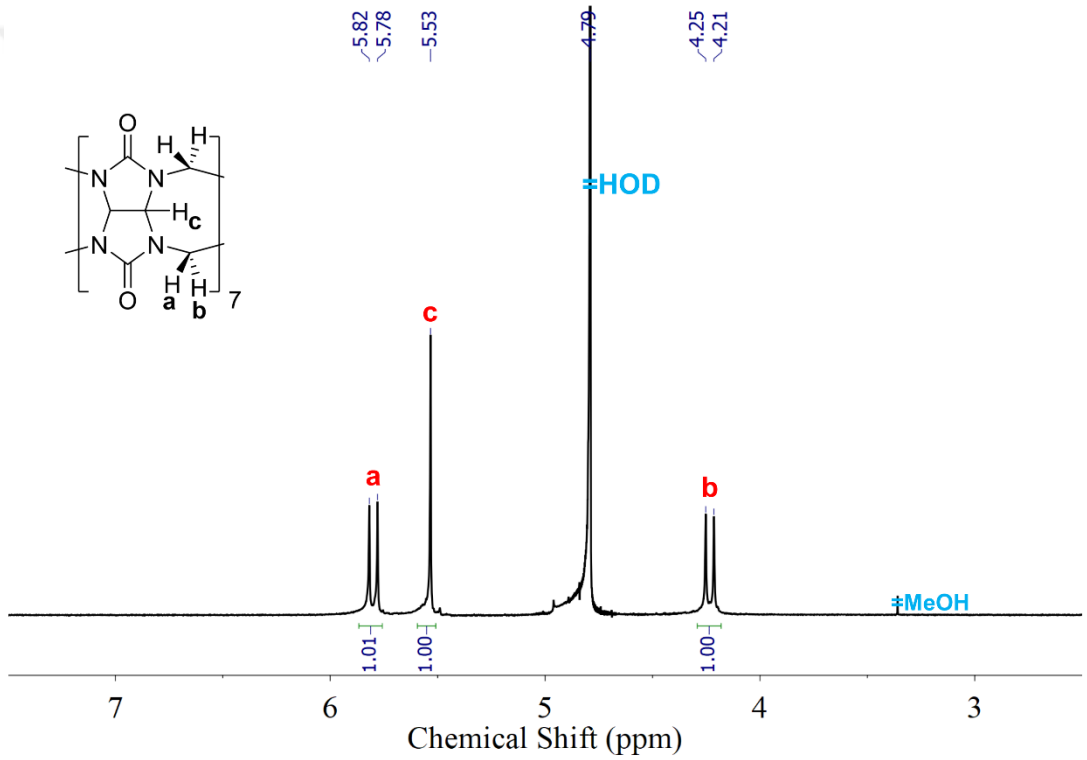


Figure 3.1 ^{1}H NMR spectrum of CB7 in D_2O.

In ^{13}C NMR spectrum of CB7, three different signals are located at 52.6, 71.3 and 156.6 ppm that correspond to carbons at methylene bridges, glycoluril methine Cs and carbonyl Cs, respectively (Figure 3.2).

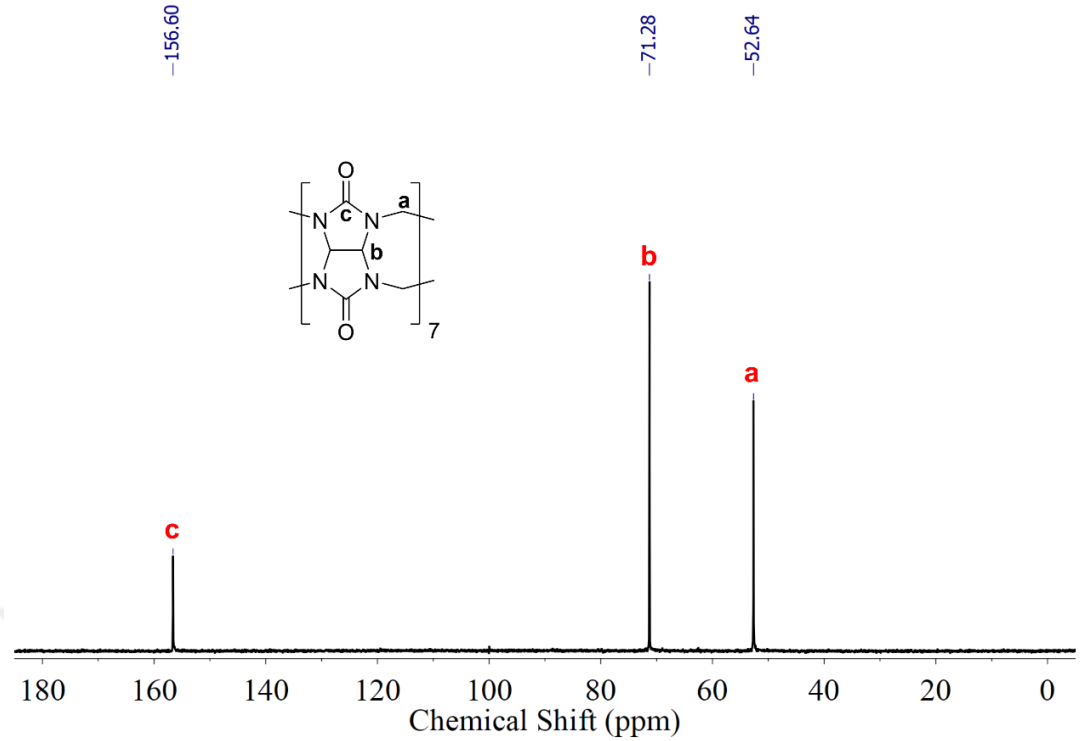


Figure 3.2 ^{13}C NMR spectrum of CB7 in D_2O.

+ESI-MS spectrum of CB7 clearly shows singly and doubly charged sodium adducts of the molecular ion as labelled in Figure 3.3. There is no signal that may arise from the presence of CB6 and CB8, which suggests that CB7 was successfully purified from the other CB homologues and oligomers.

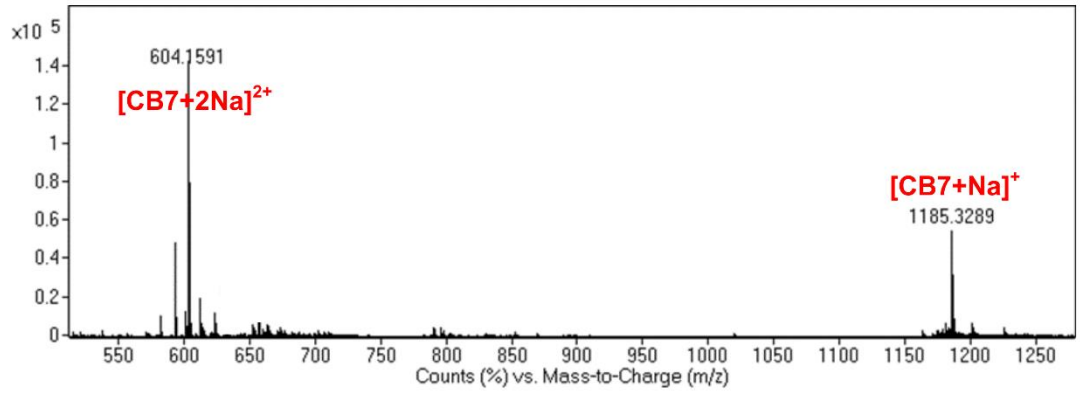


Figure 3.3 +ESI-MS spectrum of CB7.

In FT-IR spectrum of CB7 (Figure 3.4), the most characteristic signal at 1725 cm^{-1} is given by C=O stretching. The broad signal around 3400 cm^{-1} is attributed to O-H stretching because of moisture. Although the product is well dried in oven and vacuum, O-H peak still persists since CB[n] homologues are extremely hygroscopic. Weak signals around 2882 and 3001 cm^{-1} are assigned respectively to asymmetric and symmetric stretchings of C-H bond.

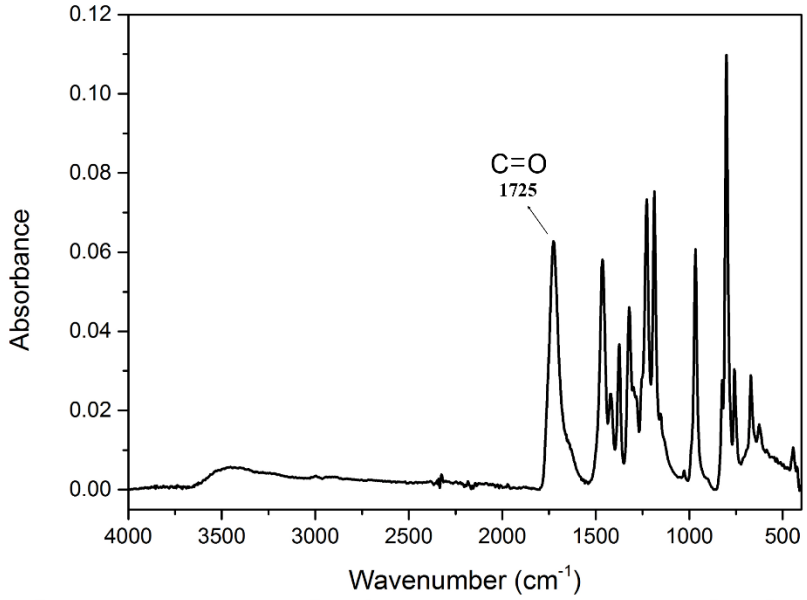


Figure 3.4 FT-IR absorption spectrum of CB7.

3.2.3. Synthesis of MonohydroxyCB7 (2)

Synthesis and purification of CB7-$(OH)_1$ (**2**) was performed according to literature.[45] $K_2S_2O_8$ was used as oxidizing agent. Although the reaction mechanism has not been established to date, it is thought that the redox reaction between $K_2S_2O_8$ and K_2SO_4 trigger the formation of free radicals that may lead to the generation of OH radicals, which oxidize CB7 via radical reactions.

As seen in Figure 3.5, ^{1}H NMR spectrum of CB7-$(OH)_1$ is much more complicated than that of CB7. Presence of only one -OH group on the equatorial position significantly distorts the electronic environment, which ends up with a total of nine sets of signals in ^{1}H NMR spectrum assigned as H_1-H_9. Here, the most significant signal is the one at 5.33 ppm, which is assigned to the glycoluril methine hydrogen in the hydroxylated unit. The -OH hydrogen is not seen due to fast exchange with D_2O. The integration values add up to 41 protons as expected.

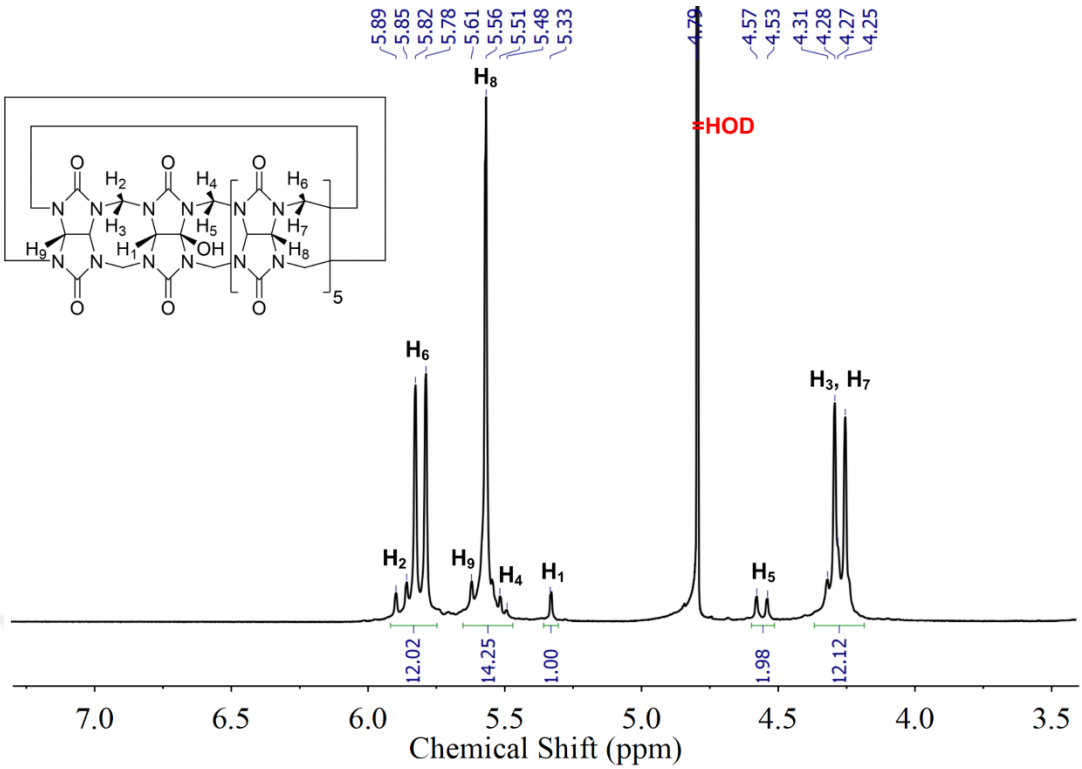


Figure 3.5 ^{1}H NMR spectrum of CB7-(OH)$_1$ in D_2O.

Figure 3.6 shows the presence of seven chemically non-equivalent carbons in ^{13}C NMR spectrum of CB7-(OH)$_1$, which is caused by the change in molecular symmetry upon hydroxylation.

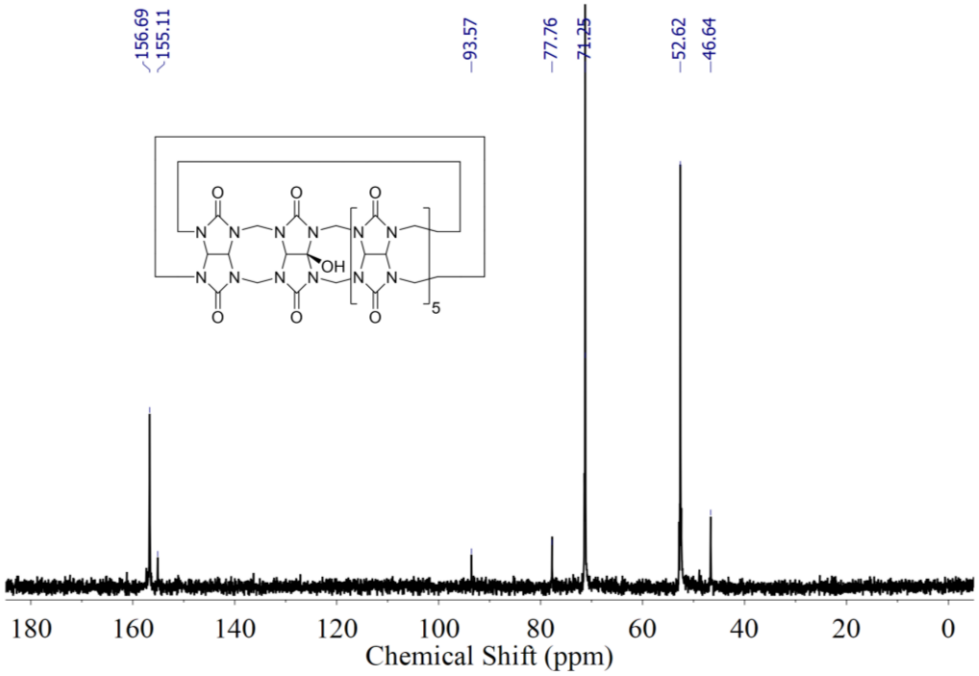


Figure 3.6 ^{13}C NMR spectrum of CB7-(OH)$_1$ in D_2O.

In +ESI-MS spectrum of CB7-$(OH)_1$, the compound is detected in the form of singly and doubly charged species as sodium and potassium adducts (Figure 3.7).

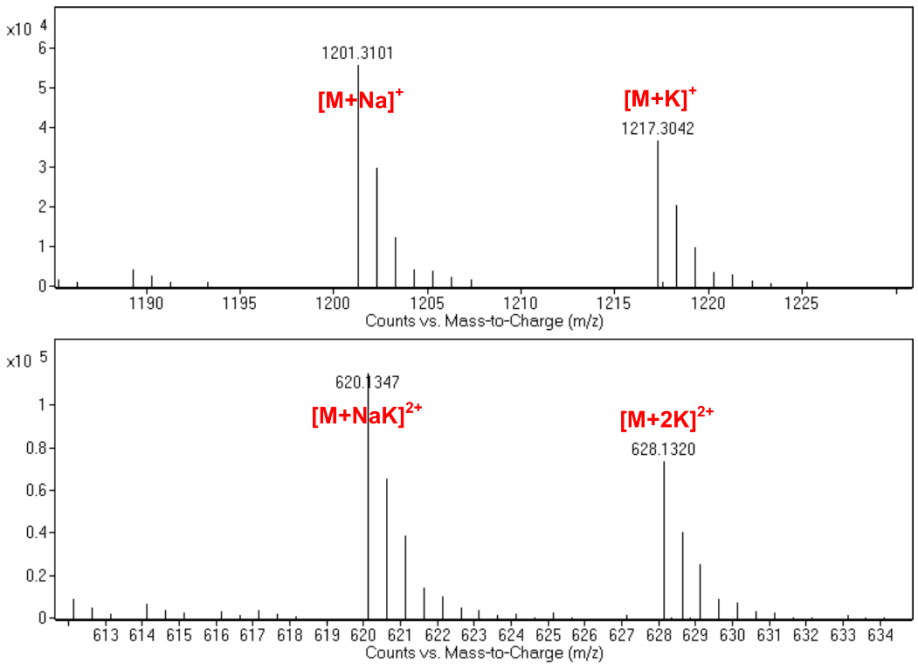


Figure 3.7 +ESI-MS spectrum of CB7-$(OH)_1$.

FT-IR spectrum is very similar to that of CB7, C=O stretching at 1729 cm^{-1} being the most characteristic peak and broad band around 3400 cm^{-1} is due to moisture. Two weak signals around 2900 and 3000 cm^{-1} are due to C-H asymmetric and symmetric stretchings (Figure 3.8).

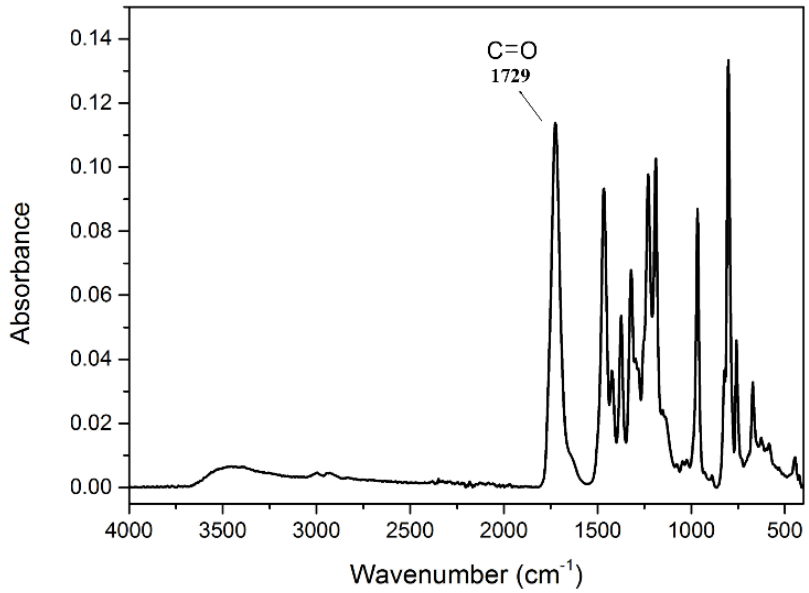


Figure 3.8 FT-IR absorption spectrum of CB7-$(OH)_1$.

3.2.4. Synthesis of MonopropargyloxyCB7 (3)

After deprotonating the hydroxyl group of CB7-$(OH)_1$ with a strong base NaH, S_N2 reaction with propargyl bromide yielded CB7-(O-propargyl)$_1$ (**3**).

^{1}H NMR spectrum of the product contains eight chemically non-equivalent hydrogen sets (Figure 3.9). Terminal alkyne hydrogen gives a singlet around 2.52 ppm (H_8), which confirms the attachment of propargyl group on CB7. The hydrogens on the methylene bridge of propargyl group (H_7) are downfield shifted to 5.65 ppm as expected since they are neighbor to electronegative oxygen atom. The molecule has 45 hydrogen atoms in total and the integration values also satisfy this.

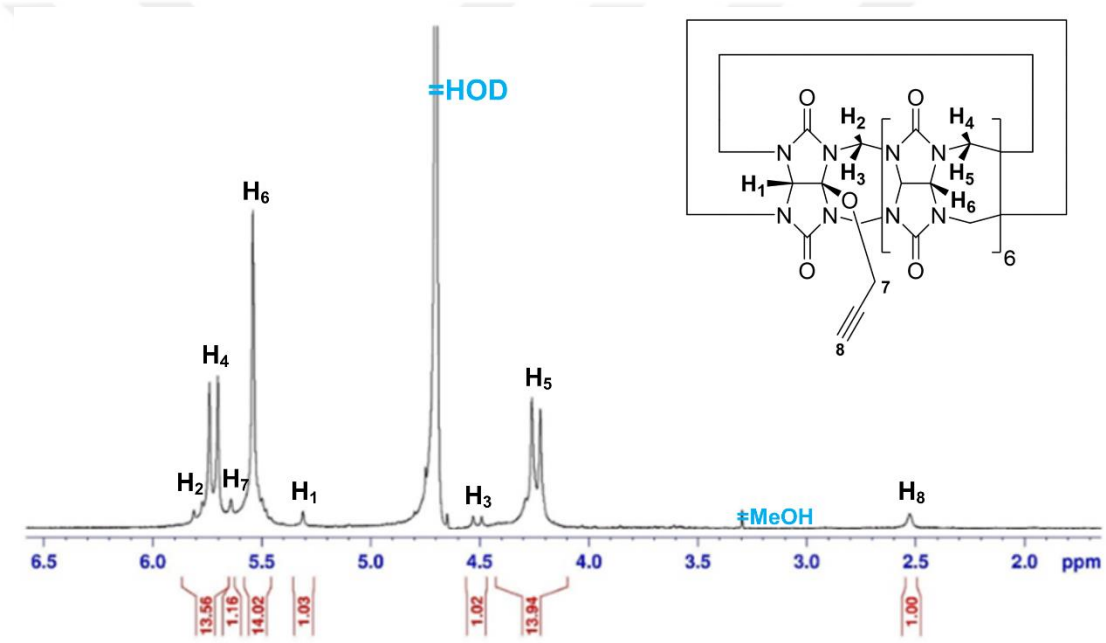


Figure 3.9 ^{1}H NMR spectrum of CB7-(O-propargyl)$_1$ in D_2O+NaCl.

^{13}C NMR spectrum of CB7-(O-propargyl)$_1$ indicates nine signals, two of which are assigned to methylene bridge (49.2 ppm) and terminal alkyne (127.2 ppm) carbons of propargyl group (Figure 3.10).

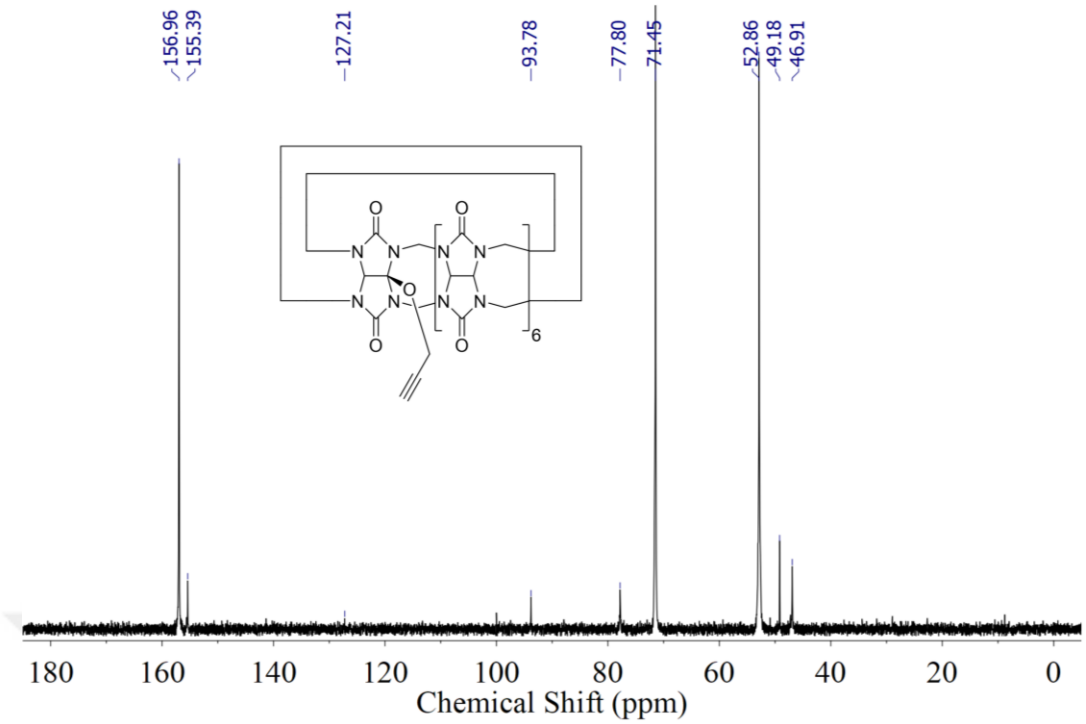


Figure 3.10 ^{13}C NMR spectrum of CB7-(O-propargyl)$_1$ in D_2O+NaCl.

In +ESI-MS spectrum, two positively singly charged species are found as sodium and potassium adducts of the compound (Figure 3.11).

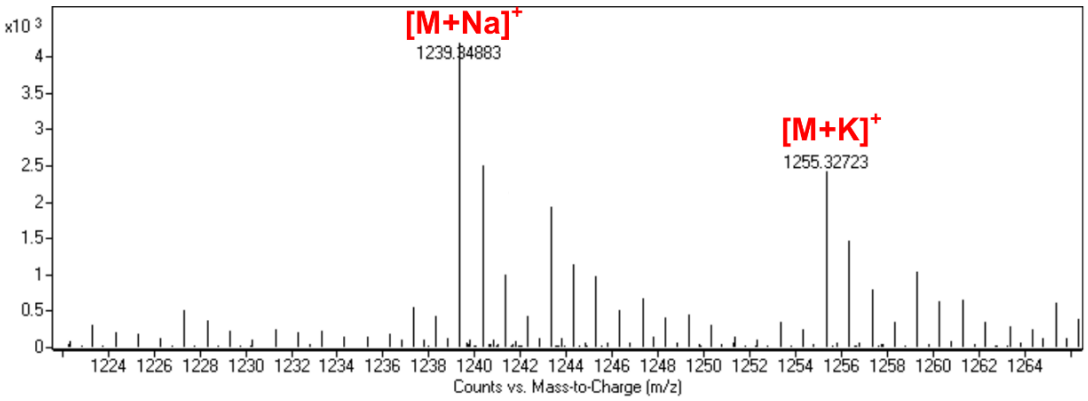


Figure 3.11 +ESI-MS spectra of CB7-(O-propargyl)$_1$.

In the FT-IR spectrum of the compound (Figure 3.12), -C≡C- stretching peak at 2114 cm^{-1} and C≡C-H stretching peak at 3277 cm^{-1} verify the successful synthesis of CB7-(O-propargyl)$_1$. C=O peak at 1723 cm^{-1} and the broad band around 3500 cm^{-1} due to moisture are characteristic for all CB[n] derivatives.

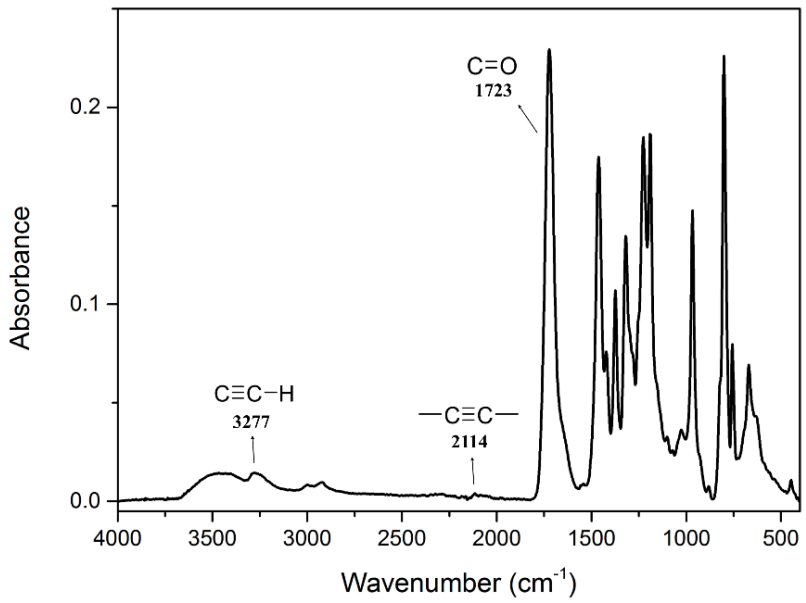


Figure 3.12 FT-IR absorption spectrum of CB7-(O-propargyl)$_1$.

Thermal stability of CB7-(O-propargyl)$_1$ was checked with thermal gravimetric analysis (TGA) and it was found that the compound starts to decompose at 376 °C and reaches the maximum decomposition rate at 402 °C (Figure 3.13).

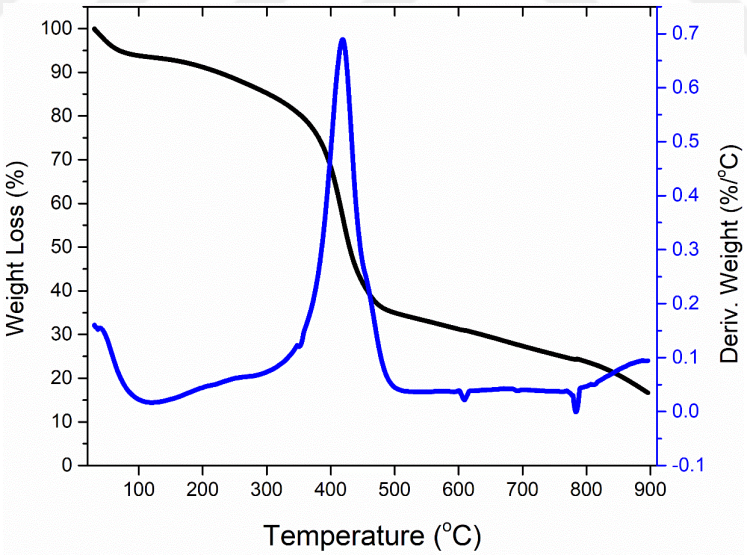
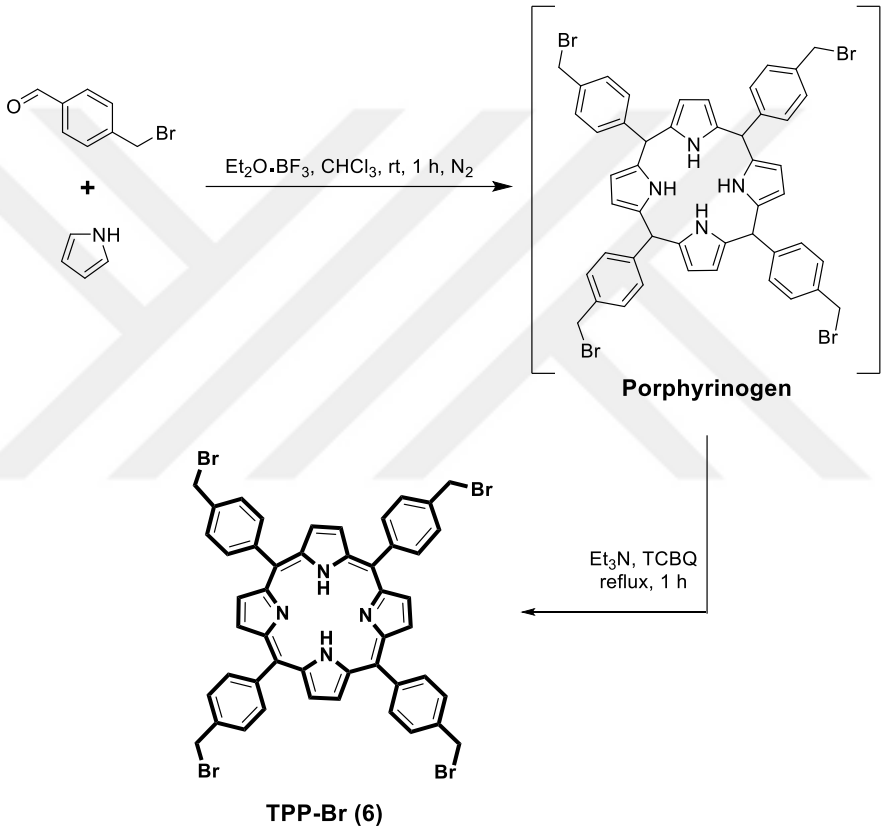


Figure 3.13 TGA graph of CB7-(O-propargyl)$_1$.

3.2.5. Synthesis of 5,10,15,20-tetrakis(α-bromo-*p*-tolyl)porphyrin (6)

TPP-Br (**6**) was synthesized through a condensation reaction of α-bromo-*p*-tolualdehyde and pyrrole using $Et_2O \cdot BF_3$ as Lewis acid catalyst.[147] The formation mechanism of TPP-Br involves a series of pyrrole and α-bromo-*p*-

tolualdehyde condensation reactions. Pyrrole acts as a nucleophile and α-bromo-*p*-tolualdehyde acts as an electrophile. $Et_2O \cdot BF_3$ speeds up the reaction by increasing the electrophilicity of α-bromo-*p*-tolualdehyde, which makes it more available for a nucleophilic attack from pyrrole. This also prevents self-polymerization of pyrrole. Porphyrininogen forms as a stable intermediate as shown in Scheme 3.3. To the reaction mixture that contains the porphyrinogen, then, triethylamine is added to deprotonate the pyrrolic –NH groups, followed by the addition of tetrachloro-1,4-benzoquinone to yield TPP-Br. (Scheme 3.3).



Scheme 3.3 One-pot synthesis of TPP-Br. Condensation of the aldehyde with pyrrole yields porphyrinogen, which is then oxidized to TPP-Br.

As seen in Figure 3.14, ^{1}H NMR spectrum of TPP-Br is very clean and all the chemical shifts and integrations are well-matching. Pyrrolic N-hydrogens (a) are extremely shielded within the aromatic macrocycle and therefore resonate at -2.81 ppm. All the other pyrrolic hydrogens (b) are chemically equivalent and highly deshielded, thus they give a singlet at 8.84 ppm. Each of aromatic benzene hydrogens (c and d) give a doublet at 8.19 and 7.80 ppm, respectively. Benzylic hydrogens (e) come at 4.80 ppm as a singlet.

ESI-MS spectrum of TPP-Br is also very clean, showing an intense signal for the hydrogen adduct of the compound in positive scan mode (Figure 3.15).

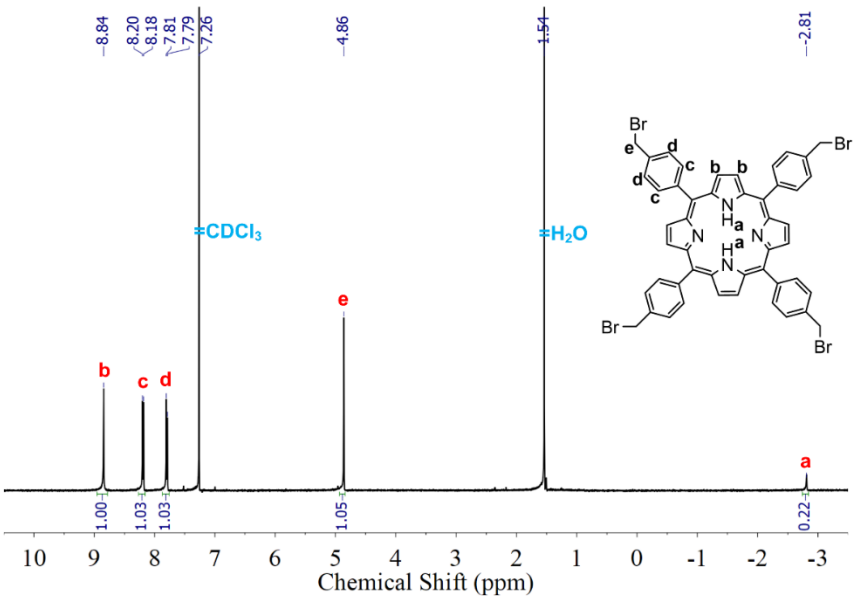


Figure 3.14 ^{1}H NMR spectrum of TPP-Br in $CDCl_3$.

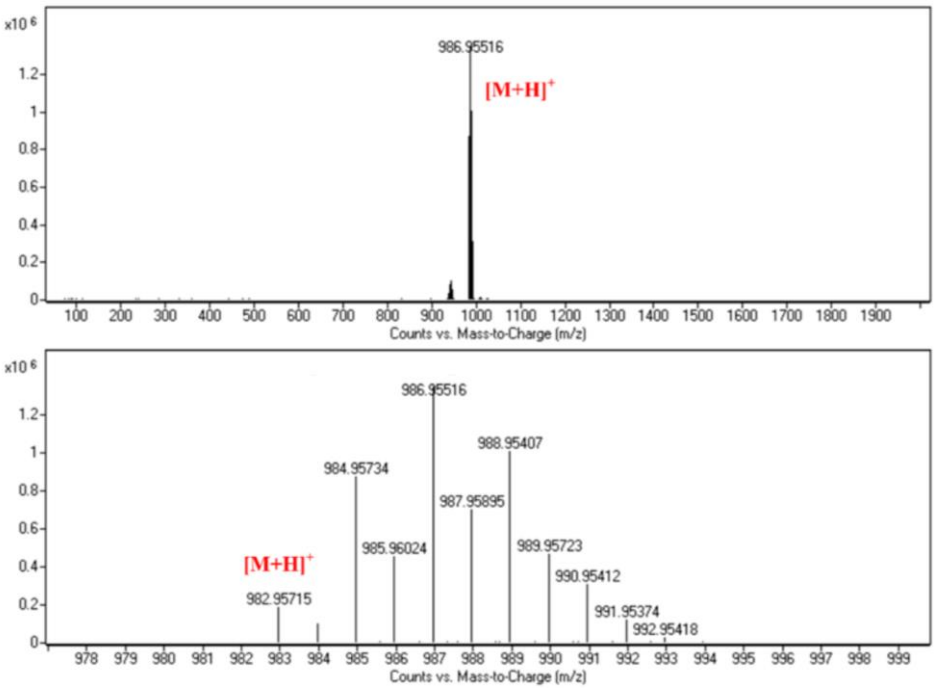


Figure 3.15 +ESI-MS spectra of TPP-Br.

TPP-Br has a Soret band at 420 nm and four Q-bands at 515, 551, 590, 645 nm, which are caused by transitions from ground state to two vibrational excited states and further splitting of these bands due to breakage of molecular symmetry in the presence of pyrrolic N-hydrogens. It has two fluorescence maxima at 652 and 716 nm.

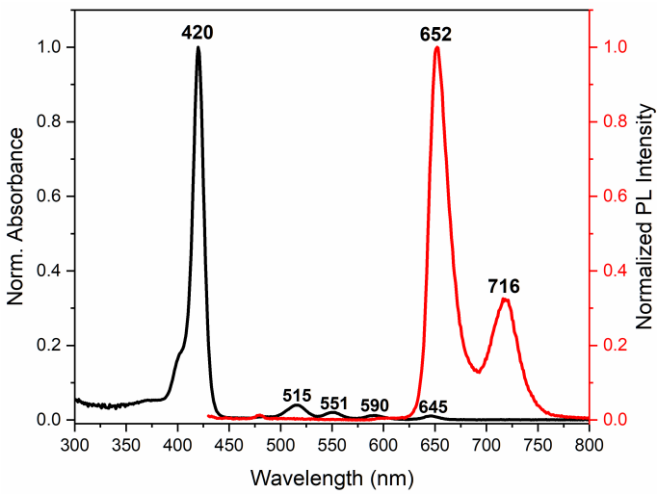


Figure 3.16 UV-Vis absorbance and fluorescence spectra of TPP-Br in DMSO.

3.2.6. Synthesis of TPP-N_3 (7)

Compound **6** was azidated through an S_N2 reaction with NaN_3 to obtain TPP-N_3 (**7**).

The most noticeable change in ^1H NMR spectrum of TPP-N_3 as compared to that of TPP-Br is the slight upfield shift of benzylic proton (e) since -N_3 group is less electronegative as compared to Br (Figure 3.17).

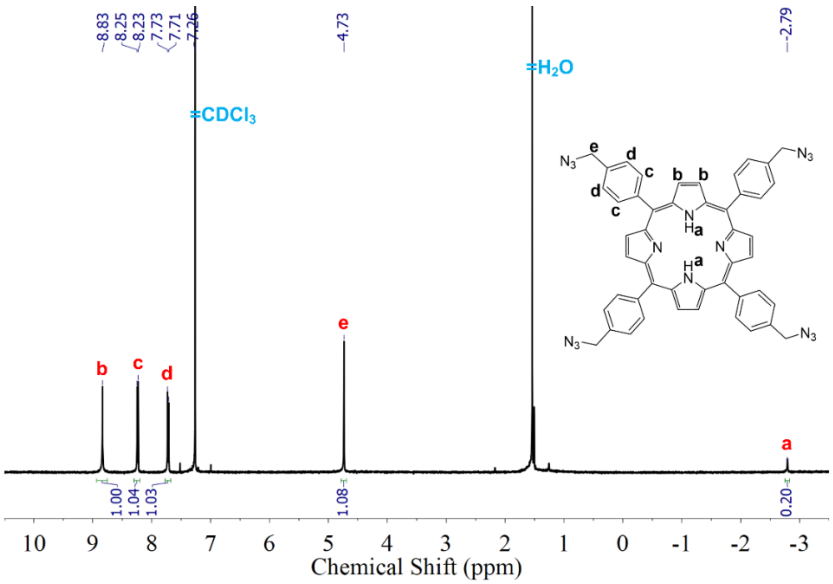


Figure 3.17 ^1H NMR spectrum of TPP-N_3 in $CDCl_3$.

In Figure 3.18, ESI-MS spectrum of TPP-N_3 that demonstrates the positively singly charged adduct of compound with hydrogen confirms the success of the synthesis.

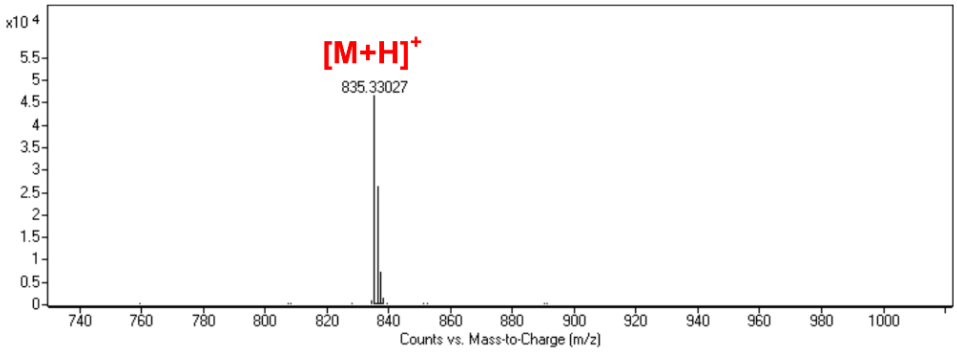


Figure 3.18 +ESI-MS spectrum of TPP-N_3.

3.2.7. Synthesis of Zn-TPP-N_3 (8)

Before proceeding with Cu-catalyzed azide-alkyne cycloaddition (CuAAC) reactions, the core of TPP-N_3 (**7**) was metalated with Zn so as to prevent inclusion of Cu that will decrease its catalytic effect. Metalation was successfully achieved by refluxing compound **7** with $Zn(OAc)_2$ in chloroform/methanol mixture.

In ^{1}H NMR spectrum (Figure 3.19), disappearance of singlet at -2.79 ppm is the proof for the successful metalation because pyrrolic N-hydrogens are removed by acetate ions prior to metalation.

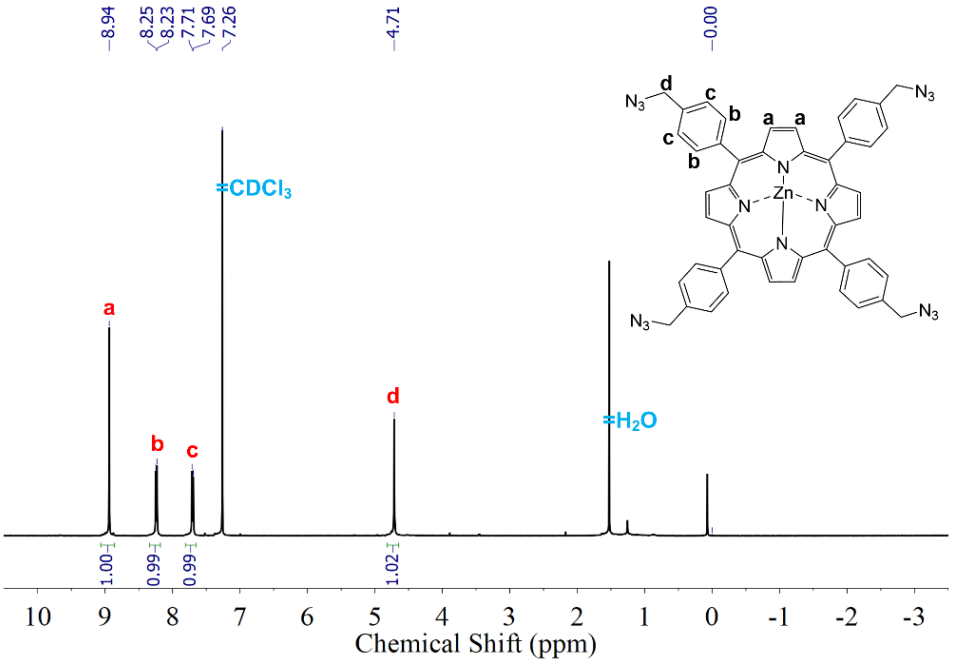


Figure 3.19 ^{1}H NMR spectrum of Zn-TPP-N_3 in $CDCl_3$.

+ESI-MS spectrum of Zn-TPP-N_3 shows the signal coming from the molecular ion of the compound and confirms the successful metalation (Figure 3.20).

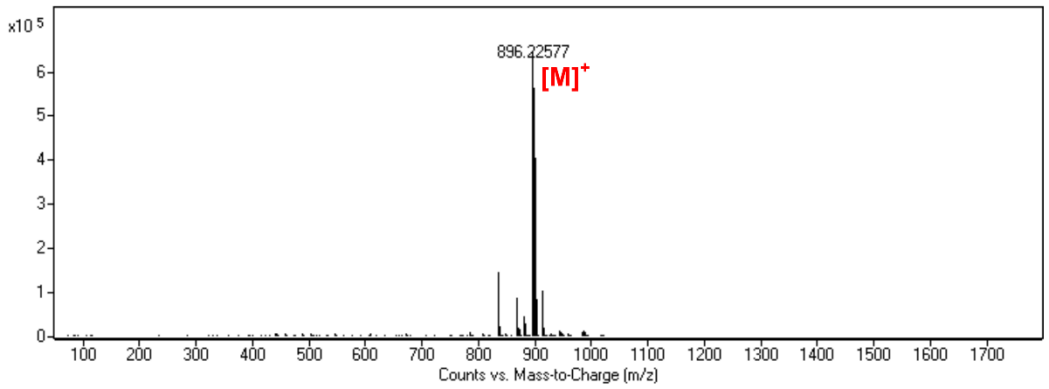


Figure 3.20 +ESI-MS spectrum of Zn-TPP-N_3.

FT-IR spectrum of Zn-TPP-N_3 given in Figure 3.21 has the characteristic -N_3 stretching peak, which provides a strong proof for the retention of reactive azide groups after metalation.

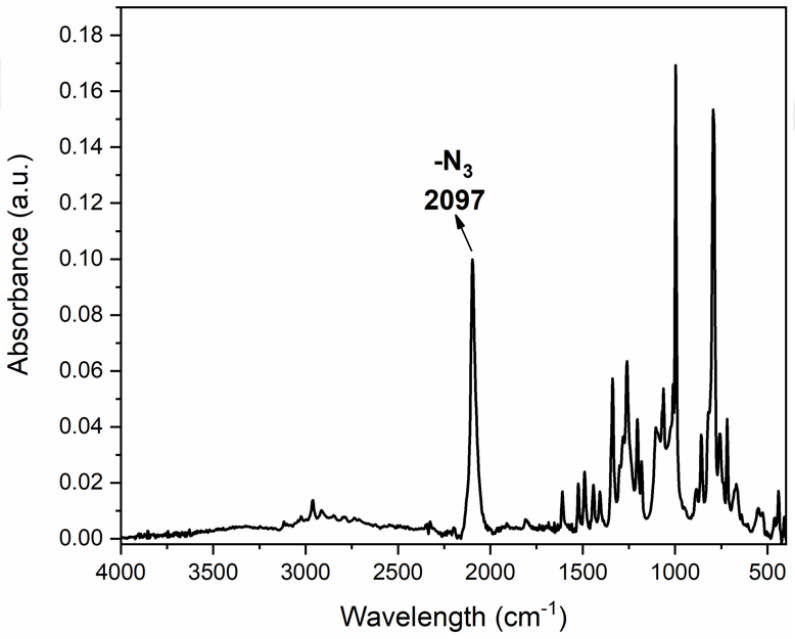


Figure 3.21 FT-IR spectrum of Zn-TPP-N_3.

In UV-Vis absorbance spectrum of Zn-TPP-N_3, the Soret band is slightly red-shifted from 420 to 424 nm when compared to free-base TPP-N_3 and there are now two Q-bands at 554 and 595 nm due to the increase in molecular symmetry. The fluorescence spectrum indicates a significant blue shift of two maxima from 652 and 716 nm to 605 and 654 nm, respectively (Figure 3.22).

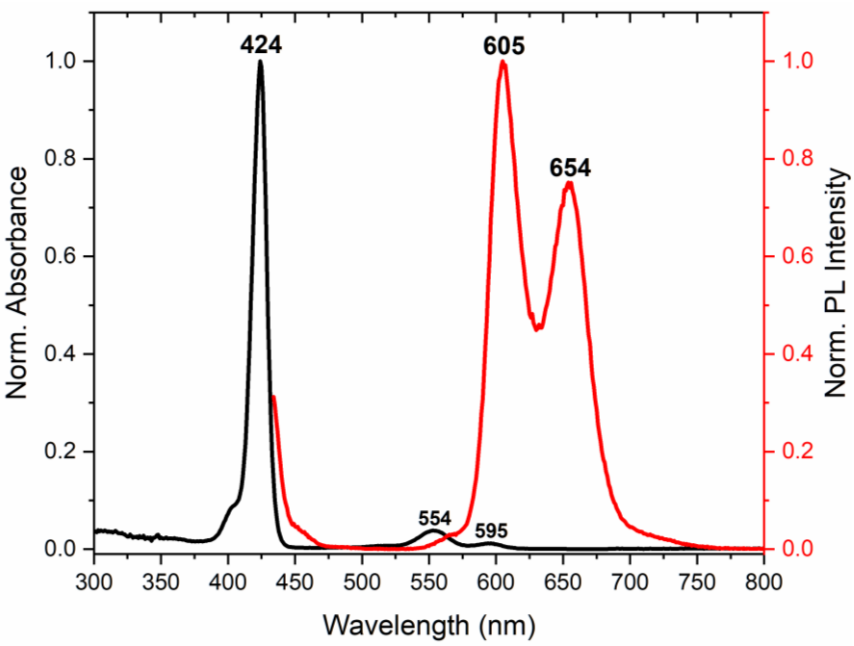


Figure 3.22 UV-Vis absorbance and fluorescence spectra of Zn-TPP-N_3 in chloroform.

Thermal stability of Zn-TPP-N_3 was checked with TGA and two types of decomposition were observed. The first decomposition starts at 233 °C that is due to the loss of azide groups from the structure. The second decomposition that starts around 517 °C is probably for the loss of benzene rings attached to the core (Figure 3.23).

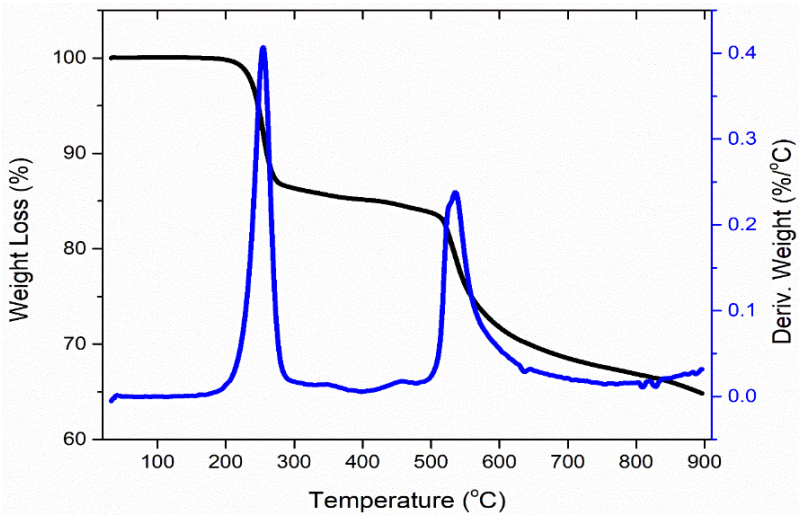


Figure 3.23 TGA graph of Zn-TPP-N_3.

3.2.8. Glycosylation of Zn-TPP-N_3

CuAAC reaction between Zn-TPP-N_3 and acetylated propargylated mannose yielded a mixture of mono-, di-, tri- and tetra-mannose clicked TPP analogues.

Di-mannose clicked TPP was present in trans-A_2B_2 and cis-A_2B_2 forms whose R_f values were almost identical on TLC (Figure A7). The isolation of the analogues was achieved by a silica gel column chromatography using 1-2% MeOH/DCM mixture as eluent. Especially di-, tri- and tetra-substituted compounds were very close to each other ($R_f = 0.57$, 0.46 and 0.35, respectively) and therefore the column was run extremely carefully. TPP-Az-3AcMan (tri-clicked analogue) was isolated in 50% yield together with 4% of TPP-3Az-AcMan (mono-clicked analogue), 26% of TPP-2Az-2AcMan (di-clicked analogue, trans-A_2B_2 isomer is dominant), and 20% of TPP-4AcMan (tetra-clicked analogue).

Our initial goal was to employ TPP-2Az-2AcMan (**12**) for the construction of CB7-attached multifunctional assembly. Therefore, first, we proceeded with it and synthesized TPP-2Man-2CB7 (**14**). However, the resulting assembly was not soluble well in any solvent including DMSO and water, which would restrict its use in further applications. For this reason, we switched to TPP-Az-3AcMan (**9**) and utilized it in the synthesis of CB7-attached assembly, TPP-3Man-CB7 (**11**) that have considerably better solubility than TPP-2Man-2CB7.

In the next section, studies on the synthesis and characterization of TPP-2Man-2CB7 will be shared and after that, the works on the synthesis and characterization of TPP-3Man-CB7 will be given.

3.2.9. Synthesis of TPP-2Man-2CB7 (14)

Let's first begin with the characterization of TPP-2Az-2AcMan (**12**). Its ^{1}H NMR spectrum is given in Figure 3.24. The most characteristic peaks come from triazole hydrogens at 8.56 ppm (f), benzylic hydrogens at 6.00 ppm (e) that are next to triazole rings and acetyl hydrogens around 2.00 ppm (n). Other than these, a bunch of signals from 4.08 ppm to 5.18 ppm is assigned to mannose hydrogens (g, h, i, j, k, l and m. d is assigned to benzylic hydrogen of azidated moieties). The benzene hydrogens labelled as c are now split into two doublets, one of which is from azidated site (c) and the other is from mannose-bearing arms (c_1). The integral ratio of c_1/c (4/4) is 1 as expected.

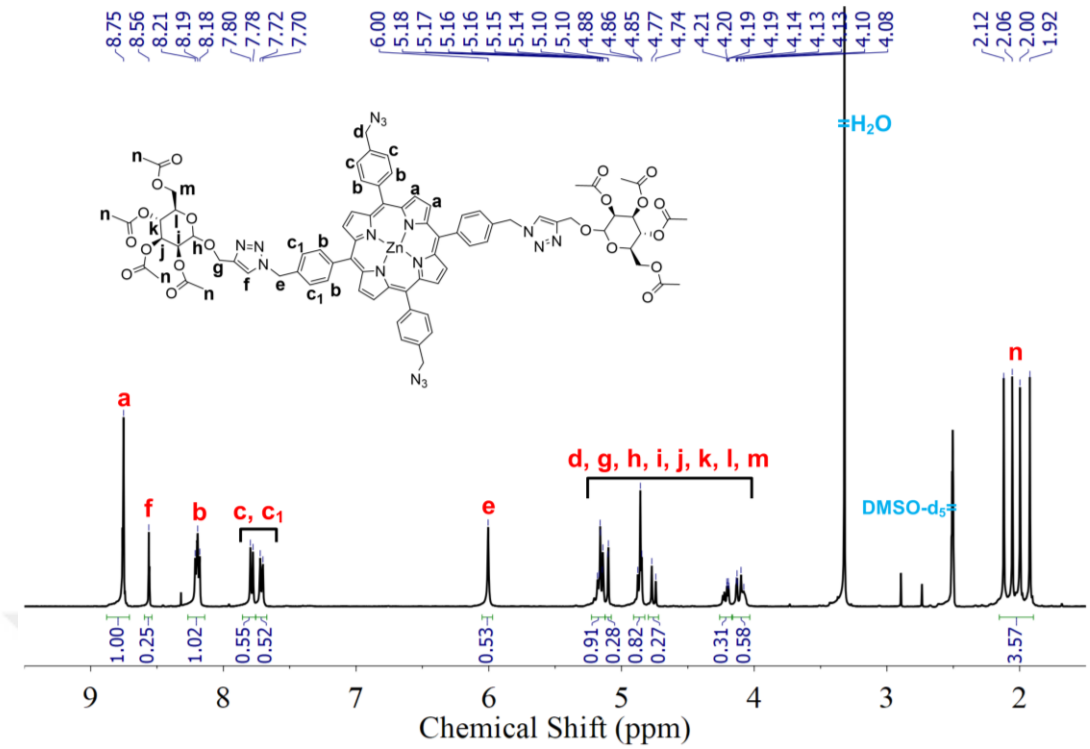


Figure 3.24 ^{1}H NMR spectrum of TPP-2Az-2AcMan in DMSO-d_6.

The peak around 170 ppm in ^{13}C NMR coming from carbonyl carbon confirms the presence of acetylated mannose groups attached to TPP (Figure 3.25).

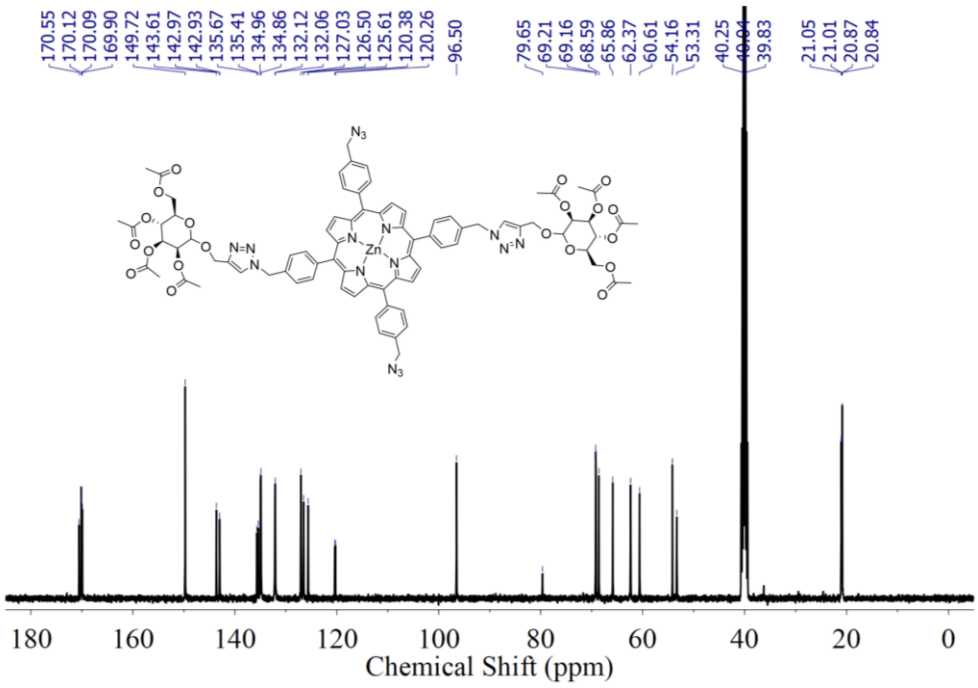


Figure 3.25 ^{13}C NMR spectrum of TPP-2Az-2AcMan in DMSO-d_6.

Figure 3.26 shows the positive mode ESI-MS spectrum of TPP-2Az-2AcMan, which contains single-charged sodium adduct with m/z value of 1691.47.

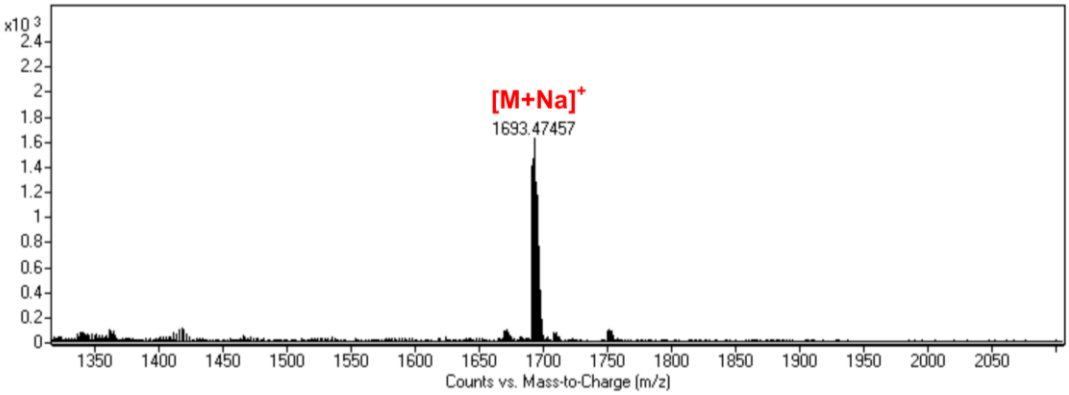


Figure 3.26 +ESI-MS spectrum of TPP-2Az-2AcMan.

Another important proof for the formation of TPP-2Az-2AcMan was obtained from FT-IR spectrum that shows the partial reduction of -N_3 stretching at 2100 cm^{-1} and the existence of C=O stretching at 1739 cm^{-1} that comes from acetyl groups on mannose units (Figure 3.27).

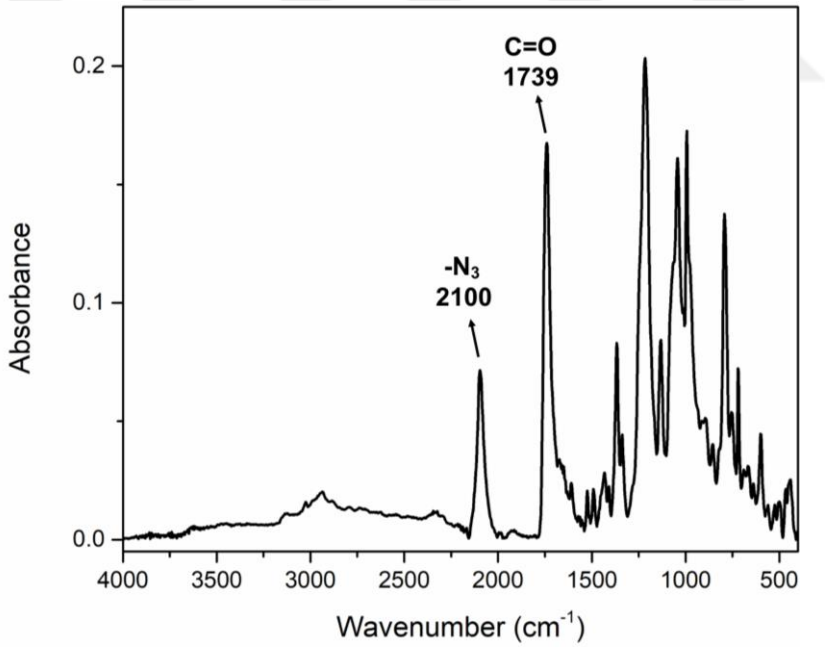


Figure 3.27 FT-IR spectrum of TPP-2Az-2AcMan.

Before the final synthetic step, acetyls on mannose groups of TPP-2Az-2AcMan (**12**) were hydrolyzed via Zemplén deacetylation using sodium methoxide solution in methanol, yielding TPP-2Az-2Man (**13**) that dissolves in DMSO and methanol, but not in water.

In ^{1}H NMR spectrum of TPP-2Az-2Man (Figure 3.28), the disappearance of acetyl hydrogen peaks around 2.00 ppm confirm the success of deacetylation reaction. The hydrogen peaks of sugar units are more upfield shifted than those in TPP-2Az-2AcMan since they become more shielded in the presence of neighboring hydroxyl groups. The integration values are in accordance with the numbers of protons in the chemical structure of TPP-2Az-2Man.

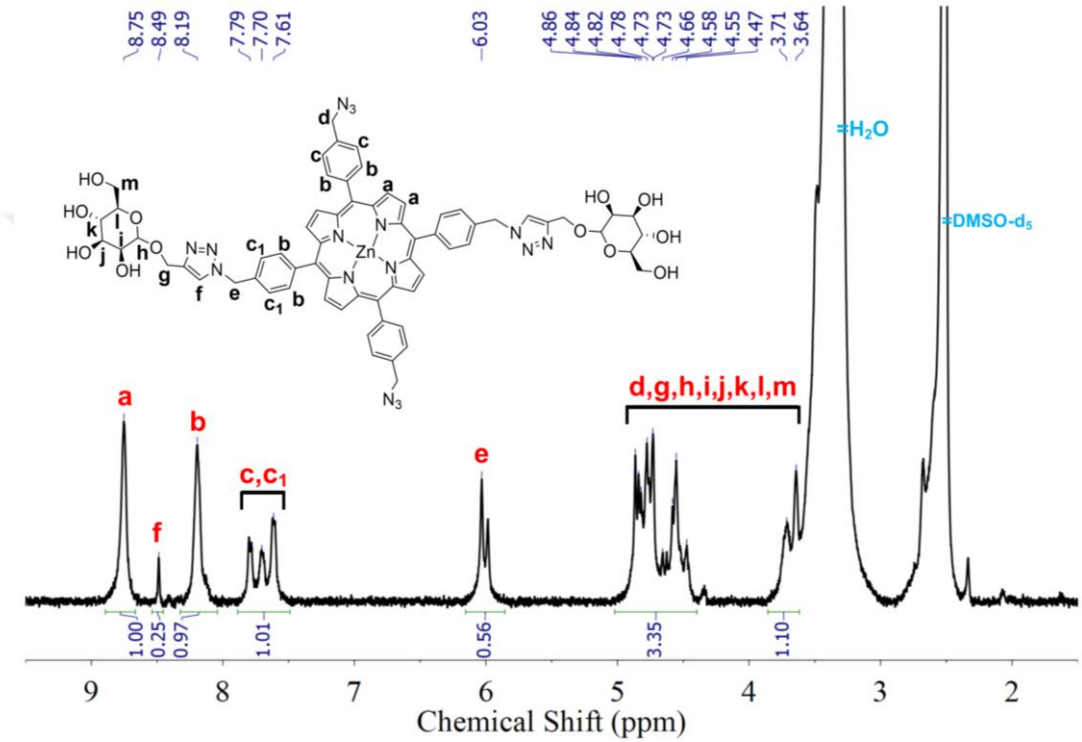


Figure 3.28 ^{1}H NMR spectrum of TPP-2Az-2Man in DMSO-d_6.

^{13}C NMR spectrum of TPP-2Az-2AcMan is given in Figure 3.29. The characteristic carbonyl carbon peak around 170 ppm is not seen in this spectrum, which is another important indication for the successful deacetylation of mannose groups.

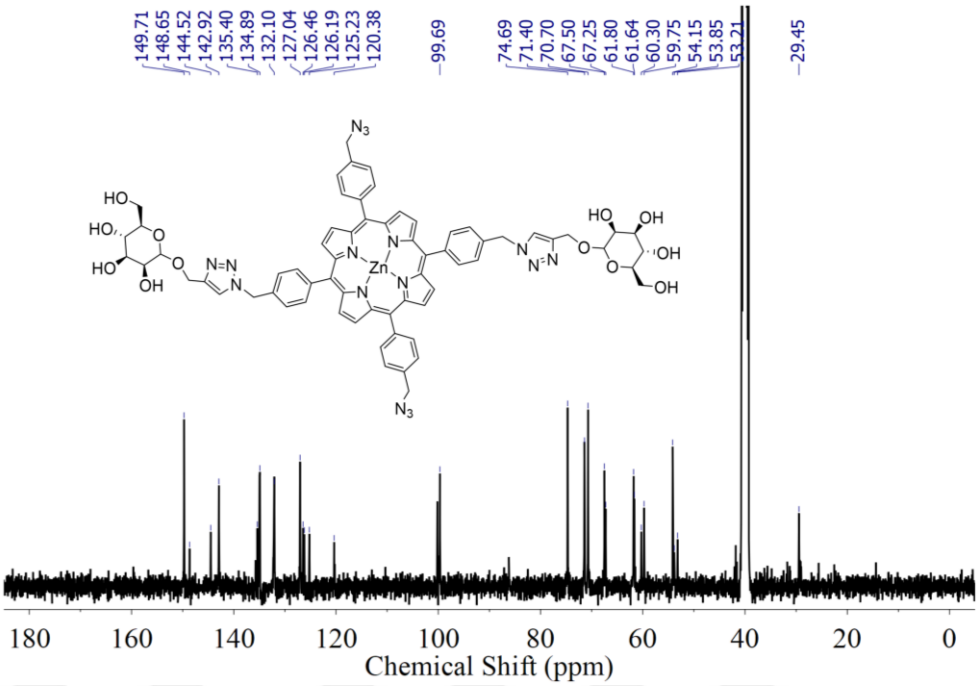


Figure 3.29 ^{13}C NMR spectrum of TPP-2Az-2Man in DMSO-d_6.

ESI-MS spectrum clearly shows the singly positively-charged Na and K adducts of TPP-2Az-2Man at m/z values of 1355.36 and 1371.34, respectively.

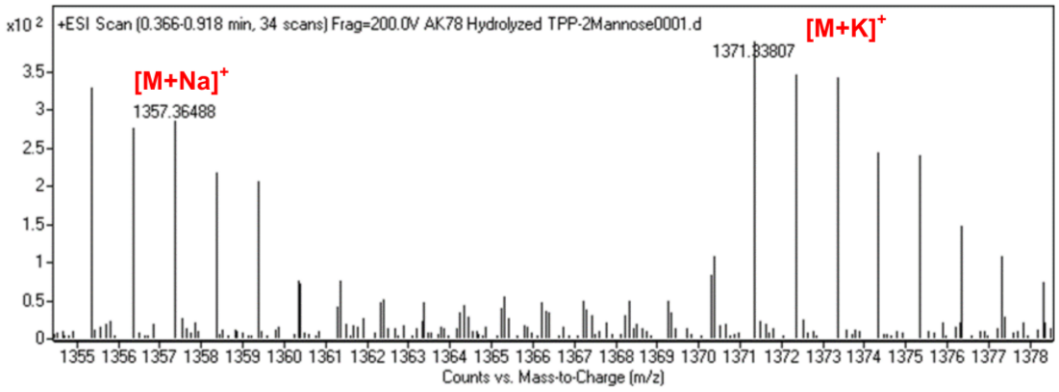


Figure 3.30 -ESI-MS spectrum of TPP-2Az-2Man.

Disappearance of the C=O stretching peak at 1739 cm^{-1} in FT-IR spectrum along with the emergence of a broad peak at 3350 cm^{-1} for hydroxyl groups confirm the successful synthesis of TPP-2Az-2Man (Figure 3.31).

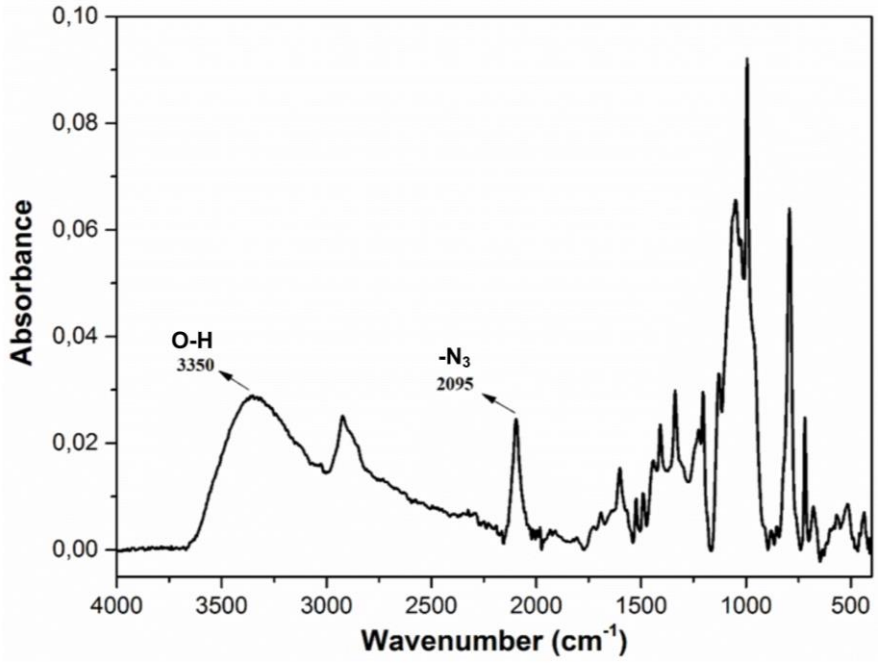


Figure 3.31 FT-IR spectrum of TPP-2Az-2Man.

After confirming the structure of TPP-2Az-2Man, TPP-CB7 conjugate, TPP-2Man-2CB7 (**14**), was synthesized through a second CuAAC reaction between TPP-2Az-2Man (**13**) and excess CB7-(O-propargyl)$_1$ (**3**) in DMSO. The product was purified by washing with excess of hot water and methanol. After drying in oven, it was observed that the solubility of TPP-2Man-2CB7 is very low in any solvent. It only has a limited solubility in DMSO. This limited solubility in DMSO allowed us to take a ^{1}H NMR spectrum that is given in Figure 3.32.

In ^{1}H NMR spectrum of TPP-2Man-2CB7, the signals are not resolved very well due to low solubility of the assembly in the NMR solvent. Porphyrin and mannosyl protons have sharper peaks than that of CB7 protons. The integral ratio of singlet 'a' to singlet 'f' that come from triazole hydrogens is 2, indicating a total number of 4 triazole units. This is a significant indication of a successful click reaction. The last important observation in ^{1}H NMR spectrum of TPP-2Man-2CB7 is the change in integration value of the peak 'e' assigned to benzylic hydrogens at the clicked sites. After the attachment of CB7, the integration value of 'e' is matching with a total number of 8 protons as expected (Figure 3.32).

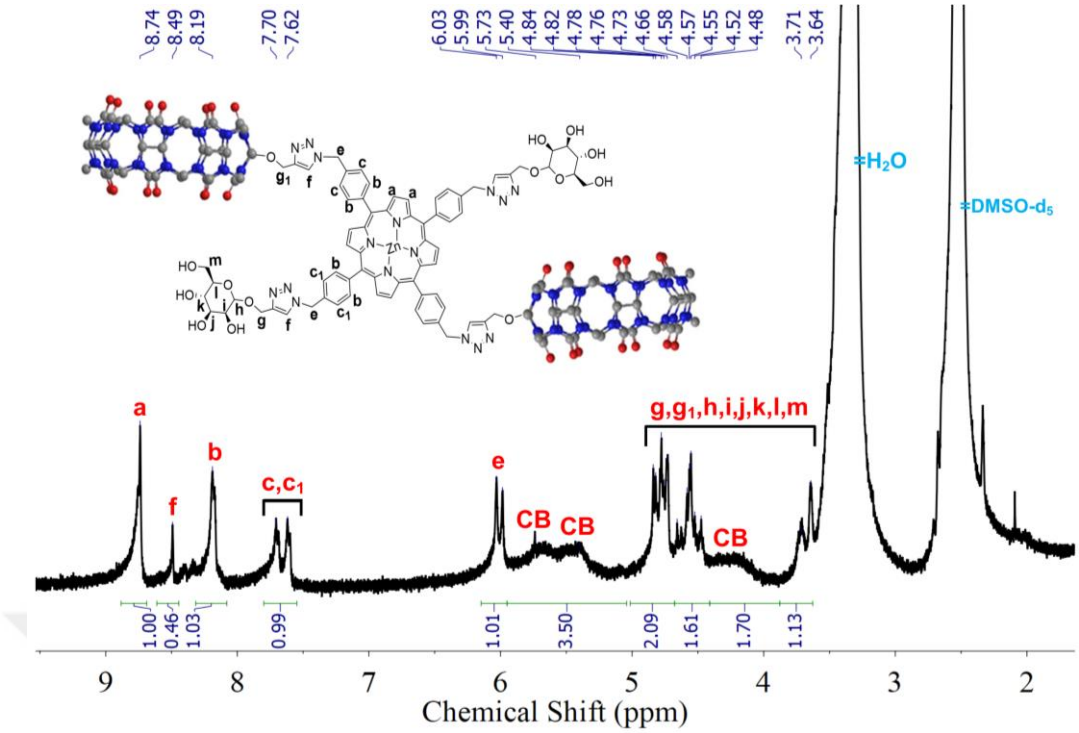


Figure 3.32 ^{1}H NMR spectrum of TPP-2Man-2CB7 in DMSO-d_6.

FT-IR spectrum of TPP-2Man-2CB7 is given in Figure 3.33. Strong –N_3 stretching peak at 2100 cm^{-1} disappears, confirming that the available azide groups in TPP-2Az-2Man reacted with CB7-(O-propargyl)$_1$ through CuAAC and consumed. C=O signal appearing at 1728 cm^{-1} is due to the carbonyl groups in CB7 units. Broad –OH stretching centered at 3360 cm^{-1} are due to hydroxyl groups on mannosyl units.

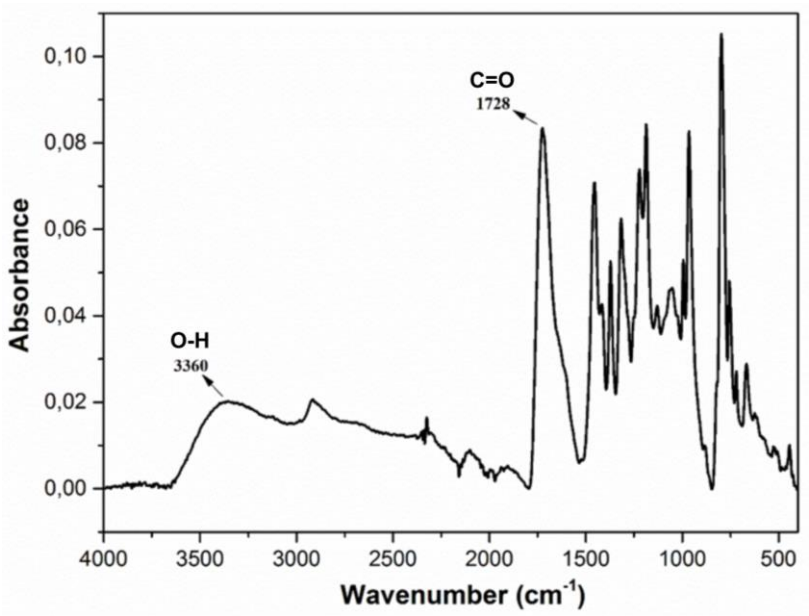


Figure 3.33 FT-IR spectrum of TPP-2Man-2CB7.

3.2.10. Characterization of TPP-Az-3AcMan (9)

Synthesis and isolation of TPP-Az-3AcMan (**9**) was described in section 3.2.8. Full characterization of TPP-Az-3AcMan will be discussed in this section and further studies for the synthesis and characterization of TPP-3Man-CB7 (**11**) will be shared in the upcoming sections.

^{1}H NMR spectrum of TPP-Az-3AcMan is given in Figure 3.34. The most characteristic peaks come from triazole hydrogens at 8.55 ppm (f), benzylic hydrogens at 6.00 ppm (e) that are next to triazole rings and acetyl hydrogens around 2.00 ppm (n). Other than these, a set of signals from 4.07 ppm to 5.17 ppm are assigned to mannose hydrogens (g, h, i, j, k, l and m. d is assigned to benzylic hydrogen of azidated moiety). The benzene hydrogens labelled as c are now split into two doublets, one of which is from azidated site (c) and the other is from mannose-bearing arms (c_1). The integral ration of c_1/c (6/2) is around 3 as expected.

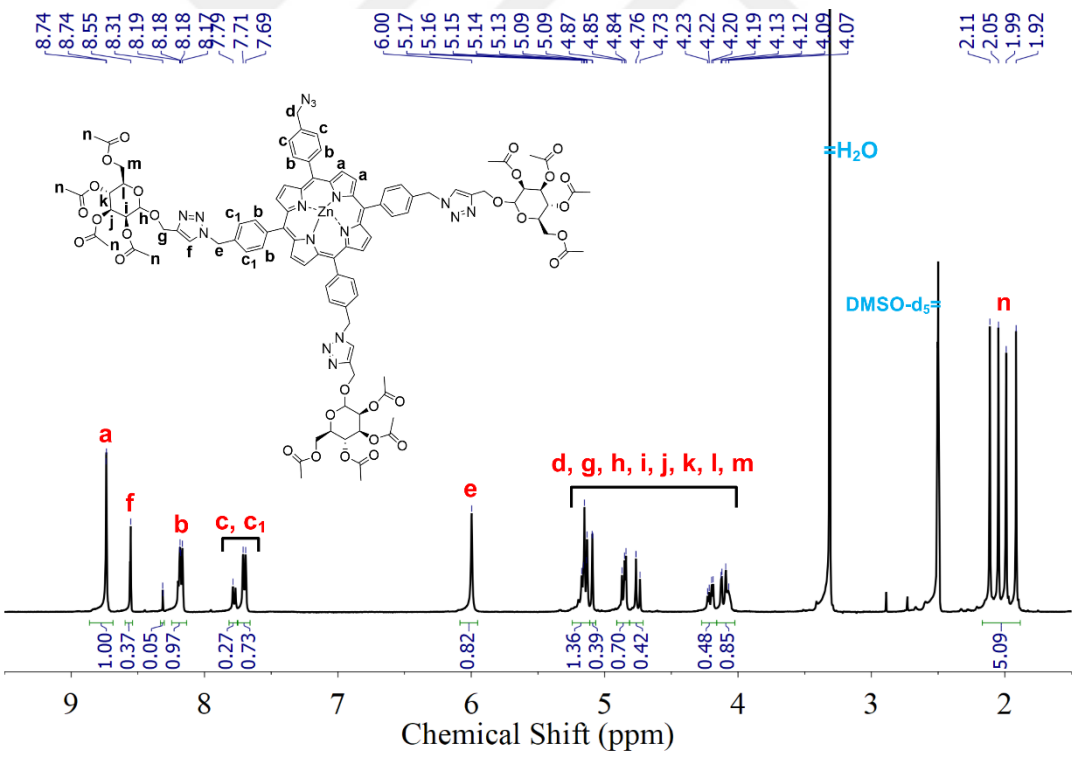


Figure 3.34 ^{1}H NMR spectrum of TPP-Az-3AcMan in DMSO-d_6.

The peak around 170 ppm in ^{13}C NMR coming from carbonyl carbon confirms the presence of acetylated mannose groups attached to TPP (Figure 3.35).

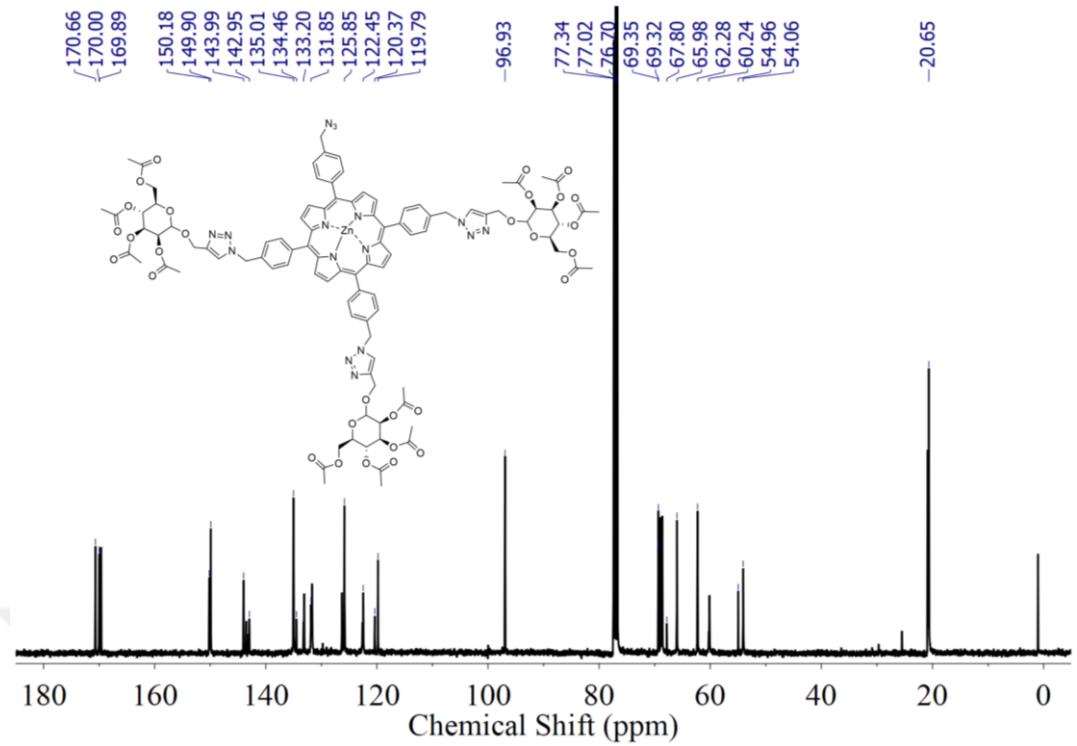


Figure 3.35 ^{13}C NMR spectrum of TPP-Az-3AcMan in $CDCl_3$.

Figure 3.36 represents the positive mode ESI-MS spectrum of TPP-Az-3AcMan, which contains single- and double-charged sodium adducts of the compound.

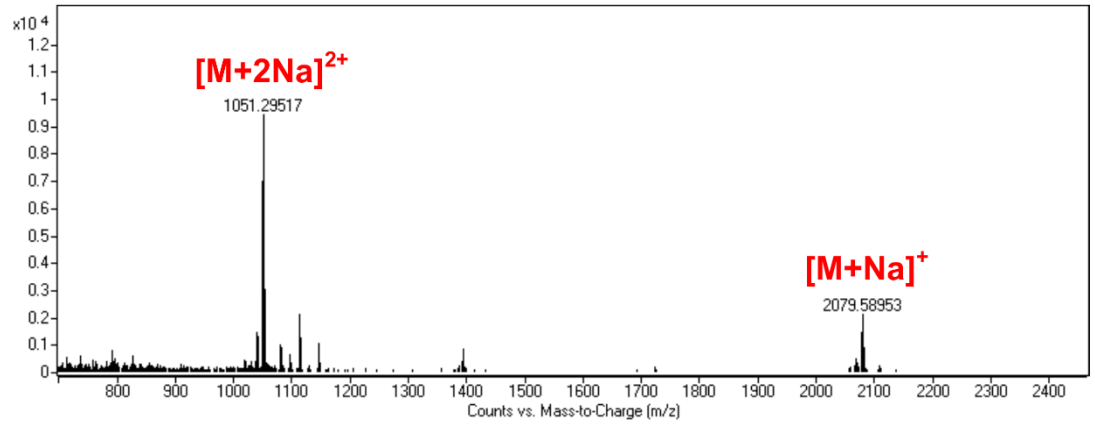


Figure 3.36 +ESI-MS spectrum of TPP-Az-3AcMan.

Another important proof for the formation of TPP-Az-3AcMan was obtained from FT-IR spectrum that shows the partial reduction of $-N_3$ stretching at 2099 cm^{-1} and the existence of C=O stretching at 1740 cm^{-1} that comes from acetyl groups on mannose units (Figure 3.37).

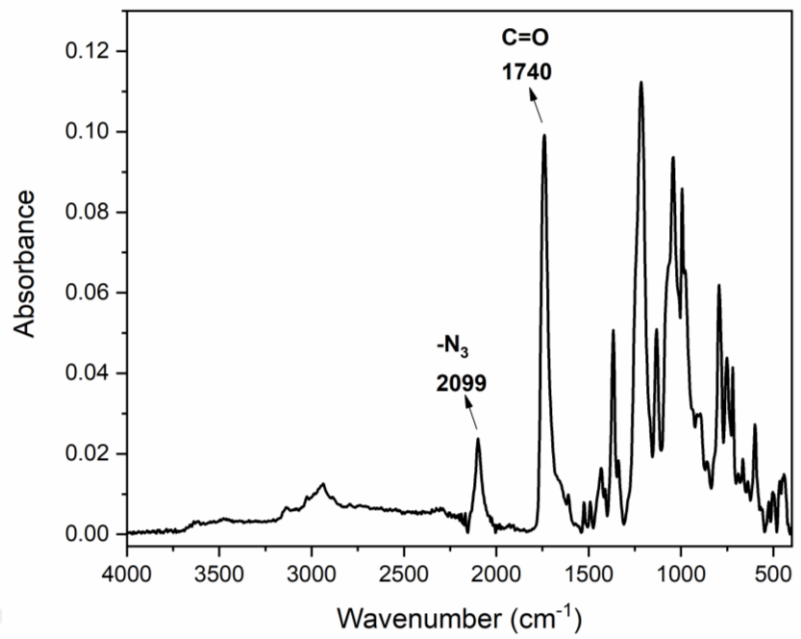


Figure 3.37 FT-IR spectrum of TPP-Az-3AcMan.

3.2.11. Synthesis of TPP-Az-3Man (10)

Prior to set up the final synthetic step, acetyls on mannose groups of TPP-Az-3AcMan (**9**) were hydrolyzed via Zemplén deacetylation using sodium methoxide solution in methanol, yielding TPP-Az-3Man (**10**) that dissolves well in DMSO and partially in methanol but poorly in water.

In ^{1}H NMR spectrum of TPP-Az-3Man (Figure 3.38), the disappearance of acetyl hydrogen peaks around 2.00 ppm confirm the success of deacetylation reaction. Apart from this, the aromatic region is almost the same as in ^{1}H NMR spectrum of TPP-Az-3AcMan as expected and the hydrogen peaks of sugar units are slightly upfield shifted since they become more shielded in the presence of hydroxyl groups.

^{13}C NMR spectrum of TPP-Az-3AcMan is given in Figure 3.39. The characteristic carbonyl carbon peak around 170 ppm is not seen in this spectrum, which is another important indication for the successful deacetylation of mannose groups.

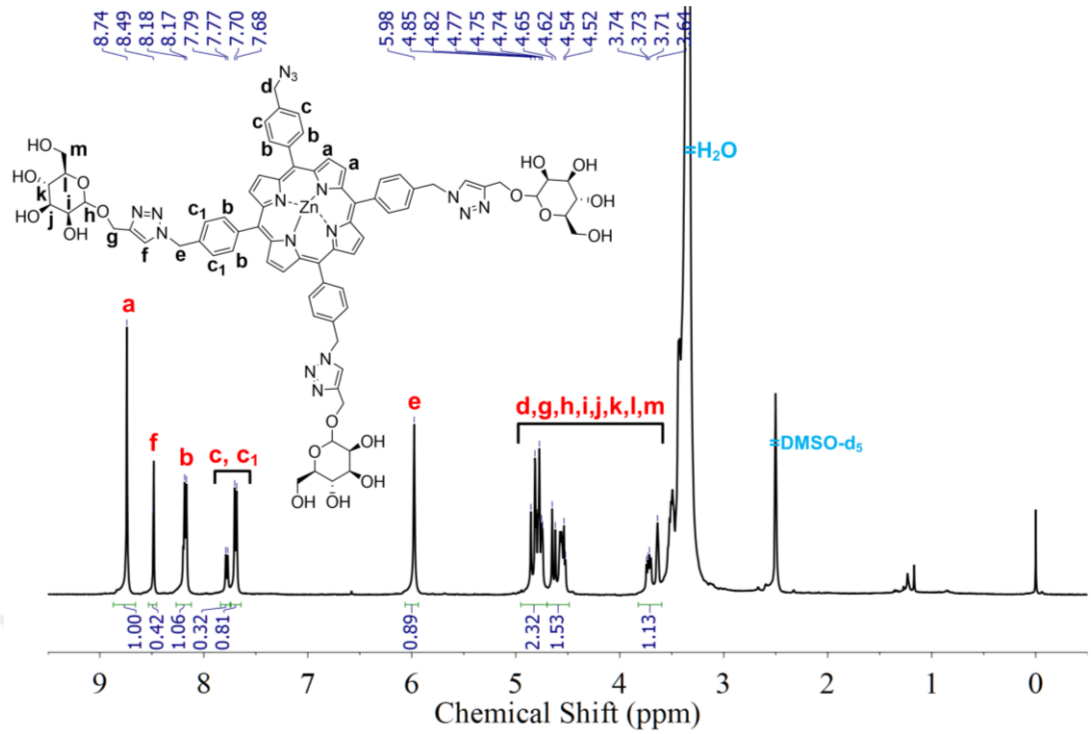


Figure 3.38 ^{1}H NMR spectrum of TPP-Az-3Man in DMSO-d_6.

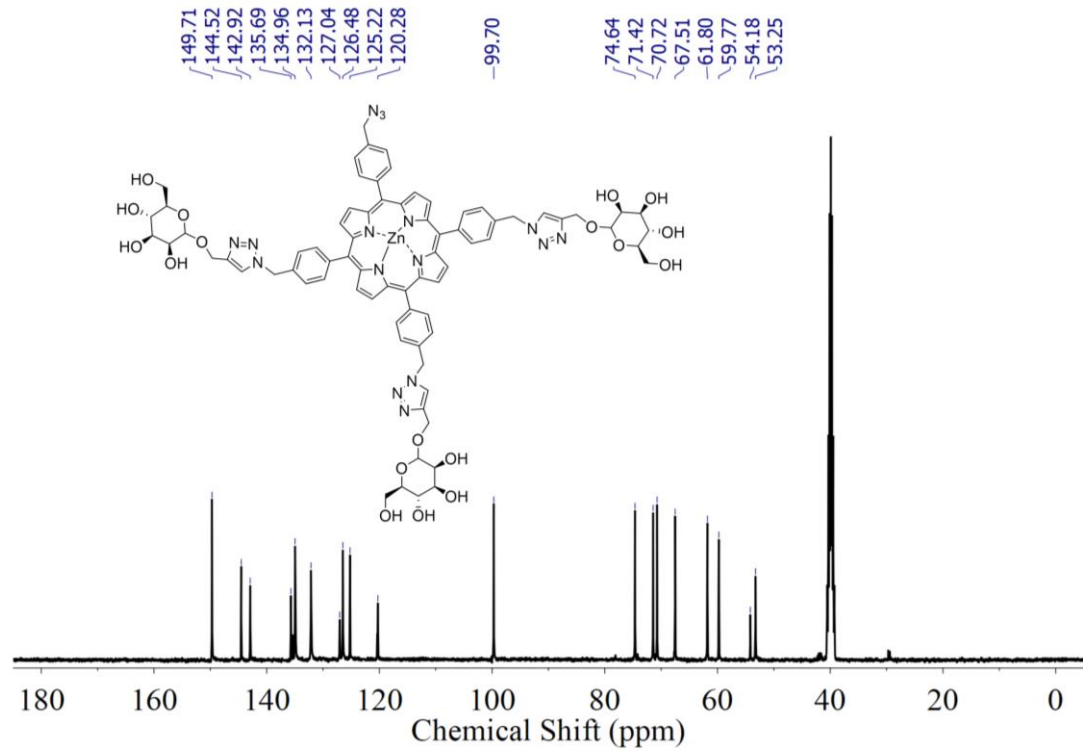


Figure 3.39 ^{13}C NMR spectrum of TPP-Az-3Man in DMSO-d_6.

ESI-MS spectrum clearly shows the negatively charged ion of TPP-Az-3Man after removal of one proton and there is no trace from the acetylated form (Figure 3.40).

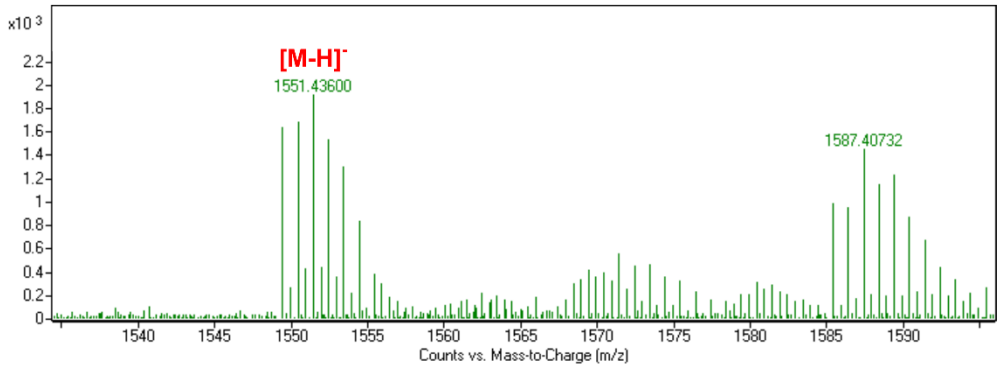


Figure 3.40 -ESI-MS spectrum of TPP-Az-3Man.

Disappearance of the C=O stretching peak at 1748 cm^{-1} in FT-IR spectrum along with the emergence of a broad peak at 3330 cm^{-1} for hydroxyl groups confirm the success of TPP-Az-3Man formation (Figure 3.41).

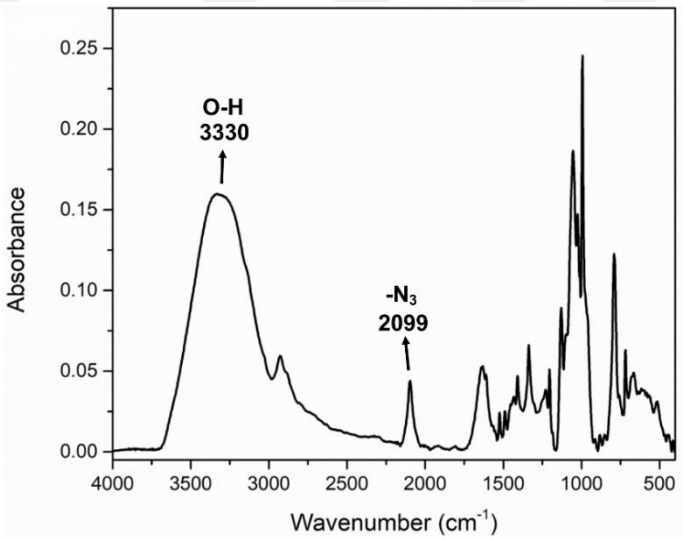


Figure 3.41 FT-IR spectrum of TPP-Az-3Man.

3.2.12. Synthesis of TPP-3Man-CB7 (11)

In the final step, TPP-CB7 conjugate, TPP-3Man-CB7 (**11**), was synthesized through a second CuAAC reaction between TPP-Az-3Man (**10**) and excess CB7-(O-propargyl)$_1$ (**3**) in DMSO:H_2O (4:1) mixture. The pure product was obtained after purification through a sephadex G-25 column (H_2O:MeOH, 1:1, v/v) in 91% yield. The solubility properties of TPP-3Man-CB7 were investigated and summarized as follows: in DMSO, 10 mg/mL; in H_2O, 0.2 mg/mL and in H_2O:DMSO (4:1, v/v), 2 mg/mL. It also dissolves in acidic water (e.g. 0.1 M aq. HCl solution). It has poor solubility in neat water,

propably due to extensive H-bonding between mannosyl -OH groups, but the presence of even small amount of DMSO weakens the interactions and solubilizes the assembly in water.

In ^{1}H NMR spectrum of TPP-3Man-CB7 given in Figure 3.42, porphyrin and mannosyl protons have sharp peaks but the peaks of CB7 protons are quite broad. The peak at 8.49 ppm is assigned to the hydrogens of triazole and its integration value is in accordance with a total number of 4 hydrogens as expected. Another important change in ^{1}H NMR spectrum of TPP-3Man-CB7 is the disappearance of the doublet 'c' previously observed in the spectrum of TPP-Az-3Man due to the non-clicked phenyl site. After clicking CB7 to this available site, the hydrogens labelled as 'c' now have the same chemical shift as 'c_1' and this is supported with an increase in integration value of the peak 'c_1', which now corresponds to 8 hydrogens in total. The last significant observation in ^{1}H NMR spectrum of TPP-3Man-CB7 is the change in integration value of the peak 'e' assigned to benzylic hydrogens at the clicked sites. After the attachment of CB7, the integration value of 'e' is matching with a total number of 8 protons as expected.

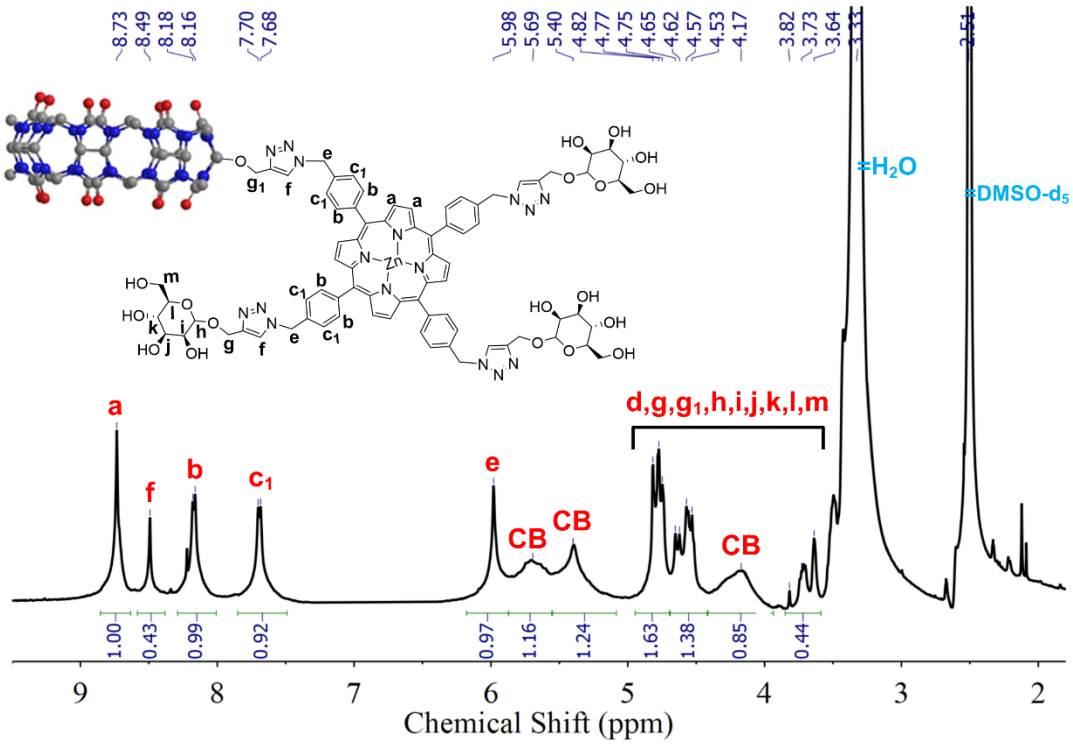


Figure 3.42 ^{1}H NMR spectrum of TPP-3Man-CB7 in DMSO-d_6.

In ^{13}C NMR spectrum of TPP-3Man-CB7, the peak at 155.6 ppm for the carbonyl carbons of CB7 further confirms the success of the click reaction (Figure 3.43).

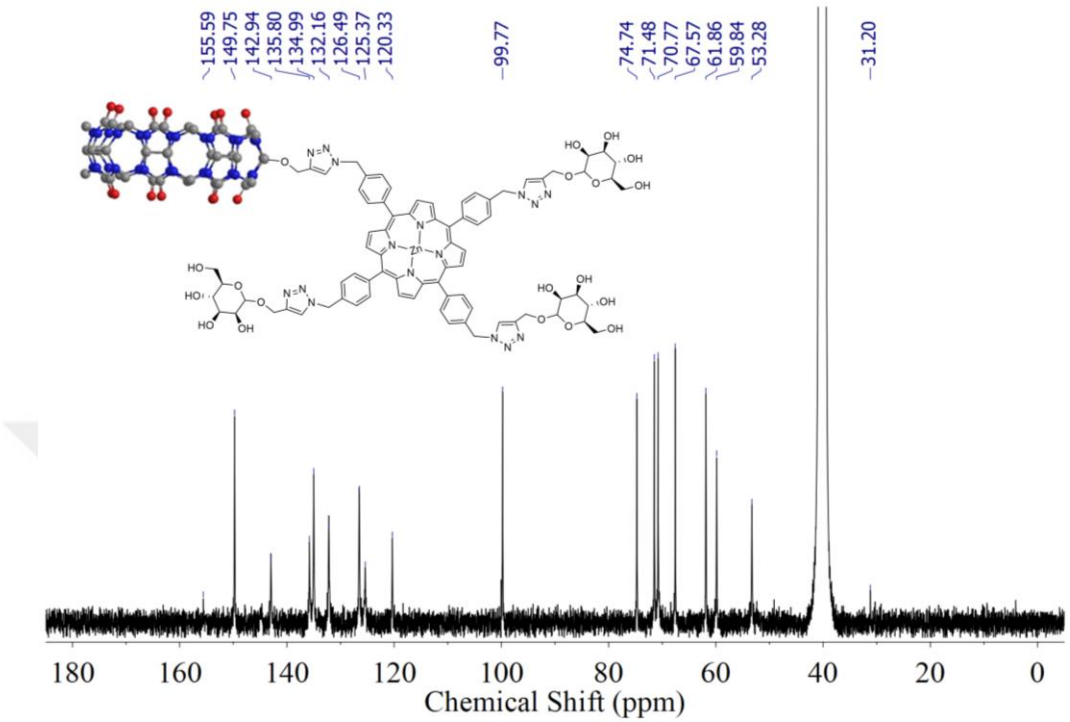


Figure 3.43 ^{13}C NMR spectrum of TPP-3Man-CB7 in DMSO-d_6.

In +ESI-MS spectrum, the related signal is readily assigned to the corresponding doubly-charged proton adduct as shown in Figure 3.44.

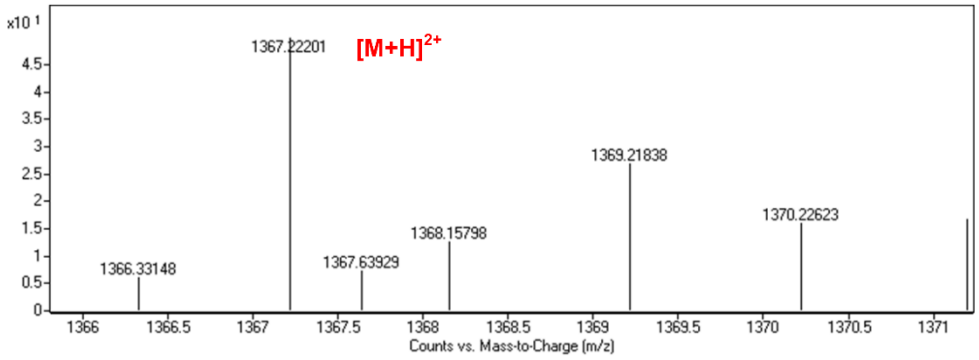


Figure 3.44 +ESI-MS spectrum of TPP-3Man-CB7.

FT-IR spectrum of TPP-3Man-CB7 represents two significant changes (Figure 3.45). The first change is the presence of C=O stretching peak at 1731 cm^{-1} due to CB7 carbonyls. The second change is the disappearance of $-N_3$ stretching peak around 2100 cm^{-1}, which confirms that all remaining azide groups reacted successfully with CB7-(O-propargyl)$_1$ via CuAAC. Broad O-H

stretching peak appears around 3300 cm^{-1} due to hydroxyl groups on mannosyl moieties.

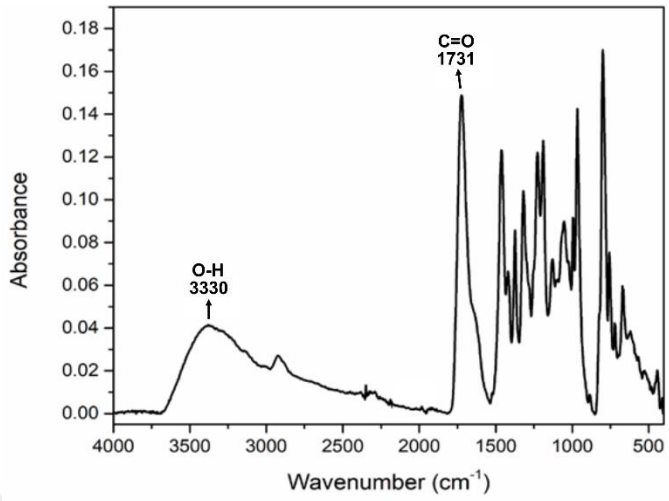


Figure 3.45 FT-IR spectrum of TPP-3Man-CB7.

3.2.13. Comparison of ^{1}H NMR and FT-IR spectra of TPP-Az-3AcMan, TPP-Az-3Man and TPP-3Man-CB7

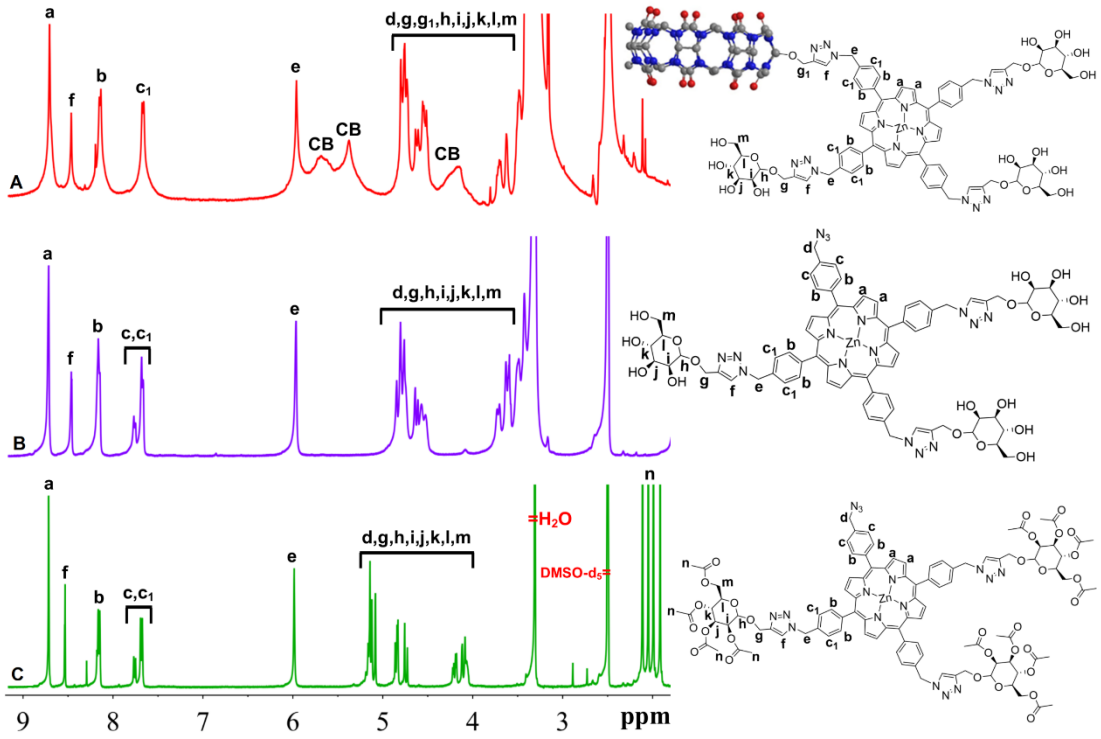


Figure 3.46 Overlay of ^{1}H NMR spectra of **(A)** TPP-3Man-CB7, **(B)** TPP-Az-3Man and **(C)** TPP-Az-3AcMan (Spectra were recorded in DMSO-d_6).

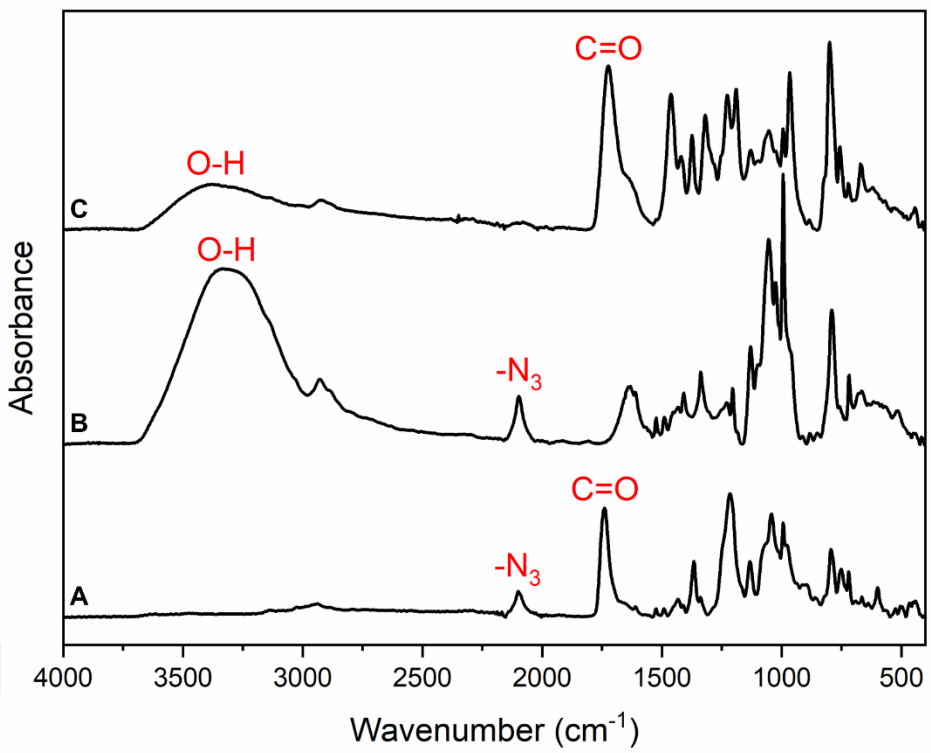


Figure 3.47 Overlay of FT-IR spectra of **(A)** TPP-Az-3AcMan, **(B)** TPP-Az-3Man and **(C)** TPP-3Man-CB7.

3.2.14. Investigation of CB7's Behaviour as a Host in the Assembly

In order to find out if CB7 will be available as a host in the assembly, ^{1}H NMR experiment was performed using 1,1'-(1,4-phenylenebis(methylene))-bis(3-methyl-1*H*-imidazol-3-ium) iodide, (bisimidazolium), which is known to have strong binding affinity towards CB7.[149] As can be seen from ^{1}H NMR spectrum of bisimidazolium guest recorded in D_2O (Figure 3.48A), chemical shifts for the phenyl (f) and imidazole (b and c) protons overlap and resonate at 7.5 ppm. However, upon addition of 1 equivalent CB7-$(OH)_1$, the phenyl protons (f) exhibit an upfield shift of around 1.1 ppm and imidazole protons (b and c) appear as two distinct peaks (Figure 3.48B). These changes indicate the encapsulation of phenyl moiety of the imidazole guest by CB7-OH_1 as the suggested inclusion complex structure shown on Figure 3.48B. We have also observed similar changes in the ^{1}H NMR spectrum of the TPP-3Man-CB7 (Figure 3.48C) when bisimidazolium solution in D_2O (1 equiv.) was added to the NMR tube containing the DMSO-d_6 solution of TPP-3Man-CB7. Furthermore, the broadened CB7 peaks acquired their well-defined shapes after complexing with bisimidazolium guest. These observations confirm that CB7 is

available as a host for complexation and there is no conformational restriction for CB7 in the assembly to exhibit its nature as being a receptor.

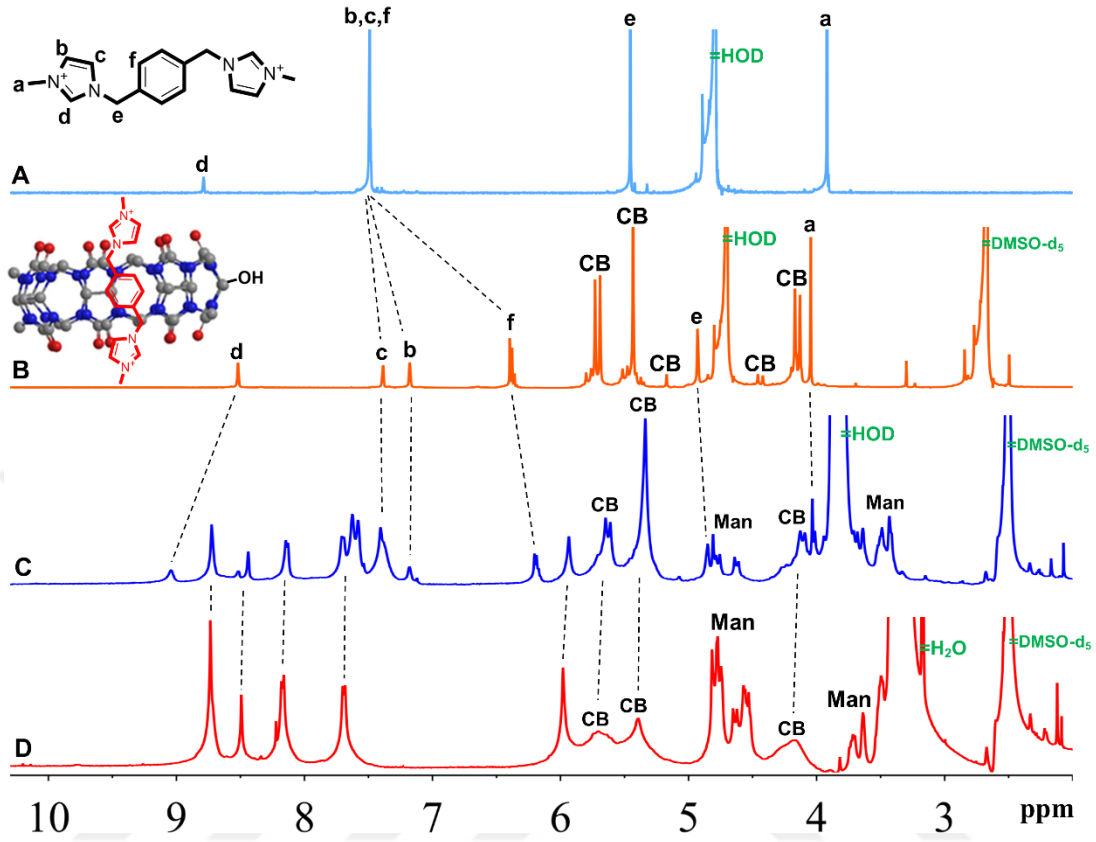


Figure 3.48 ^{1}H NMR spectra of **(A)** 1,1'-(1,4-phenylenebis(methylene))bis(3-methyl-1H-imidazol-3-ium) iodide, (bisimidazolium) (in D_2O); **(B)** CB7-$(OH)_1$+1 equiv. bisimidazolium, (in DMSO-d_6:D_2O mixture, 1:2, v/v); **(C)** TPP-3Man-CB7+1 equiv. bisimidazolium (1.2 mM, in DMSO-d_6:D_2O mixture, 2:1, v/v); **(D)** TPP-3Man-CB7 (1.2 mM, DMSO-d_6).

3.2.15. Photophysical Properties of TPP-Az-3AzMan, TPP-Az-3Man and TPP-3Man-CB7

Photophysical properties of TPP-3Man-CB7, TPP-Az-3AcMan and TPP-Az-3Man in DMSO were investigated. Figure 3.49 shows an overlay of the UV-Vis absorbance and fluorescence spectra of TPP-Az-3AcMan, TPP-Az-3Man and TPP-3Man-CB7. UV-Vis absorbance spectra show no significant difference in a typical sharp Soret band (λ_{max} = 428 nm) and Q-bands (λ_{abs} = 561 and 600 nm). Similarly, emission spectra also do not show any significant difference (λ_{em} = 608 and 661 nm). The molar absorptivity (ε) of the Soret band of TPP-3Man-CB7 was calculated using Beer-Lambert equation and found be 6.7x10^5

$M^{-1}cm^{-1}$. The fluorescence quantum yields (Φ_f) of TPP-Az-3Man and TPP-3Man-CB7 in DMSO were found to be 0.041 and 0.035, respectively. The fluorescence lifetime (τ) is 1.8 ns for both TPP-3Man-CB7 and TPP-Az-3Man (Figure 3.50).

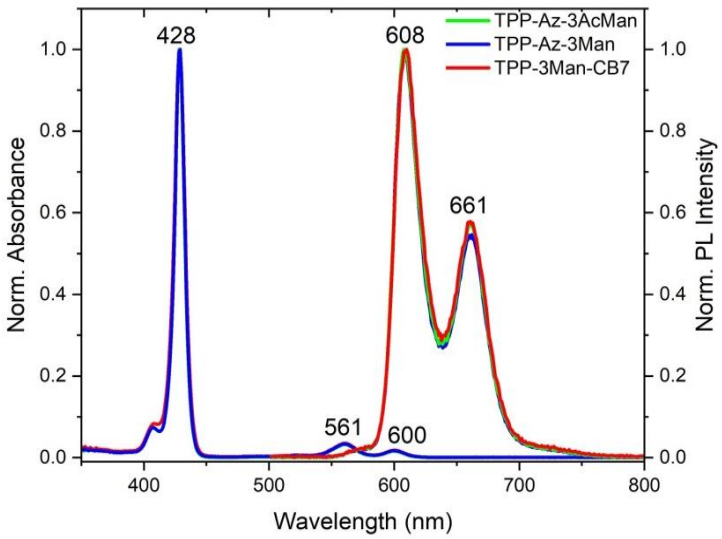


Figure 3.49 Normalized UV-Vis absorbance and fluorescence spectra of TPP-Az-3AcMan (green), TPP-Az-3Man (blue),and TPP-3Man-CB7 (red) in DMSO.

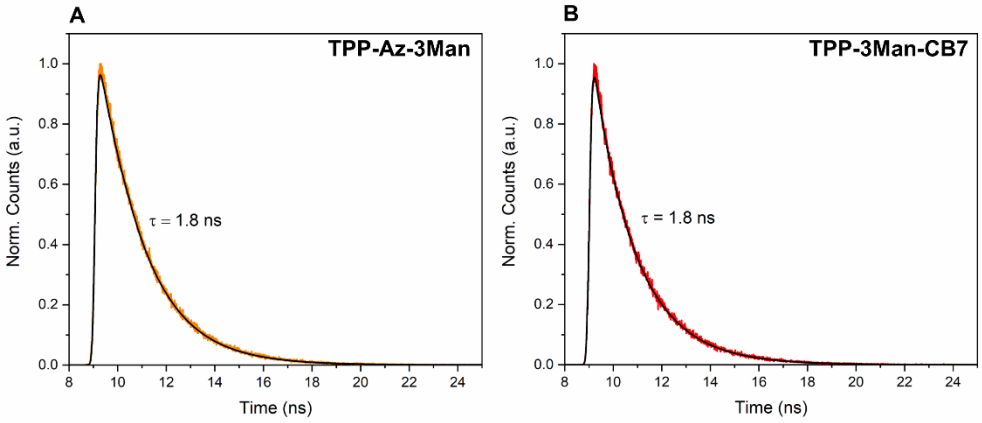
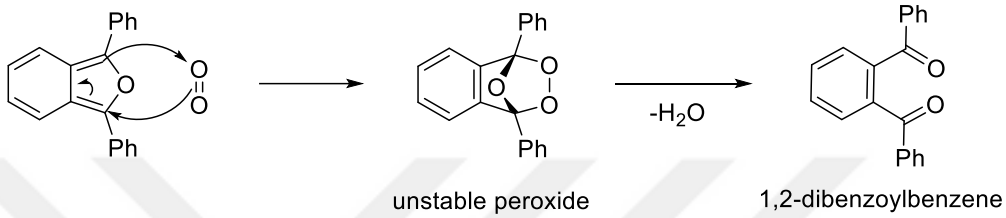


Figure 3.50 Time-resolved fluorescence spectra of **(A)** TPP-Az-3Man and **(B)** TPP-3Man-CB7 in DMSO.

3.2.16. Singlet Oxygen ($^1O_2$) Generation Capacities of TPP-Az-3AcMan, TPP-Az-3Man and TPP-3Man-CB7

Low fluorescence quantum yields of these compounds would suggest us that the excited molecules may follow nonradiative relaxation pathways, which could possibly increase their $^1O_2$ generation capacity. In order to prove this, a widely known indirect method for the determination of produced $^1O_2$ was

employed. 1,3-diphenylisobenzofuran (DPBF) was used as $^1O_2$ trapping agent and time-dependent decrease in the absorbance of DPBF in the presence of photosensitizer upon irradiation was correlated with the amount of $^1O_2$ generated. For this experiment, the samples in DMSO were irradiated with 460 nm LED with 10 sec intervals. The reduction in the absorbance intensity of DPBF was monitored with the increasing irradiation time (Figure 3.51). Detailed discussion of $^1O_2$ formation was made in Section 1.2.2.2. The reaction between $^1O_2$ and DPBF is given in Scheme 3.4.



Scheme 3.4 Reaction between $^1O_2$ and DPBF and subsequent formation of colorless 1,2-dibenzoylbenzene.

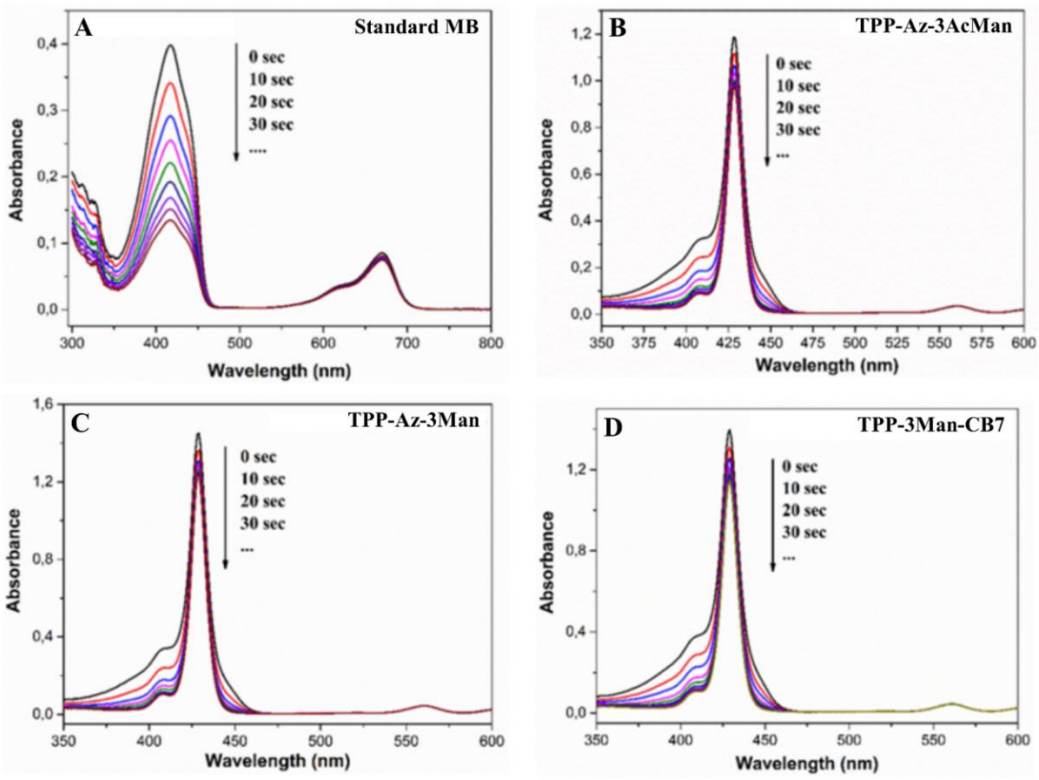


Figure 3.51 Decrease in the absorbance intensity of DPBF with 10 sec irradiation intervals in the presence of **(A)** methylene blue, **(B)** TPP-Az-3AcMan, **(C)** TPP-Az-3Man and **(D)** TPP-3Man-CB7.

From the absorbance graphs, -ln[DPBF]/[DPBF]$_0$ vs. time plots were extracted as shown in Figure 3.52 to indirectly calculate $^1O_2$ quantum yields of the samples using the equation below:

$$\Phi_{sam} = \Phi_{MB}(m_{sam}/m_{MB})(F_{MB}/F_{sam})$$

where the subscripts 'MB' and 'sam' stand for methylene blue ($\Phi_{MB} = 0.52$ in DMSO) and TPP-Az-3AcMan, TPP-Az-3Man and TPP-3Man-CB7, respectively. m is the slope of –ln[DPBF]/[DPBF]$_0$ vs. time plot and F is the absorption correction factor that is given by F=1-10^{-OD} (OD: optical density at the irradiation wavelength). The $^1O_2$ quantum yields of the corresponding samples can be order as:

TPP-Az-3Man ⫤ TPP-3Man-CB7 < TPP-Az-3AcMan;

$[\Phi_\Delta = 0.77 ⫤ 0.77 < 0.80]$

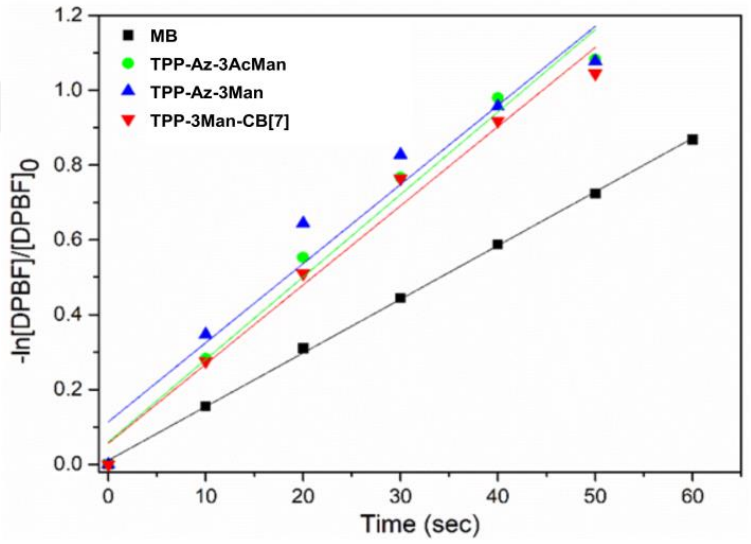


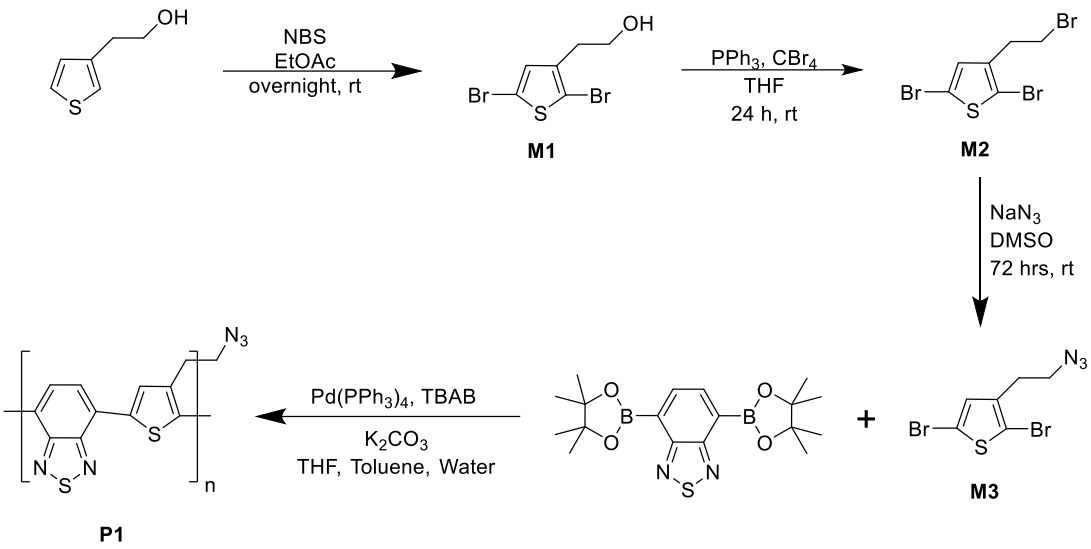
Figure 3.52 Linearized plots based on the decrease in the absorbance intensity of DPBF in the presence of methylene blue, TPP-Az-3AcMan, TPP-Az-3Man and TPP-3Man-CB7 irradiated at 460 nm with 10 sec intervals.

The $^1O_2$ quantum yield of unfunctionalized TPP was reported as 0.60 in DMF.[150] The synthesized new materials were seen to have $^1O_2$ quantum yields around 80%, which are significantly higher than that of TPP. The reason of high $^1O_2$ quantum yields could be explained by reduced π–π interactions between the porphyrin cores resulted from the presence of bulky functional groups (mannosyl and CB7).

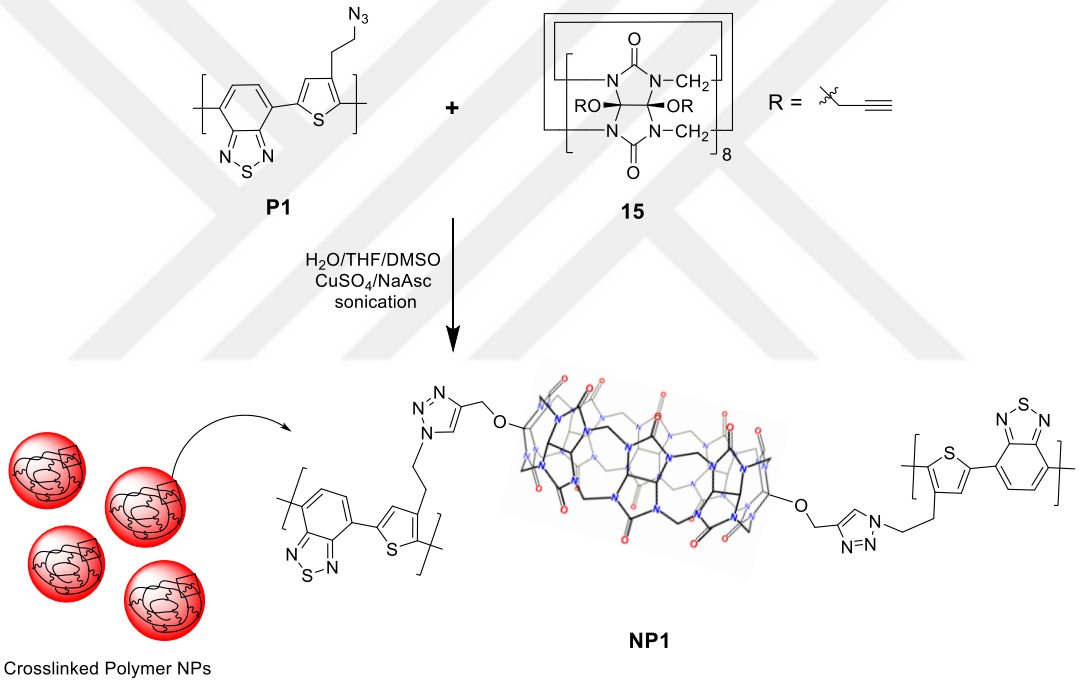
3.3. Synthesis of Supramolecular Nanomaterials through Covalent Attachment of Cucurbiturils to Conjugated Polymers

3.3.1. Aim of the Study

The goal of this study is to synthesize multifunctional platforms that incorporate a conjugated polymer or an oligomer and covalently attached functionalized cucurbituril. We aimed to obtain nanoparticles with multireceptors and utilize them in image-guided drug and biomolecule delivery. Multifunctionalized CB[n] derivatives can be attached to a polymer whose side chains are functionalized suitably through azide-alkyne click reaction in order to obtain crosslinked conjugated polymer nanoparticles that can be used as drug/biomolecule delivery and bioimaging agent. Conjugated polymer was synthesized according to the Scheme 3.5. First, 3-thiopheneethanol monomer was modified from 2^{th} and 5^{th} sites with bromine using NBS as bromination agent to obtain compound **M1**. Alcohol part was also converted to -Br (**M2**) via Appel reaction and then to $-N_3$ (**M3**) using NaN_3. Suzuki coupling of the suitably-modified thiophene monomer with 2,1,3-benzothiadiazole-4,7-bis(boronic acid pinacol ester) gave the azide-functionalized conjugated polymer (**P1**). The polymer was designed to emit at near infrared end of visible spectrum so that background autofluorescence in tissues can minimized and high tissue penetration can be achieved. As shown in Scheme 3.6, nanoparticles (**NP1**) are prepared by click reaction between **P1** and multipropargylated CB8 (**15**). Alternatively, monofunctionalized CB[n] can be attached to the polymer. When a dye is encapsulated by CB[n], polymer and dye can have donor-acceptor type interaction, which will give way to an effective Förster resonance energy transfer (FRET). If this is achieved, optical properties of the conjugated polymer could be modified that will make generation of white light possible.



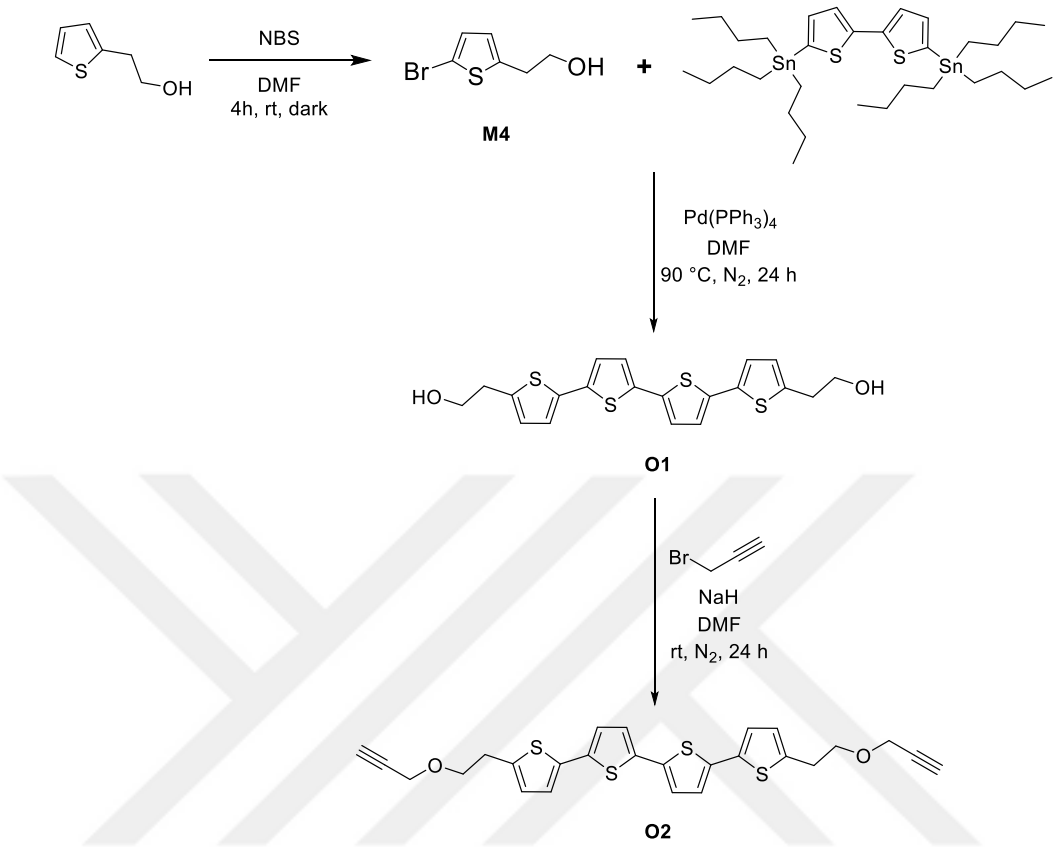
Scheme 3.5 Synthetic pathway for azide-functionalized conjugated polymer (**P1**).



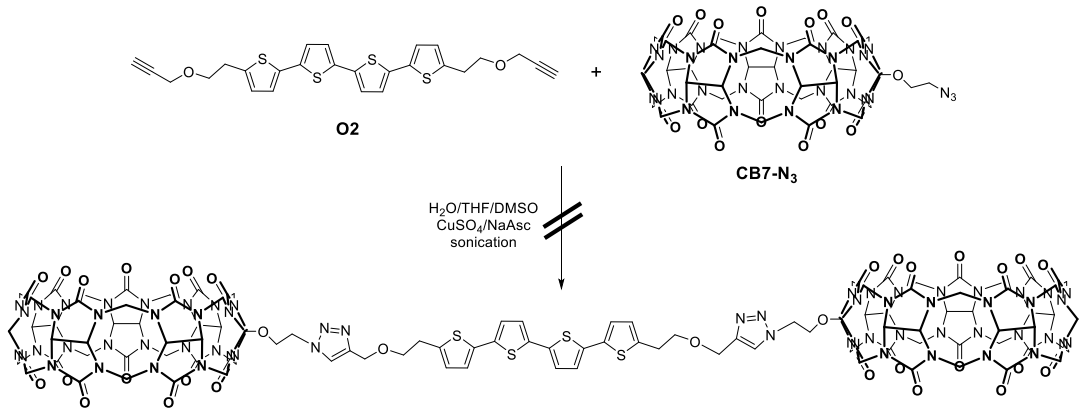
Scheme 3.6 Preparation of Red-emitting crosslinked polymer nanoparticles (**NP1**).

Similar to the CPNs, conjugated oligomer nanoparticles (CONs) can be synthesized using CB[n] as crosslinker. Biological and optical applications can be performed using oligomer-CB[n] conjugates. Synthetic pathway of the conjugated oligomer (**O2**) is given in Scheme 3.7. 2-thiopheneethanol was brominated using NBS to yield **M4**, which then underwent Stille coupling with 5,5'-bis(tributylstannyl)-2,2'-bithiophene to form tetrathiophene oligomer (**O1**). Finally, propargyl units were added to the functional sites using propargyl bromide to obtain the desired oligomer (**O2**). We aimed to attach azide-functionalized cucurbiturils (CB-N_3) to **O2** as demonstrated in Scheme

3.8. However, this work could not be completed in that the efforts to synthesize CB-N_3 did not yield promising results.



Scheme 3.7 Synthesis of propargylated tetrathiophene.



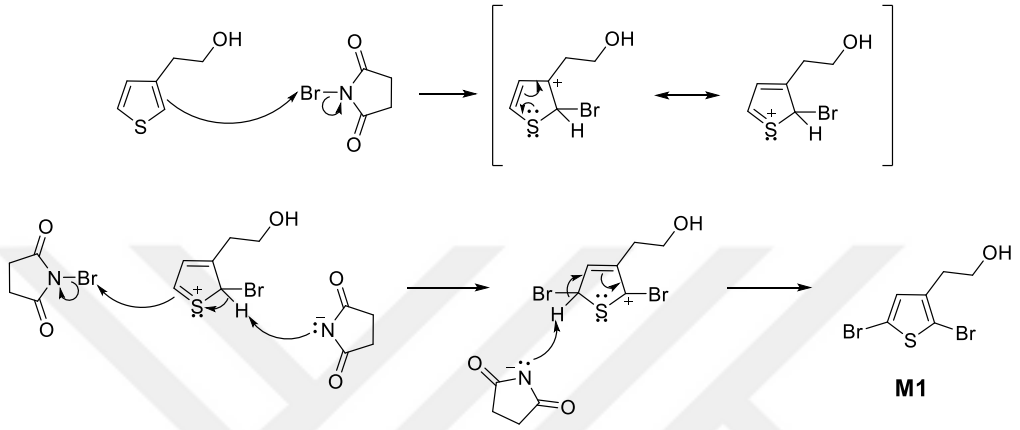
Scheme 3.8 Preparation of **O2-CB7** conjugate through CuAAC.

The chemical structure of the compounds were characterized by ^{1}H and ^{13}C NMR, FT-IR spectroscopies and ESI-MS spectrometry. The photophysical properties of the fluorescent compounds were investigated by UV-Vis absorbance and fluorescence spectroscopies and fluorescence quantum yield measurements. Nanoparticles were characterized using DLS, zeta potential, TEM and UV-Vis absorbance and fluorescence spectroscopies.

3.3.2. Synthesis of Azide-functionalized Conjugated Polymer

3.3.2.1. Synthesis of 2-(2,5-dibromothiophen-3-yl)ethan-1-ol (M1)

3-Thiopheneethanol reacted with N-bromosuccinimide to give 2-(2,5-dibromothiophen-3-yl)ethan-1-ol (**M1**) by electrophilic substitution reaction as shown in Scheme 3.9.



Scheme 3.9 Formation mechamism of **M1**.

^{1}H NMR spectrum of compound **M1** is given in Figure 3.53. Two triplets at 2.83 (b) and 3.84 (a) ppm are assigned to the hydrogens at methylene groups. Protons at position 'a' are more deshielded since they are next to -OH group that withdraws electrons through inductive effect.

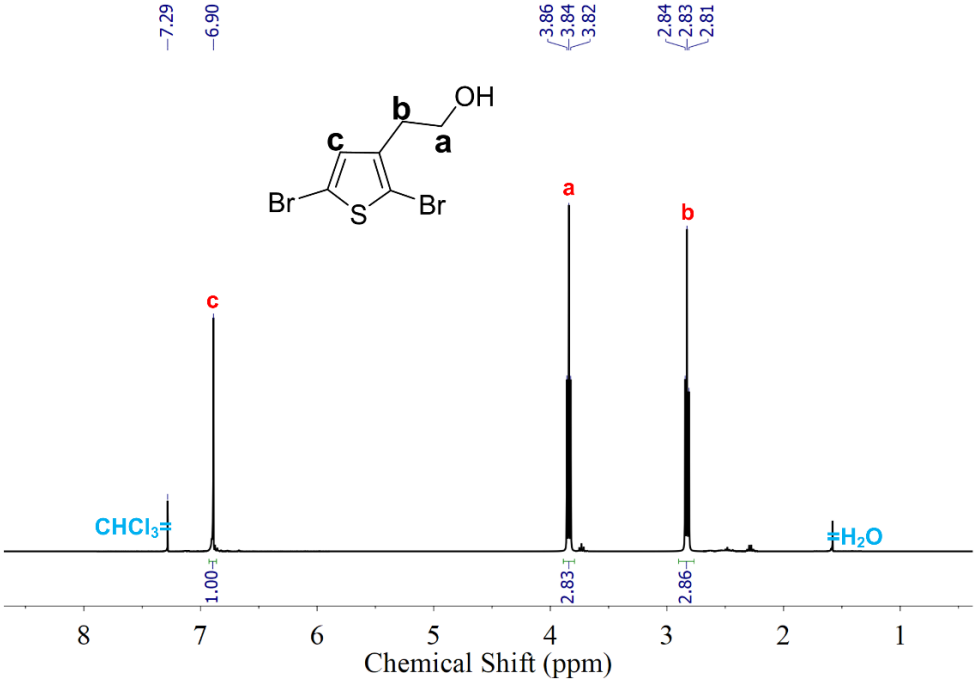


Figure 3.53 ^{1}H NMR spectrum **M1** in $CDCl_3$.

^{13}C NMR spectrum of **M1** is also very clean (Figure 3.54). The carbons on aromatic thiophene core (c, d, e and f) are seen between 108-139 ppm and the carbons at the aliphatic chain (a and b) are seen at 62 and 33 ppm, respectively.

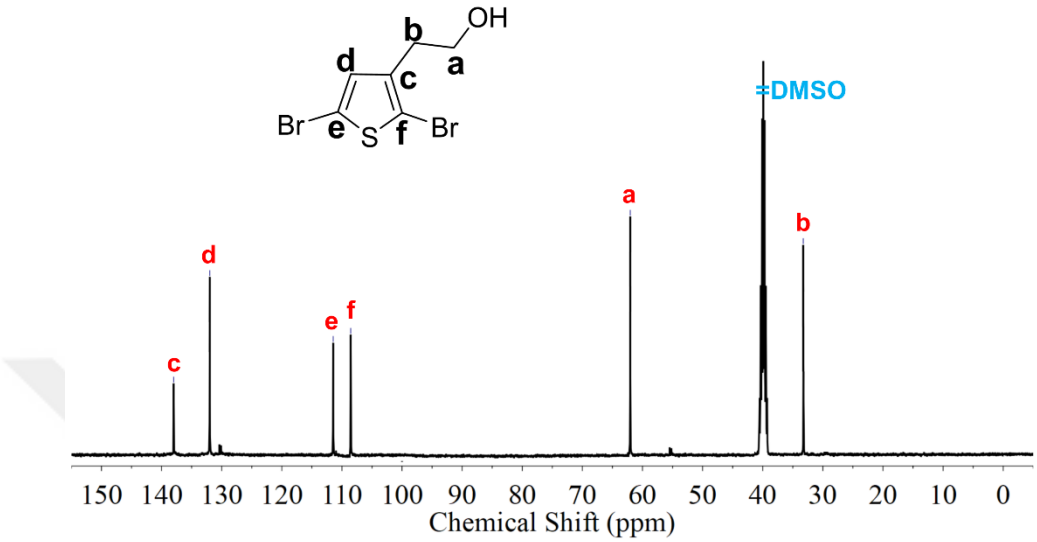
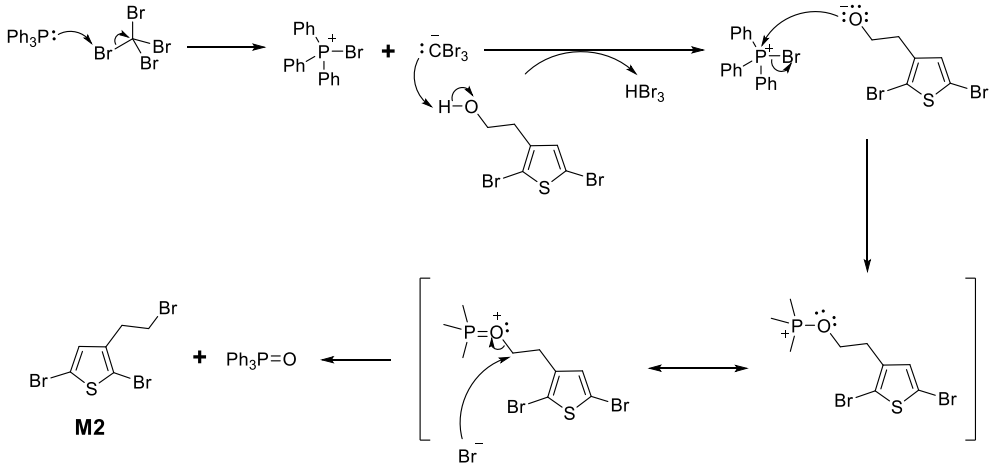


Figure 3.54 ^{13}C NMR spectrum of **M1** in DMSO-d_6.

3.3.2.2. Synthesis of 2,5-dibromo-3-(2-bromoethyl)thiophene (M2)

2,5-dibromo-3-(2-bromoethyl)thiophene (**M2**) was synthesized via Appel reaction of **M1** in the presence of CBr_4 and PPh_3. The mechanism of the reaction is shown in Scheme 3.10.



Scheme 3.10 Formation mechanism of **M2** through Appel reaction.

In ^{1}H NMR spectrum of **M2** (Figure 3.55), it is seen that the triplet 'a' is slightly upfield shifted and the triplet 'b' is slightly downfield shifted after converting –OH group to –Br.

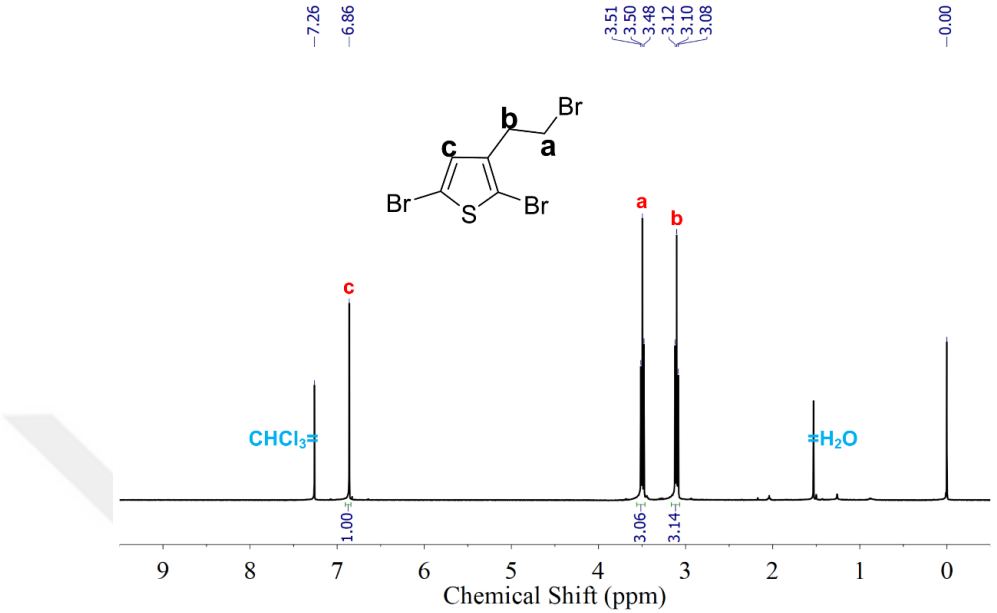


Figure 3.55 ^{1}H NMR spectrum of **M2** in $CDCl_3$.

^{13}C NMR spectrum of M2 is given in Figure 3.56. A significant upfield shift occurs for 'a' due to the change of the neighboring functional group from –OH to -Br, which is less electron withdrawing.

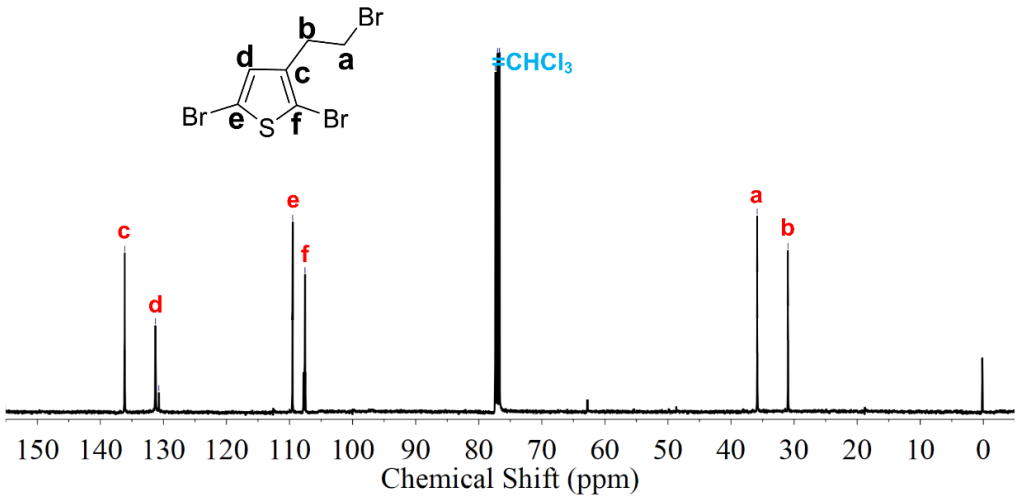


Figure 3.56 ^{13}C NMR spectrum of **M2** in $CDCl_3$.

3.3.2.3. Synthesis of 3-(2-azidoethyl)-2,5-dibromothiophene (M3)

M2 was reacted with NaN_3 through S_N2 reaction to yield 3-(2-azidoethyl)-2,5-dibromothiophene (**M3**).

In ^1H NMR spectrum of **M3** (Figure 3.57), chemical shifts of the protons labelled as 'a' and 'b' appear to change significantly as compared to that of M2. 'a' shifts from 3.50 ppm to 2.82 ppm and 'b' shifts from 3.10 ppm to 3.46 ppm. These changes occur due to the electron donating nature of $-N_3$ group.

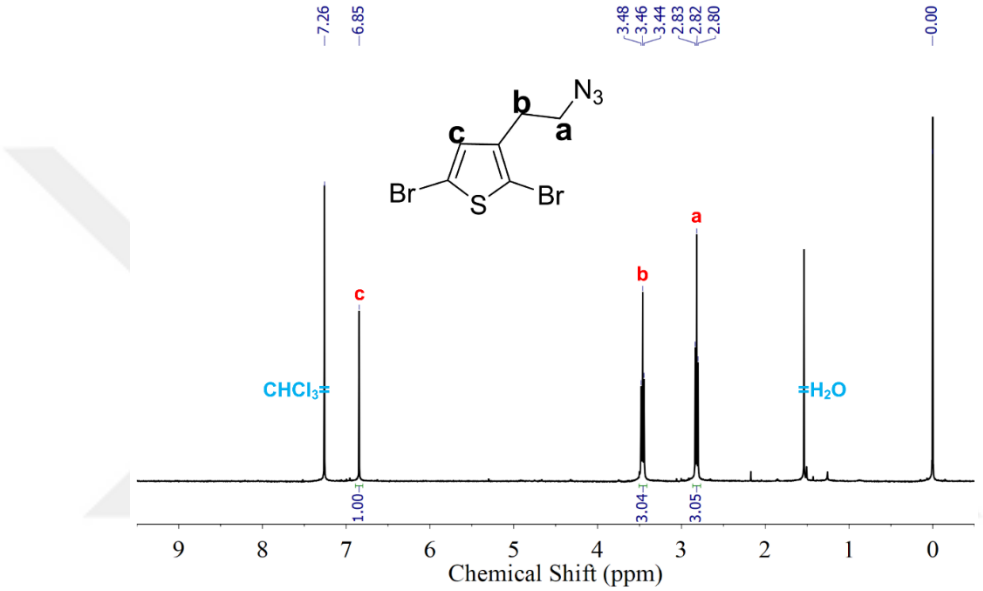


Figure 3.57 ^1H NMR spectrum of **M3** in $CDCl_3$.

^{13}C NMR spectrum of **M3** is given in Figure 3.58. Switching from –Br to $-N_3$ group downfield shifts 'a' carbon while the other signals does not shift to a considerable degree.

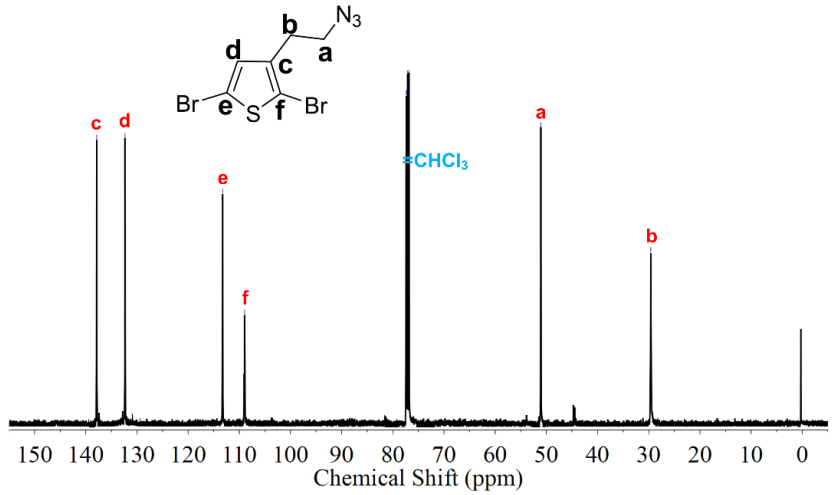


Figure 3.58 ^{13}C NMR spectrum of **M3** in $CDCl_3$.

In FT-IR spectrum of **M3**, sharp peak at 2086 cm^{-1} is attributed to $-N_3$ stretching, which confirms the successful azidation of the compound (Figure 3.59).

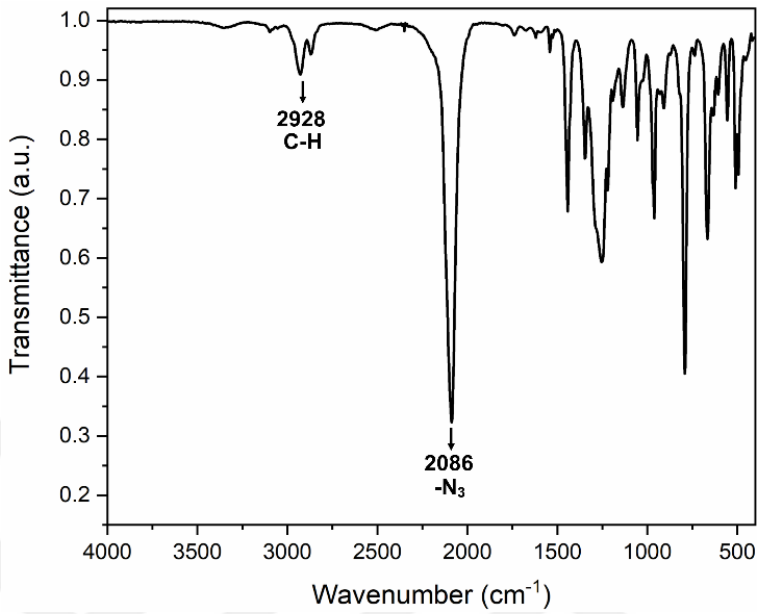


Figure 3.59 FT-IR spectrum of **M3**.

3.3.2.4. Synthesis of Red-emitting Azide-functionalized Thiophene-Benzothiadiazole Copolymer (P1)

Synthesis of azide-functionalized thiophene-benzothiadiazole copolymer (**P1**) was achieved by Suzuki coupling that was discussed in Section 1.2.1.1. **M3** was reacted with 2,1,3-Benzothiadiazole-4,7-bis(boronic acid pinacol ester) using $Pd(PPh_3)_4$ as catalyst and K_2CO_3 as base in THF/toluene/H_2O solvent system.

^{1}H NMR spectrum of **P1** is given in Figure 3.60. Protons of methylene groups are observed as broad peaks located at 3.11 ppm (a) and 3.68 ppm (b) and their integration values are 1:1, which is in accordance with the structure of the repeating unit. The aromatic peaks are distributed in the range of 7.6-8.5 ppm and their integration confirms a total number of 3 aromatic protons per repeating unit as expected.

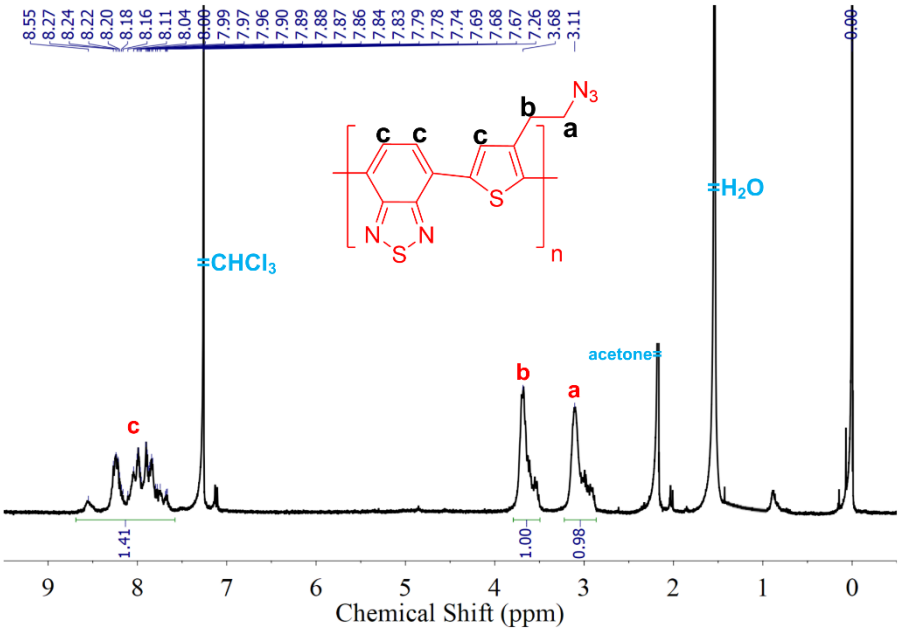


Figure 3.60 ^{1}H NMR spectrum of **P1** in $CDCl_3$.

In ^{13}C NMR spectrum of **P1**, the peaks of methylene groups are located around 29.7 ppm (b) and 51.1 ppm (a) similar to that of **M3**. The carbons on the aromatic backbone appear in a wide range from 125.3 to 154.2 ppm as labelled in Figure 3.61.

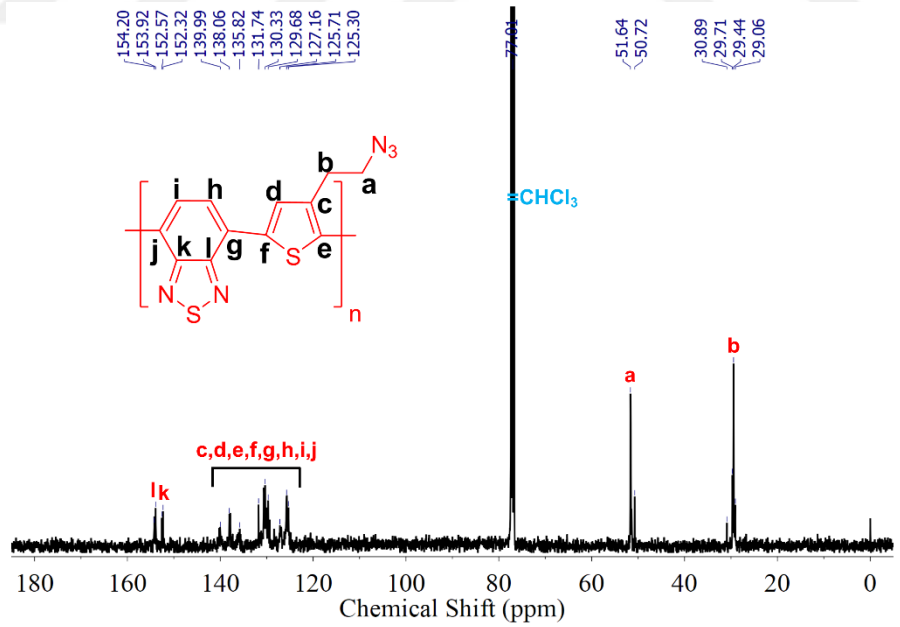


Figure 3.61 ^{13}C NMR spectrum of **P1** in $CDCl_3$.

FT-IR spectrum of **P1** has a sharp $-N_3$ stretching peak at 2094 cm^{-1}, confirming the conservation of azide functionality as polymerization successfully takes place (Figure 3.62).

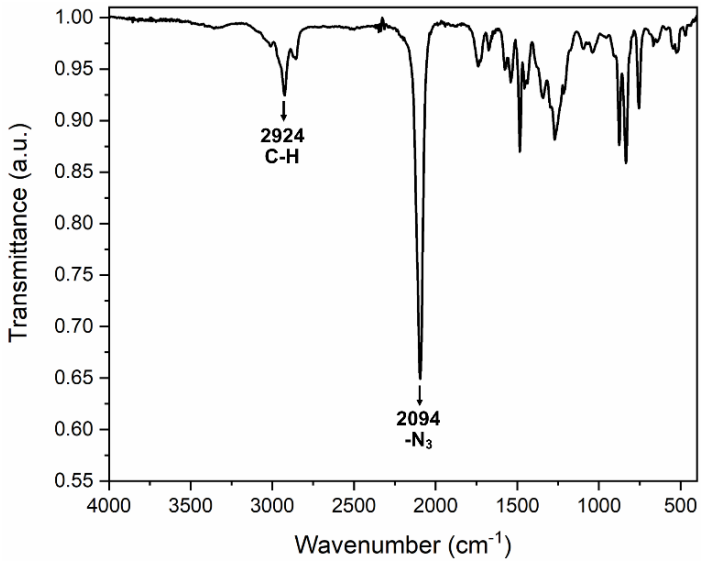


Figure 3.62 FT-IR spectrum of **P1**.

3.3.2.5. Photophysical Properties of P1

P1 has two absorbance bands having maxima at 319 nm and 494 nm and one fluorescence band with a maximum at 620 nm and extending towards the near-infrared region as shown in Figure 3.63. **P1** has a molar absorptivity of 1.2×10^4 $Lmol^{-1}cm^{-1}$ at 494 nm and its fluorescence quantum yield is calculated as 0.18 in THF.

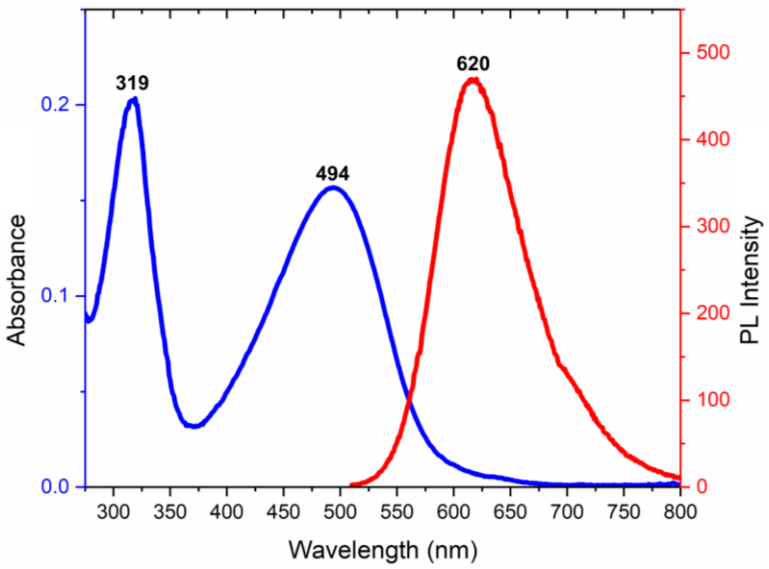
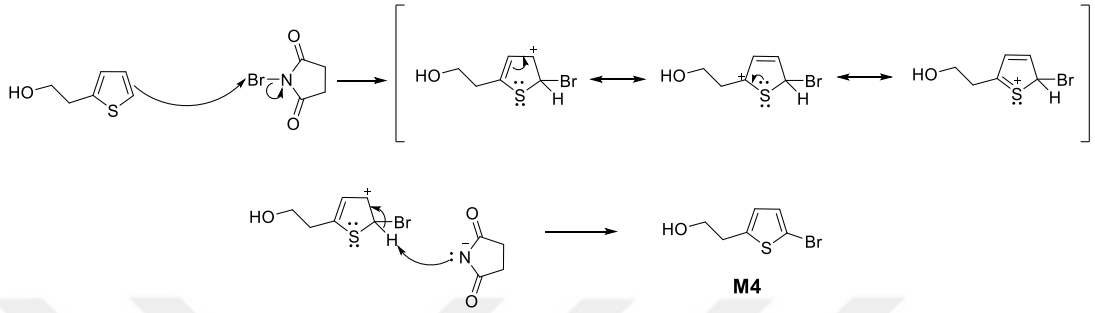


Figure 3.63 UV-Vis absorbance and fluorescence spectra of **P1** in THF.

3.3.3. Synthesis of Tetrathiophene Oligomer

3.3.3.1. Synthesis of 2-(5-Bromo-2-thienyl)ethanol (M4)

2-thiopheneethanol was brominated with N-bromosuccinimide to yield 2-(5-Bromo-2-thienyl)ethanol (**M4**) as shown in Scheme 3.11.



Scheme 3.11 Formation mechanism of **M4** through Appel reaction.

^{1}H NMR spectrum of **M4** is given in Figure 3.64. Triplets at 3.01 (b) and 3.84 (a) ppm are assigned to the hydrogens at methylene groups. The signal 'a' is more downfield shifted because these protons are located in the vicinity of electronegative oxygen atom. There are two doublets (d and c) in the aromatic region as expected. The integral values also confirm the structure of the monomer **M4**.

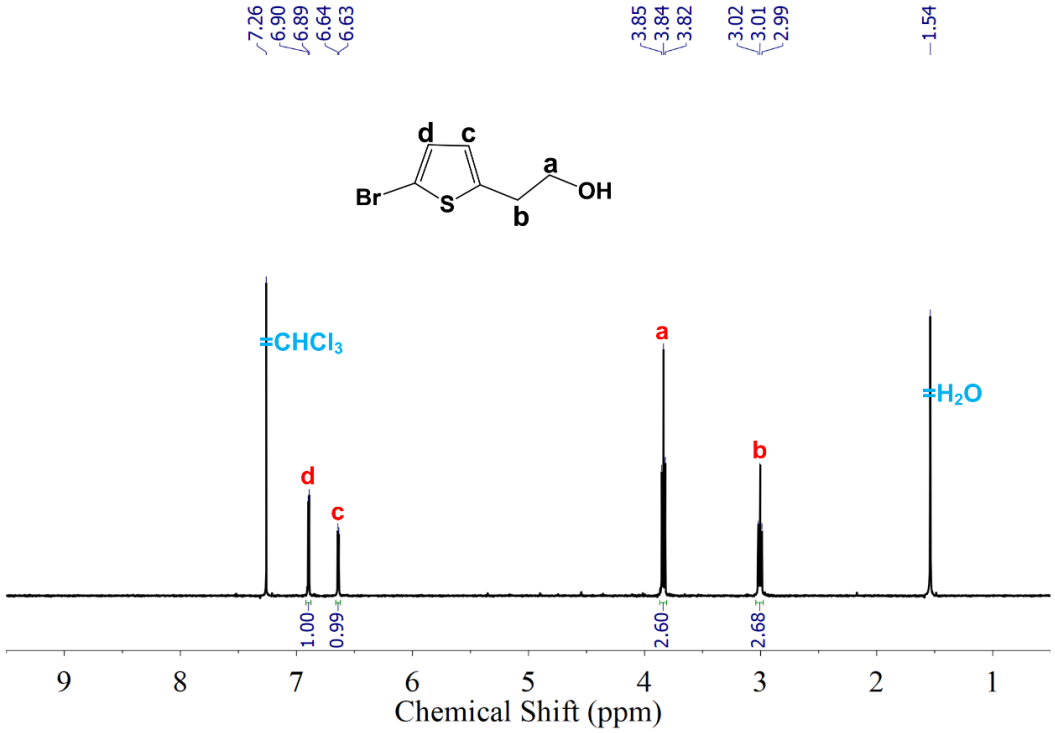


Figure 3.64 ^{1}H NMR spectrum of **M4** in $CDCl_3$.

In ^{13}C NMR spectrum of **M4**, there are two signals at 33 (b) and 63 (a) ppm that comes from aliphatic chain carbons and the remaining four carbon atoms (c-f) in thiophene ring resonate in the range of 110 to 143 ppm (Figure 3.65).

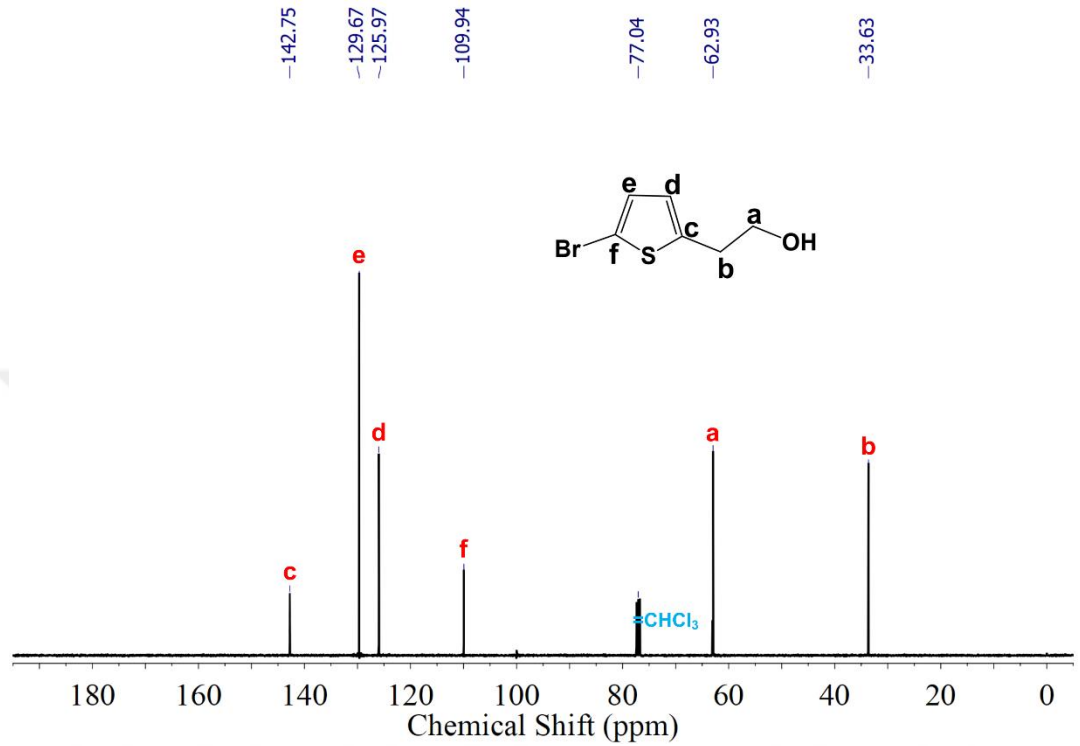


Figure 3.65 ^{13}C NMR spectrum of **M4** in $CDCl_3$.

3.3.3.2. Synthesis of 2,2'-([2,2':5',2'':5'',2'''-quaterthiophene]-5,5'''-diyl)diethanol (O1)

Synthesis of thiophene-based tetramer (**O1**) was done via Stille coupling that was discussed in Section 1.2.1.1. **M4** was reacted with 5,5'-bis(tributylstannyl)-2,2'-bithiophene using $Pd(PPh_3)_4$ as catalyst in DMF.

^1H NMR spectrum of **O1** is given in Figure 3.66. Triplet (a) at 4.86 ppm is asigned to the proton of –OH group that couples with neighboring protons 'b'. Hydrogens labelled as 'b' couple with both a' and 'c' protons to give a quartet at 3.64 ppm while hydrogens at position 'c' give a triplet at 2.92 ppm. When the aromatic region is zoomed in (6.85-7.26 ppm), four distinct doublets can be seen as expected from the molecular symmetry. Since the doublets in the range of 7.15-7.26 are very close, they are all labelled as 'e' for simplicity.

The integrations of the signals are compatible with the number of protons in the molecule, which indicates the successful synthesis of the tetramer (**O1**).

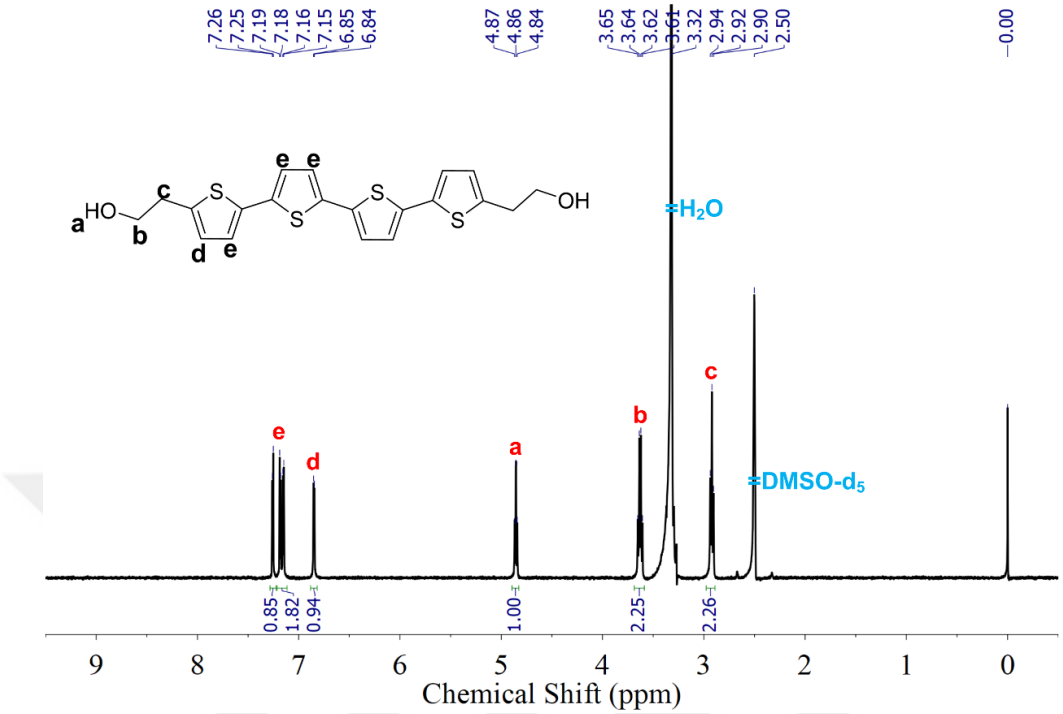


Figure 3.66 ^{1}H NMR spectrum **O1** in DMSO-d_6.

All the signals in ^{13}C NMR spectrum of **O1** are readily assigned to the corresponding carbon atoms in the molecule as given in Figure 3.67.

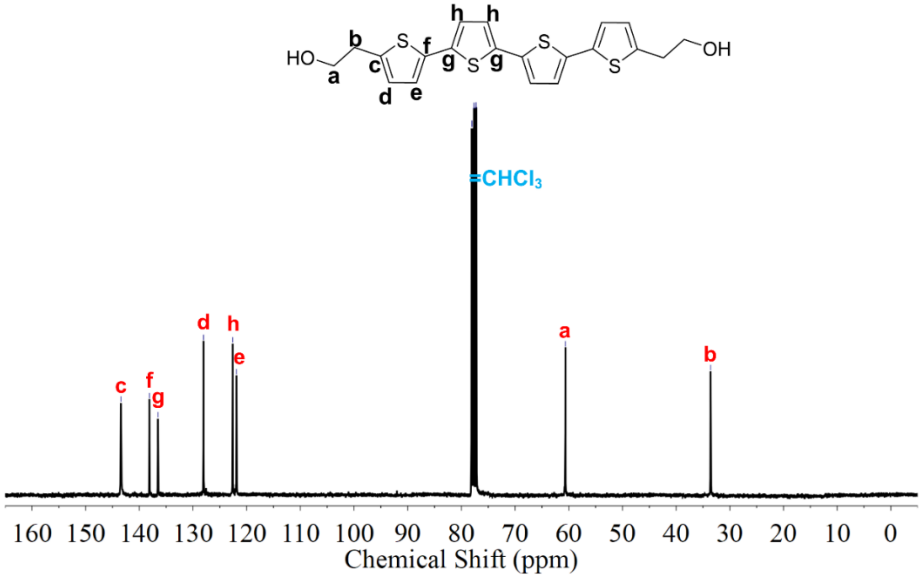


Figure 3.67 ^{13}C NMR spectrum **O1** in $CDCl_3$.

In +ESI-MS spectrum, singly-charged molecular ion signal of **O1** is clearly seen as shown in Figure 3.68.

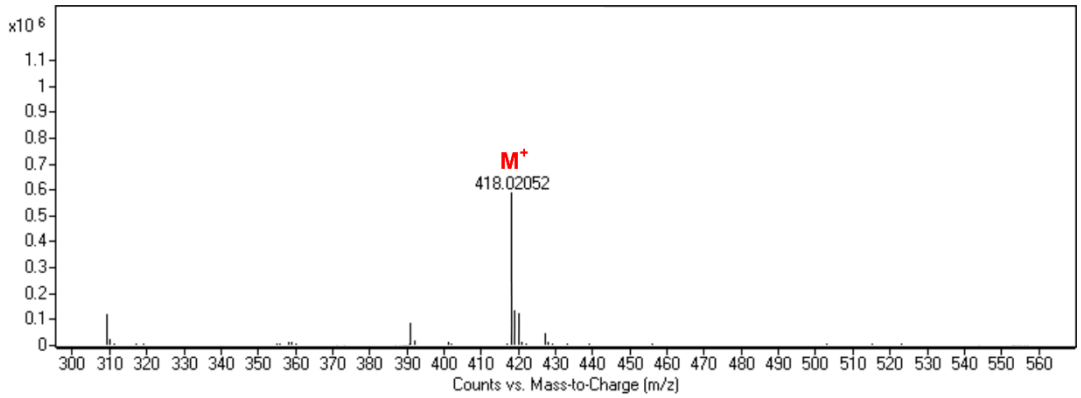


Figure 3.68 +ESI-MS spectrum **O1**.

3.3.3.3. Synthesis of 5,5'''-bis(2-(prop-2-yn-1-yloxy)ethyl)-2,2':5',2'':5'',2'''-quaterthiophene (O2)

Tetramer **O1** was subjected to propargylation using NaH as deprotonating agent and propargyl bromide as electrophile to produce **O2**.

In ^{1}H NMR spectrum of **O2** (Figure 3.69), there are two significant peaks (a and b) indicating the success of the reaction. Triplet at 2.38 ppm is attributed to terminal alkyne hydrogen (a), which couples with two protons at position 'b'. Doublet at 4.14 ppm is assigned to methylene group hydrogens (b) at the propargyl units. The rest of the spectrum is very similar to that of **O1** as expected.

Propargyl group give characteristic signals in ^{13}C NMR spectrum. As compared to ^{13}C NMR spectrum of **O1**, there new signals (a, b and c) in the range of 60-80 ppm can be observed that come from three carbon atoms in propargyl unit as assigned in Figure 3.70.

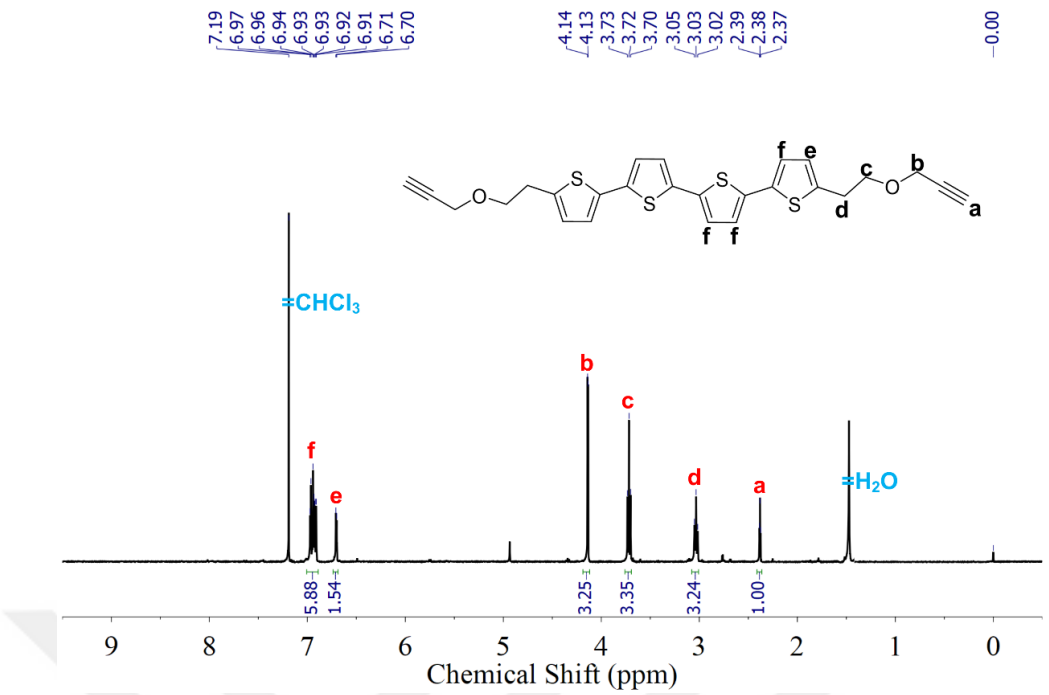


Figure 3.69 ^{1}H NMR spectrum of **O2** in $CDCl_3$.

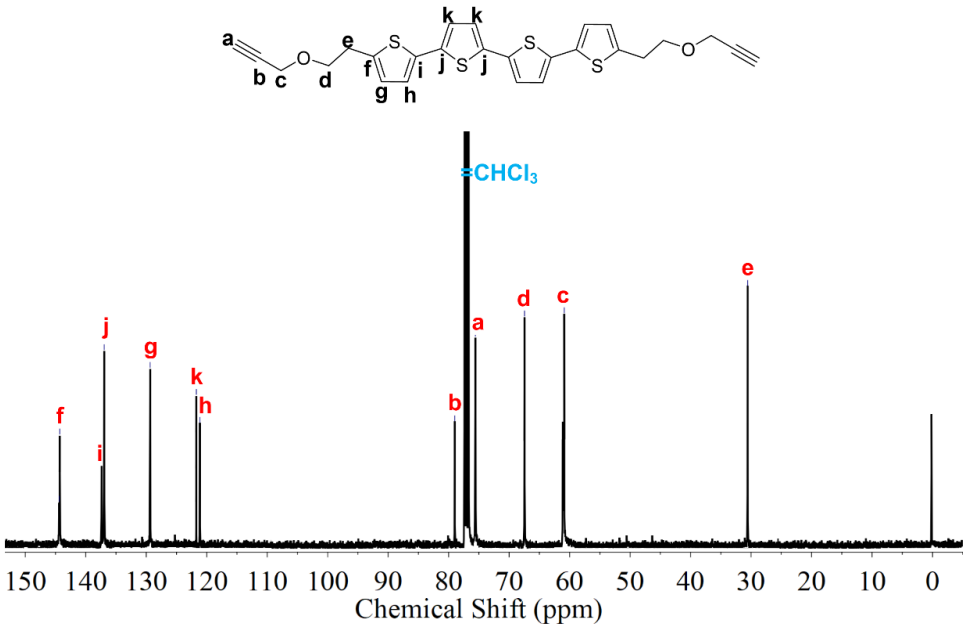


Figure 3.70 ^{13}C NMR spectrum of **O2** in $CDCl_3$.

3.3.3.4. Synthesis and Characterization of Crosslinked Polymer Nanoparticles (NP1)

Synthesis of crosslinked polymer nanoparticles (**NP1**) of azide-functionalized thiophene-benzothiadiazole copolymer (**P1**) with multipropargylated CB8 (**15**) through CuAAC reaction was studied in water as shown in Scheme 3.6. Each

repeating unit of the conjugated polymer contains one reactive azide group and each of compound **15** molecule contains more than 2 propargyl units that can undergo CuAAC reaction. Thus, the degree of crosslinking can be adjusted by varying the ratio of the two components in the reaction medium and NP characteristics in terms of size, stability ad optical properties can be adjusted. To this aim, several experiments were performed by keeping **P1:15** mole ratio at 2:1, 4:1, 8:1 and 16:1.

First, **P1:15** (2:1) NPs experiment was performed. 0.075 mg ($2.62x10^{-4}$ mmol) of **P1** in 150 µL THF was mixed with 0.288 mg of compound **15** ($1.31x10^{-4}$ mmol) in 150 µL DMSO and sonicated for 3 minutes. Then, this solution was dropwise added to 10 mL of water that contains $CuSO_4$ (0.1 eq.) and sodium ascorbate (0.2 eq.) under ultrasonication and continued to sonicate for 1 hour. However, this experiment did not form nicely dispersed NPs. Instead, it resulted in agglomeration in water probably due to low solubility of compound **15** in the organic phase.

In the next trials, the ratio of **15** to **P1** was reduced as low as 1:16 to have all available **15** soluble in the organic phase prior to NP formation. To prepare **P1:15** (4:1) NPs, 0.075 mg ($2.62x10^{-4}$ mmol) of **P1** in 150 µL THF was mixed with 0.144 mg **15** ($6.57x10^{-5}$ mmol) in 150 µL DMSO and sonicated for 3 minutes. Then, this solution was dropwise added to 10 mL of water that contains $CuSO_4$ (0.1 eq.) and sodium ascorbate (0.2 eq.) under ultrasonication and continued to sonicate for 1 hour. Following the same procedure **NP1** with **P1:15** ratio of 8:1 and 16:1 were prepared, too. TEM, DLS and UV-Vis absorbance and fluorescence results of these NP samples are given in Figure 3.71. In the case of **P1:15** (4:1), even though there was no visible sedimentation in the solution, TEM image shows the presence of large agglomerates and a little amount of NP formation. This suggested that we must further decrease the ratio of **15** in the reaction. For **P1:15** (8:1), the average size of NPs were measured as 37 nm by DLS. TEM image of the sample showed the presence of spherical NPs below 100 nm, but the polydispersity of the sample was a bit high, which complies with the DLS result (PdI: 0.308). DLS of **P1:15** (16:1) sample indicated the presence of even smaller NPs with average size of 28 nm, which was supported by TEM. However, similar to the previous sample, the polydispersity of **P1:15** (16:1) was high, too (PdI: 0.359). The decrease in the average size of NPs as the amount of available **15** goes down can be attributed to the extend of intermolecular crosslinkage. It seems that the more **15** is

available in the medium, the larger the extent of intermolecular crosslinking between **P1** and **15** is, leading to the formation of larger NPs.

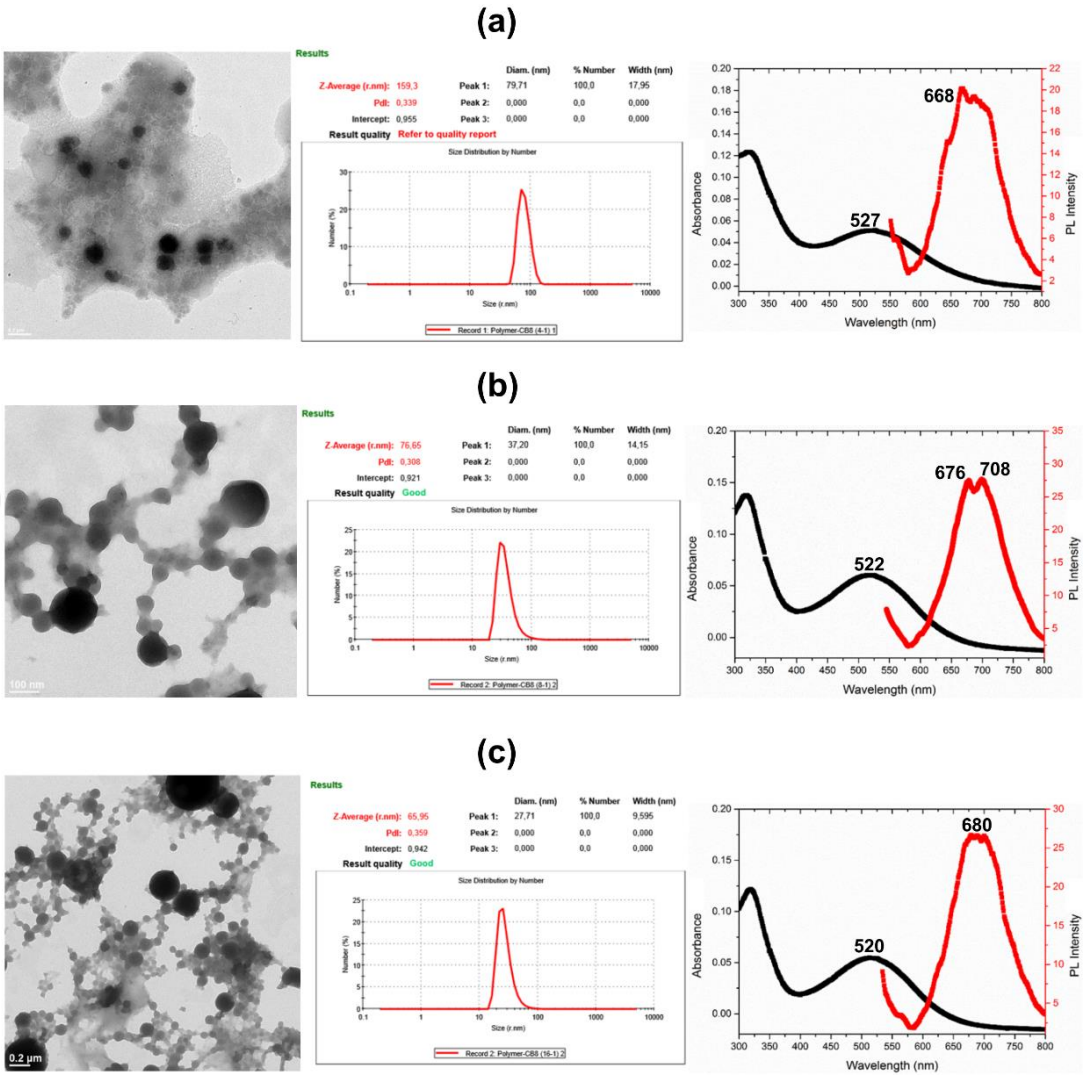


Figure 3.71 TEM, DLS and UV-vis absorbance and fluorescence graphs of **(a) P1:15** (4:1), **(b) P1:15** (8:1) and **(c) P1:15** (16:1).

The UV-Vis absorbance and fluorescence spectra of **P1:15** NPs given in Figure 3.71 represent that their absorbance maxima are red-shifted to ~520 nm as well as the emission maxima to 670-700 nm range, as compared to the polymer solution in chloroform whose absorbance and emission maxima are at 494 nm and 620 nm, respectively. These observed red-shifts can be explained by intensified chain-chain interactions due to π-π stacking of polymer chains as well as the polarity differences in the solvents (THF vs. water). Fluorescence quantum yield of **P1:15** NPs in water was measured to be 0.02, which is quite lower than that of P1 in THF (0.18). The huge decrease in the fluorescence intensity of the NP samples can be attributed to the nonradiative decay

pathways being more dominant because of enhanced interaction between polymer chains.

Since very low concentrations of the reactants were used in the preparation of NPs, they needed to be concentrated so that they can be used in further studies. For this purpose, the volume of the solutions were decreased under reduced pressure, but unexpectedly, the nanoparticles formed agglomerates as the volume of the solution decreased. Therefore, no further study could be conducted with **P1:15** NPs. The success of the click reaction between **P1** and **15** was confirmed by FT-IR spectroscopy. The **NP1** sample used in the FT-IR measurement was obtained after drying the NPs solution under reduced pressure. Figure 3.72 represents the FT-IR spectra of **P1:15** (1:8) before and after NP formation. The above spectrum in Figure 3.72 belongs to the mixture of **P1** and **15** before ultrasonication. Strong stretching peaks of $-N_3$ at 2100 cm^{-1} from **P1** and C=O at 1730 cm^{-1} from **15** are clearly seen in this spectrum. In the below spectrum that was taken after NP formation, a sharp decrease in the intensity of $-N_3$ stretching is apparent while C=O peak from **15** is maintained. This results reveals the success of the CuAAC reaction between **P1** and **15**.

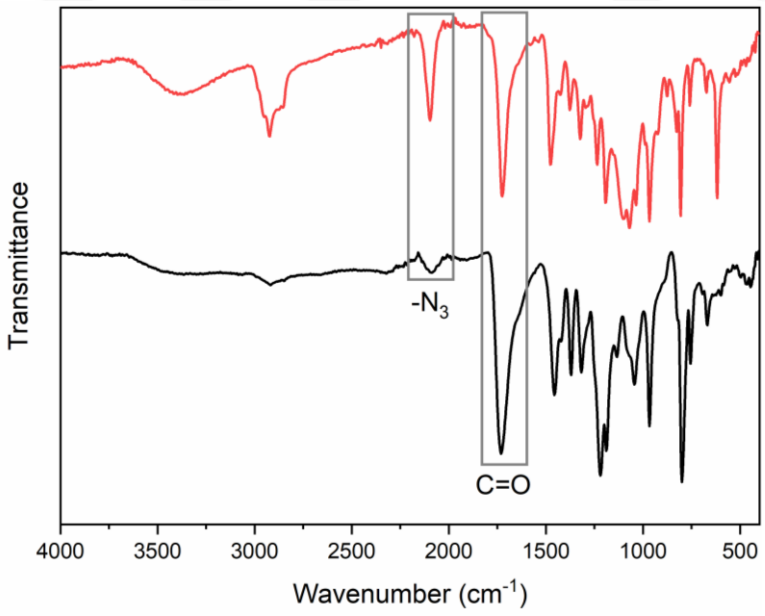


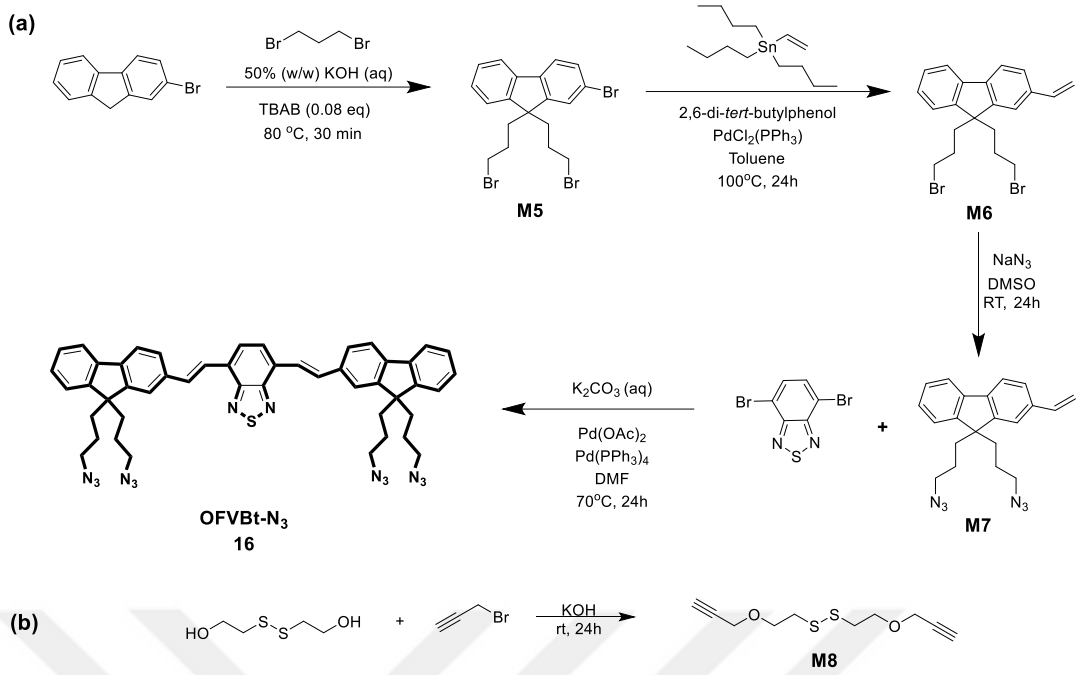
Figure 3.72 FT-IR spectra of **P1:15** (1:8) before (red) and after (black) NP formation.

3.4. Crosslinked Conjugated Oligomer Nanoparticles

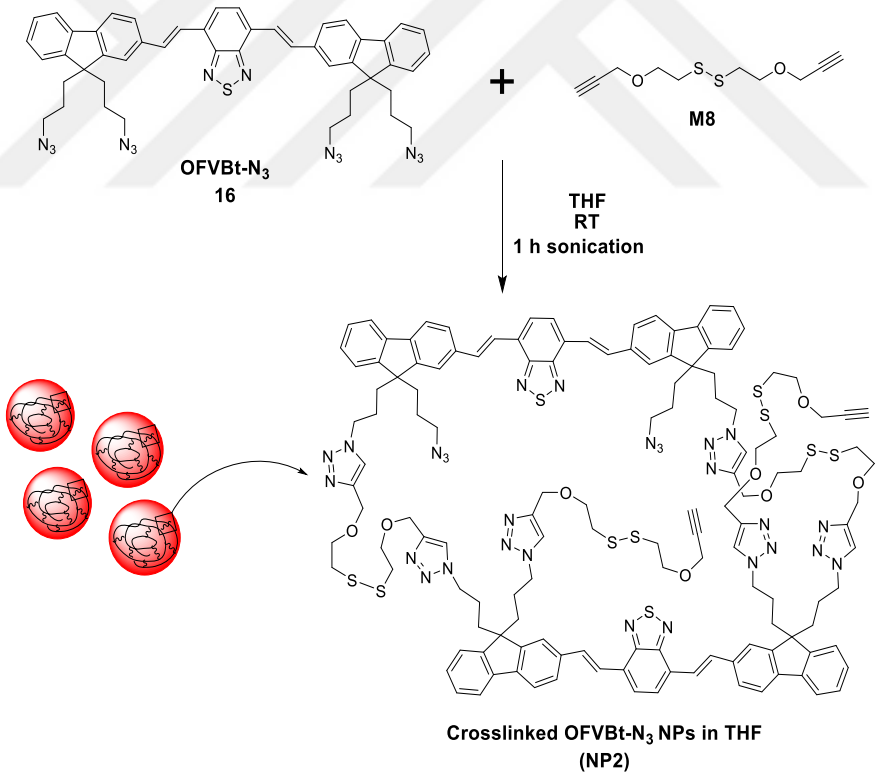
3.4.1. Aim of the Study

The aim of this study is to synthesize redox responsive red-emitting crosslinked conjugated oligomer nanoparticles (CONs) that can be utilized in theranostic studies. CONs can be used as multifunctional agents with remarkable features including high fluorescence quantum yield, enhanced photostability and low cytotoxicity. It is also known that nanoparticles, when they are administered to bloodstream, have tendency to accumulate in tumor tissues due to enhanced permeability and retention effect. These properties of CONs render them promising candidates for theranostic applications such as cell imaging and drug delivery. To this aim, azide-functionalized fluorene-benzothiadiazole oligomer (**OFVBt-N_3**) and propargylated crosslinker with disulfide bond (**M8**) were synthesized according to Scheme 3.12. Oligomer was selected to emit at near infrared end of visible spectrum so that background autofluorescence in tissues can be minimized and high tissue penetration can be achieved. The crosslinker **M8** was designed in a way that it can easily crosslink the oligomer as nanoparticles form. It also includes S-S bond that can be cleaved by glutathione (GSH), giving way to the release of cargo from the NPs. NPs in THF (**NP2**) were prepared by crosslinking **OFVBt-N_3** oligomer in the presence of **M8** via ultrasound-assisted azide-alkyne click reaction (Scheme 3.13). Then, water-dispersed NPs (**NP3**) were prepared from THF solutions and finally disulfide bond cleavage studies using GSH were done.

OFVBt-N_3 and **M8** were characherized by ^{1}H NMR, FT-IR and UV-Vis absorbance and fluorescence spectroscopies. Click reaction during crosslinking in THF was monited by FT-IR spectroscopy. Nanoparticles were characterized using DLS, zeta potential, SEM, TEM and UV-Vis absorbance and fluorescence spectroscopy.



Scheme 3.12 Synthetic routes for **(a)** OFVBt-N_3 oligomer **(b)** disulfide bond-containing crosslinker (**M8**).



Scheme 3.13 Preparation of crosslinked OFVBt-N_3 NPs (**NP2**) in THF. (Note the given crosslinking pattern within the NPs is just a probable pattern out of many possibilities)

3.4.2. Characterization of OFVBt-N_3 (16) and Disulfide Crosslinker (M8)

OFVBt-N_3 oligomer (**16**) was previously synthesized through the synthetic route given in Scheme 3.12. C9-H position of fluorene is weakly acidic in solution and deprotonates easily to form fluorenyl that is a stable aromatic anion and acts as nucleophile. Thus, **M5** was obtained through S_N2 reaction between 2-bromofluorene and excess of 1,3-dibromopropane in the presence of KOH as a base and tetrabutylammonium bromide as phase-transfer catalyst. Stille coupling of **M5** with tributyl(vinyl)tin yielded **M6**, which was then reacted with NaN_3 to give **M7**. Finally, **M7** underwent Heck coupling with 4,7-dibromobenzo[c]-1,2,5-thiadiazole to give OFVBt-N_3 (**16**).

^{1}H NMR spectrum of OFVBt-N_3 is given in Figure 3.73. Two triplets at 3.02 ppm (a) and 2.17 ppm (c) and one quintet at 0.93 ppm (b) come from the propyl chains attached to the 9th position on fluorene units. The rest of the molecule is conjugated, having deshilded protons that resonate around 7.37-8.50 ppm. Integral values are in accordance with the number of hydrogens in each set of chemically equivalent protons.

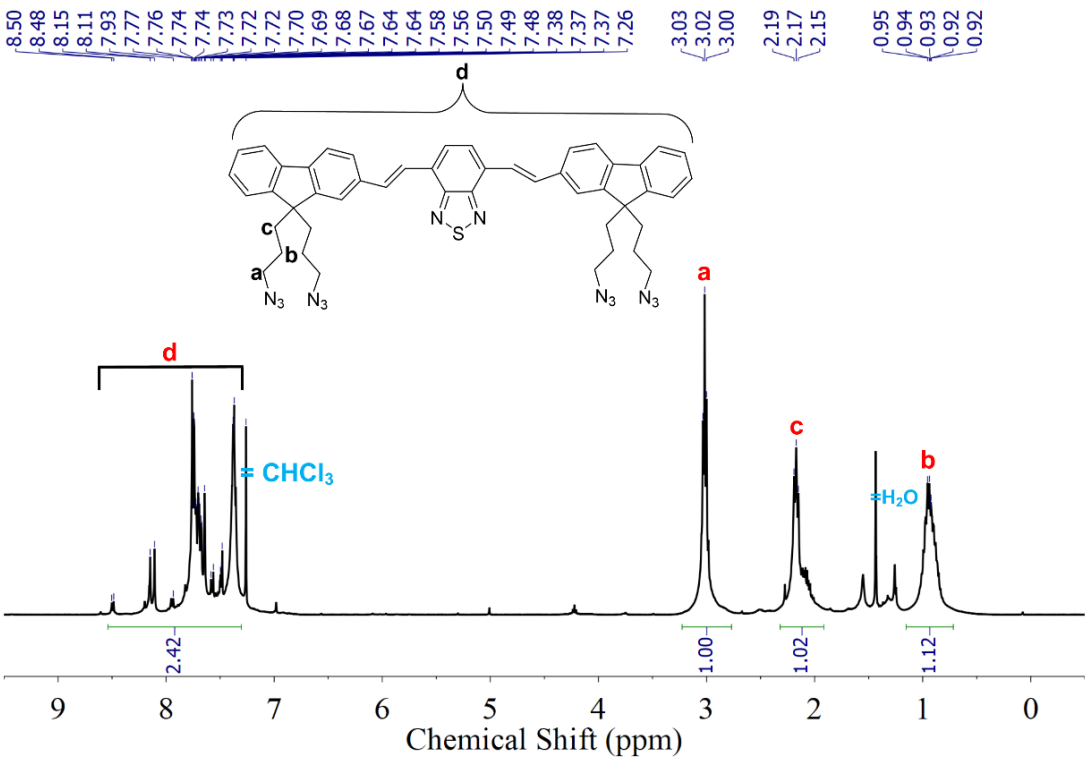


Figure 3.73 ^{1}H NMR spectrum of OFVBt-N_3 in $CDCl_3$.

FT-IR spectrum of OFVBt-N_3 shows a sharp $-N_3$ stretching peak at 2086 cm^{-1} as expected (Figure 3.74).

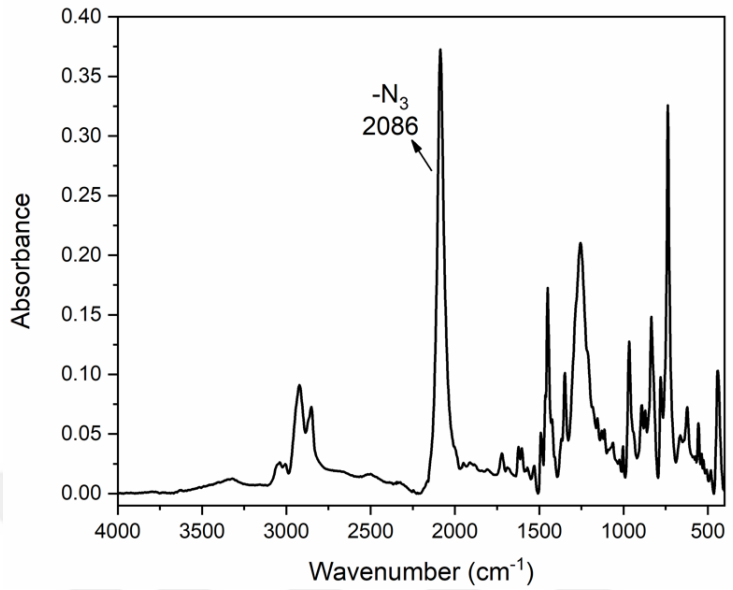


Figure 3.74 FT-IR spectrum of OFVBt-N_3.

OFVBt-N_3 has two absorbance maxima at 348 nm and 476 nm and it emits at 576 nm in THF (Figure 3.75). Its fluorescence quantum yield in THF was calculated as 0.54.

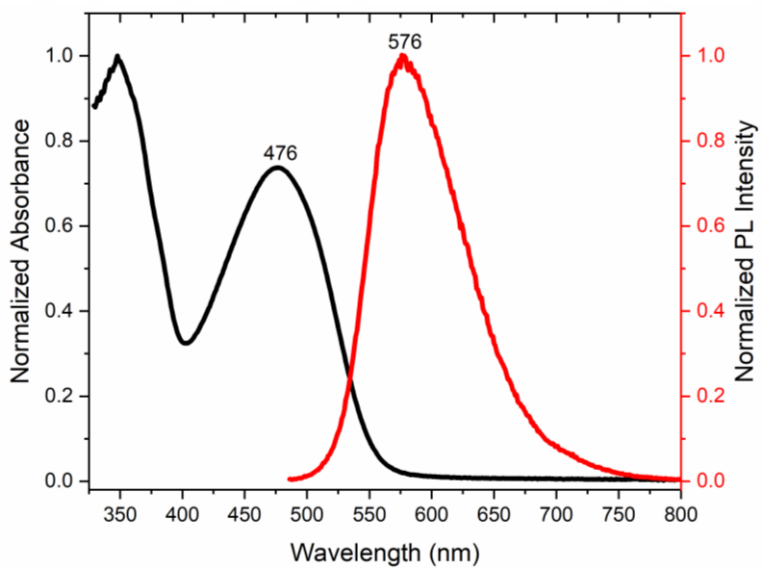


Figure 3.75 UV-Vis absorbance and fluorescence spectra of OFVBt-N_3 in THF.

Disulfide crosslinker (**M8**) was simply synthesized via S_N2 reaction between 2,2'-disulfanediylbis(ethan-1-ol) and propargyl bromide.

^{1}H NMR spectrum of **M8** has four different proton sets as expected. The terminal alkyne hydrogen signal comes at 3.44 ppm (a) as triplet. The other signals are assigned as shown in Figure 3.76.

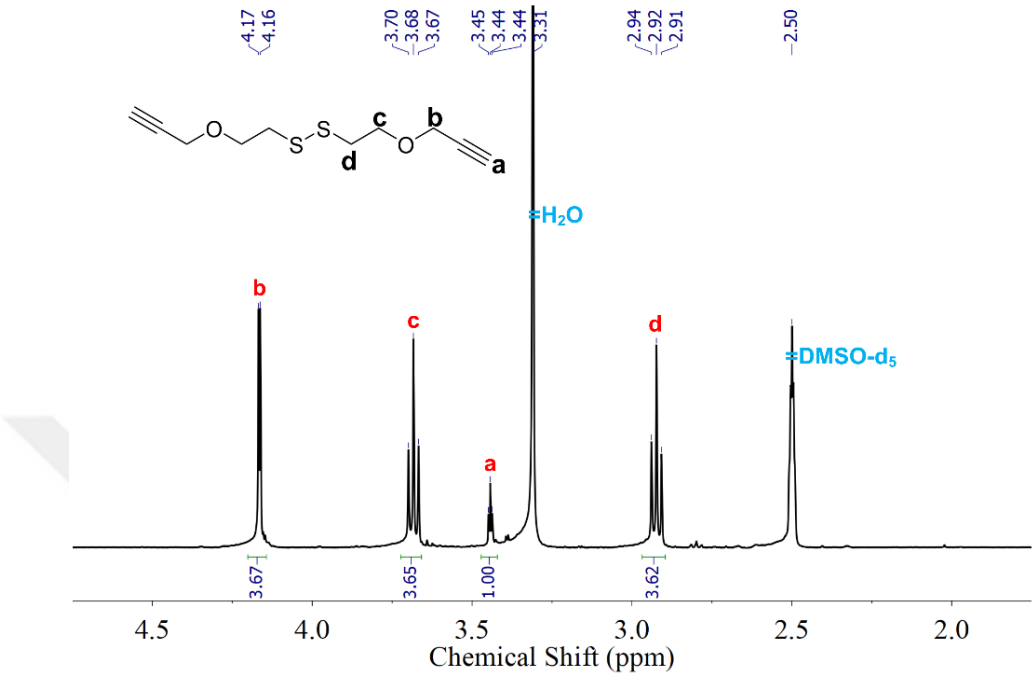


Figure 3.76 ^{1}H NMR spectrum of **M8**.

In FT-IR spectrum of **M8**, -C≡C- stretching at 2115 cm^{-1} and C≡C-H stretching at 3287 cm^{-1} confirm the successful synthesis of the compound (Figure 3.77).

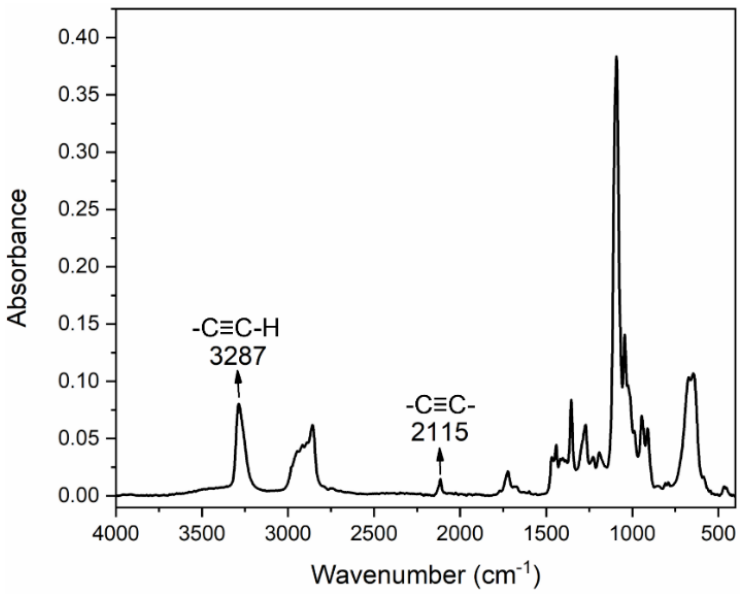


Figure 3.77 FT-IR spectrum of **M8**.

3.4.3. Synthesis of Crosslinked OFVBt-N_3 Nanoparticles in THF (NP2)

Crosslinked OFVBt-N_3 nanoparticles (**NP2**) were synthesized through ultrasound-assisted click reaction in THF. Different conditions were tried as given in Section 2.3.4.1 and the reactions were monitored by FT-IR spectroscopy. In studies where **16** to **M8** ratio is 1:1 (azide to alkyne ratio is 2:1), little amount of product formed and no good NPs in both THF and water obtained. The best results (in terms of amount of crosslinkage, formation of NPs below 100 nm and their stability in THF and water) were acquired in the case of **16:M8** (1:2).

FT-IR spectra in Figure 3.78 represents the change in -N_3 and C≡C-H stretching intensities as NPs form during ultrasonication and after 1 day. 70% decrease in both -N_3 and C≡C-H peaks was recorded just after 1 hour ultrasonication, which roughly tells 70% of the functional groups reacted in the click reaction as **NP2** forms. There was no noticeable change in the instensity of these peaks after leaving aside the **NP2** for 1 day. Duration of ultrasonication was extended up to 5 hours but no further reduction was observed in the intensity of -N_3 and C≡C-H peaks. Therefore, 1 hour ultrasonication was selected as the optimal duration for **NP2** formation. The reason why small portion of both azide and alkyne functional groups remained unreacted could be attributed to steric hindrance that develops as **NP2** form.

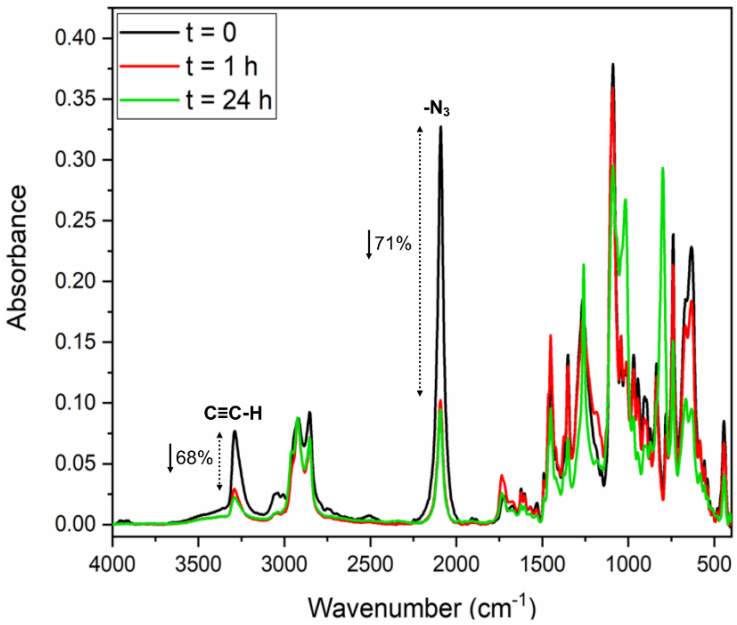


Figure 3.78 Time-dependent FT-IR spectra of **16:M8** (1:2) NPs.

Size and stability of **16:M8** (1:2) NPs in THF were checked by DLS and zeta potential (Figure 3.79). DLS gives an average size of 47 nm with a small polydispersity index and -40 mV zeta potential tells the NPs are perfectly stable in THF.

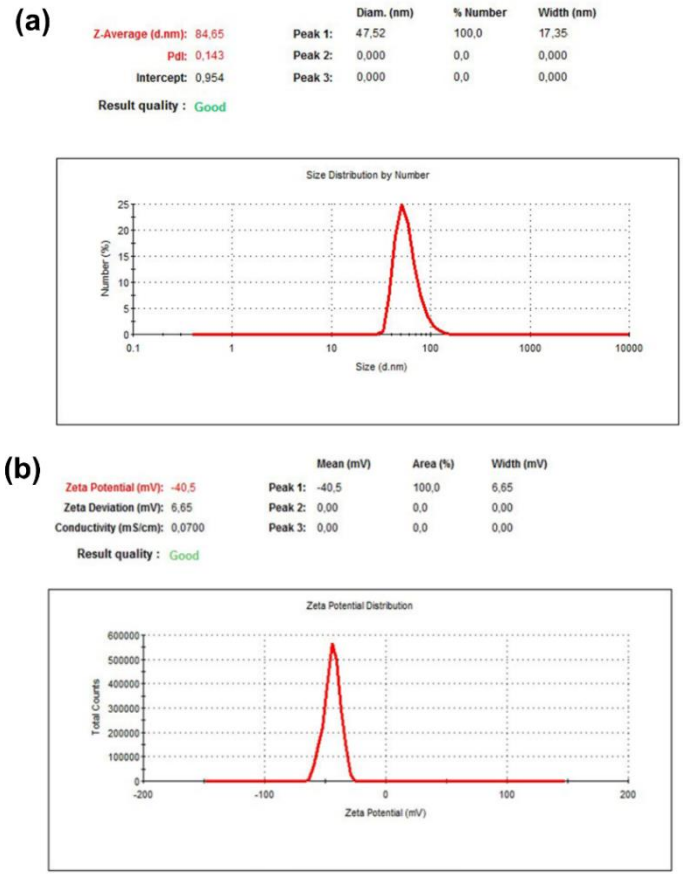


Figure 3.79 **(a)** DLS and **(b)** zeta potential results of **16:M8** (1:2) NPs in THF.

Morphology of **16:M8** (1:2) NPs in THF were visualized by SEM (Figure 3.80a) and TEM (Figure 3.80b). Both images show spherical nanoparticles with average size that is line with the DLS result (≈50 nm).

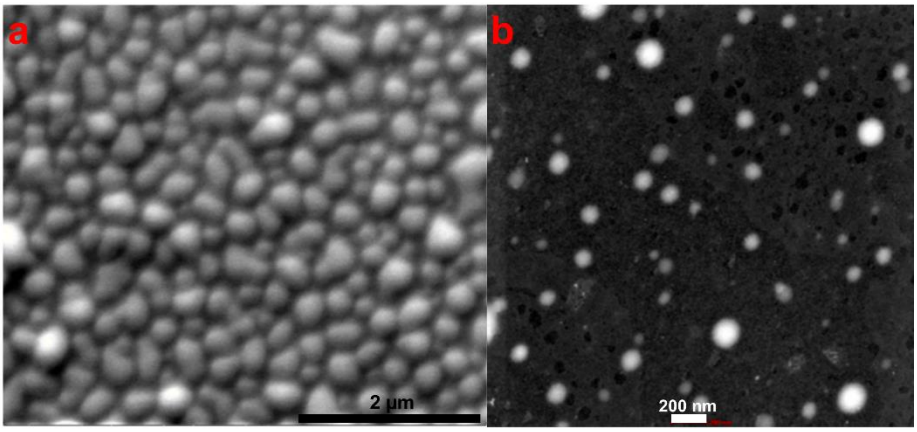


Figure 3.80 **(a)** SEM and **(b)** TEM image of **16:M8** (1:2) NPs in THF.

16:M8 (1:2) NPs in THF have absorbance and fluorescence characteristics similar to the oligomer itself (Figure 3.81). Its fluorescence quantum yield in THF is 0.61.

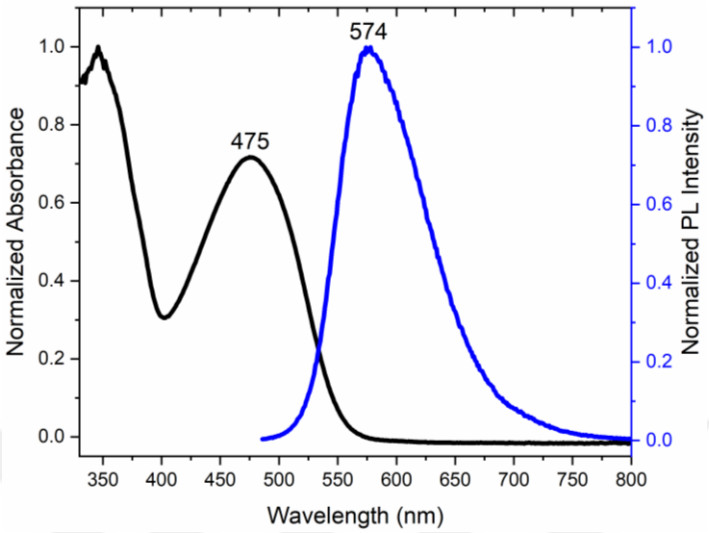


Figure 3.81 UV-Vis absorbance and fluorescence spectra of **16:M8** (1:2) NPs in THF.

3.4.4. Dispersion of Crosslinked OFVBt-N_3 Nanoparticles in Water (NP3)

As the aim in synthesizing **16:M8** (1:2) NPs is to use them in biological applications, they should be nicely dispersed in aqueous medium in high concentrations. Water-dispersed **16:M8** (1:2) NPs (**NP3**) at 0.5 mg/mL and 1.0 mg/mL were prepared according to the procedures given in Section 2.3.4.2(a, b).

DLS and zeta potential results of **NP3** at 0.5 mg/mL and 1.0 mg/mL are given in Figure 3.82. At 0.5 mg/mL, average size (56 nm) and stability (zeta potential = -43 mV) of nanoparticles were better than those with 1.0 mg/mL concentration. Therefore, nanoparticles with 0.5 mg/mL concentration in water were used for further studies.

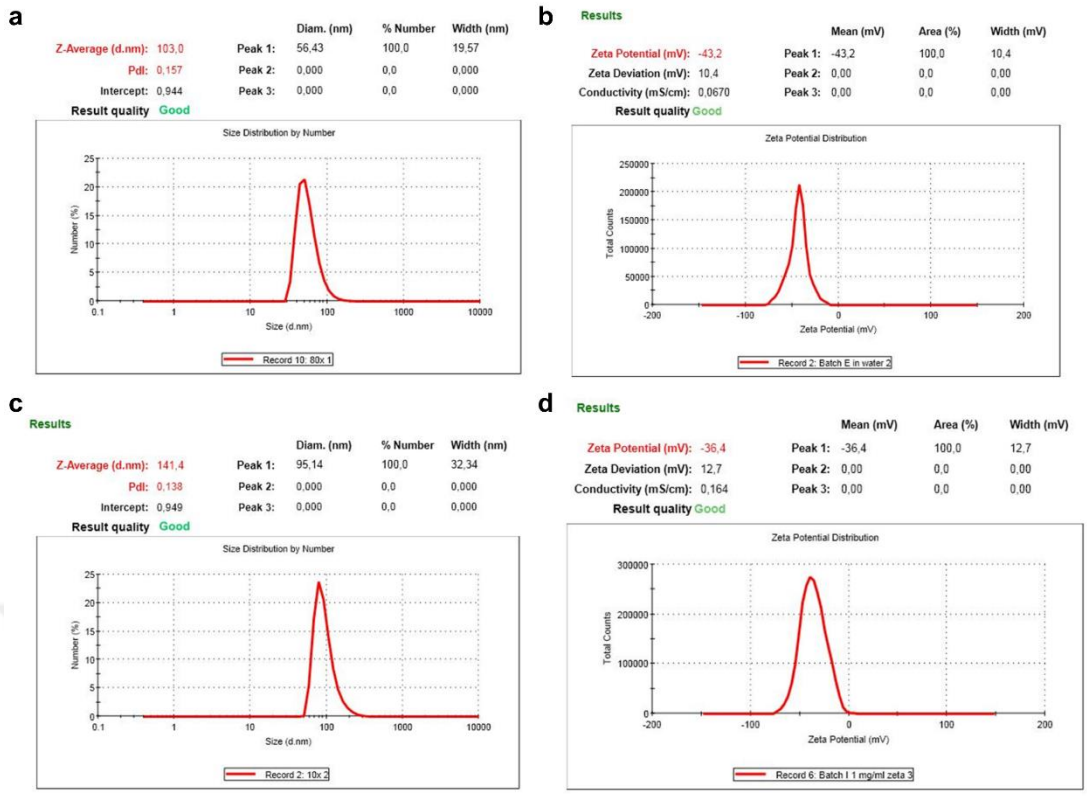


Figure 3.82 **(a)** DLS and **(b)** zeta potential results of **NP3** at 0.5 mg/mL, and **(c)** DLS and **(d)** zeta potential results of **NP3** at 1.0 mg/mL.

In Figure 3.83, SEM and TEM images **NP3** at 0.5 mg/mL shows spherical nanoparticles with sizes around 60 nm, which is in line with the data acquired from DLS measurement.

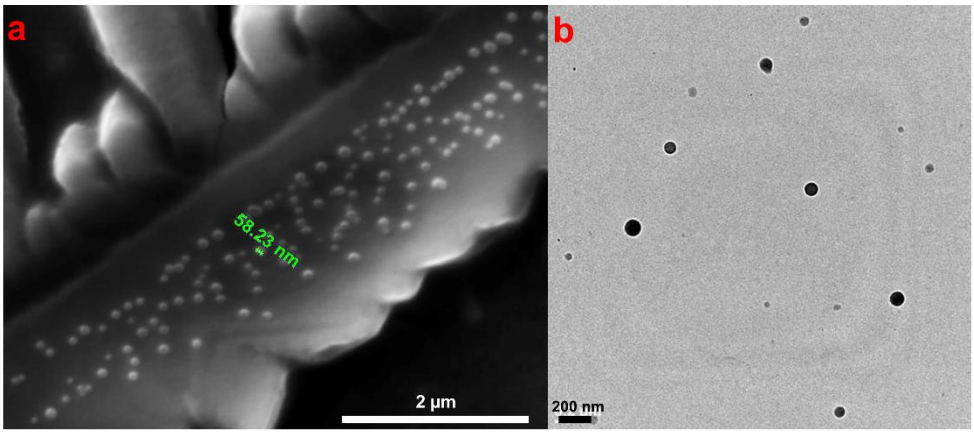


Figure 3.83 **(a)** SEM and **(b)** TEM images of **NP3** at 0.5 mg/mL.

Absorbance spectra of **16:M8** (1:2) NPs in THF and **NP3** at 0.5 mg/mL are almost same, but there is a significant red shift in the fluorescence band of **NP3**, which can be related to enhanced interchain interactions between

oligomers as well as the solvent polarity. (Figure 3.84) Its fluorescence quantum yield is 0.25.

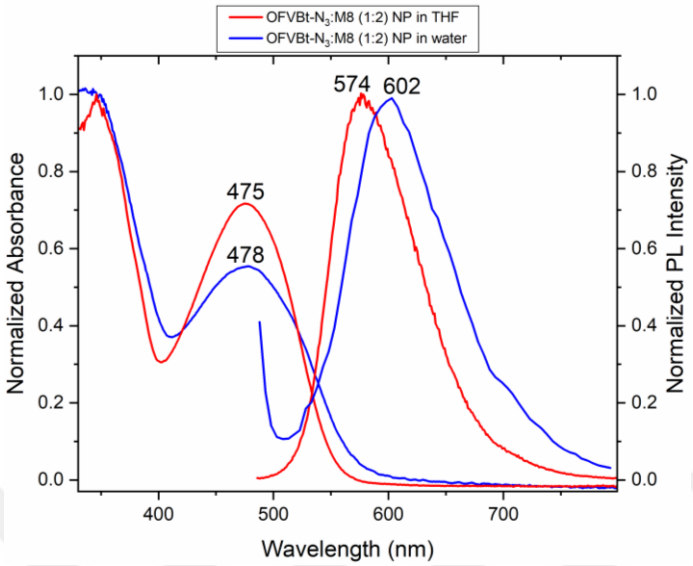


Figure 3.84 UV-Vis absorbance and fluorescence spectra of **16:M8** (1:2) NPs in THF (red) and **NP3** at 0.5 mg/mL (blue).

3.4.5. Disulfide Bond Cleavage by Glutathione (GSH)

Disulfide bond cleavage studies were conducted using GSH as S-S bond cleaving agent as described in Section 2.3.4.3(a, b). The change in the size of **NP3** was monitored by DLS. There was no significant change in the size of NPs when 2 equivalent GSH is present in the medium. In another experiment, 10 mM GSH concentration was used since in the literature it is reported that the intracellular GSH concentration is around 10 mM and cancer tissues have even higher GSH concentration.[151]

After addition of 10 mM GSH into **NP3** at 0.5 mg/mL, the solution started to become cloudy in 1 hour. This change in solution appearance was further supported by more than 2-fold increase in NPs size as seen in Figure 3.85(a). Next day, it was seen that huge amount of the material has already precipitated because the cleavage of disulfide bonds results in oligomer pieces that are no more dispersible in water. Thus, GSH-induced rapid disruption of NPs would suggest that when these NPs encapsulate anticancer drugs, it can be possible to deliver and release the drug in tumor sites in the body via GSH activated S-S bond cleavage.

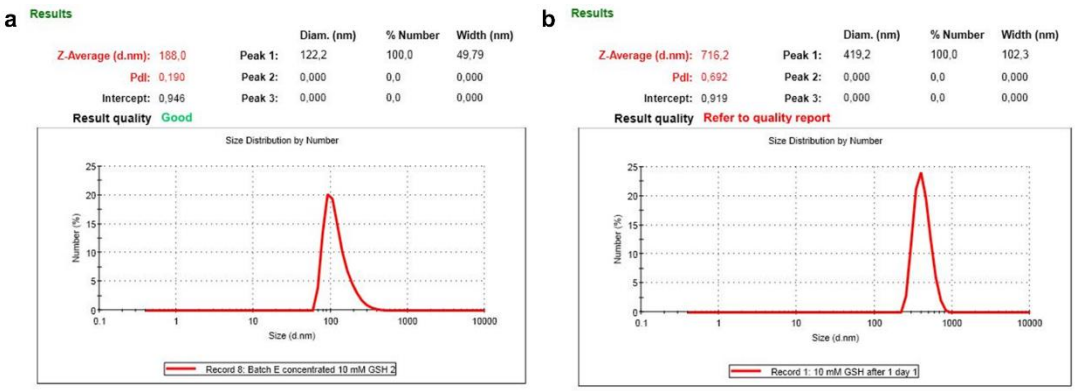


Figure 3.85 DLS results of **NP3** upon addition of GSH after **(a)** 1 hour and **(b)** 1 day.

CHAPTER 4

Conclusions and Future Works

Photoactive mannosylated porphyrin and covalently attached monofunctionalized CB7 based supramolecular assembly was synthesized and fully characterized for the first time. Trimannosylated tetraphenylporphyrin, TPP-Az-3AcMan, was synthesized via CuAAC reaction of 1-α-propargyloxymannose and Zn-TPP-N_3, followed by deacetylation of mannosyl groups to give TPP-Az-3Man. CB7 was synthesized and monofunctionalized to obtain monopropargyloxyCB7, which will undergo CuAAC reaction with TPP-Az-3Man to yield the desired multifunctional assembly. The resulting assembly dissolves in DMSO (10 mg/mL), in H_2O (0.2 mg/mL), in H_2O:DMSO mixture (4:1, v/v; 2 mg/mL) and in aqueous HCl solution. ^1H NMR experiments were done to show the availability of CB7 as a host in the assembly by taking advantage of a guest molecule, bisimidazolium, that forms strong inclusion complex with CB7. $^1O_2$ quantum yield of the assembly was calculated to be 0.77, which is significantly higher than that of unfunctionalized TPP (0.60 in DMF). This rationally designed assembly can be employed in multimodal chemo- and photodynamic therapies. TPP core can act as an efficient photosensitizer in photodynamic therapy and at the same time an anticancer drug or antibiotic can be carried and delivered by CB7. Mannose groups help to increase solubility as well as act to target certain tumor sites where mannose receptors are overexpressed. Alternatively, this assembly can also be used for photocatalysis and energy transfer processes in which CB7 units can encapsulate an analyte and donor/acceptor molecules.

Azide-functionalized thiophene-benzothiadiazole copolymer (**P1**) was synthesized by Suzuki cross-coupling of suitably-functionalized monomers and its chemical and optical properties were fully characterized. Crosslinked sub-50 nm-sized nanoparticles of **P1** with multipropargylated CB8 were prepared via CuAAC reaction. Both UV-Vis absorbance and emission spectra of the NPs showed significant red-shifts. The major drawback of the work was that the concentration of the NPs in water was quite low. They needed to be

concentrated for further use, but removal of the solvent induced rapid agglomeration of the NPs. Therefore, alternative ways should be devised to fabricate these NPs in concentrated form. Backbone of the polymer might be changed or some side chains may be added to the backbone to increase the stability of the polymer chains in NPs in the solution. On the other side, a propargyl-functionalized tetrathiophene oligomer (**O2**) was synthesized via Stille coupling and characterized. Azide-functionalized cucurbituril could be attached to this oligomer to produce a multifunctional assembly, but the synthesis of azide-functionalized cucurbituril did not produce good results despite the intense efforts.

Finally, crosslinked conjugated oligomer nanoparticles (CONs) were synthesized as potential candidates for targeted drug delivery. First, conjugated oligomer, OFVBt-N_3, and disulfide crosslinker, M8, were fully characterized. A crosslinker with S-S bond was chosen for targeting cancer cells since glutathione (GSH), an effective S-S bond cleaver, is overexpressed in cancer cells. Synthesis of spherical CONs with average size of 47 nm was achieved by ultrasound-assisted copper-free click reaction in THF. CONs were then dispersed in water 0.5 mg/mL) and it was seen that they stay perfectly stable in water with average size of 56 nm, which is quite promising for biological applications. The response of the CONs in the presence of GSH was studied in aqueous medium. It was observed that the CONs are rapidly disrupted by GSH, which implies that when nanoparticles are loaded with an anticancer drug, the drug can be specifically targeted and delivered to cancer cells by cooperative action of EPR effect and S-S bond cleavage. Behavior of the CONs in biological media can be further investigated by *in vitro* and *in vivo* studies.

References

[1] https://www.nobelprize.org/nobel_prizes/chemistry/laureates/1987/

[2] J. W. Steed, D. R. Turner, K. J. Wallace, Core Concepts in Supramoleular Chemistry and Nanochemistry, Wiley, **2007**.

[3] J.W. Steed, J. L. Atwood, Supramolecular Chemistry, 2nd edition, Wiley, **2009**.

[4] D. J. Cram, The Design of Molecular Hosts, Guests, and Their Complexes, Nobel Lecture, 8 December **1987**.

[5] F. Huang, E. V. Anslyn, *Chem. Rev.*, **2015**, *115*, 6999-7000.

[6] J-M. Lehn, *Chem. Soc. Rev.*, **2017**, *46*, 2378.

[7] H. M. Powell, *J. Chem. Soc.*, **1948**, *0*, 61-73.

[8] R. D. Hancock, J. Chem. Ed., **1992**, *69*, 615-621.

[9] D. J. Cram, *Angew. Chem. Int. Ed.*, **1986**, *25*, 1039-1134.

[10] A. Hossain, J. A. Liljegren, D. Powell, K. Bowman-James, *Inorg. Chem.*, **2004**, *43*, 3751-3755.

[11] S. Boudon, A. Decian, J. Fischer, M. W. Hosseini, J-M. Lehn, G. Wipff, *J. Coord. Chem.*, **1991**, *23*, 113-135.

[12] C. J. Pedersen, *J. Am. Chem. Soc.*, **1967**, *89*, 7017-7036.

[13] G. Crini, *Chem. Rev.*, **2014**, *114*, 10940-10975.

[14] R. Behrend, E. Meyer, F. Rusche, *Liebigs Ann. Chem.*, **1905**, *339*, 1-37.

[15] W. A. Freeman, W. L. Mock, N. Y. Shih, *J. Am. Chem. Soc.*, **1981**, *103*, 7367-7368.

[16] J. Kim, I.-S. Jung, S.-Y. Kim, E. Lee, J.-K. Kang, S. Sakamoto, K. Yamaguchi, K. Kim, *J. Am. Chem. Soc.* **2000**, *122*, 540–541.

[17] A. Day, A. P. Arnold, R. J. Blanch, B. Snushall, *J. Org. Chem.* **2001**, *66*, 8094–8100.

[18] E. Masson, X. Ling, R. Joseph, L. Kyeremeh-Mensah, X. Lu, *RSC Adv.,* **2012**, *2*, 1213–1247.

[19] S. Gürbüz, M. Idris, D. Tuncel, *Org. Biomol. Chem.,* **2015**, *13*, 330–347.

[20] K. I. Assaf, W. M. Nau, *Chem. Soc. Rev.,* **2015**, *44*, 394–418.

[21] D. Shetty, J. K. Khedkar, K. M. Park, K. Kim, *Chem. Soc. Rev.,* **2015**, *44*, 8747–8761

[22] S. J. Barrow, S. Kasera, M. J. Rowland, J. Del Barrio, O. A. Scherman, *Chem. Rev.*, **2015**, *115*, 12320–12406.

[23] S. Walker, R. Oun, F. J. McInnes, N. J. Wheate, *Isr. J. Chem.*, **2011**, *51*, 616−624.

[24] S. Angelos, N. M. Khashab, Y.-W. Yang, A. Trabolsi, H. A. Khatib, J. F. Stoddart, J. I. Zink, *J. Am. Chem. Soc.*, **2009**, *131*, 12912-12914.

[25] J. Liu, X. Du, X. Zhang, *Chem. Eur. J.*, **2011**, *17*, 810-815.

[26] C. Kim, S. S. Agasti, Z. Zhu, L. Isaacs, V. M. Rotello, *Nat. Chem.*, **2010**, *2*, 962-966.

[27] S. K. Kim, K. M. Park, K. Singha, J. Kim, Y. Ahn, K. Kim, W. J. Kim, *Chem. Commun.*, **2010**, *46*, 692-694.

[28] C. Hang, Z. Fang-fang, Z. Jian-xin, Z. Xi, T. Zhu, X. Sai-feng, Z. Qian-jiang, *Catal. Commun.*, **2009**, *11*, 167−170.

[29] S. Y. Jon, Y. H. Ko, S. H. Park, H. J. Kim, K. Kim, *Chem. Commun.*, **2001**, 1938−1939.

[30] T. C. Krasia and J. H. G. Steinke, *Chem. Commun.*, **2002**, 22.

[31] D. Tuncel, M. Katterle, *Chem. Eur. J.*, **2008**, *14*, 4110-4116.

[32] A. Praetorius, D. M. Bailey, T. Schwarzlose, W. M. Nau, *Org. Lett.*, **2008**, *10*, 4089-4092.

[33] I. Hwang, A. Y. Ziganshina, Y. H. Ko, G. Yun, K. Kim, *Chem. Commun.*, **2009**, 416-418.

[34] D. Tuncel, J. K. G. Steinke, *Chem. Commun.*, **1999**, 1509-1510.

[35] C. J. Bruns, H. Liu, M. B. Francis, *J. Am. Chem. Soc.*, **2016**, *138*, 15307-15310.

[36] S. Kasera, L. O. Hermann, J. del Barrio, J. J. Baumberg, O. A. Scherman, *Sci. Rep.*, **2014**, *137*, 3663-3669.

[37] J. M. Chinai, A. B. Taylor, L. M. Ryno, N. D. Hargreaves, C. A. Morris, P. J. Hart, A. R. Urbach, *J. Am. Chem. Soc.*, **2011**, *133*, 8810-8813.

[38] W.-H. Huang, S. Liu, L. Isaacs, Cucurbit[n]urils, in: Modern Supramolecular Chemistry: Strategies for Macrocycle Synthesis, ed. F. Diederich, P. J. Stang and R. R. Tykwinski, Wiley-VCH Verlag GmbH & Co., Weinheim, **2008**, 113.

[39] A. Thangavel, A. M. M. Rawashdeh, C. Sotiriou-Leventis, N. Leventis, *Org. Lett.*, **2009**, *11*, 1595.

[40] D. Jiao, N. Zhao, O. A. Scherman, *Chem. Commun.*, **2010**, *46*, 2007.

[41] A. Flinn, G. C. Hough, J. F. Stoddart, D. J. Williams, *Angew. Chem., Int. Ed. Engl.*, **1992**, *31*, 1475.

[42] J. Z. Zhao, H.-J. Kim, J. Oh, S.-Y. Kim, J. W. Lee, S. Sakamoto, K. Yamaguchi and K. Kim, *Angew. Chem. Int. Ed.*, **2001**, *40*, 4233.

[43] S. Y. Jon, N. Selvapalam, D. H. Oh, J-K. Kang, S-Y. Kim, Y-J. Jeon, J-W. Lee, K. Kim, *J. Am. Chem. Soc.*, **2003**, *125*, 10186.

[44] N. Zhao, G. O. Lloyd and O. A. Scherman, *Chem. Commun.*, **2012**, *48*, 3070–3072.

[45] Y. Ahn, Y. Jang, N. Selvapalam, G. Yun and K. Kim, *Angew. Chem. Int. Ed.*, **2013**, *52*, 3140–3144.

[46] B. Vinciguerra, L. Cao, J. R. Cannon, P. Y. Zavalij, C. Fenselau and L. Isaacs, *J. Am. Chem. Soc.*, **2012**, *134*, 13133–13140.

[47] L. Gilberg, M. S. A. Khan, M. Enderesova and V. Sindelar, *Org. Lett.*, **2014**, *16*, 2446–2449.

[48] L. Isaacs, S.-K. Park, S. M. Liu, Y. H. Ko, N. Selvapalam, Y. Kim, H. Kim, P. Y. Zavalij, G.-H. Kim, H.-S. Lee and K. Kim, *J. Am. Chem. Soc.*, **2005**, *127*, 18000.

[49] Y. Miyahara, K. Goto, M. Oka, T. Inazu, *Angew. Chem. Int. Ed.*, **2004**, *43*, 5019-5022.

[50] W.-H. Huang, S. M. Liu, P. Y. Zavalij and L. Isaacs, *J. Am. Chem. Soc.*, **2006**, *128*, 14744.

[51] W.-H. Huang, P. Y. Zavalij and L. Isaacs, *Angew. Chem. Int. Ed.*, **2007**, *46*, 7425.

[52] J. Svec, M. Necas, V. Sindelar, *Angew. Chem., Int. Ed.*, **2010**, *49*, 2378-2381.

[53] J. Lagona, P. Mukhopadhyay, S. Chakrabarti, L. Isaacs, *Angew. Chem. Int. Ed.*, **2005**, *44*, 4844-4870.

[54] J. W. Lee, S. Samal, N. Selvapalam, H.-J. Kim, K. Kim, *Acc. Chem. Res.,* **2003**, *36*, 621-630.

[55] H.-J. Buschmann, E. Cleve, K. Jansen, A. Wego, E. Schollmeyer, *Mater. Sci. Eng. C*, **2001**, *114*, 35-39.

[56] K. Jansen, H.-J. Buschmann, A.Wego, D. Döpp, C. Mayer, H. J. Drexler, H. J. Holdt, E. Schollmeyer, *J. Inclusion Phenom. Macrocyclic Chem.*, **2001**, *39*, 357-363.

[57] S. Moghaddam, C. Yang, M. Rekharsky, Y. H. Ko, K. Kim, Y. Inoue and M. K. Gilson, *J. Am. Chem. Soc.*, **2011**, *133*, 3570.

[58] I. Hwang, K. Baek, M. Jung, Y. Kim, K. M. Park, D.-W. Lee, N. Selvapalam, K. Kim, *J. Am. Chem. Soc.*, **2007**, *129*, 4170.

[59] D. Sobransingh, A. E. Kaifer, *Langmuir*, **2006**, *22*, 10540.

[60] L. P. Cao, M. Sekutor, P. Y. Zavalij, K. Mlinaric-Majerski, R. Glaser, L. Isaacs, *Angew. Chem. Int. Ed.*, **2014**, *53*, 988.

[61] M. Sekutor, K. Molcanov, L. P. Cao, L. Isaacs, R. Glaser, K. Mlinaric-Majerski, *Eur. J. Org. Chem.*, **2014**, 2533.

[62] W. L. Mock, N.-Y. Shih, *J. Org. Chem.*, **1986**, *51*, 4440-4446.

[63] W. L. Mock, N.-Y. Shih, *J. Am. Chem. Soc.*, **1988**, *110*, 4706.

[64] H. Letheby, *J. Chem. Soc.*, **1862**, *15*, 161-163.

[65] C. K. Chiang, M. A. Druy, S. C. Gau, A. J. Heeger, E. J. Louis, A. G. MacDiarmid, Y. W. Park, H. Shirakawa, *J. App. Phys.*, **1983**, *54*, 3255-3259.

[66] A. J. Epstein, J. M. Ginder, F. Zuo, R. W. Bigelow, H. Woo, D. B. Tanner, A. F. Richter, W. Huang, G. A. MacDiarmid, *Synth. Met.*, **1987**, *18*, 303-309.

[67] C. K. Chiang, C. R. Fincher, Y. W. Park, A. J. Heeger, H. Shirakawa, E. J. Louis, S. C. Gau, A. G. MacDiarmid, *Phys. Rev. Lett.*, **1977**, *39*, 1098-1101.

[68] https://www.nobelprize.org/nobel_prizes/chemistry/laureates/2000/

[69] N. Toshima, S. Hara, *Prog. Polym. Sci.*, **1995**, *20*, 155.

[70] J. Roncali, *Chem. Rev.*, **1992**, *92*, 711.

[71] S. Sadki, P. Schottland, N. Brodie, G. Sabouraud, *Chem. Soc. Rev.*, **2000**, *29*, 283.

[72] https://www.nobelprize.org/nobel_prizes/chemistry/laureates/2010/

[73] R. F. Heck, J. P. Nolley, *J. Org. Chem.*, **1972**, *37*, 2320-2322.

[74] D. Milstein, J. K. Stille, *J. Am. Chem. Soc.*, **1978**, *100*, 3636-3638.

[75] D. Milstein, J. K. Stille, *J. Am. Chem. Soc.*, **1979**, *101*, 4992-4998.

[76] N. Miyaura, K. Yamada, A. Suzuki, *Tetrahedron Lett.*, **1979**, *20*, 3437-3440.

[77] N. Miyaura, A. Suzuki, *J. Chem. Soc., Chem. Commun.*, **1979**, 866-867.

[78] Y-J. Cheng, S-H. Yang, C-S.Hsu, *Chem. Rev.*, **2009**, *109*, 5868-5923.

[79] A. Imamura, Y. Aoki, *Int. J. Quantum Chem.*, **2006**, *106*, 1924-1933.

[80] J. C. Koziar, D. O. Cowan, *Acc. Chem. Res.*, **1978**, *11*, 334-341.

[81] G. Li, W-H. Chang, Y. Yang, *Nat. Rev. Mater.*, **2017**, *2*, 17043.

[82] M. Liu, Y. Gao, Y. Zhang, Z. Liu, L. Zhao, *Polym. Chem.*, **2017**, *8*, 4613-4636.

[83] H. Yao, W. Zhao, Z. Zheng, Y. Cui, J. Zhang, Z. Wei, J. Hou, *J. Mater. Chem. A*, **2016**, *4*, 1708-1713.

[84] W. Zhong, K. Li, J. Cui, T. Gu, L. Ying, F. Huang, Y. Cao, *Macromolecules*, **2017**, *50*, 8149-8157.

[85] J. H. Burroughes, D. D. C. Bradley, A. R. Brown, R. N. Marks, K. Mackay, R. H. Friend, P. L. Burns, A. B. Holmes, *Nature*, **1990**, *347*, 539-541.

[86] Z. Hu, K. Zhang, F. Huang, Y. Cao, *Chem. Commun.*, **2015**, *51*, 5572-5585.

[87] X. Yang, G. Zhou, W-Y. Wong, *J. Mater. Chem. C.*, **2014**, *2*, 1760-1778.

[88] M. Morales-Vidal, P. G. Boj, J. M. Villavilla, J. A. Quintana, Q. Yan, N-T. Lin, X. Zhu, N. Ruangsupapichat, J. Casado, H. Tsuji, E. Nakamura, M. A. Diaz-Garcia, *Nature Communications*, **2015**, *6*, 8458.

[89] X. Wu, B. Xu, H. Tong, L. Wang, *Macromolecules*, **2011**, *44*, 4241-4248.

[90] X. Wang, Y-G. Kim, C. Drew, B-C. Ku, J. Kumar, L. A. Samuelson, *Nano Letters*, 2004, *4*, 331-334.

[91] K. Krukiewicz, J. K. Zak, *J. Mater. Sci.*, **2014**, *49*, 5738-5745.

[92] S. Liu, Y. Fu, G. Li, L. Li, H. K. Law, X. Chen, F. Yan, *Adv. Mater.*, **2017**, *29*, 1701733.

[93] X. Feng, F. Lv, L. Liu, H. Tang, C. Xing, Q. Yang, S. Wang, *ACS Appl. Mater. Interfaces*, **2010**, *2*, 2429-2435.

[94] T. Repenko, A. Rix, S. Ludwanowski, D. Go, F. Kiessling, W. Lederle, A. J. C. Kuehne, *Nature Communications*, **2017**, *8*, 470.

[95] K. Landfester, *Adv. Mater.*, **2001**, *13*, 765-768.

[96] L. Feng, C. Zhu, H. Yuan, L. Liu, F. Lv, S. Wang, *Chem. Soc. Rev.*, **2013**, *42*, 6620-6633.

[97] E-J. Park, T. Erdem, V. Ibrahimova, S. Nizamoglu, H. V. Demir, D. Tuncel, *ACS Nano*, **2011**, *5*, 2483-2492.

[98] F. A. Boroumand, P. W. Fry, D. G. Lidzey, *Nano Lett.*, **2005**, *5*, 67-71.

[99] T. Kietzke, D. Nehrer, K. Landfester, R. Montenegro, R. Guntner, U. Scherf, *Nature Mater.*, **2003**, *2*, 408.

[100] S. Gunes, H. Neugebauer, N S. Sariciftci, *Chem. Rev.*, **2007**, *107*, 1324-1338.

[101] C. F. Wu, T. Schneider, M. Zeigler, J. B. Yu, P. G. Schiro, D. R. Burnham, J. McNeill, D. T. Chiu, *J. Am. Chem. Soc.*, **2010**, *132*, 15410–15417.

[102] X. L. Feng, G. M. Yang, L. B. Liu, F. T. Lv, Q. Yang, S. Wang, D. B. Zhu, *Adv. Mater.*, **2012**, *24*, 637–641.

[103] P. K. Kandel, L. P. Fernando, P. C. Ackroyd, K. A. Christensen, *Nanoscale*, **2011**, *3*, 1037–1045.

[104] X. L. Feng, Y. L. Tang, X. R. Duan, L. B. Liu, S. Wang, *J. Mater. Chem.*, **2010**, *20*, 1312–1316.

[105] A. T. Silva, A. Nguyen, C. M. Ye, J. Verchot, J. H. Moon, *BMC Plant Biol.*, **2010**, *10*, 291–304.

[106] C. F. Xing, Q. L. Xu, H. W. Tang, L. B. Liu, S. Wang, *J. Am. Chem. Soc.*, **2009**, *131*, 13117–13124.

[107] L. D. Lu, F. H. Rininsland, S. K. Wittenburg, K. E. Achyuthan, D. W. McBranch, D. G. Whitten, *Langmuir*, **2005**, *21*, 10154–10159.

[108] P. Rothemund, *J. Am. Chem. Soc.*, **1935**, *57*, 2010-2011.

[109] P. Rothemun, *J. Am. Chem. Soc.*, **1936**, *58*, 625-627.

[110] P. Rothemund, A. R. Menotti, *J. Am. Chem. Soc.*, **1941**, *63*, 267-270.

[111] A. D. Adler, F. R. Longo, W. Shergalis, *J. Am. Chem. Soc.*, **1964**, *86*, 3145-3149.

[112] A. D. Adler, F. R. Longo, J. D. Finarelli, J. Assour, L. Korsakoff, *J. Org. Chem.*, **1967**, *32*, 476.

[113] Z-C. Sun, Y-B. She, Y. Zhou, X-F. Song, K. Li, *Molecules*, **2011**, *16*, 2960-2970.

[114] J. S. Lindsey, I. C. Schreiman, H. C. Hsu, P. C. Kearney, A. M. Marguerettaz, *J. Org. Chem.*, **1987**, *52*, 827-836.

[115] L. T. Nguyen, M. O. Senge, K. M. Smith, *J. Org. Chem.*, **1996**, *61*, 998-1003.

[116] M. R. Johnston, M. J. Latter, R. N. Warrener, *Org. Lett.*, **2002**, *4*, 2165-2168.

[117] J.G. Levy, M. Obochi, *Photochem. Photobiol.* **1996**, *64*, 737–739.

[118] T. J. Dougherty, C. J. Gomer, B. W. Henderson, G. Jori, D. Kessel, M. Korbelik, J. Moan, Q. Peng, *J. Natl. Cancer Inst.*, **1998**, *90*, 889-905.

[119] R. Bonnett, G. Martinez, *Tetrahedron*, **2001**, *57*, 9513-9547.

[120] D. E. Dolmans, D. Fukumura, R. K. Jain, *Nat. Rev. Cancer*, **2003**, *3*, 380-387.

[121] M. Ethirajan, Y. Chen, P. Joshi, R. K. Pandey, *Chem. Soc. Rev.*, **2011**, *40*, 340-362.

[122] P. Agostinis, K. Berg, K. A. Cengel, T. H. Foster, A. W. Girotti, S. O. Gollnick, S. M. Hahn, M. R. Hamblin, A. Juzeniene, D. Kessel, M. Korbelik, J. Moan, P. Mroz, D. Nowis, J. Piette, B. C. Wilson, J. Golab, *CA Cancer J. Clin.*, **2011**, *61*, 250-281.

[123] R. L. Lipson, E. J. Baldes, *Arch. Dermatol.*, **1960**, *82*, 508.

[124] G. Casiraghi, M. Cornia, F. Zanardi, G. Rassu, E. Ragg, R. Bortolini, *J. Org. Chem.*, **1994**, *59*, 1801-1808.

[125] J. Kralova, Z. Kejik, T. Briza, P Pouckova, A. Kral, P. Martasek, V. Kral, *J. Med. Chem.*, **2010**, *53*, 128-138.

[126] K. Nakano, K. Tajima, *Adv. Mater.*, **2017**, *29*, 1603269.

[127] S. E. Root, S. Savagatrup, A. D. Printz, D. Rodriquez, D. J. Lipomi, *Chem. Rev.*, **2017**, *117*, 6467.

[128] A. C. Grimsdale, K. L. Chan, R. E. Martin, P. G. Jokisz, A. B. Holmes, *Chem. Rev.*, **2009**, **109**, 897.

[129] A. Facchetti, *Chem. Mater.*, **2011**, *23*, 733.

[130] A. Koc, D. Tuncel, *Isr. J. Chem.*, **2018**, *58*, 334-342.

[131] R. Eelkema, K. Maeda, B. Odell, H. L. Anderson, J. Am. Chem. Soc., **2007**, *129*, 12384-5.

[132] A. Farcas, P.-H. Aubert, J. Mohanty, A. I. Lazar, S. Cantin, W. M. Nau, European Polymer Journal, **2015**, *62*, 124–129.

[133] M. Idris, M. Bazzar, B. Guzelturk, H. V. Demir, D. Tuncel, RSC Adv., **2016**, *6*, 98109.

[134] T. Erdem, M. Idris, H. V. Demir, D. Tuncel, Macromol. Mater. Eng., **2017**, *302*, 1700290.

[135] J. Pennakalathil, E. Jahja, E. Sıla Ozdemir, O. Konu, D. Tuncel, Biomacromolecules, **2014**, *15*, 3366-3375.

[136] H. Bai, H. Chen, R. Hu, M. Li, F. Lv, L. Liu, S. Wang, ACS Appl. Mater. Interfaces, 2016, 8, 31550-31557. [137] H. Bai, H. Yuan, C. Nie, B. Wang, F. Lv, L. Liu, S. Wang, *Angew. Chem., Int. Ed.*, **2015**, *54*, 13208-13213.

[138] H. Bai, H. Zhang, R. Hu, H. Chen, F. Lv, L. Liu, S. Wang, *Langmuir*, **2017**, *33*, 1116-1120.

[139] D. Tuncel, N. Cındır, U. Koldemir, *J. Incl. Phenom. Macrocycl. Chem.*, **2006,** *55*, 373-380.

[140] J. Mohanty, A. C. Bhasikuttan, S. D. Choudhury, H. Pal, *J. Phys. Chem. B*, **2008**, *112*, 10782-10785.

[141] N. Barooah, A. C. Bhasikuttan, V. Sudarsan, S. D. Choudhury, H. Pal, J. Mohanty, *Chem. Commun.*, **2011**, *47*, 9182-9184.

[142] M. Fathalla, N. L. Strutt, J. C. Barnes, C. L. Stern, C. Ke, J. F. Stoddart, *Eur. J. Org. Chem.*, **2014**, 2873-2877.

[143] K. Liu, Y. Liu, Y. Yao, H. Yuan, S. Wang, Z. Wang, X. Zhang, *Angew. Chem., Int. Ed.*, **2013**, *52*, 8285-8289.

[144] L. Chen, H. Bai, J-F. Xu, S. Wang, X. Zhang, *ACS Appl. Mater. Interfaces*, **2017**, *9*, 13950-13957.

[145] W. Lei, G. Jiang, Q. Zhou, B. Zhang, X. Wang, *Phys. Chem. Chem. Phys.*, **2010**, *12*, 13255–13260.

[146] J. Caceres, J. Robinson-Duggon, A. Tapia, C. Paiva, M. Gomez, C. Bohne, D. Funetalba, *Phys. Chem. Chem. Phys.*, **2017**, *19*, 2574.

[147] L. Wen, M. Li, J. B. Schlenoff, *J. Am. Chem. Soc.*, **1997**, *119*, 7726-7733.

[148] B. F. Hoskins, R. Robson, D. A. Slizys, J. Am. Chem. Soc., **1997**, *119*, 2952-2953.

[149] D. Jiao, F. Biedermann, O. A. Scherman, *Org. Lett.*, **2011**, *12*, 3044-3047.

[150] R. Khan, M. Idris, D. Tuncel, *Org. Biomol. Chem.*, **2015**, *13*, 10496-10504.

[151] R. A. Caims, I. S. Harris, T. W. Mak, *Nat. Rev. Cancer*, **2011**, *11*, 85.

[152] K. Kim, N. Selvapalam, D. H. Oh, *J. of. Incl. Phenom. Macrocyclic Chem.*, **2004**, *50*, 31-36.

[153] J. Q. Umberger, V. K. LaMer, *J. Am. Chem. Soc.*, **1945**, *67*, 1099-1109.

[154] R. F. Kubin, A. N. Fletcher, *J. Lumin.*, **1983**, *27*, 455-462.

[155] A. Koc, R. Khan, D. Tuncel, *Chem. Eur. J.*, **2018**, *24*, 15550-15555.

Appendix

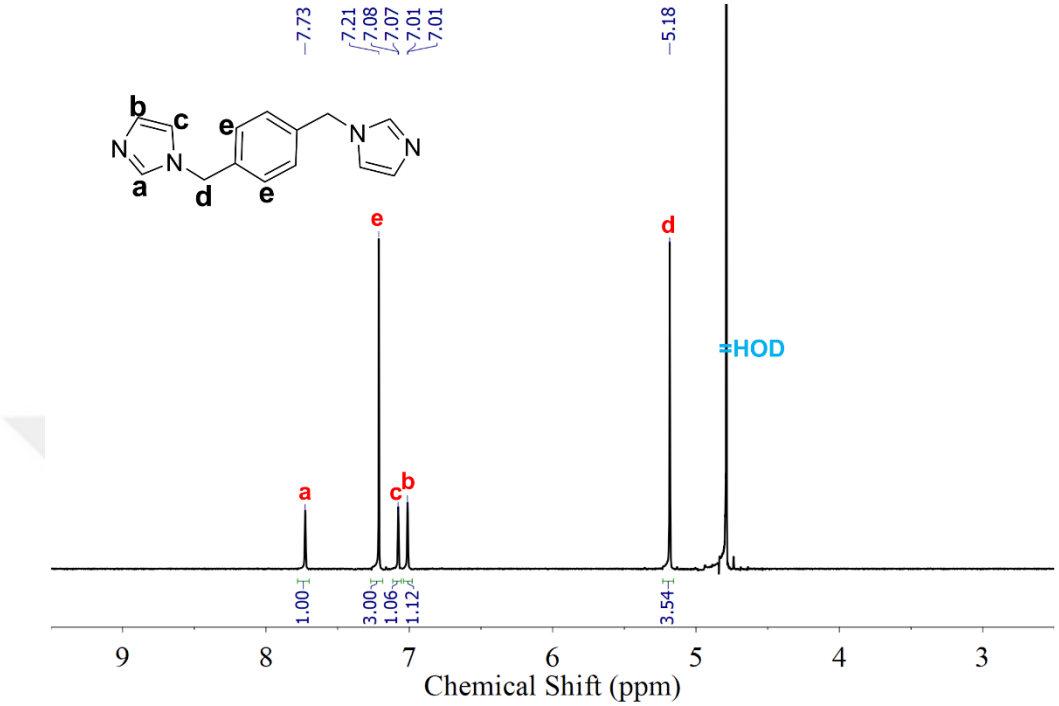


Figure A1 ^{1}H NMR spectrum of compound **4** in D_2O.

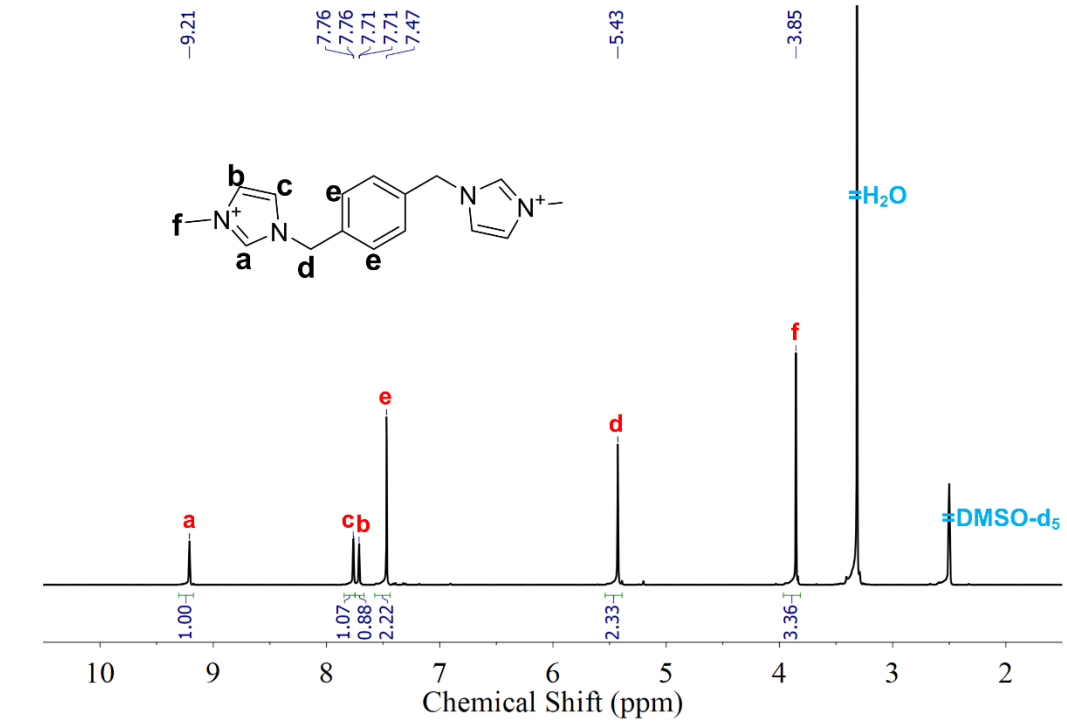


Figure A2 ^{1}H NMR spectrum of compound **5** in DMSO-d_6.

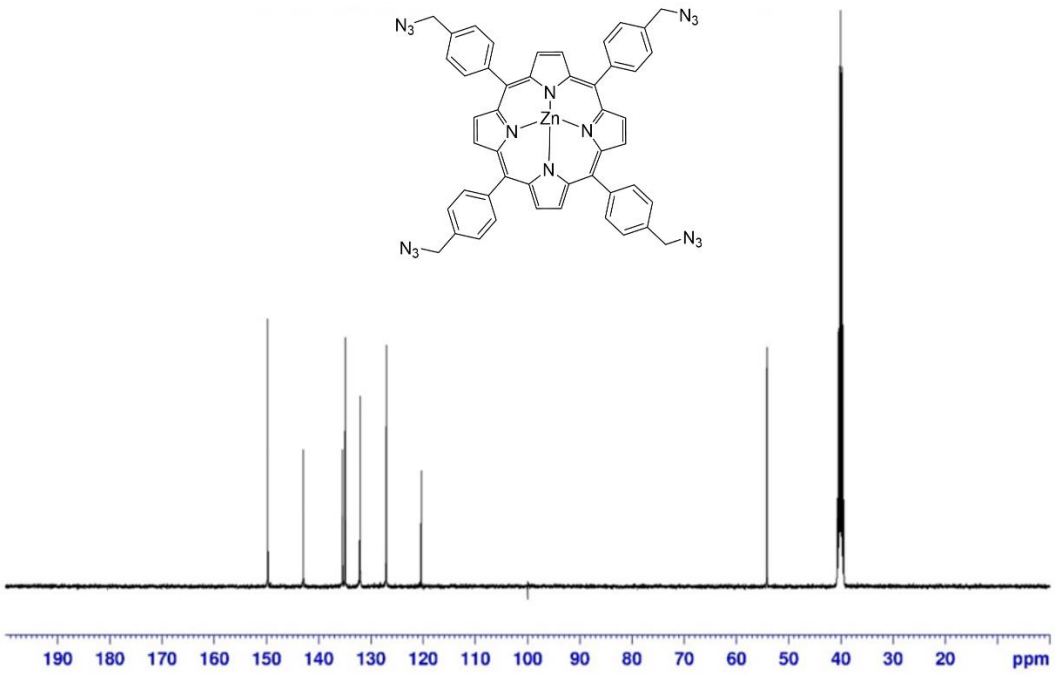


Figure A3 ^{13}C NMR spectrum of Zn-TPP-N_3 in DMSO-d_6.

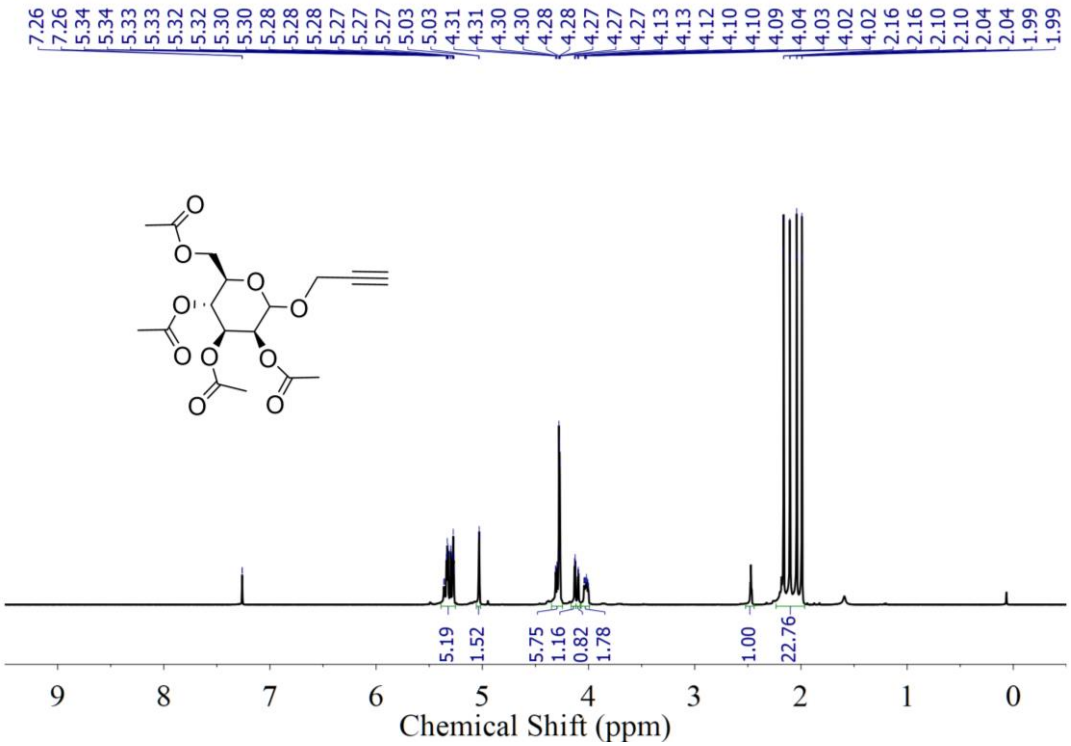


Figure A4 ^{1}H NMR spectrum of acetylated propargylated mannose in $CDCl_3$.

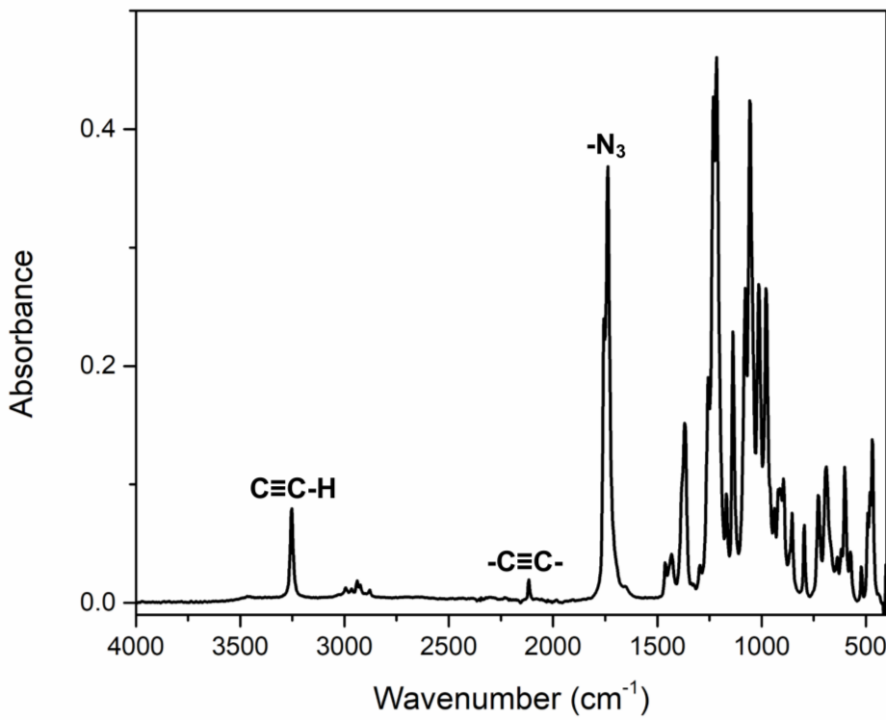


Figure A5 FT-IR spectrum of acetylated propargylated mannose.

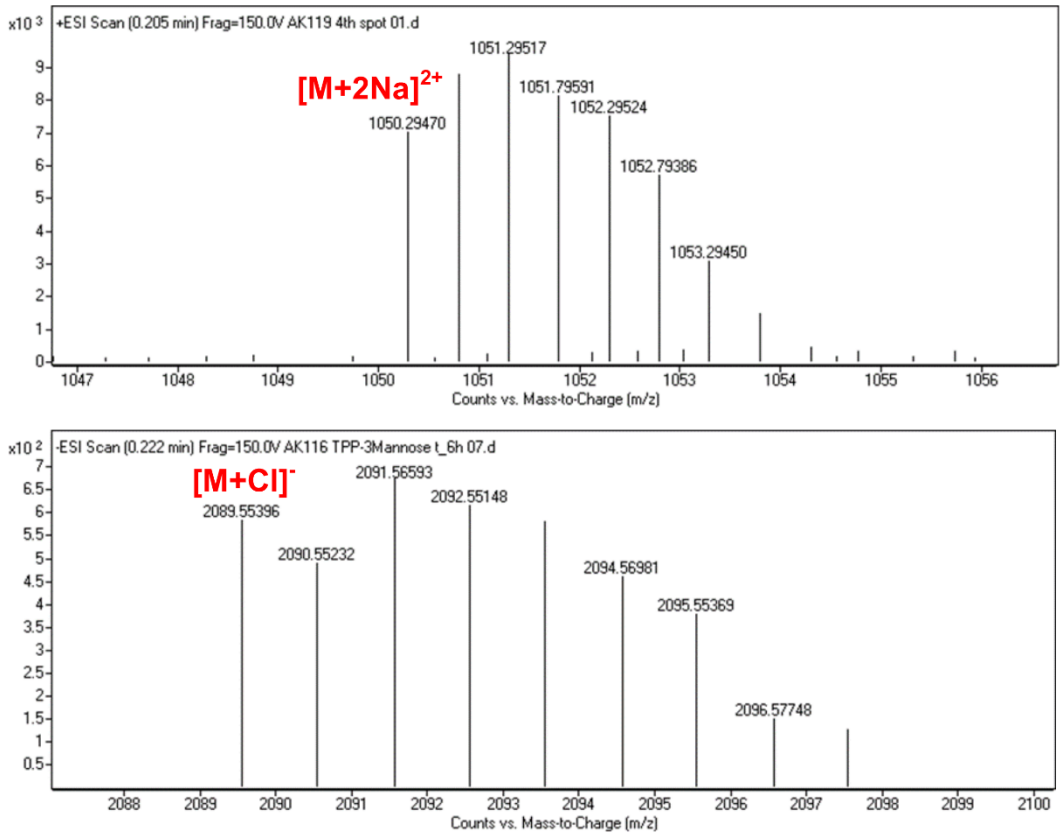


Figure A6 ESI-MS spectra of TPP-Az-3AcMan.

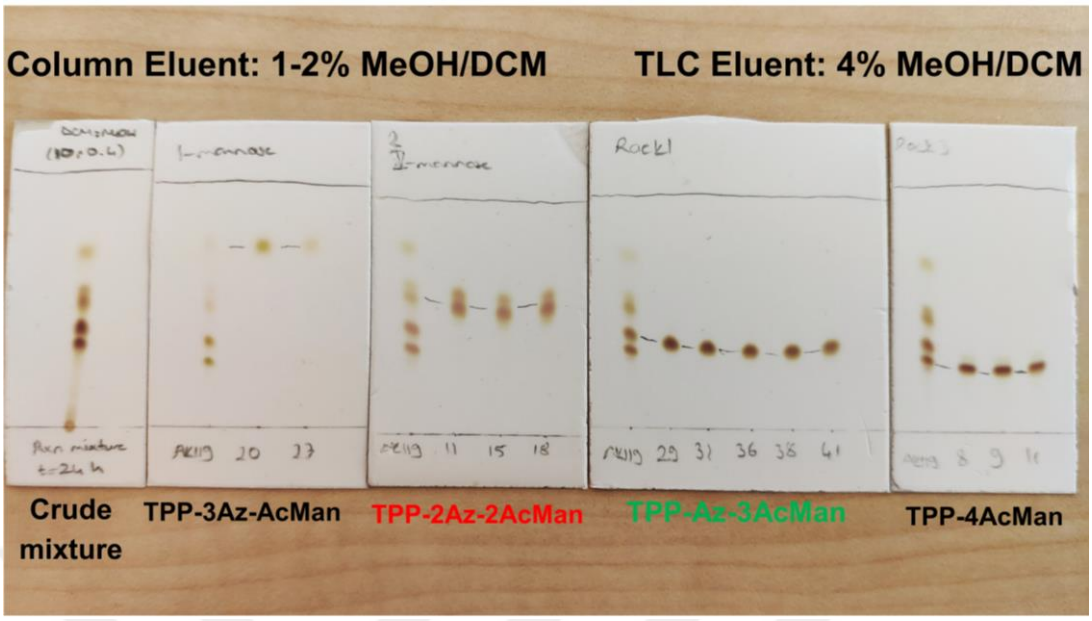


Figure A7 Photos of the TLC plate of crude mixture after mannosylation of TPP and TLC monitoring of the silica gel column for the separation of products: TPP-3Az-AcMan, TPP-2Az-2AcMan, TPP-Az-3AcMan, TPP-4AcMan.



Figure A8 A sample of TPP-3Man-CB7 (**11**) in water/DMSO (4/1, v/v) mixture. Solution is clear over several days.

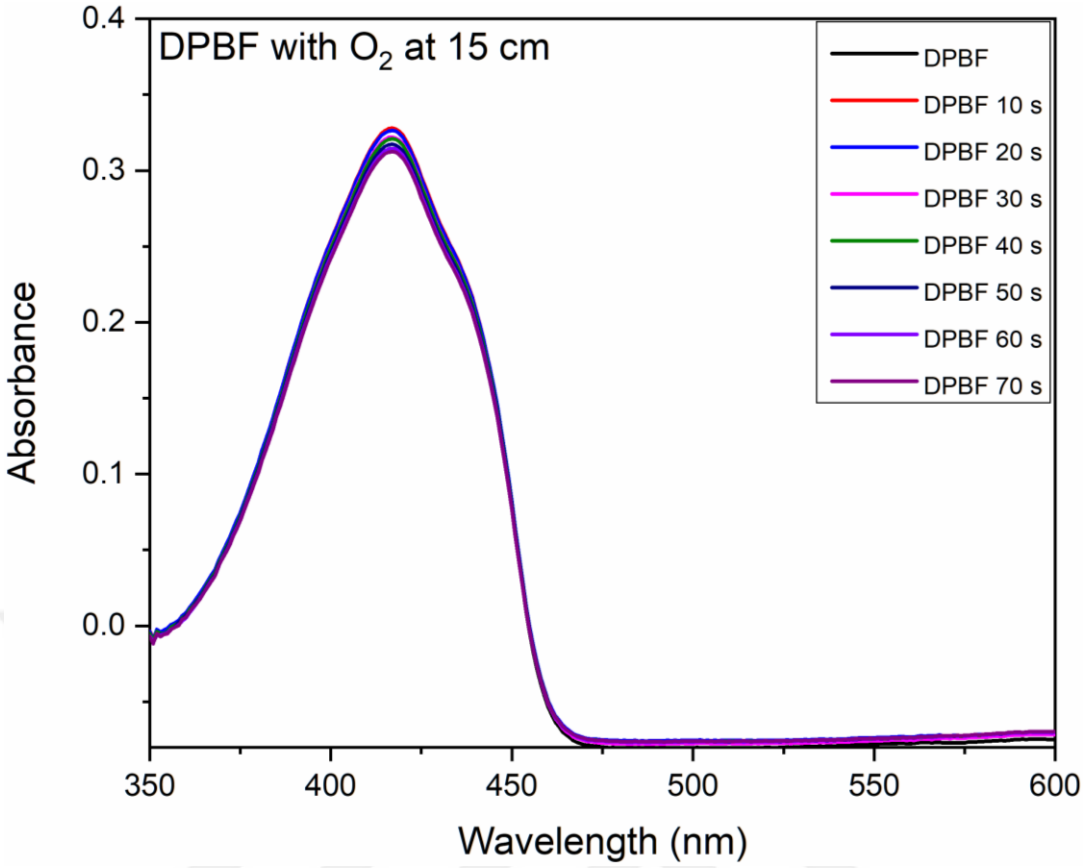


Figure A9 Monitoring the change in absorbance intensity of DPBF saturated with O_2 with 10 sec irradiation intervals in the absence of any photosensitizers. Its seen that absorbance intensity of DPBF does not decrease when there is no photosensitizer in the solution that can generate $^1O_2$.

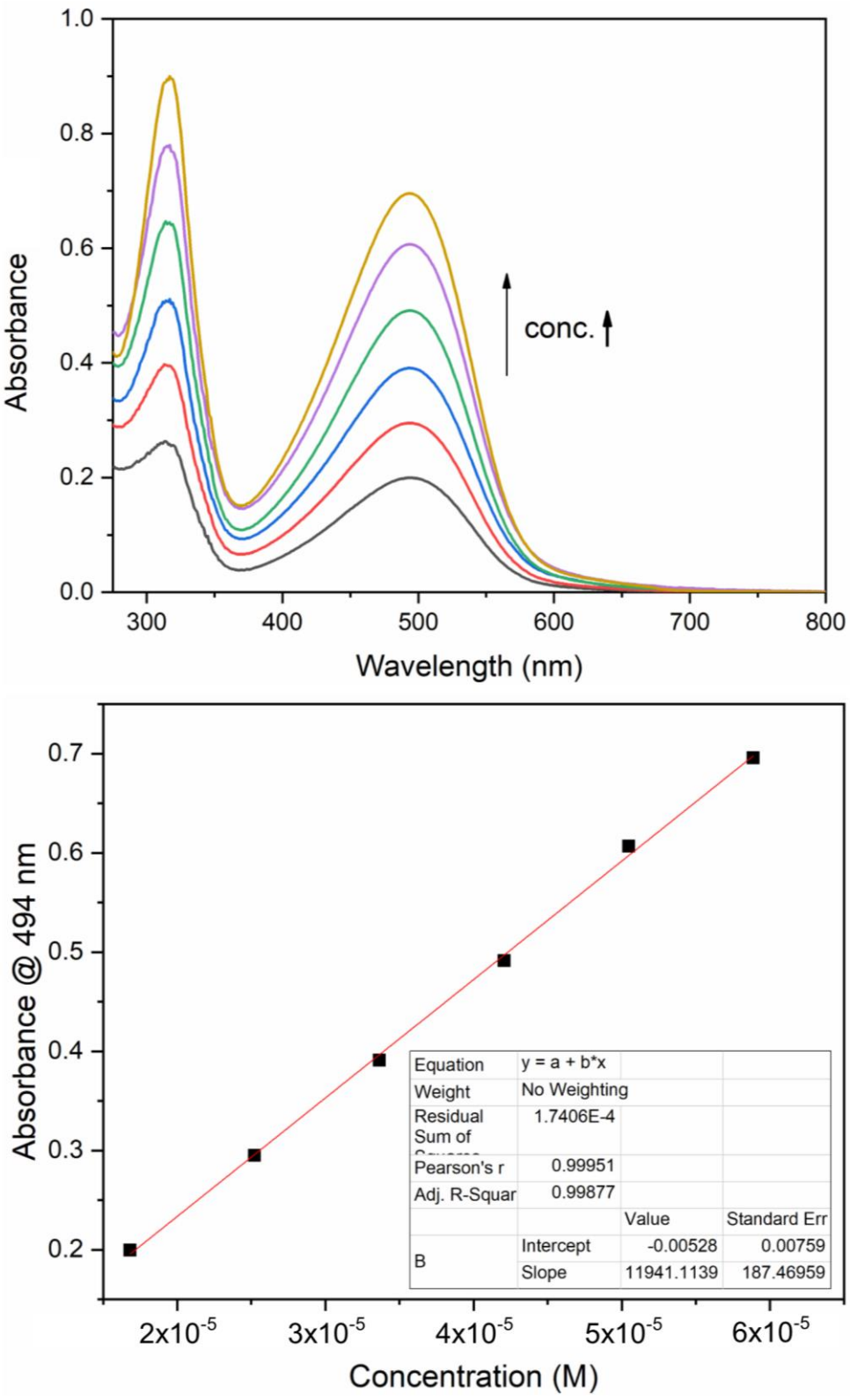


Figure A10 UV-Vis absorbance spectra of **P1** at different concentrations and absorbance vs. concentration plot for the calculation of molar extinction coefficient.

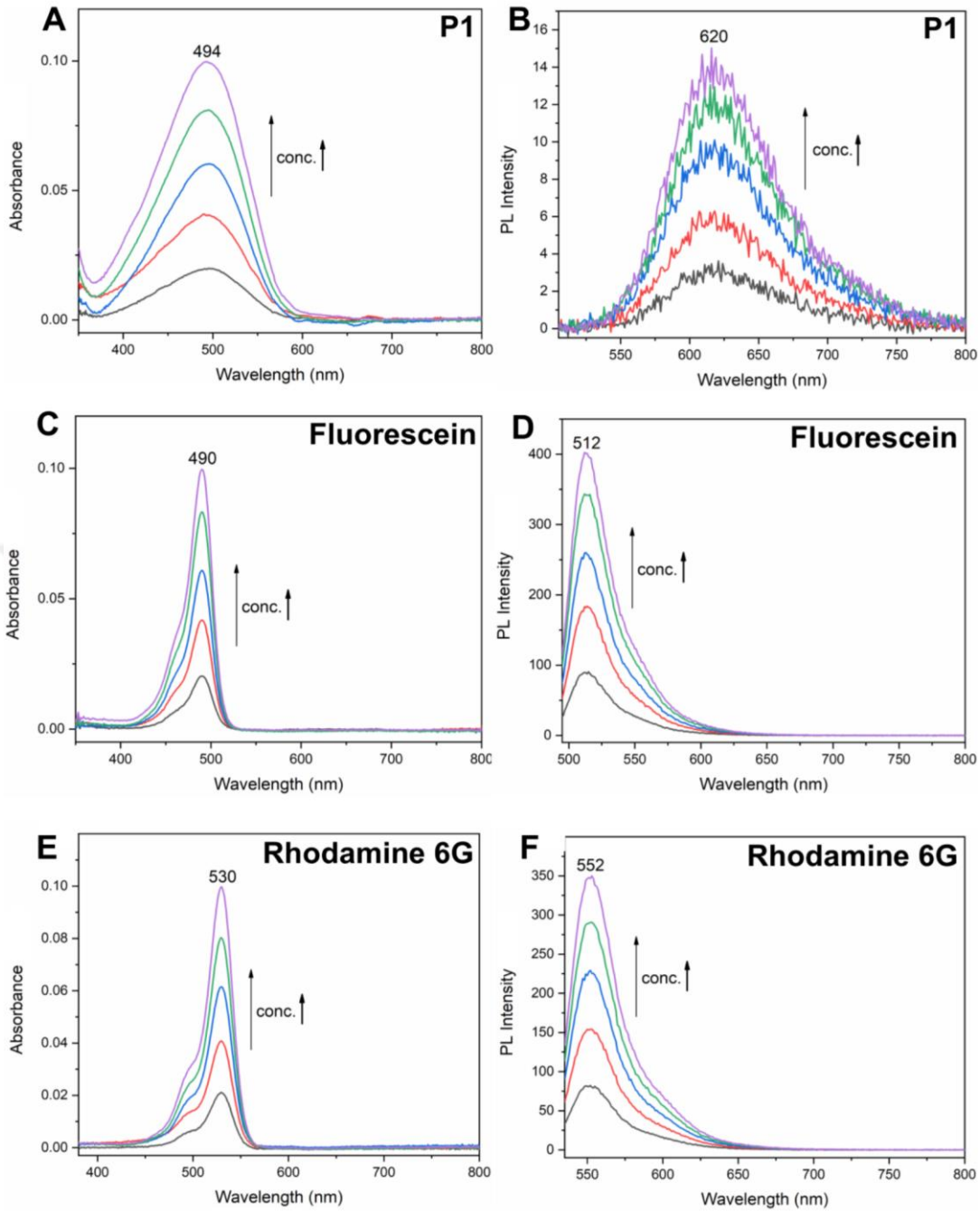


Figure A11 UV-Vis absorbance and fluorescence spectra of **P1** (A, B), Fluorescein (C, D) and Rhodamine 6G (E, F) at various concentrations for fluorescence quantum yield calculations.

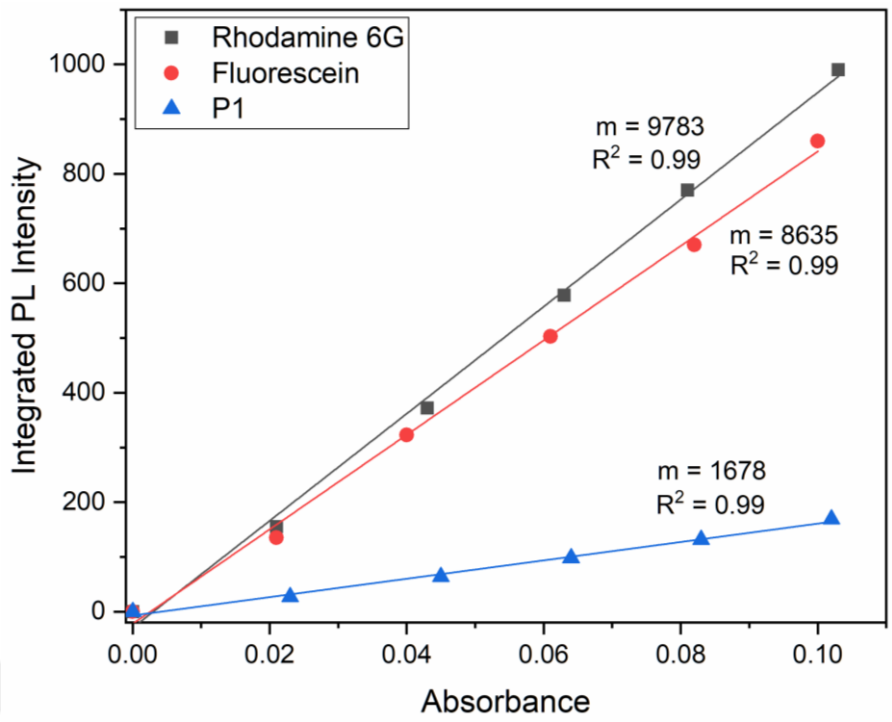


Figure A12 Linearized integrated PL intensity vs. absorbance graphs of **P1** (A, B), Fluorescein (C, D) and Rhodamine 6G (E, F) at various concentrations for fluorescence quantum yield calculations.